UAB

Universitat Autònoma de Barcelona

Atomic layer deposition:
From molecular chemistry to functional oxide coatings

UAB

Universitat Autònoma
de Barcelona

Pengmei Yu

Thesis submitted for the degree of Doctor of Philosophy
PhD programme in Materials Science

Supervisor: Dra. Mariona Coll

Institut de Ciència de Materials de Barcelona
(ICMAB-CSIC)

October 2020

UAB
Universitat Autònoma de Barcelona

Memòria presentada per aspirar al Grau de Doctor per:

PENGMEI YU

Vist i plau directors:

……………………….

Dra. Mariona Coll
Supervisor
Superconductor Materials and Large-Scale Nanostructures,
Institut de Ciència de Materials de Barcelona (ICMAB-CSIC)

……………………….

Dra. Eva Pellicer Vilà
Tutor
Physics Department, Sciences Faculty
Autonomous University of Barcelona

Bellaterra, October 2020

The only way
of discovering the limits of the possible
is to venture a little way past them into the impossible

- Arthur C. Clarke

Acknowledgements

Motivation

Nano-sized transition metal oxides offer high richness in composition, structure and properties that are intriguing for diverse aspects of modern technology such as batteries, solar cells, flat panel displays, sensors, memories and drug delivery. Accordingly, the fabrication of nanostructured transition metal oxides, specially thin films, with atomic precision, is undoubtedly a generic goal in materials science. Being an enabling technique, the development of new atomic layer deposition (ALD) synthesis strategies for transition metal oxide nanomaterials could significantly improve the materials performance and broaden their application fields.

In order to progress in this direction, it is crucial to dispose from a wide variety of metalorganic precursors with rich chemistries to be able to synthesize the target materials with desired compositions. Also, it is important to better understand the relationship between the precursor chemistry and the final film properties.

Among the family of transition metal-based oxides, multicomponent oxides based on ferrites and rare-earth elements have captivated considerable attention owing to their magnetic, magneto-optical and ferroelectric properties. Being able to synthesize them as ultrathin films with nanoscale control can bring benefits in various electronic technologies. Nonetheless, the range of compatible metalorganic precursors is rather narrow. The evaluation of tailor-made precursors for the development of ALD processes will offer many opportunities to prepare these materials and engineer their properties.

Another key aspect, specially when conformal coatings are pursued, is to investigate the reactivity between the metalorganic precursor with the substrate surface. The deposition of transition metal oxides on inert carbon nanotubes, for instance, has been a long-standing challenge among researchers. Investigating approaches to activate and improve the reactivity on carbonaceous surfaces for the subsequent metal oxide deposition can give us valuable information and be of great relevance in the development of future technologies such as the fabrication of electrode materials for energy-storage devices.

In this thesis, it is expected to help broadening the ALD toolkit with precursor choices and processes for ALD Co_3O_4 and $Gd_xFe_yO_z$ systems, and contribute to the understanding of the surface chemistry between ALD Fe_2O_3 and carbon surfaces, which would be of interest not only for the

ALD community but it can also impact the fabrication of improved devices for energy-storage (Co_3O_4 and Fe_2O_3), and for magnetic and spintronic applications ($Gd_xFe_yO_z$).

Abstract

The synthesis of transition metal oxides by atomic layer deposition (ALD) is contributing to the development of nanomaterials, structures and devices that are difficult to achieve by traditional deposition techniques and hold promising characteristics for various application areas such as energy, electronics and health. Research on developing more robust ALD processes for transition metal oxides, expanding the library of compositions and facilitating their integration with other materials are thus of great relevance. The main objective of this thesis is to contribute to the development of ALD processes of transition metal oxide-based thin films and conformal coatings, and to shed light on the relevant reactivity between the metalorganic precursors and substrate surfaces to guide potential applications. In particular, the efforts have been focused on the following aspects:

1. Explore a novel cobalt precursor (β-heteroarylalkenolate Cobalt) to deposit ALD Co_3O_4 films. The introduction of heteroaryl moieties and CF_3- groups, compared to commercial precursors, offers higher precursor stability and safe handling at ambient conditions. ALD deposition conditions have been thoroughly investigated by optimizing precursor pulse length, deposition temperature and film thickness dependence on the number of ALD cycles. It is shown that this chemistry favors the formation of ALD Co_3O_4 thin films and conformal coatings when combined with ozone as oxidant.

2. Compare the suitability of a heterobimetallic Gd-Fe precursor versus separate metalorganic sources of Gd and Fe to deposit magnetic $Gd_xFe_yO_z$ ternary oxide thin films. The novel heterobimetallic single-source Gd-Fe complex which contains 1Gd:1Fe stoichiometric ratio, facilitates the epitaxial stabilization of $GdFeO_3$ thin films on $SrTiO_3$ single crystal substrates when combined with ozone. Alternatively, we seek the opportunity to synthesize $Gd_xFe_yO_z$ ternary oxides from separate Gd and Fe precursors, with different precursor chemistries, via the supercycle approach. For that, it has been explored the use of two tailor-made precursors: a fully N-coordinated gadolinium guanidinate and a mixed O,N- coordinated iron ketoiminate. The behavior of the iron ketoiminate has been compared to the commercially available ferrocene. The

reactivity of each precursor has been tested with water and ozone as co-reactants. It is shown that the precursor chemistry affects both the composition and crystallinity of the deposited films. Magnetic properties of the resultant $Gd_xFe_yO_z$ oxide systems have been evaluated.

3. Investigate the influence of plasma treatments (N_2, H_2O) for carbon nanotubes (CNTs) on the subsequent deposition of conformal Fe_2O_3 coatings by ALD. It has been demonstrated that surface functionalization of the CNTs is essential to obtain more anchoring sites for achieving desirable coating homogeneity and that the ozone co-reactant plays a key role on it as well. Electrochemical measurements on the Fe_2O_3@CNTs nanocomposites have been carried out to correlate surface functionalization and ALD Fe_2O_3 layer quality with the electrochemical performance. This opens new opportunities for the fabrication of more efficient anodes for supercapacitors.
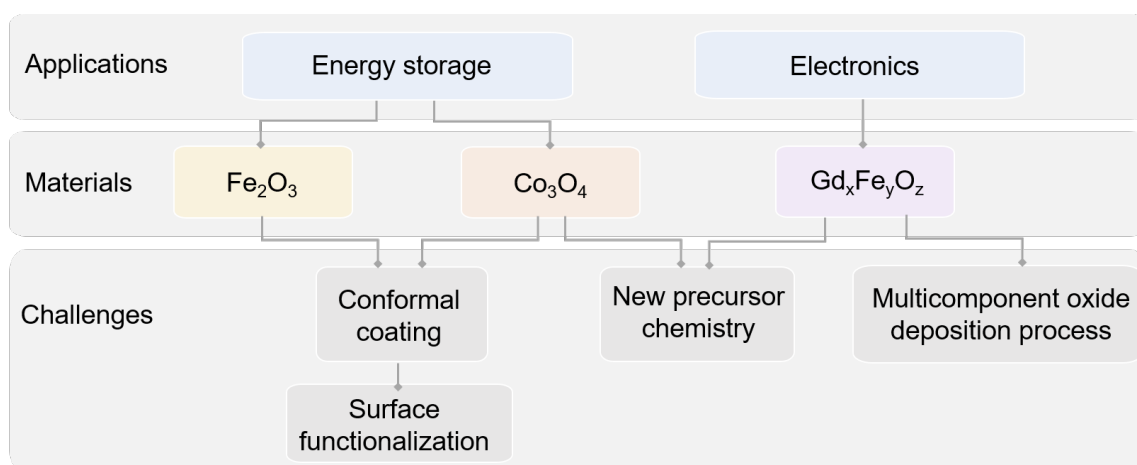
Scheme of the thesis identifying materials and challenges investigated by ALD and future applications.

Resumen

La síntesis de óxidos de metales de transición por depósito de capas atómicas (ALD) está contribuyendo al desarrollo de nanomateriales, estructuras y dispositivos que son difíciles de lograr mediante técnicas de depósito tradicionales y tienen características prometedoras para diversas áreas de aplicación como energía, electrónica y salud. Es importante desarrollar procesos de ALD más robustos para óxidos de metales de transición, ampliando la biblioteca de composiciones y facilitando su integración con otros materiales. El principal objetivo de esta tesis es contribuir al desarrollo de procesos de ALD para fabricar películas delgadas basadas en óxidos de metales de transición y recubrimientos conformales, y arrojar luz sobre la reactividad entre los precursores metalorgánicos y la superficie del sustrato para guiar posibles aplicaciones. En particular, los esfuerzos se han centrado en los siguientes aspectos:

1. Explorar un nuevo precursor de cobalto (β -heteroarilalquenolato de cobalto) para depositar películas de Co_3O_4 por ALD. La introducción de ligandos heteroarilo y grupos CF_3-, en comparación con los precursores comerciales, ofrece una mayor estabilidad del precursor y una manipulación segura en condiciones ambientales. Las condiciones de depósito de ALD se han investigado a fondo optimizando la duración del pulso del precursor, la temperatura de depósito y la dependencia del espesor de la película con el número de ciclos de ALD. Se muestra que esta química favorece la formación de películas delgadas de ALD Co_3O_4 y recubrimientos conformados cuando se combinan con ozono como oxidante.

2. Comparar la idoneidad de un precursor heterobimetálico de Gd-Fe versus fuentes metalorgánicas separadas de Gd y Fe para depositar películas delgadas de óxido ternario magnéticos de $Gd_x Fe_y O_z$. El novedoso complejo heterobimetálico de Gd-Fe, que contiene una relación estequiométrica de 1Gd: 1Fe, facilita la estabilización epitaxial de películas delgadas de $GdFeO_3$ en sustratos monocristalinos de $SrTiO_3$ cuando se combina con ozono. Alternativamente, buscamos la oportunidad de sintetizar óxidos ternarios de $Gd_x Fe_y O_z$ utilizando precursores separados de Gd y Fe sintetizados a medida: un guanidinato de gadolinio y un cetoiminato de hierro coordinado con O, N. El comportamiento del cetoiminato de hierro se ha comparado con el ferroceno, disponible

comercialmente. La reactividad de cada precursor se ha probado con agua y ozono como agentes oxidantes. Se muestra que la química del precursor afecta tanto a la composición como a la cristalinidad de las películas depositadas. Se han evaluado las propiedades magnéticas de los sistemas de óxido $Gd_x Fe_y O_z$ resultantes.

3. Investigar la influencia de los tratamientos con plasma (N_2, H_2O) en nanotubos de carbono (CNTs) en el posterior depósito de recubrimientos conformales de Fe_2O_3 por ALD. Se ha demostrado que la funcionalización de la superficie de los CNTs es esencial para obtener más sitios de anclaje para lograr la deseada homogeneidad del recubrimiento. El agente oxidante ozono también juega un papel clave. Se han llevado a cabo medidas electroquímicas en los nanocompuestos Fe_2O_3@CNTs para correlacionar la funcionalización de la superficie y la calidad de la capa de ALD Fe_2O_3 con el rendimiento electroquímico. Esto abre nuevas oportunidades para la fabricación de ánodos más eficientes para supercondensadores.
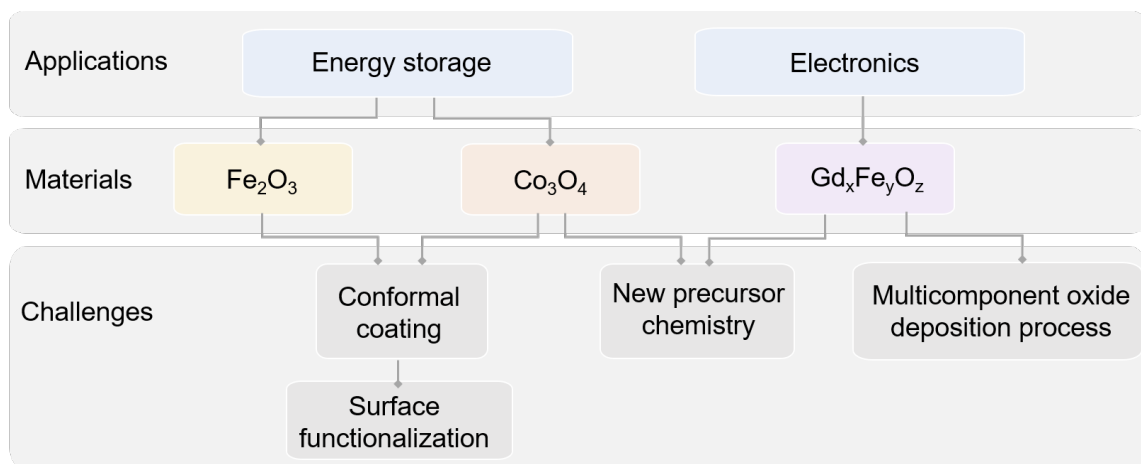
Esquema de la tesis resaltando el tipo de material, retos y posible futuras aplicaciones de dichos materiales preparados por ALD.

Outline

This thesis is organized as a set of three publications. First, there is an introductory chapter detailing the relevance to develop reliable processes to synthesize transition metal oxides with atomic precision and the basics of the atomic layer deposition technique. Then, there is a second chapter describing the experimental techniques employed. These two chapters are important to fully understand the work summarized on the subsequent publications. After the three publications accepted by the Doctoral committee, another chapter follows, named further insights, dedicated to summarize the work carried out in the last period of the PhD thesis that could not be presented as a form of accepted manuscript due to time restrictions. Finally, a conclusions and future perspectives chapter closes the PhD thesis.

The manuscripts accepted by the Doctoral Committee are listed below:

I   A cobalt(II) heteroarylalkenolate precursor for homogeneous Co_3O_4 coatings by atomic layer deposition. Büyükyazi, M., Fischer, T., Yu, P., Coll, M., Mathur, S. (2017). Dalton Transaction, 46(38), 12996–13001.

II Homogeneous Fe_2O_3 coatings on carbon nanotube structures for supercapacitors. Yu, P., Coll, M., Amade, R., Alshaikh, I., Pantoja-Suárez, F., Pascual, E., Andújar, J. L., Serra, E. B. (2020). Dalton Transactions, 49(13), 4136–4145.

III Atomic scale growth of $GdFeO_3$ perovskite thin films. Bohr, C.,* Yu, P.,* Scigaj, M., Hegemann, C., Fischer, T., Coll, M., Mathur, S. (2020). Thin Solid Films, 698, 137848. (* Contributed equally to this work)

Other articles that have been published during this PhD thesis but are not directly related to the main research lines are:

I   Enhancing magneto-ionic effects in magnetic nanostructured films via conformal deposition of nanolayers with oxygen acceptor/donor capabilities. Navarro-Senent, C., Quintana, A.,

Isarain-Chávez, E., Weschke, E., Yu, P., Coll, M., Pellicer, E., Menéndez, E., Sort, J. (2020). ACS Applied Materials & Interfaces, 12(12), 14484–14494.

II Magneto-ionic control of magnetism in two-oxide nanocomposite thin films comprising mesoporous cobalt ferrite conformally nanocoated with HfO_2. Robbennolt, S., Yu, P., Nicolenco, A., Mercier Fernandez, P., Coll, M., Sort, J. (2020). Nanoscale, 12(10), 5987–5994.

Table of contents

Nomenclature

Acronyms / Abbreviations

AFM   Atomic force microscopy

ALD   Atomic layer deposition

ALEt   Atomic layer etching

CV   Cyclic voltammetry

EDX   Energy-dispersive X-ray spectroscopy

EIS   Electrochemical impedance spectroscopy

GIXRD   Grazing incidence X-ray diffraction

GPC   Growth per cycle

LIBs   Lithium ion batteries

MLD   Molecular layer deposition

RBS   Rutherford Backscattering Spectrometry

SCs   Supercapacitors

SEM   Scanning electron microscopy

SE   Spectroscopic Ellipsometry

SQUID   Superconducting quantum interference device

TEM   Transmission electron microscopy

TMO   Transition metal oxide

XPS   X-ray photoelectron spectroscopy

XRD   X-ray diffraction

XRR   X-ray reflectivity

Chapter 1

INTRODUCTION

1.1 Nanomaterials

Nanomaterials, including ultrathin films, quantum dots, nanowires, nanoparticles, and so forth, display altered physical and chemical properties compared to their bulk counterparts due to the high surface area to volume ratio and possible appearance of quantum effects at the nanoscale. Their unique properties offer new possibilities for various technical applications covering a wide range of fields such as energy, electronics and medicine.[1,2] In energy conversion and storage, for example, the specific surface area, surface energy and chemistry play a decisive role. They influence the thermodynamics of heterogeneous reactions, the materials nucleation and subsequent growth, and the small dimensions offer favorable mass, heat and charge transfer.[3] On the other hand, in the field of electronics, the development of extraordinarily small electronic devices with dissimilarly engineered materials with reduced weight and power consumption can dramatically increase the capabilities of the devices letting us forget about the Moore's Law. This involves increasing the density of memory chips, reducing the size, improving display screens, etc.[4] Therefore, the development of new synthesis strategies affording an effective control at the nanometer level is crucial.

Coordinated actions to advance in the processing techniques and employment of new materials have speeded up the fabrication of smaller devices with improved performances. Still, more complex materials, uniform conformal functional coatings for innovative 3D structures, and heterostructures with perfect interfaces are needed. Thus, it is desirable to find alternative processing solutions and to achieve atomic-level precision for tackling the challenges in the processing and manipulation of nanomaterials to better tune their properties and understand their structure–property relationships.[5]

Atomic layer deposition (ALD) is an advantageous tool for bottom-up synthesis of functional

materials thin films with unrivaled uniformity and conformality due to its unique self-limiting reaction mechanism. Its unprecedented excellence includes the atomic-scale control over the composition and thickness, superior ability in the tuning and engineering of interfaces, and potential compatibility with other production steps thanks to its mild processing conditions.[6–9]

1.2   Atomic layer deposition (ALD)

The origin of ALD is shared among the Soviet Union and Finland. They independently investigated a "Molecular Layering" deposition method (Soviet Union, 1960s) and an "Atomic Layer Epitaxy" approach (Finland, 1970s).[10–12] Along the road its name has seen an evolution from Atomic Layer Epitaxy, through synonyms such as Molecular Layer Epitaxy (MLE) and Atomic Layer Chemical Vapor Deposition (ALCVD), to the most popular name at present: Atomic Layer Deposition. Subsequently, the term ALD is commonly adopted which properly reflects its unique deposition mechanism which enables precise control over the film deposition process and tailoring of material performance at atomic scale perfection[7] (Section 1.2). More recently, a trend in adopting the term Atomic Scale Processing[13,14] or Atomic Layer Processing[14] arises with the aim to group both ALD and Atomic Layer Etching (ALEt)[15,16] for reflecting their common surface-controlled self-limiting characteristics and shared growing importance in the materials production lines. ALEt, as the etching counterpart of ALD, covers isotropic and anisotropic ALEt processes.[14,15] Under this concept, important derivative techniques such as area-selective ALD, spatial ALD and plasma-enhanced ALD are also included. Some might also group the sister technique Molecular Layer Deposition[17] (MLD) under the ALD category, considering the similar patterns of both techniques and their atomic/molecular-level control over the layer by layer deposition processes for inorganic/organic materials. For simplification, in this thesis we mainly use the term ALD and discuss the synthesis of inorganic materials.

ALD is a vapor-based chemical method for thin film synthesis that requires low temperature (typically < 400 °C) and low vacuum (usually ~ 0.1 - 10 Torr) conditions. Regarding this, ALD contrasts with other commonly used techniques such as chemical vapor deposition (CVD)[18] or physical vapor deposition methods (*e.g.* pulsed laser deposition (PLD) and molecular beam epitaxy (MBE))[19,20] that demand either higher deposition temperature or (ultra-)high vacuum.

The unique feature of ALD is that it comprises sequential self-limiting surface reactions realized via alternate pulsing of precursors. Usually, one precursor per element in the final compound are used. A typical ALD process for the synthesis of a binary material can be divided into two half-reactions. During the first half-reaction, the first precursor, carried by inert gas into the reaction chamber, adsorbs on the sample surface via chemisorption or physisorption and

reacts with all the available surface sites until a new surface is formed and saturated with new species from the incoming precursor.[21] Then, the excess precursor and reaction byproducts are all purged away by inert gas. The next half-reaction begins with the second gaseous precursor being carried into the reactor chamber and reacting with the newly formed surface, followed by a purge step, analogous to the first one. Until then, an ALD cycle is completed and the surface restores the initial state, as illustrated in Figure 1.1 with the case of ALD Al_2O_3 from $Al(CH_3)_3$ (TMA) and water (H_2O). Such ALD cycles repeat themselves and films are ideally formed in the layer-by-layer manner to reach the desired thickness. In ALD, the film growth rate is evaluated cycle-wise, that is, total film thickness divided by the number of ALD cycles employed, instead of per time unit. This growth rate is often referred to as *growth per cycle* (GPC). Not surprisingly, surface chemistry that involves precursors and the surface actives sites plays a critical role in ALD, which will be discussed in the following Section 1.2.1 and Section 1.2.2, respectively.
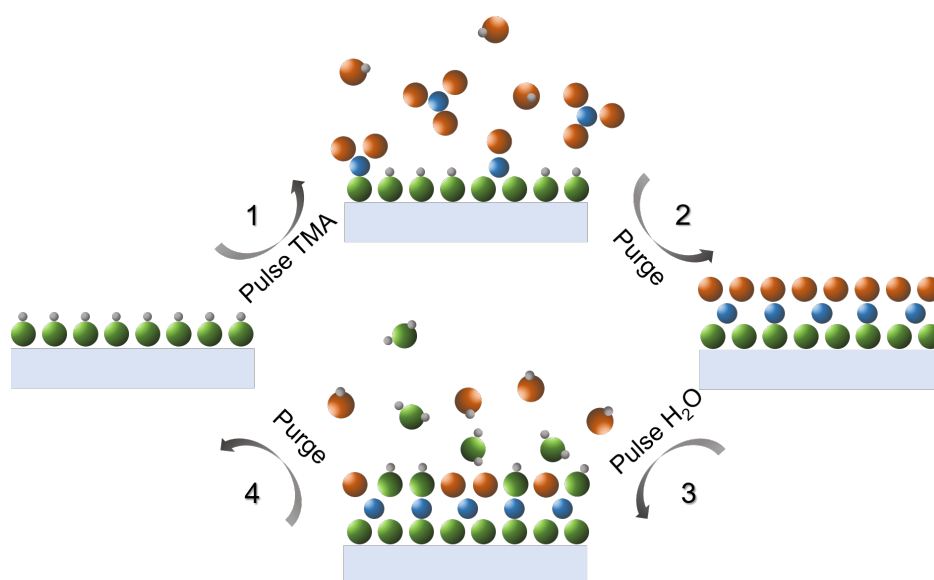
Fig. 1.1 Illustration of the step-wise ALD surface reactions showcasing the representative Al_2O_3 ALD from $Al(CH_3)_3$ (TMA) and water (H_2O). A simple ALD cycle consists of four steps: 1) pulse and 2) purge of the first precursor source TMA in the first half-reaction, 3) pulse and 4) purge of the second precursor H_2O in the second half-reaction, during which the sample surface changes accordingly to the sequential reactions.

To determine if a process is in the ALD regime, there are three factors that are routinely evaluated. First and most relevantly, one should identify a constant growth rate versus precursor pulse, termed a saturation curve, Figure 1.2a. It is helpful to determine the optimal precursor dosing time so as to avoid unnecessary time consumption and precursor waste. The curve shape complies with the Langmuir absorption model,[22,23] reflecting the ALD precursors' self-limiting chemisorption behavior on the surface. The reaction self-hindered to stop once all the surface reactive sites have

been consumed, resulting in a surface saturated with new species. Secondly, a steady growth rate is desirable in a certain range of temperature, or ALD window, under which the precursor reaches the sample surface intact and reacts in a controlled way, see Figure 1.2b. The upper limit of this window is dictated by the precursor decomposition or desorption from the surface, while the lower limit defines precursor condensation and poor reactivity towards the surface. This ALD window is critical for the synthesis of multicomponent materials such that compatible processing temperature could be identified if several precursors are used, which will be discussed later in Section 1.3.1. Thirdly, working within the ALD window and saturation zone, a linear film thickness dependence on the ALD number of cycles is preferable, facilitating digital control over the film thickness, Figure 1.2c.
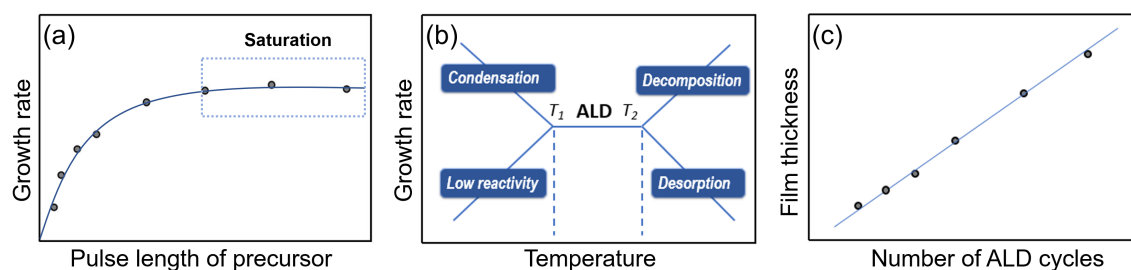
Fig. 1.2 Three factors that are important for ALD processes: (a) A saturated constant growth rate versus precursor pulse; (b) A steady growth rate in an ALD temperature window; (c) A linear film thickness dependence on the ALD number of cycles that facilitates digital control (Adapted from Ref 9).

1.2.1 Precursor chemistry

Since ALD is built upon self-limiting chemical surface reactions between the precursors and the active sites on the surface, precursor chemistry, which is closely related to the precursor performances, becomes one of the key aspects in ALD.

The principle requirements for ALD precursors, see Scheme 1.1, include high volatility, moderate thermal stability, high reactivity toward surface species, clean decomposition to avoid impurities formation, suitable size, low toxicity and low cost.[7,21,24] Suitable precursor size is essential for avoiding polymerization of the precursor molecules and ultimately altering the volatility of the precursor, which is dictated by the ligand bulkiness (carbon chain lengths, branched or straight chain, etc), metal size and coordination number.[21] The effect of the precursor sizes on the deposition process will be presented later in Section 1.2.2. The volatility, thermal stability, reactivity and decomposition behavior are closely related to the nature of the ligand and metal-ligand interactions, which will be reviewed according to the types of precursors below.
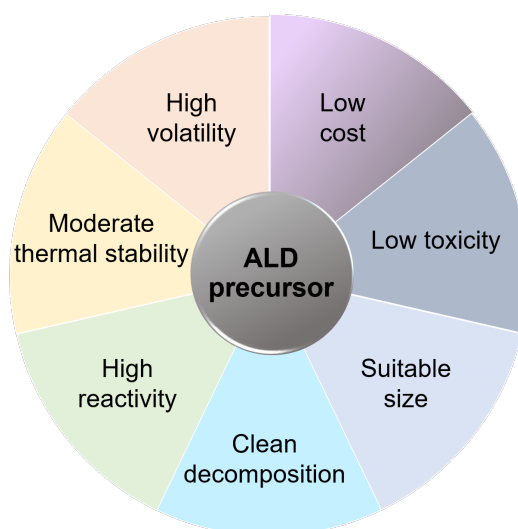
Scheme 1.1 Schematic illustration of the requirements for ALD precursors in terms of volatility, thermal stability, reactivity, decomposition behavior, precursor size, toxicity and cost.

Precursors that have been investigated for ALD can be generally classified into three categories: pure metal elements, inorganic and metalorganic compounds. Amid these three classes, pure metals lack broad usage due to their poor vapor pressures, with few exceptions being Zn, Cd and Hg. The inorganic and metalorganic precursors compose the most commonly used precursors in ALD. Inorganic compounds are mainly from the metal halides family, while the metalorganic complexes possess abundant varieties with metal center coordinated with various ligands such as alkanes, metallocenes, alkoxides, amides or imides, as displayed in Figure 1.3.[7,21] The different metal-ligand interactions in these compounds have led to varied thermal stability and reactivity of the precursors, which are described below.

Among these ALD precursors, halide compounds that contain halogen ligands (Figure 1.3a), exhibit exceptional thermal stability and small steric hindrance. They have been incorporated for extensive industrial usages such as $TiCl_4$, $HfCl_4$, WF_6, CuCl, etc.[7,21,24] However, the corrosive nature of halide precursors and their halogen-containing byproducts toward the deposited films, substrates and ALD reactors discourage their further popularity. In addition, possible unintentional incorporation of halogens as impurities in the final film could also deteriorate film properties.[25,26] The metal alkyls have been proven to be a popular group of ALD precursors as well, Figure 1.3b, the most widely known being TMA, or $Al(CH_3)_3$, with almost ideal properties. These chemicals contain metal-carbon bonds, thereby they are usually highly reactive or even in some cases show pyrophoric behavior. As a result, special attentions are required for safe-handling of these precursors during the process. Metallocenes are usually coordinated with aromatic carbon rings that have delocalized π bond, a typical ligand being the five-membered cyclopentadienyl ring (Cp), see Figure 1.3c. By virtue of the equivalent pentahapto (η_5^-) bonding of the carbon

5

INTRODUCTION
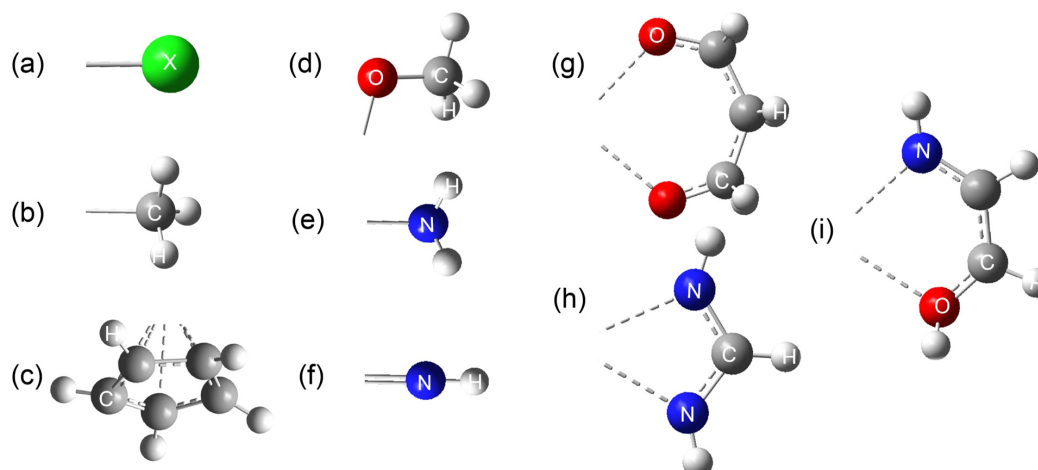
Fig. 1.3 Illustration of some examples of ligands in ALD precursors: (a) halogens, (b) alkyls, (c) cyclopentadinyls, (d) alkoxides, (e) amides, (f) imides and chelate structures such as (g) β - dikitonates, (h) amidinates and (i) donor-functionalized alkoxides and their derivatives (Adapted from Ref 24).

atoms to the metal center, metallocenes appear to be more thermally stable precursors[21] and have been intensively studied in ALD, such as $Fe(Cp)_2$,[27–31] $Co(Cp)_2$,[32–35] and $Ru(Cp)_x$,[36–38] to name a few. On the other hand, the metal-Cp bonds are so strong that carbon contamination has been commonly observed in some of the deposited films.[27,39,40]

Metal alkoxides, with metal-oxygen bond, usually react readily with water and offer high quality films, Figure 1.3d. However, due to insufficient volatility or thermal stability at elevated temperature, the reactions using metal alkoxides are oftentimes restrained. Typical alkoxide precursors for ALD include rare earth complexes, $RE(OCMe_2{}^iPr)_3$ (RE = Y, Gd, La or Pr), (Me = Methyl, ^iPr = isopropyl), and group IV complexes such as $Ti(O^iPr)_4$.[41] Likewise, metal amides or imides containing single or double metal-nitrogen bond (Figure 1.3ef) are also highly reactive and are very suitable for low temperature processing, an extraordinary example being $Hf(N(MeEt)_4$ (Et = ethyl) for HfO_2 deposition. However, nitrogen-based precursors also suffer from low thermal stability.[7,21]

In many cases, a compromise has to be made between desirable reactivity and high stability. Ligand mixing can be viable for achieving desirable properties, such as the mixing of alkyls with halogens or alkyls with cyclopentadienyls. The full or partial substitution by cyclopentadienyl rings of metal alkyls tends to stabilize the molecules due to the delocalized π bond.[21] Examples encompass the combination of modified Sr and Ba precursors $Sr(C_5{}^iPr_3H_2)_2$, $Ba(C_5Me)_2$ or $Ba(C_5{}^tBu_3H_2)_2$ (^tBu = tert-butyl) together with $Ti(O^iPr)_4$ for the synthesis of $BaTiO_3$[42] and $SrTiO_3$[43].

Furthermore, introducing bidentate structures into the molecules has been an effective strategy in enhancing the precursor thermal stability by so-called "chelate effects"[21,44] that can effectively

increase the saturation degree of the metal center. Typical precursors include β-diketonates, amidinates or donor-functionalized alkoxide, as are shown in Figure 1.3g-i. According to the improved thermal stability, usually stronger counter reagent (*e.g.* O_3) or higher deposition temperature are required in the reactions using these precursors.

Typically, ALD has been employed in depositing binary compounds using complementary precursors each containing one element for the target compound. In this approach, the scenario could be further complicated for ternary or more complex compounds when multi-sources are involved. To simplify the surface reactions for ternary compounds formation, there is a growing field of single-source heterobimetallic precursors in ALD.[45,46] In these precursors, two or more metal elements are included in the molecular structure, Figure 1.4, thus rendering them very appealing for the preparation of complex oxides by ALD. The main advantages are three-fold: firstly, the pre-fixed elemental ratio enables strict control over the cation stoichiometry in the deposited films; secondly, obviating the necessity of multi-sources facilitates much simplified deposition processes in the aspects of precursor delivery, carrier gas flow and deposition temperature; lastly, predetermined chemical compatibility between the selected precursor and the target film favors their successful incorporation. Nonetheless, probable low volatility of this kind of molecules might fail as a suitable ALD precursor. Besides, premature fragmentation could lead to incomplete precursor delivery and varied composition.[47] These precursors will be further discussed for the complex oxide synthesis in Section 1.3.1.
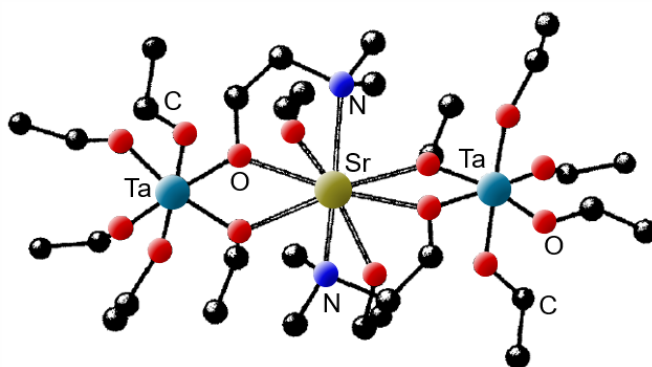
Fig. 1.4 Molecular structure of an exemplary single-source heterometallic precursor $Sr[Ta(OEt)_5(dmae)]_2$ (dmae = $OCH_2CH_2NMe_2$) for the synthesis of $SrTa_2O_6$ ternary oxide by ALD (Adapted from Ref 45).

In view of all above information, cautious design and fine-tuning of the chemical structures of novel precursors offer great opportunities to synthesize and engineer simple and complex material systems with improved performance.

One research direction of this thesis is aimed to develop ALD processes using novel or tailor-made

metalorganic precursors to synthesize transition metal oxide-based thin films: a β-heteroarylalkenolate Cobalt, a heterobimetallic tert-butoxide pyridine Gd-Fe complex, and separate guanidinate Gd and ketoiminate Fe precursors for ALD Co_3O_4 and $Gd_xFe_yO_z$ respectively, Article I and III, Chapter 4.

1.2.2   Surface reactions and surface functionalization

Following the discussion of ALD precursor chemistry, it is necessary to review how ALD reactions occur through different surface reaction mechanisms.

In general, there are two main processes that contribute to ALD material formation: precursor adsorption to the surface and diffusion of the formed nucleates.[48] Differing from CVD or PLD, where either the source precursors coexist in the gas phase, or the target material approach the substrate surface in plasma plumes, in ALD the gas phase precursors reach the surface sequentially in the intact form and initiate the process via surface reactions between the precursor and the functionalized surface with active sites, Figure 1.5a-c.

Ideally, following the precursor adsorption and surface reaction, ALD films should grow uniformly in the layer by layer manner,[49] as displayed in Figure 1.5d,g. However in practice, the reaction mechanism in ALD is often oversimplified and not fully understood. Nucleation delays have been observed in some ALD processes. In addition, after adsorption and nucleation, one could oftentimes find coalesced nanoparticles or islands, instead of the continuous film formation. These ALD processes deviate from the ideal model due to the sparse nucleation sites or diffusion process and affects the quality of the final film, as displayed in Figure 1.5e,f,h,i.

To obtain further insight into the complexity in ALD and better control over the processes, it is necessary to thoroughly review the surface adsorption and diffusion steps. The diffusion step is dictated by atomistic processes such as adatom aggregation and formation of nuclei, Ostwald ripening, and nanoparticle diffusion and coalescence.[48,50] In the resulted island growth mode, even though a film material could still be achieved from the coalesced nanoparticles with enough number of cycles and higher mass loading, the surface morphology may be rougher, Figure 1.5h,i.
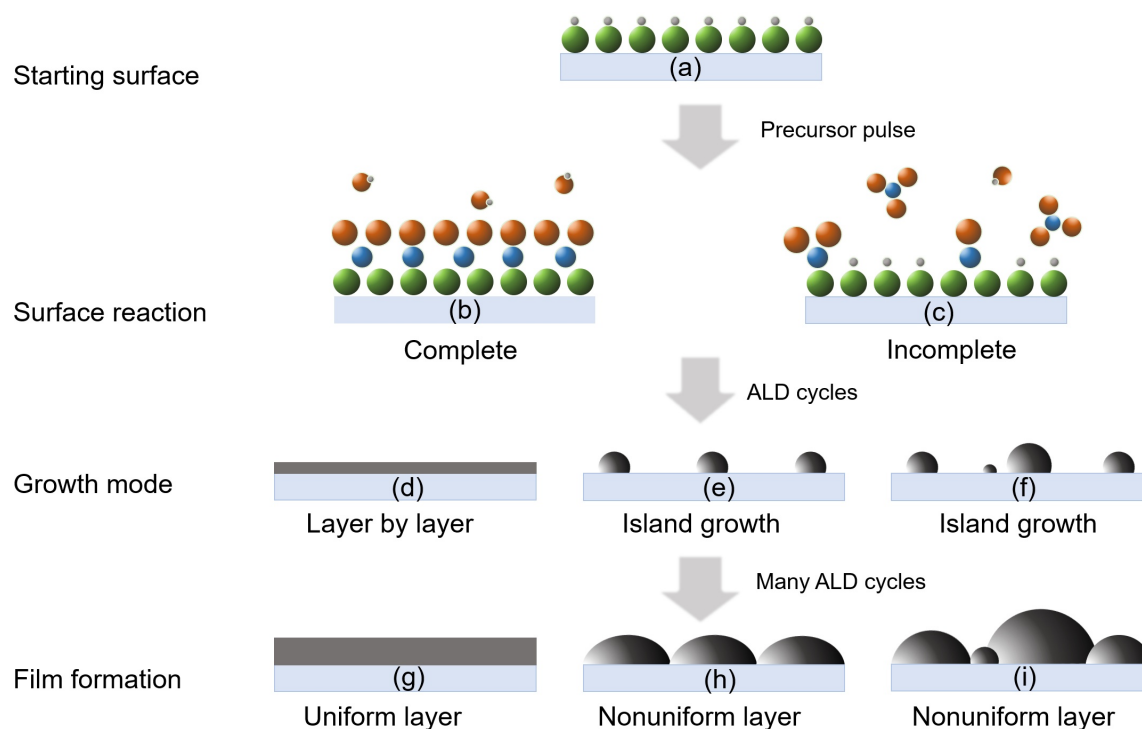
Fig. 1.5 Illustration of the precursor chemisorption and ALD material growth at different stages of the deposition process. Starting from the (a) bare substrate with active sites, the precursor pulse could lead to (b) complete reaction or (c) incomplete reaction between the precursor and surface active sites; the initial nucleation steps via the (d) layer by layer growth mode, or island growth mode (e) without or (f) with diffusion in the first few ALD cycles will lead to (g) uniform film or (i) nonuniform film formation after many ALD cycles (Adapted from Ref 48).

Herein, we mainly focus on the surface chemistry in the initial material nucleation stage which is vital for ALD reactions. This could be unraveled by taking a closer look at the precursor - surface interactions, considering the precursor adsorption mechanisms, influence of surface active sites and steric effect, see Scheme 1.2.

First, when a precursor approaches a surface, successive adsorption processes occur as a function of precursor pulses and self-limits to form at most a monolayer each time. Especially, the adsorption kinetics (and gas flow regime) are very relevant in ALD coatings of complex 3D architectures and nanometric features.

The adsorption process could occur through primarily chemisorption or physisorption. The chemisorption processes are mostly irreversible, in comparison to the weak intermolecular physisorption interactions such as van der Waals forces or hydrogen bonds. Thus, chemisorption are usually strong driving forces that explain most of the reaction steps in ALD, which will be the main focus in the following. Chemisorption mechanisms could be commonly classified into the following four subgroups: ligand exchange, dissociation, association and oxidation (Scheme 1.2).

9

INTRODUCTION

We will describe each subgroup in more detail below.
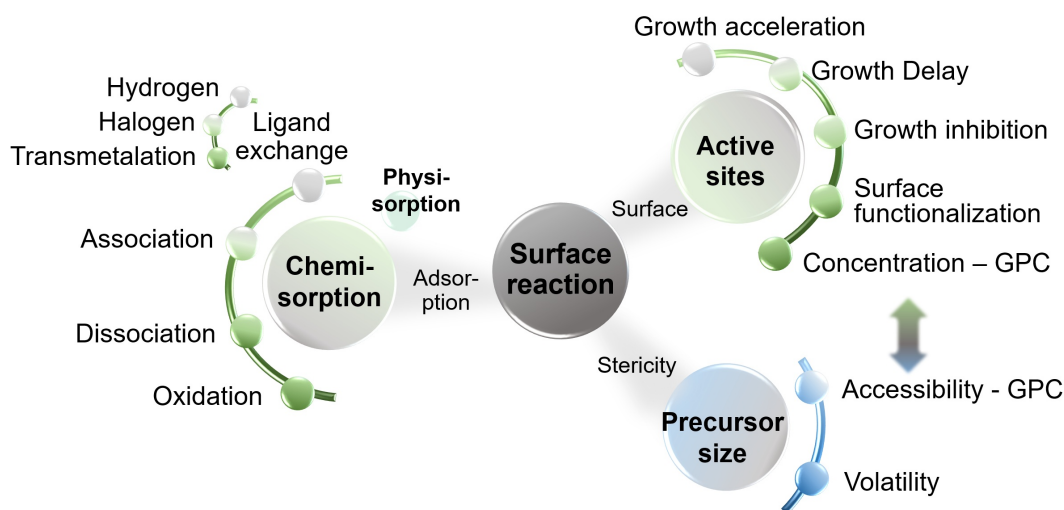
Scheme 1.2 Schematic illustration of the imperative elements in ALD surface reaction: adsorption mechanisms (physisorption, chemisorption), surface active sites and steric effect.

Chemisorption process through ligand exchange involves ligand swapping between the precursor and the surface species in which at least two bonds break and the same amount of new bonds form. A typical type of ligand exchange reaction is the hydrogen transfer[21] (or proton transfer[48]) through Brønsted-Lowry (BL) acid-base reactions where an acid, or a proton donor, transfers its proton to its conjugate base, or proton acceptor. In these reactions, the metalorganic precursors are usually considered to act as BL bases and accept the proton from the more BL acidic surface groups. In these systems, the samples surface are alternating between the protonated states and residue ligand saturated states. The starting surface with protonated states could come from the hydroxylated surface of the substrate, from either its initial state or functionalization treatments, or be restored in the co-reactant pulses using typical non-oxidizing compounds such as H_2, NH_3, H_2O, and H_2S for the synthesis of metals, metal nitrides, metal oxides or metal sulfides, respectively. The corresponding residue ligand saturated states come from the precursors pulses. Typical BL basic metalorganic precursors are the ones with more ionic metal-ligand bond, such as metal alkyls or amides.[48] During these reactions, the reaction byproducts must be volatile and capable to desorb from the surface intact in the protonated state, so that they can leave the reaction chamber in the following purging step. The hydrogen transfer mechanism could be clearly exemplified by the archetype ligand exchange process of Al_2O_3 ALD synthesis using TMA and H_2O, Figure 1.6ab. In the first half-reaction, TMA is pulsed and chemisorbs onto the surface by hydrogen atom transferring from hydroxyl group to methyl group in the precursor leaving as gas-phase methane resulting in a methyl-terminated surface, Figure 1.6a. Then in the next half-reaction, water vapor is

pulsed substituting surface methyl groups leaving again as gas-phase methane with one hydrogen atom transferred, as displayed in Figure 1.6b. Halogen abstraction is another subgroup in ligand exchange mechanisms when metal halides and non-metal halogen-philic compounds are used. Another subgroup is transmetalation where two metalorganic compounds exchange ligands with each other.[48]
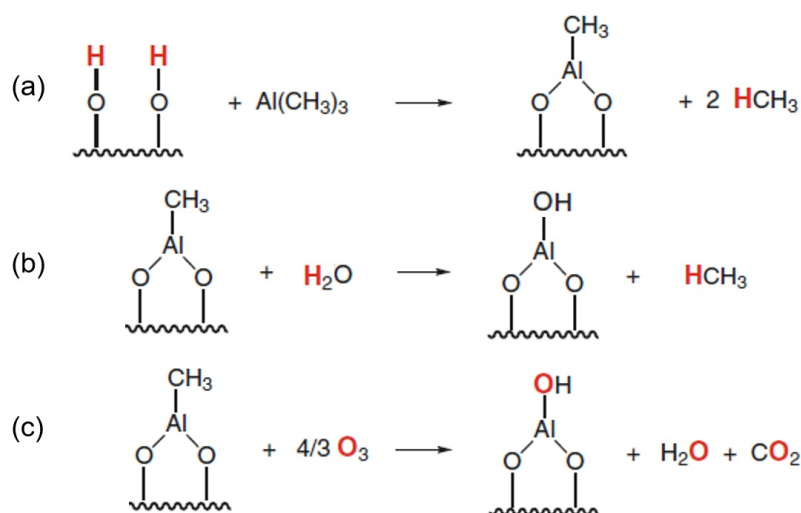
Fig. 1.6 Illustration of Al_2O_3 ALD from TMA and H_2O or O_3 comprising subcycles with different chemisorption mechanisms: (a)(b) ligand exchange or more specifically, hydrogen transfer and (c) oxidation.[21,48]

Chemisorption through dissociation reaction undergoes precursor breaking into several fragments that totally or partially adsorb onto the surface. Dissociation often happens on high surface energy substrates such as noble metals. It can happen to metalorganic precursors or co-reactants (*e.g.* H_2 or O_2 that split into their atomic counterparts) on the surface.[48] Also, if the precursors are not monomeric, the dissociation process usually is needed to separate the dimers or oligomers so that the metal centers have available empty orbitals for association to happen.

Chemisorption through association process typically occurs for halide precursors by forming coordination bond without breaking existing bonds.[48] The associative bond forms when an electron deficient metal atom (usually with empty orbitals) accepts lone pairs of electrons from the Lewis base. Often, association is considered as an intermediate state prior to ligand exchange. For instance, first principle calculations show that in the ALD Al_2O_3 process using $Al(CH_3)_3$ and water, associative surface-(OH)-$Al(CH_3)_3$ species are more preferable to form preceding the ligand exchanges between TMA and surface hydroxyl groups.[51] The association processes are usually barrierless and reversible, but it differs from physisorption processes in that the coordinative bond formation requires orbitals overlapping and thus facilitating saturation behavior which is crucial

INTRODUCTION

for ALD.

Chemisorption through oxidation processes[48] (or oxygen transfer[21]) usually happen when oxidizing co-reactants are used such as H_2O_2, O_2, O_2 plasma or O_3 for the synthesis of metal oxide. In comparison to hydrogen transferring processes with intact ligand detachments, oxidation reactions are usually associated with the total combustion of organic fragments and oxygen incorporation into the films. For example, when depositing Al_2O_3 using TMA and O_3, following the same ligand exchange half-reaction as the process using TMA and H_2O (Figure 1.6a), the O_3 pulses in the second half-reaction hydroxylate the sample surface by oxidizing surface methyl groups into water and carbon dioxide, see Figure 1.6c.[21] However, in the case of noble metals, the surface was partially oxidized through a combination of dissociation and oxidation mechanisms with oxidant pulses facilitating the metal precursor chemisorption process.[48]

Secondly, the active sites on the starting substrate surface is of vital importance for film nucleation, especially in the case of ultrathin films (Scheme 1.2).[8,9] Thus, in many cases surface functionalizations are needed to prepare the surface prior to the next ALD process. First factor to be considered is the concentration of the active sites. If the concentration is too small, ALD will happen with sparse nucleations that hinders film formation and lowers film GPC. According to calculations, there is a linear correlation between the GPC of ALD Al_2O_3 and the surface hydroxyl group concentration from TMA and H_2O.[52] Apart from the concentration, the chemical compatibility between surface groups and the precursor also plays an important role. It can lead to growth acceleration, delay (an incubation period)[9,53] or even inhibited growth.[54] For instance, the nucleation difficulties have been observed of metal oxides on H-Si(100), metal on oxides and metal oxides on carbonaceous materials.[8,26] Specifically, the challenges for ALD oxide nucleation on carbonaceous materials are the chemical perfectness and inertness of the carbon. Without pre-treatments, ALD of oxide on carbon materials can only occur from surface defects. Functionalizing carbon surface with suitable species via non-covalent modification,[55–57] acid treatment[58,59] or doping[60] have been proven viable approaches to promote the nucleation of oxides on carbon-surfaces. In this thesis, we will address this topic in Article II for ALD Fe_2O_3 coatings on carbon nanotubes based on plasma treatments.

Thirdly, steric effect of the organic ligands in metal precursors influence the film nucleation by blocking active sites and limiting the precursor accessibility to the surface (Scheme 1.2). Assuming that one ALD reaction is taking place with sufficient surface sites and without time limitations (thus slow reaction mechanisms will not be a problem), the GPC of the reaction would be closely related to the steric hindrance of the precursor molecules, which greatly influences the way and the number of precursors to chemisorb onto the surface and react with the surface. High steric hindrance often leads to poor surface coverage, then results in sparse nucleations and

sub-monolayer growth.[61,62]

Furthermore, the ALD instrumentation systems are of vital importance providing various driving forces for ALD reactions. Traditionally, ALD relies on thermal power for reaction activation, in which the precursor and substrates are heated up throughout the process. Hence, exergonic processes (with $\Delta G < 0$) and the ΔG values as negative as possible would be preferred in these cases because the more aggressive the process, the shorter the cycle time.[62] Alternatively, the employment of more reactive co-reactants such as H_2O_2, O_2, O_3, or plasma[14] could lead to energy enhanced ALD processes at reduced reaction temperature, bypass slow reaction mechanisms and open the possibilities for thermally restricted reactions.[62]

However, in practice, further complications in ALD can come from various reasons as will be discussed below. For instance, in most cases the actual mechanistic steps and the types or the number of intermediates are unclear.[48] In the above mentioned deposition process for Al_2O_3, the reaction pathways seem quite straightforward and have been well-understood. However, the exact number of ligands involved in each subcycle remains unknown which could only be resolved by using D_2O isotope labeling instead of using H_2O.[7] Another fact that contributes to process intricacy is that the film surface changes constantly with precursor pulses making the system in an non-equilibrium state. During the process, the surface morphology and surface area can be easily altered along with material growth rate, which is exclusively severe in the case of complex oxide synthesis. Therefore, when precursors with novel chemistries are evaluated or two or more precursors of unknown reactivity are combined, they represent a imperative challenge for the researcher to develop the deposition process, as will be discussed later in Section 1.3.1, and addressed in Article III and Chapter 4.

Progress for better understanding reaction mechanisms requires in-situ characterization methods, and it remains a challenge in ALD. Although this topic will not be addressed in this thesis, here it is briefly mentioned the most used characterization techniques in the following.

To examine real-time mass changes during the deposition process, quadrupole mass spectroscopy (QMS) is typically integrated with ALD for the gas-phase byproducts analysis; complementary analysis of the mass changes of the sample by quartz crystal microbalance (QCM) further corroborates QMS results.[63] Surface-sensitive optical measuring techniques could offer more information for resolving ALD reaction mechanisms, such as spectroscopic ellipsometry (SE), infrared spectroscopy (IR) or optical emission spectroscopy (OES).[64] In addition, the in-situ heat probing by absorption calorimetry was also demonstrated to be useful for identifying the exo/endothermal reaction steps which provides mechanistic insight for ALD reactions.[65] Besides, with an ultra-high vacuum ALD reactor more characterization techniques can be integrated, such as highly surface sensitive X-ray photoelectron spectroscopy (XPS) for studying surface chem-

istry and synchrotron based techniques such as grazing incidence small angle x-ray scattering (GISAXS), x-ray fluorescence (XRF), and x-ray absorption spectroscopy (XAS) measurements.[66]

1.2.3 Crystallinity and purity of atomic layer deposited films

Oftentimes, the atomic layer deposited films are found amorphous or poorly crystallized in the as-deposited stage due to the relatively low deposition temperature. Amorphous materials could be beneficial under some circumstances. For instance, for electrochemical energy storage, amorphous materials might be preferred due to the easy accessibility of electrolytes enabled by its richness in defects and better cycling performance enabled by the isotropic deformation during the charge/discharge process. However, these materials could exhibit low charge carrier mobility. In many cases, crystalline materials are desired by virtue of their unique anisotropic electrical, optical and mechanical properties allowed by the structural regularity. Film crystallinity can depend on the proper atom intermixing and distribution delivered by careful design of the deposition process in the subcycle sequence, ratio, etc.[6] For obtaining crystalline materials, post-deposition thermal treatments are usually needed to force atom rearrangements and induce lattice deformation.[6] It is common that the films could be composed of several crystalline phases upon thermal treatment. Note that the phase-selective synthesis of metastable phases is a challenging task. Sometimes, ALD epitaxial growth has been achieved in the as-deposited stage by properly choosing a lattice matched substrates. It has been shown as an attractive solution to stabilize metastable phases, *e.g.* spinel Co_2FeO_4 on (100) and (110) oriented $SrTiO_3$ single crystals,[35] and to obtain epitaxial (100) $LaNiO_3$ on (100) $SrTiO_3$ and $LaAlO_3$.[67] This offers the opportunity to obtain crystalline/epitaxial films at low temperature being a highly desired feature for the fabrication of devices on Si or on substrates that cannot stand the deposition conditions of traditional processing techniques.

Also, the chemical impurity levels should always be evaluated in ALD films because as a chemical deposition technique, there are always risks of film poisoning with residues remaining in the films, *e.g.* reaction byproducts, etching, persisting species, etc.[62,68] The causes could be insufficient purge times, as is the case for water-based alumina deposition at low deposition temperature. The choice of co-reactants could also contribute. For example, using ozone in batch ALD alumina deposition was demonstrated to be advantageous compared to water based process: the films showed lower interface defect density, higher negative charge density and no blistering.[69] Yet, in many cases ozone reactions were reported with carbon contamination.[39,40]

1.2.4 Applications of atomic layer deposited materials

At present, a wide range of materials has been synthesized by ALD, covering almost all the elements in the periodic table. As revealed in Figure 1.7, aside from oxides, nitrides, carbides, sulfides or fluorides, pure elements can be constructed by ALD as well.[70,71] These materials in the form of high-quality ultrathin films and high conformality coating layers could be achieved by virtue of the unique self-limiting reaction mechanism between the gaseous precursor and the substrate surface, and the processing conditions at low temperature and low vacuum. In accordance, the flourishing materials with improved properties favored the broadening of various application fields, covering vast research disciplines, from materials science, engineering, optics, to electrochemistry and energy, which will be detailed below.
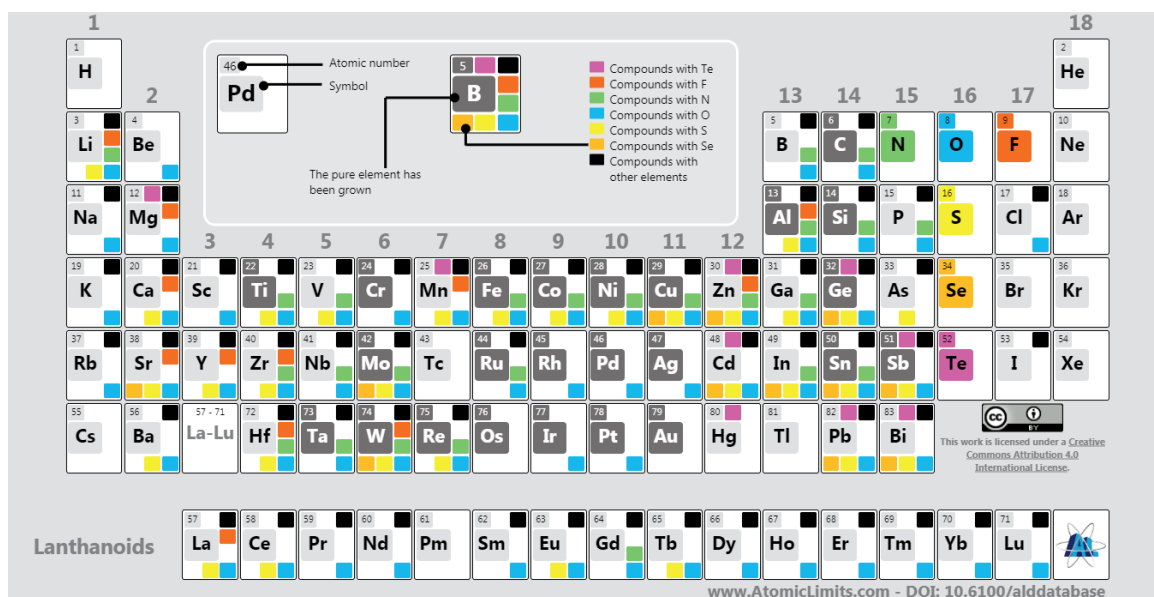
Fig. 1.7 Periodic table summarizing the materials that have been synthesized by ALD up to date. In the white frame different colors have been assigned to various types of materials: tellurides, florides, nitrides, oxides, sulfides, selenides, etc. Elements appearing in dark grey signifies that the specific pure element has been synthesized by ALD (Collected from online ALD processes database[71]).

First, the excellent conformality of ultrathin ALD coating layers on demanding three-dimensional substrates is facilitated by the vapor-based self-limiting ALD surface reactions. This is due to the fact that gas phase precursor molecules can disperse or diffuse to everywhere in the reaction chamber which are not limited by line-of-sight, if time permitted. For instance, the perfect replica of butterfly wing scales has been showcased with ALD Al_2O_3. The replicas are robust and flexible while keeping the fine structures of the wing scales, as exhibited in Figure 1.8ab.[72]

INTRODUCTION
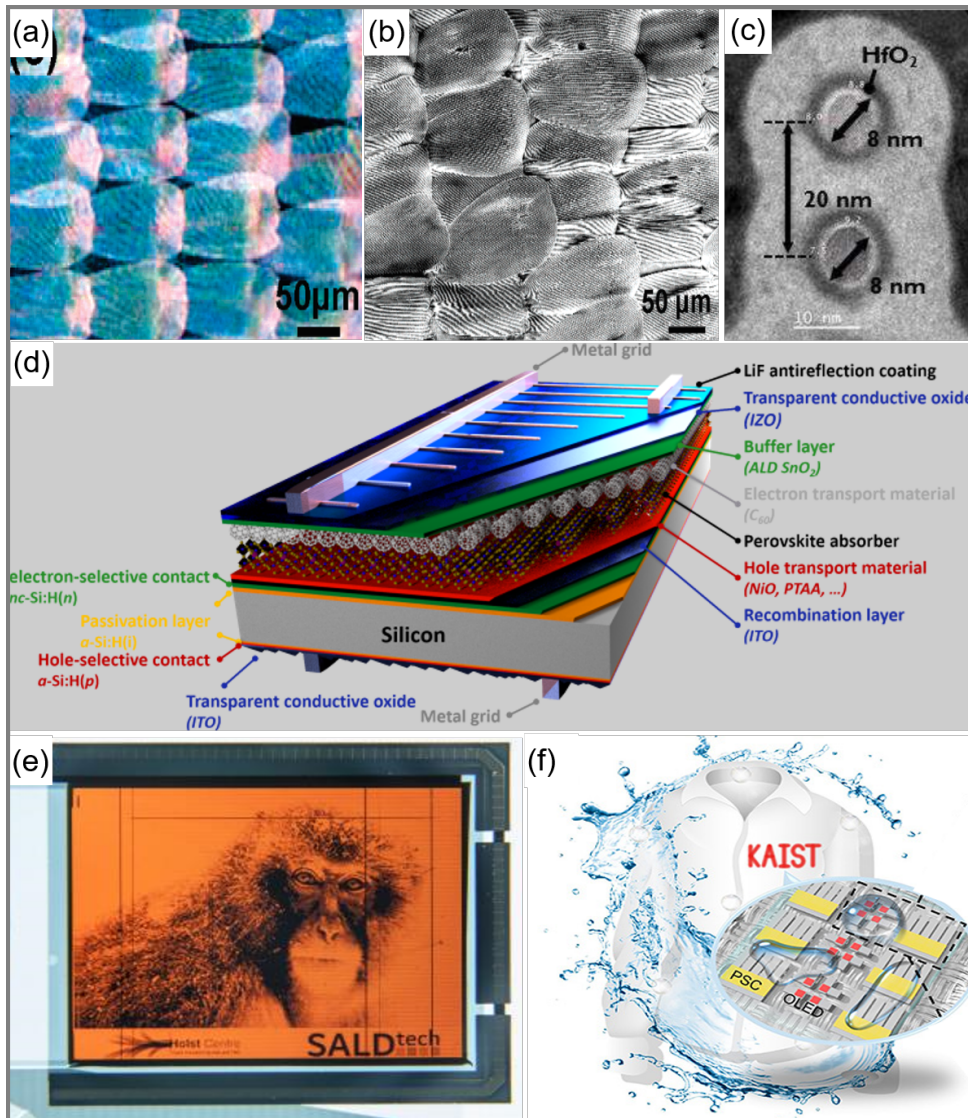
Fig. 1.8 (a) Optical microscope image of butterfly wing scales and (b) SEM image of the alumina replicas of the butterfly wing scales by ALD at 100 °C (Reprinted from Ref 72); (c) TEM image of two 8 nm stacked Si nanowires conformally deposited with ALD high-k HfO$_2$ layers in a gate-all-around field emitting transistor (Reproduced from Ref 73); (d) Illustration of the ALD compact TiO$_2$ layer for improving the performances of organometal halide perovskite solar cells (Reproduced from Ref 74); (e) Picture of the first transparent plastic foil based display with both the semiconductor and dielectric layer created by spatial ALD below 200 °C (Reproduced from Ref 75); (f) Schematic design showing ALD Al$_2$O$_3$ and ZnO at 70 °C as encapsulation barrier for self-powered smart clothing (Reproduced from Ref 76).

Meanwhile, ALD has been a method of choice with the continuous miniaturization of semiconductor electronics devices which is experiencing constant research interest both in academia and in industry.[73,77–79] ALD high-*k* oxides materials (Al$_2$O$_3$, ZrO$_2$, HfO$_2$) have been incorporated in the industry as alternative gate dielectrics to SiO$_2$ in metal-oxide semiconductor field-effect transistors (MOSFETs) to avoid tunneling current. In 2017, the 8 nm technology has been demonstrated with gate-all-around field emitting transistors (GAAFETs) containing two 8 nm diameter Si nanowires

16

conformally coated by ALD HfO$_2$ layers, Figure 1.8c.[73] Earlier this year, 5 nm chips have been put in volume production (although not GAAFETs configuration), and the race for 3 nm nodes has already begun which are expected to be delivered in the very near future. Furthermore, ALD has been under intensive research for synthesizing improved core-shell electrode materials for energy storage devices such as Li-ion batteries (LIBs) and supercapacitors (SCs).[80,81]

In addition, the unique self-limiting reaction mechanisms of ALD enables the generation of pinhole-free, crack-free compact films with comparable film density to their bulk counterparts. The prime film quality renders ALD truly powerful for protective coatings such as anti-corrosion coating for sensors, diffusion barrier for LIBs, compact layer and passivation layer for solar cells,[74,82] encapsulation layers for displays and for self-powered smart clothing,[76] as displayed in Figure 1.8d-f.

Secondly, ALD is advantageous when low temperature and low vacuum process conditions are required. This has made it feasible to integrate ALD in the semiconductor industry for Si-based devices and greatly lowered thermal budget. Particularly, the viability of low temperature processing favors compatibility with thermal sensitive substrates such as biomaterials,[72,83] plastics[75,84] or textiles,[85,86] see Figure 1.8ab,e,f. Apart from the conventional fabrication of insulator thin films, top electrodes or the afore-mentioned encapsulation layers, more recently, the potential of ALD in this area has been further manifested with deposition of both the semiconductor indium gallium zinc oxide (IGZO) layer and dielectric alumina layer on low-cost transparent plastic foils below 200 °C using atmospheric spatial ALD for an organic light-emitting diode display (OLED), Figure 1.8e.[75]

In accordance with the industrial interests, the ALD equipment market has developed rapidly over billion-dollars size which is closely related to the continuous emergence of new applications.[14,87] To satisfy big volume production, commercial ALD reactors are available for large scale capacity.[88–90] For instance, with roll-to-roll spatial ALD reactors one can realize high speed production rate incorporating large flexible substrates with width up to 625 mm,[88] while ALD batch reactors are capable of depositing highly uniform thin films on 50 pieces of substrates (each with diameter of up to 200 mm) within a single run.[89] Plasma-enhanced ALD with its advantageous low temperature processing feature appears a useful and integrable tool for back-end-of-line segment of interconnect technology, which is also an available tools for production.[14,90] One could foresee that with advanced nano-patterning, enabled by the combination of ALD with e-beam lithography or ALEt, or by area-selective ALD, can further boost semiconductor industry for producing smaller, faster and more efficient processors.[91,92]

In brief, the significance of ALD is expanding in a broad variety of fields, from microelectronics

to biomaterials and energy.

1.3   Oxide thin films by ALD

Oxide materials generally possess rich compositional and structural diversity, and the fascinating complexity in their properties derived therefrom makes them even more glamorous. Hence, oxides offer great potential to design and produce desirable functional materials with high chemical stability and environmentally benign nature.[78] Unsurprisingly, oxide materials are a significant class among the many types of materials that have been synthesized by ALD, as previously illustrated in Figure 1.7. Their popularity could be perceived from the huge endeavour in the studies on oxides ALD for electronics[77,78,93] and energy related applications.[81,94,95]

Most recently, there has been a thriving interest in ALD multicomponent compounds synthesis including doped, ternary and quaternary oxides. Structurally, these materials can be classified into perovskite (ABO_3),[77] spinels (AB_2O_4),[35] delafossites (ABO_2) and scheelites (ABO_4)[6,68] where A, B stand for different cations. Among them, perovskite oxides are a prevalent family because they exhibit diverse properties ranging from catalytic activity, superconductivity, ferro-electricity, magnetism, multiferroicity to photovoltaic effect, etc. Exemplary ones that have been synthesized by ALD are high-k $BaTiO_3$[42] and $SrTiO_3$,[43] ferroelectric $BiFeO_3$[96] and $BaTiO_3$,[97] magnetic $REMnO_3$ (RE = Y, La, Sm, Yb, Lu), ferro-/piezoelectric $PbZrO_3$ and $PbTiO_3$, and so forth.[6] In addition, their compositional flexibility enables further property modifications by cation substitutions in A, B sites. For instance, the stoichiometric insulator La_2CuO_4 turned into a superconductor $La_{2-x}Sr_xCuO_{4-y}$ after ALD Sr substitution.[98]

Yet, complex oxide synthesis is being a technical challenge for ALD. In the following, we will discuss the challenges in complex oxides ALD and different strategies that have been employed for tackling the problem.

1.3.1   Challenges in complex oxides synthesis

As mentioned earlier, in typical binary ALD processes, each precursor contributes one individual element to the target compound. Consequently, the deposition of binary compounds is relatively easy since only one metal precursor and one co-reactant are involved.[99,100] By contrast, the multicomponent films are deposited by alternate binary subcycles each contributing one metal element to the target films using the so-called supercycle approach.

As can be imagined, when more than two metal precursors are present, intricacy in the ALD

process design arises from both thermal and chemical compatibility between the sources. The thermal compatibility demands the identification of a common ALD window between the two binary processes, which confines precursor choices and restricts reaction temperature for the ternary oxide process. The chemical compatibility, on the other hand, is more vital in determining the film formation since the sequential reactions occurs only on the surface which varies along with different precursor pulses. Furthermore, the fuzzy reaction pathways and surface variation during complex compound synthesis can deteriorate the self-limiting characteristic of ALD and can lead to diverged film composition or smaller growth rates for ALD complex oxides, instead of ideal linear combination of the binary reactions,[101] as mentioned in Section 1.2.2.

In Figure 1.9, different kinds of A-B-O multicomponent oxide films are depicted, obtained following different combinations of the binary processes I and II for AO_x and BO_y in the supercycle, *viz.* (a) homogeneously mixed AB_zO_w film, (b) nanolaminated film containing AO_x and BO_y multilayers, or (c) doped material that features one main binary oxide with dopants of the other minor elements (*e.g.* $B:AO_x$).
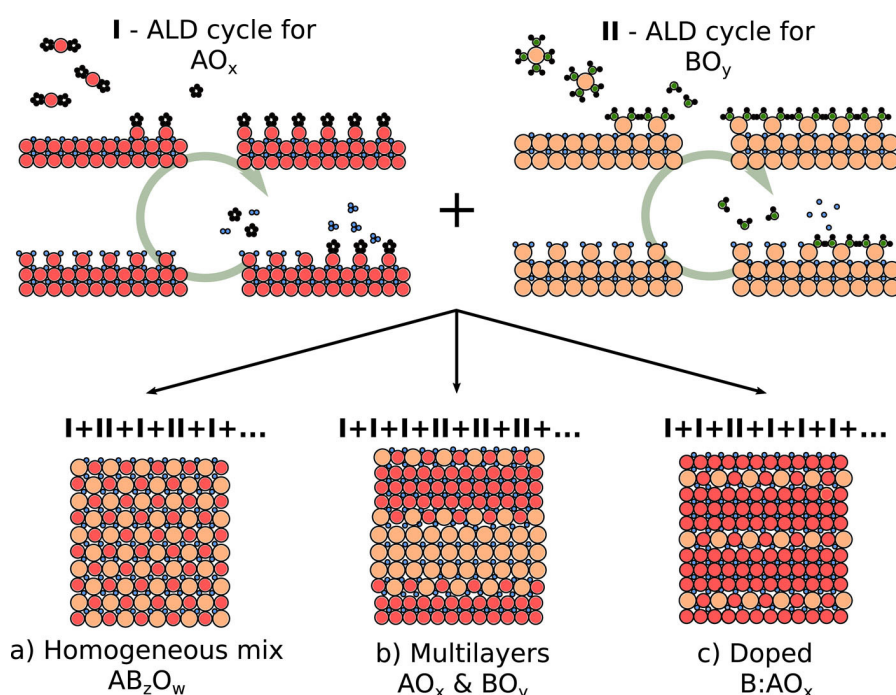
Fig. 1.9 Illustration of the supercycle approach to prepare ternary A-B-O oxide systems by ALD. By varying the combinations of binary AO_x and BO_y processes in the supercycle, different A-B-O films can be formed, *e.g.* (a) homogeneously mixed AB_zO_w film, (b) nanolaminated AO_x and BO_y layers, or (c) doped material ($B:AO_x$) (Reproduced from Ref 6).

The feasibility of the supercycle approach has been exemplified by the low temperature epitaxy of highly electrically conductive $LaNiO_3$ at 225 °C and metastable magnetic spinel Co_2FeO_4 at

19

250 °C with no annealing required, which signifies big steps for multicomponent ALD towards all-oxide electronics.[35,67] Although in many cases the complex oxide ALD is complicated by the afore-mentioned restrictions, it is not always so daunting: it has been reported that the applicable ALD window for Mn(thd)$_3$ has bee shown to be elevated to *ca.* 330 °C in ternary LaMnO$_3$ and CaMnO$_3$ processes from the maximum of *ca.* 240 °C for binary MnO$_2$ process.[101] Furthermore, one could stop the problematic BaO/Ba(OH)$_2$(H$_2$O)$_n$ hydration/dehydration cycles by adding titanium methoxide - water cycles, and achieve self-limiting ternary Ba-Ti-O film deposition.[102] Certainly, surface chemistry in complex compounds ALD is far more complicated than expected. In addition, it was demonstrated that post-deposition annealing of stacked ALD HfO$_2$/Al$_2$O$_3$ layers resulted in the formation of crystalline Hf aluminate.[103] Although not applied intentionally, it could be a potential solution for complex oxide synthesis when no compatible ALD window could be defined between the binary subcycles. It also appeared to be useful when dealing with complicated cases such as to avoid possible prohibited growth between sublayers as was once reported for CuWO$_4$ growth.[54] Other strategies for complex oxides ALD from separate precursors involve co-injection of the precursors, however this approach is more frequently used in spatial ALD so it will not be discussed further here.

An attractive approach to simplify the scenario is the use of single-source heterometallic precursors which have been introduced in Section 1.2.1. Although the limited availability, probable low volatility and premature fragmentation could hinder their use in ALD, the intrinsic advantages of such molecules - pre-fixed elemental ratio, simplified deposition processes and chemical compatibility between the selected precursor and the target film - promise their advantageous application in ALD complex oxide growth.[47] The feasibility has been exemplified by the synthesis of SrTa$_2$O$_6$ and LnAlO$_x$ (Ln = Pr or Nd) ternary oxide by ALD.[45,46] Other works have demonstrated single-source precursors for the synthesis of silicates[104] and borates[105] by ALD. Above all, the single-source precursors are considered to have huge potential and the synthetic community is making efforts to broaden the library of available heterometallic complexes as ALD precursors.

1.3.2 Transition metal oxides: Materials, properties, and atomic scale growth

Transition metal oxides (TMOs) are a fascinating group of oxide materials that can be prepared from abundand and non-toxic elements, and possess rich physical and chemical properties. From the strong correlations of *d* electrons in the transition metal elements arise novel phenomena such as metal–insulator transitions, multiferroics and superconductivity which have led to an outburst of new investigation systems, *e.g.* oxide heterostructures, superlattices, double perovskites, 2D

and layers TMOs, etc.[106,107] The interest in transition metal oxide-based thin films are reviewed in two specific cases.

TMOs are a remarkable class of pseudocapacitive energy storage materials with high theoretical capacity for the energy storage devices such as LIBs and SCs. However, they suffer from low conductivity. To overcome this, TMOs (MnO_2, Fe_2O_3, Co_3O_4, etc) have been extensively studied for being coupled with highly conductive carbonaceous electrodes to produce improved cathode or anode materials for energy storage.[80,81] The synergistic effect between them for boosting device performances arises from the high capacitance of TMOs based on their rich redox converse reactions, and the outstanding conductivity, large interfacial surface area, structural and mechanical robustness of carbon. At the meantime, by developing carbon-TMOs hybrid electrodes, the carbon segregation and TMOs volume expansions that were encountered in their individual cases can be minimized.[108,109]

In the batteries or supercapacitors design, it is imperative to ensure the electrodes integrity during cycling.[110] For optimal device performance, conformal coatings with careful interfacial engineering are needed to ensure homogeneous contact between carbon and TMOs allowing for maximized accessible active sites during charge/discharge. However, the inert carbon surface could frustrate the nucleation process of ALD oxides, thus various approaches have been taken to functionalize the carbon surface. However, systematic studies are needed for understanding the surface chemistry induced by the functionalizing treatments.

Among the many investigated TMOs,[111–114] iron oxide and cobalt oxide, with high theoretical capacitance, is broadly explored, and sophisticated nanostructures have been successfully fabricated.[115–124]

For electronic applications, ALD TMOs have been thriving in application fields such as transistors, sensors, displays, etc. picturing ALD as an enabling technique for next-generation devices with ever-decreasing dimensions, as presented earlier in Section 1.2.4. Among the family of transition metal-based oxides, multicomponent oxides based on ferrites and rare-earth elements have captivated considerable attention owing to their magnetic,[125,126] magneto-optical[127–129] and ferroelectric properties.[130–134] Being able to synthesize them as ultrathin films with nanoscale control can bring benefits in various electronic technologies.[135–137] In this thesis, we aim to investigate new precursors and processes to deposit functional oxides for energy and electronic applications. Our contribution toward energy-oriented applications includes homogeneous and conformal Co_3O_4 and Fe_2O_3 coatings on TiO_2/C nanofibers or carbon nanotubes that could be of interest as anode materials for energy-storage devices, Article I and II; meanwhile, toward electronics applications, we dedicate to the synthesis of $Gd_xFe_yO_z$ ternary oxide system by ALD for magnetic and spintronic devices, Article III and Chapter 4.

INTRODUCTION

In the following, a brief description of cobalt oxide, iron oxide and gadolinium iron oxide systems is provided followed by their current research status in ALD.

1.3.2.1 Cobalt oxide

The cobalt oxides have three well-characterized cobalt oxide crystal structures, *i.e.* cubic CoO (c-CoO), hexagonal CoO (h-CoO) and spinel Co_3O_4, with Co^{2+} or Co^{3+} oxidation states.[138] The richness in chemical states and crystal structures makes the cobalt oxide system attractive for wide applications in catalysis,[139–142] sensor,[143] magnetism,[144] as well as energy storage[145] and conversion.[146,147] The two CoO monooxide polymorphs are distinguished by the Co^{2+} coordinations with oxygen atoms: c-CoO contains $[CoO_6]$ octahedras, whereas h-CoO has $[CoO_4]$ tetrahedras. As for the mixed valent spinel Co_3O_4, the cell lattices consist of $[CoO_4]$ tetrahedral geometries with Co^{2+} valency and $[CoO_6]$ octahedral geometries with Co^{3+} valency, shown in Figure 1.10a. Some open questions for this system, such as transformations between polymorphs or lack of synthesis procedure of the most stable phase Co_2O_3 under ambient conditions, make cobalt oxides very intriguing for further exploration.[138]

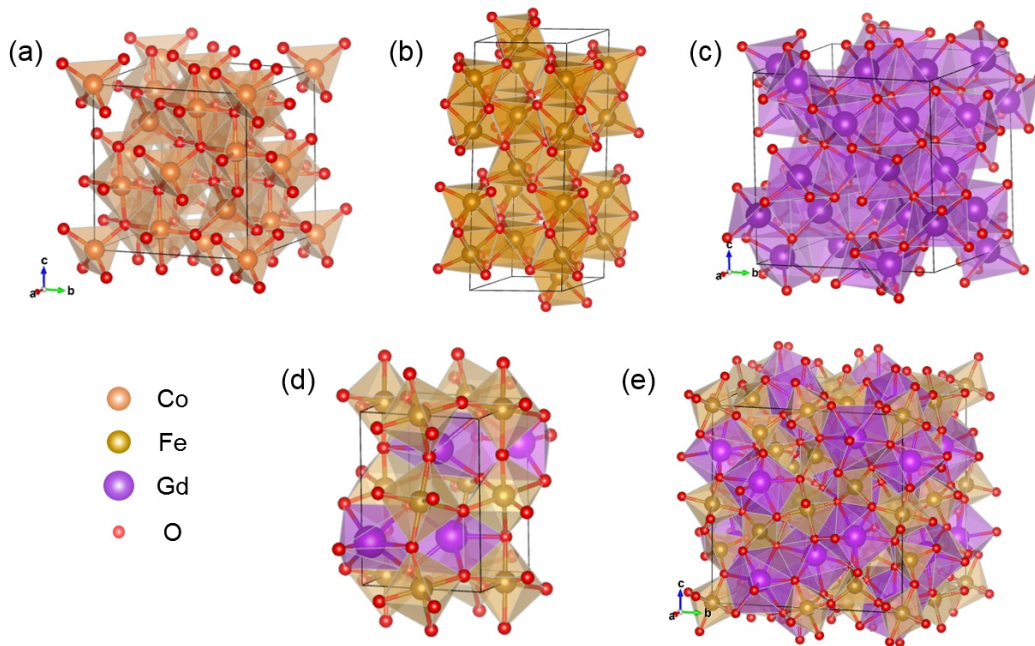**Fig. 1.10** Crystal structure of the functional oxides investigated in this thesis. (a) Cubic spinel Co_3O_4, (ICSD-36256); (b) hexagonal α-Fe_2O_3 (hematite, ICSD-15840); (c) cubic Gd_2O_3 (ICSD-40473); (d) orthorhombic gadolinium orthoferrite, $GdFeO_3$ (ICSD-23823); (e) cubic gadolinium garnet $Gd_3Fe_5O_{12}$ (ICSD-27127). ICSD stands for Inorganic Crystal Structure Database.

Cobalt oxide has been deposited by ALD using a wide variety of commercial precursors, ranging from halides CoI_2,[148] metallocenes $Co(Cp)_2$[32,33] (Cp = cyclopentadienyl), β-diketonates $Co(thd)_2$[149–151] (thd = 2,2,6,6-tetramethylheptane-3,5-dionate) and $Co(acac)_3$[152] (acac = acetylacetonate), and carbonyls $Co_2(CO)_8$,[141] or mixed functionalities such as $Co_2(CO)_6HC^tBu$[153] and $CpCo(CO)_2$.[154] Among these precursors, notably, cobalt oxide ALD using the halide source requires high deposition temperature (> 500 °C). Using metalorganic sources (Figure 1.11), the deposition temperature has been significantly reduced to the range of 100 - 400 °C. Specially, the carbonyl compound $Co_2(CO)_8$ or mixed carbonyl cyclopentadienyls $CpCo(CO)_2$ or $Co_2(CO)_6HC^tBu$ appear to be very suitable for low-temperature deposition of cobalt oxides, the process could be realized at even below 100 °C.[141,153,154] However, the low deposition temperature, enabled by the high reactivity of the precursors, is accompanied with narrow ALD windows and poor step coverage at elevated deposition temperature resulting from the low thermal stability of the cobalt precursor. Furthermore, the high reactivity of carbonyls towards water makes these compounds pyrophoric and requires special attentions for safe-handling. The conjugated π bond in cobaltocene $Co(Cp)_2$ and the bidentate structures in cobalt diketonate alkoxides $Co(thd)_2$ and $Co(acac)_3$ tend to stabilize the molecules and facilitate moderate reaction temperature. Notwithstanding, these precursors exhibit air sensitive nature and (or) low growth rate. For instance, $Co(thd)_2$ yields a growth rate of ~ 0.2 Å/cycle, which could be attributed to the high thermal stability and reduced reactivity of the compound.

The introduction of N-containing ligands into the precursor molecules seems promising for improving the precursor performances in that metal-N bond has lower strength than the metal-O bond. As a result, lower deposition temperatures compared to the β-diketonates can be enabled by the high reactivity of the compounds whilst maintain relatively high thermal stability.[155] The fully-N-coordinated bidentate Co precursors include a cobalt amidinate $Co(^iPrNCMeN^iPr)_2$[156,157] and two cobalt diazabutadienes $Co(^tBu_2DAD)_2$[158] (DAD = diazadiene) and $Co(dpdab)_2$[159] (dpdab = 1,4-di-iso-propyl-1,4-diazabutadiene), which have shown high reactivity towards water (except that $Co(^tBu_2DAD)_2$ was combined with O_3) and have enabled ALD processes for cobalt oxide at mild deposition temperatures of 120 - 300 °C with practical growth rates of > 0.5 Å/cycle. These precursors also exhibit lower evaporation temperature at 65 - 120 °C.

In addition, the nitrogen-based Co precursors mixed with halide or organic ligands have also been studied. A cobalt chloride diamine adduct $CoCl_2$(TMEDA) (TMEDA = N,N,N',N'-tetramethylethylenediamine) has been reported with water as co-reactant at 225–300 °C, however the halide ligand has led to higher source temperature (170 °C) in the ALD process.[160] More recently, a silylamide adduct $Co(BTSA)_2$(THF) (BTSA = bis(trimethylsilyl) amido, THF = tetrahydrofuran) based ALD process has been described at 75–250 °C with even lower precursor evaporation

temperature at 55 °C.[161] On the other hand, the resultant films were observed with Si impurities upon increasing deposition temperature.
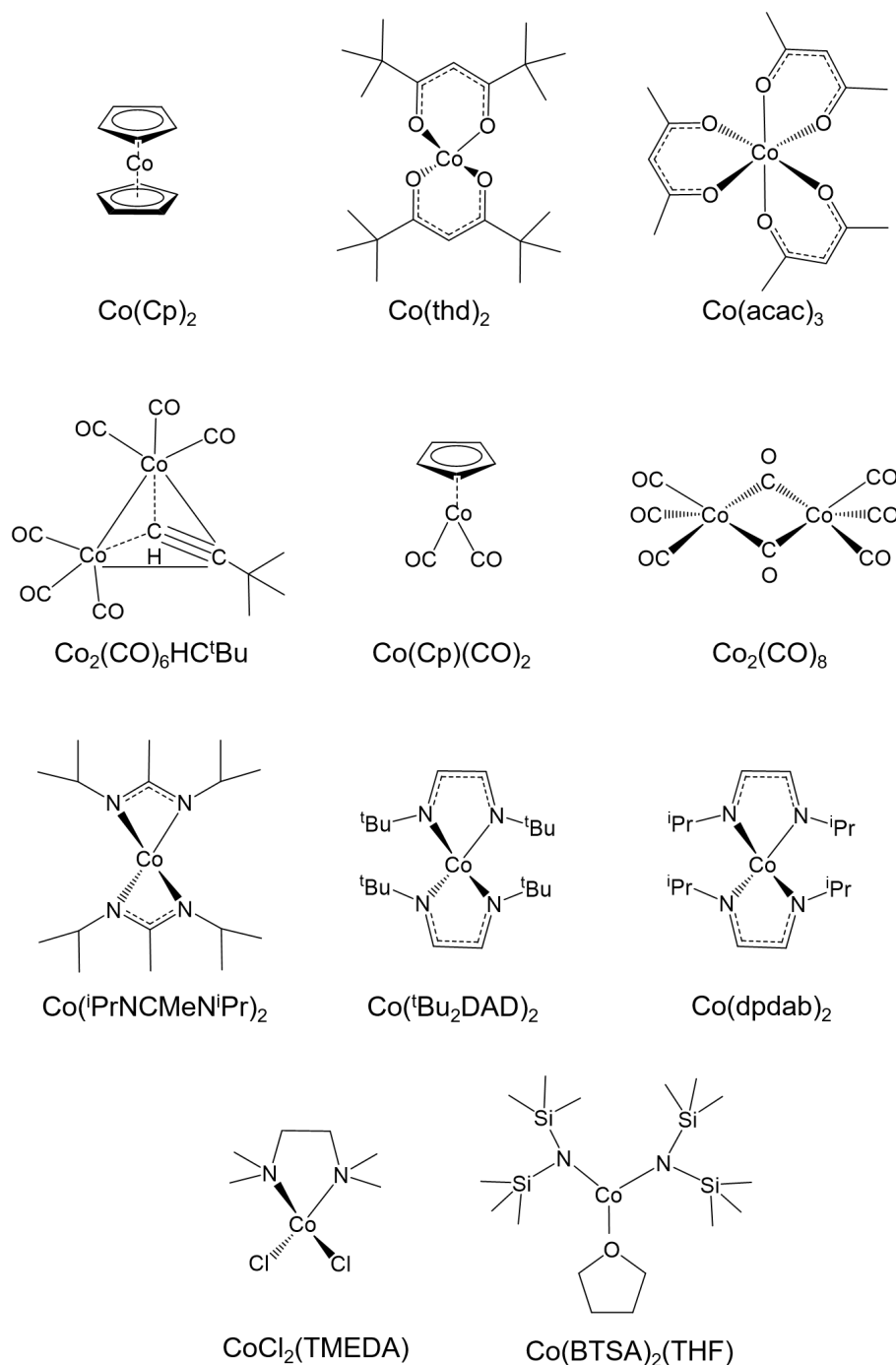
Fig. 1.11 Molecular structures of the metalorganic precursors for cobalt oxide in ALD.

Regarding the phases obtained, Co^{2+} oxide can be obtained when using less oxidant co-reactant with H_2O.[156,157,160,161] Most of the above mentioned works have been dedicated to produce

spinel Co_3O_4 phase combining the cobalt precursors with O_3. Nonetheless, the spinel phase has been commonly reported to be mixed with cubic CoO phase.[32,141,149,158,159] To summarize, the bidentate ligands, delocalized bonds help enhancing thermal stability but requires higher source temperature and deposition temperature. Nitrogen-coordinated precursors have shown promising applications as ALD cobalt precursors. On the other hand, the high reactivity toward water has been restraining the ambient stability of the precursors, so handling under inert conditions are required. A balance or compromise has to be found for designing an ALD precursor with suitable properties. Consequently, it is desirable to investigate more Co precursors for synthesizing high quality pure cobalt oxide thin films with low impurity levels at mild conditions.

In this work, we contribute to ALD spinel Co_3O_4 synthesis (Figure 1.10a) from a novel β-heteroarylalkenolate precursor $Co(DMOCHCOCF_3)_2$ ($DMOCHCOHCF_3$=1-(dimethyl-1,3-oxazol-2-yl)-3,3,3-trifluorprop-1-en-2-ol, Figure 1.12a). The mixed O, N coordination bonds and introduction of heteroaryl moieties and CF_3-groups enabled safe-handling of the precursor in ambient conditions with long term stability, presented in Article I.
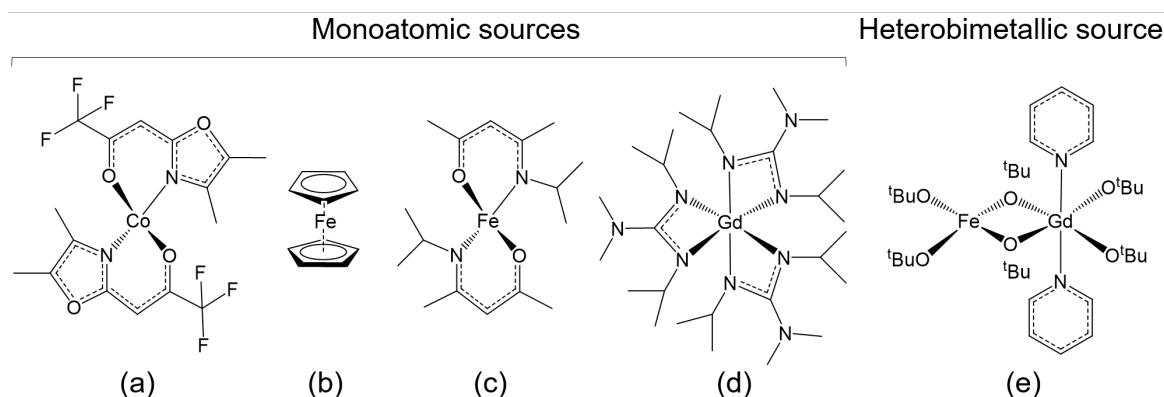
Fig. 1.12 Molecular structure of the ALD precursors that have been investigated in this thesis. Homometallic sources: (a) $Co(DMOCHCOCF_3)_2$ ($DMOCHCOHCF_3$ = 1-(dimethyl-1,3-oxazol-2-yl)-3,3,3-trifluorprop-1-en-2-ol); (b) $Fe(Cp)_2$ (Cp = cyclopentadienyl); (c) $Fe(^ipki)_2$ (^ipki = N-isopropyl ketoiminate); (d) $Gd(DPDMG)_3$ (DPDMG = N,N'-diisopropyl-2-dimethylamido-guanidinato); heterobimetallic source: (e) $GdFe(O^tBu)_6(C_5H_5N)_2$ (C5H5N = pyridine).

1.3.2.2 Iron oxide

Being in the same VIII group as Co, Fe also possesses Fe^{2+} or Fe^{3+} oxidation states, forming FeO or Fe_2O_3 with single oxidation state, or Fe_3O_4 with mixed oxidation states. Among these three iron oxides, Fe_2O_3 with trivalent Fe, remains the most interesting and potentially useful iron oxides due to its rich polymorphism, viz α-, β-, γ-, ε-, and ζ-Fe_2O_3. Each polymorh has its unique properties, in addition to being nontoxic, abundant and inexpensive, for various potential applications. For example, α-Fe_2O_3 for photocatalytic water splitting in solar cells and gas

sensing, nanosized γ-Fe_2O_3 for medical applications such as magnetic drug delivery or magnetic resonance imaging contrast agent, ε-Fe_2O_3 for advanced magnetic applications, etc.[162]

α-Fe_2O_3, or hematite, is the most thermally stable polymorph of iron oxide. It is rich in nature and can be easily synthesized in the nanoparticles or thin films forms by various techniques.[162] Structurally, hematite crystals has corundum type rhombohedral structure with octahedral $[FeO_6]$ geometries, see Figure 1.10b. Correspondingly, α-Fe_2O_3 is the most explored iron oxide in ALD, which has been synthesized using various types of precursors, such as the Fe chlorides $FeCl_3$,[163,164] and metalorganic sources (illustration of their molecular structures see Figure 1.14) such as Fe alkoxides $Fe_2(O^tBu)_6$,[28,165,166] ferrocene $Fe(Cp)_2$,[27-31,167-169] the ferrocene derivative $Fe(Cp)(^tBuCp)$,[169,170] or half-open ferrocene $Fe(2-C_7H_{11})_2$[171] (2,4-C_7H_{11} = 2,4-methylpentadienyl), β-diketonates $Fe(thd)_3$[172,173] or $Fe(acac)_3$,[174] amidinate FeAMD[175] (AMD = bis(N,N-di-t-butylacetamidinatoamidinate)) and ketoiminate $Fe(^ipki)_2$[176] (^ipki = N-isopropyl ketoiminate). Fe precursors with mixed ligands have also been investigated, such as the carbonyl cyclopentadienyl $Cp_2Fe_2(CO)_4$,[177] or a β-diketonate diamine adduct $Fe(hfa)_2TMEDA$[178] (hfa = 1,1,1,5,5,5-hexafluoro-2,4-pentanedionate, TMEDA = N,N,N′,N′-tetramethylethylenediamine). Compared to α-Fe_2O_3, the other four Fe_2O_3 polymorphs have been less explored in ALD. To our knowledge, up to date β-Fe_2O_3 or ζ-Fe_2O_3 ALD has not been reported in literature. γ-Fe_2O_3 has been demonstrated to be obtained in pure phase by controlling the ozone exposure in ALD $Fe(Cp)_2$ and O_3 reaction,[169] or sometimes appears as minor phases in α-Fe_2O_3 ALD films.[164] γ-Fe_2O_3 in the nanoparticles form has been synthesized from $Fe(Cp)_2$ and O_2 on carbon nanotubes at 350 °C.[179] While the synthesis of rare ε-Fe_2O_3 has only been reported once from $FeCl_3$ and H_2O precursor at 260–300 °C.[180]

The other two iron oxides, FeO and Fe_3O_4, have also received decreased focus. FeO has been synthesized by ALD from $Fe(O^tBuNCMeNO^tBu)_2$ and H_2O at 250 °C.[156] Meanwhile, ALD Fe_3O_4 synthesis has been achieved by direct deposition from the open metallocene complex $Fe(2-C_7H_{11})_2$ and mild reactant H_2O_2 at 120 °C,[171] or from the mixed cyclopentadienyl carbonyl $Cp_2Fe_2(CO)_4$ precursor and H_2O at 160 °C.[177] Fe_3O_4 can also be obtained through post deposition reduction process from the ALD Fe(III) oxides.[28,165]

Among these precursors, only a few precursors can react with H_2O including $FeCl_3$, $Fe_2(O^tBu)_6$, Fe(AMD), $Fe(O^tBuNCMeNO^tBu)_2$ and $Cp_2Fe_2(CO)_4$, while the others require stronger reactants such as O_2 or O_3. Notably, $Fe(Cp)_2$ is very popular and has been widely studied due to its commercial availability and low-cost. However, $Fe(Cp)_2$ differs from other metallocenes by its high thermal stability, thus in ALD it is usually combined with strong oxidants and usually works at relatively high deposition temperature. Besides, problematic iron oxides ALD have been spotted from ferrocene, including pump deterioration and commonly low growth rates unless

long precursor pulses were employed. [175,181] On the other hand, the Fe ketoiminate Fe(^{i}pki)$_2$ has found a balance between the reactivity and stability which enabled a well-defined ALD process for depositing Fe$_2$O$_3$ films. [176]
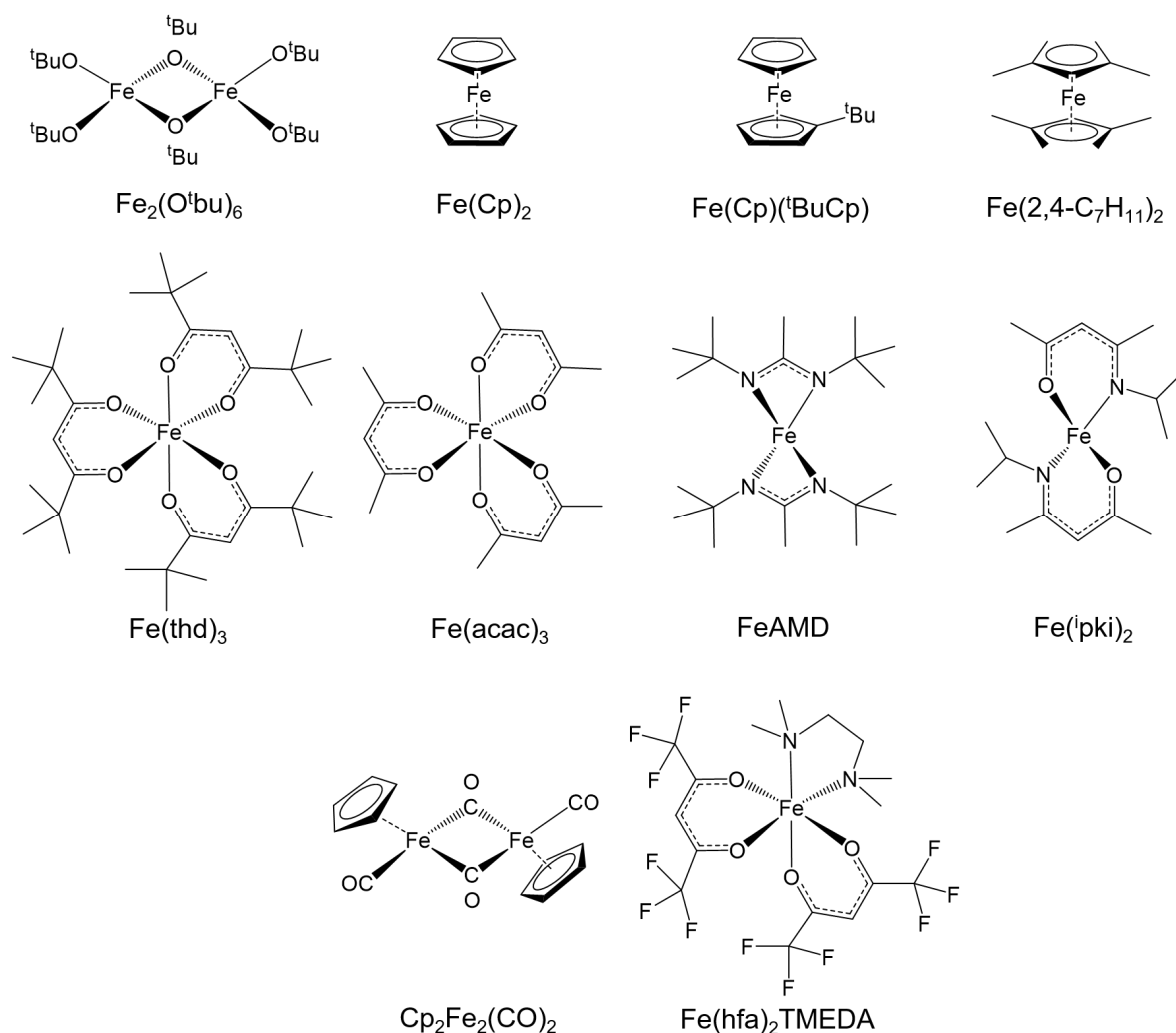
Fig. 1.13 Molecular structures of the metalorganic precursors for iron oxide in ALD.

In this thesis, Fe precursors are investigated for two aspects: 1) surface reactivity of ALD iron oxide towards carbon nanotubes surfaces upon different kinds of surface treatments. To this end, the economic commercial precursor Fe(Cp)$_2$ has been used (Article II). 2) reactivity and compatibility of separate Fe and Gd sources to prepare multicomponent Gd$_x$Fe$_y$O$_z$ ternary oxide systems. For this purpose, we explored both Fe(Cp)$_2$ and Fe(^{i}pki)$_2$ as the Fe sources for comparison. As can be appreciated in Figure 1.12bc, structurally, Fe(Cp)$_2$ is a metallocene precursor with a sandwiched structure, while Fe(^{i}pki)$_2$ is tailor-made with N-, O- ligands. Their different behavior in our ALD

reactor for depositing iron oxide and gadolinium iron oxide combined with Gd precursor will be described and compared in Chapter 4.

1.3.2.3 $Gd_xFe_yO_z$ system

The ternary $Gd_xFe_yO_z$ system consists of two representative phases, *viz.* $GdFeO_3$ and $Gd_3Fe_5O_{12}$. Although containing the mixed $[FeO_6]$ octahedra and $[GdO_8]$ polyhedra from Fe_2O_3 and Gd_2O_3, Figure 1.10bc, $GdFeO_3$ and $Gd_3Fe_5O_{12}$ do not share the same structure. The gadolinium ortho-ferrite, or $GdFeO_3$, contains one Gd^{3+} and one canted Fe^{3+} sublattices with weak ferromagnetic contribution. It is considered the prototype for $GdFeO_3$ family structures and crystallizes with the distorted orthorhombic structure, Figure 1.10d.[137,182] On the other hand, gadolinium garnet ferrite, $Gd_3Fe_5O_{12}$, contains one Gd^{3+} sublattice and two different Fe^{3+} sublattices that are an-tiferromagnetically coupled with a net magnetically reduced Fe^{3+} sublattice. It crystallizes in cubic structure, Figure 1.10e.[183,184] In both cases, Gd^{3+} sublattice only align magnetically at low temperature.

It is desirable to obtain high quality $Gd_xFe_yO_z$ films with pure phase composition for further study-ing the potential functional properties arising from the complex oxides and their interfaces.[78,185] Up till now, only a few rare earth iron oxides, namely the orthorhombic $LaFeO_3$[186] and hexagonal $ErFeO_3$,[187] have been synthesized by ALD via supercycle approach using β-diketonates precur-sors $La(thd)_3$, $Er(thd)_3$ and $Fe(thd)_3$. On the other hand, in the arising field of ALD complex oxide synthesis from heterometallic precursors, no rare earth ferrite films have been reported yet. To our knowledge, no literature have been published regarding the atomic layer deposition of $Gd_xFe_yO_z$ systems. Thus, it is very appealing and of great opportunity to take advantage of the nanoscale control of ALD to investigate the synthesis of $Gd_xFe_yO_z$.

As mentioned earlier, the supercycle approach is complicated by the compatibility of the different chemistries of the homometallic sources and their deposition conditions. With the Fe precursors reviewed in Section 1.3.2.2, here the Gd sources for ALD is briefly introduced. In contrast with the rich sources for iron oxide deposition, the ALD gadolinium oxide has mainly been synthesized from alkoxides $Gd(DMB)_3$[188] (DMB = $OCMe_2CHMe_2$)), or $Gd(mmp)_3$[189] (mmp = $OCMe_2CH_2OMe$), derived cyclopentadienyl complexes $Gd(MeCp)_3$[190] or $Gd(^iPrCp)_3$[191–193] Gd β-diketonate $Gd(thd)_3$,[190,194] silylamide $Gd[N(SiMe_3)_2]_3$,[195] guanidinate $Gd(DPDMG)_3$[196] (DPDMG = N,N'-diisopropyl-2-dimethylamido-guanidinato) and $Gd(^iPrCp)_2(^iPr-amd)$[40] (amd = Amidinate) with mixed Cp and amidinate functionalities. The processes are usually frustrating with the films contaminated with C or H impurities or lacking self-limiting behavior.[44] Specially, the $Gd(DPDMG)_3$ is tailored with fully nitrogen coordinated ligands, and has demonstrated considerable thermal stability and optimal reactivity toward H_2O which has led to well-defined

deposition behaviour for pure ALD Gd_2O_3 thin films.
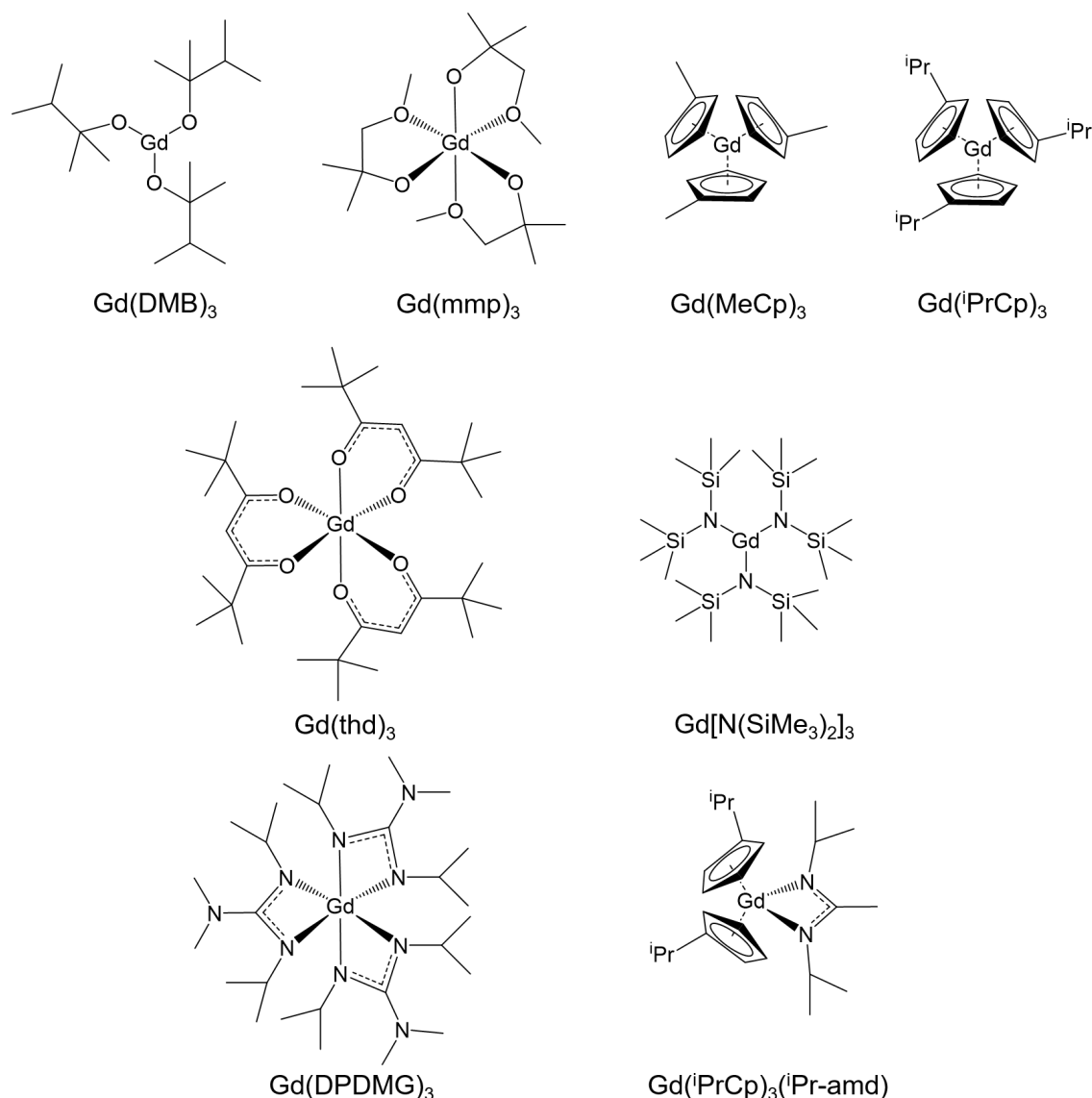
Fig. 1.14 Molecular structures of the metalorganic precursors for gadolinium oxide in ALD.

In this thesis, it is investigated the potential of ALD to control film stoichiometry, crystallinity of $Gd_xFe_yO_z$ oxides thin films using both single-source approach and separate homometallic precursors approach. For the first approach, it is explored the use of a novel heterobimetallic source $GdFe(O^tBu)_6(C_5H_5N)_2$ (Figure 1.3e) with stoichiometric metal ratio, which will be presented in Article III. The latter approach is studied combining tailor-made homometallic Fe and Gd sources $(Fe(Cp)_2, Fe(^ipki)_2$ and $Gd(DPDMG)_3$, Figure 1.3b-d), Chapter 4.

References

[1] R. Vajtai. *Springer Handbook of Nanomaterials*. Springer Berlin Heidelberg, Berlin, Heidelberg, 2013.

[2] A. Sengupta, C. Kumar, and S. Editors. *Introduction to Nano: Basics to Nanoscience and Nanotechnology*. Engineering Materials. Springer Berlin Heidelberg, Berlin, Heidelberg, 2015.

[3] Q. Zhang, E. Uchaker, S. L. Candelaria, et al. Nanomaterials for energy conversion and storage. *Chemical Society Reviews*, 42(7):3127, 2013.

[4] R. Puers, L. Baldi, M. Van de Voorde, et al. *Nanoelectronics*, volume 1. Wiley-VCH Verlag GmbH & Co. KGaA, Weinheim, Germany, 2017.

[5] R. Clark, K. Tapily, K.-H. Yu, et al. Perspective: New process technologies required for future devices and scaling. *APL Materials*, 6(5):058203, 2018.

[6] M. Coll and M. Napari. Atomic layer deposition of functional multicomponent oxides. *APL Materials*, 7(11):110901, 2019.

[7] M. Ritala and M. Leskelä. Atomic layer deposition. In *Handbook of Thin Films*, pages 103–159. Elsevier, 2002.

[8] S. M. George. Atomic Layer Deposition: An Overview. *Chemical Reviews*, 110(1):111–131, 2010.

[9] H. Knoops, S. Potts, A. Bol, et al. Atomic Layer Deposition. In *Handbook of Crystal Growth*, volume 3, pages 1101–1134. Elsevier, second edition, 2015.

[10] T. Suntola and J. Antson. Method for producing compound thin films. US Patent 4,058,430.

[11] T. Suntola. Atomic layer epitaxy. *Materials Science Reports*, 4(5):261 – 312, 1989.

[12] R. L. Puurunen. A Short History of Atomic Layer Deposition: Tuomo Suntola's Atomic Layer Epitaxy. *Chemical Vapor Deposition*, 20(10-11-12):332–344, 2014.

[13] The dawn of atomic-scale processing - The growing importance of atomic layer deposition and etching. https://www.atomiclimits.com/2017/07/03/the-dawn-of-atomic-scale-processing-the-growing-importance-of-atomic-layer-deposition-and-etching/.

[14] H. C. M. Knoops, T. Faraz, K. Arts, et al. Status and prospects of plasma-assisted atomic layer deposition. *Journal of Vacuum Science & Technology A*, 37(3):030902, 2019.

[15] T. Faraz, F. Roozeboom, H. C. M. Knoops, et al. Atomic Layer Etching: What Can We Learn from Atomic Layer Deposition? *ECS Journal of Solid State Science and Technology*, 4(6):N5023–N5032, 2015.

[16] Atomic Layer Etch Expands To New Markets. http://semiengineering.com/atomic-layer-etch-expands-to-new-markets/.

[17] X. Meng. An overview of molecular layer deposition for organic and organic–inorganic hybrid materials: mechanisms, growth characteristics, and promising applications. *Journal of Materials Chemistry A*, 5(35):18326–18378, 2017.

References

[18] A. C. Jones and M. L. Hitchman. Chapter 1. Overview of Chemical Vapour Deposition. In A. C. Jones and M. L. Hitchman, editors, *Chemical Vapour Deposition: Precursors, Processes and Applications*, pages 1–36. Royal Society of Chemistry, Cambridge, 2008.

[19] R. Eason. *Pulsed Laser Deposition of Thin Films: Applications-Led Growth of Functional Materials*. John Wiley & Sons, Inc., 2006.

[20] S. H. Herman Marian A. *Molecular Beam Epitaxy: Fundamentals and Current Status*. Springer, Berlin, Heidelberg, 1996.

[21] R. G. Gordon. ALD Precursors and Reaction Mechanisms. In C. S. Hwang, editor, *Atomic Layer Deposition for Semiconductors*, chapter 2, pages 15–46. Springer, Boston, MA, 2014.

[22] C. D. Travis and R. A. Adomaitis. Modeling ALD Surface Reaction and Process Dynamics using Absolute Reaction Rate Theory. *Chemical Vapor Deposition*, 19(1-3):4–14, 2013.

[23] M. Ylilammi, O. M. Ylivaara, and R. L. Puurunen. Modeling growth kinetics of thin films made by atomic layer deposition in lateral high-aspect-ratio structures. *Journal of Applied Physics*, 123(20): 205301, 2018.

[24] R. W. Johnson, A. Hultqvist, and S. F. Bent. A brief review of atomic layer deposition: From fundamentals to applications. *Materials Today*, 17(5):236–246, 2014.

[25] K. Kukli, M. Ritala, T. Sajavaara, et al. Comparison of hafnium oxide films grown by atomic layer deposition from iodide and chloride precursors. *Thin Solid Films*, 416(1-2):72–79, 2002.

[26] I. K. Oh, B. E. Park, S. Seo, et al. Comparative study of the growth characteristics and electrical properties of atomic-layer-deposited HfO_2 films obtained from metal halide and amide precursors. *Journal of Materials Chemistry C*, 6(27):7367–7376, 2018.

[27] M. Rooth, A. Johansson, K. Kukli, et al. Atomic layer deposition of iron oxide thin films and nanotubes using ferrocene and oxygen as precursors. *Chemical Vapor Deposition*, 14(3-4):67–70, 2008.

[28] J. Escrig, J. Bachmann, J. Jing, et al. Crossover between two different magnetization reversal modes in arrays of iron oxide nanotubes. *Physical Review B*, 77(21):214421, 2008.

[29] J. R. Scheffe, A. Francés, D. M. King, et al. Atomic layer deposition of iron(iii) oxide on zirconia nanoparticles in a fluidized bed reactor using ferrocene and oxygen. *Thin Solid Films*, 517(6): 1874–1879, 2009.

[30] A. B. F. Martinson, M. J. DeVries, J. A. Libera, et al. Atomic layer deposition of Fe_2O_3 using ferrocene and ozone. *The Journal of Physical Chemistry C*, 115(10):4333–4339, 2011.

[31] X. Li, N. C. Fan, and H. J. Fan. A micro-pulse process of atomic layer deposition of iron oxide using ferrocene and ozone precursors and Ti-doping. *Chemical Vapor Deposition*, 19(4-6):104–110, 2013.

[32] M. Diskus, O. Nilsen, and H. Fjellvåg. Thin Films of Cobalt Oxide Deposited on High Aspect Ratio Supports by Atomic Layer Deposition. *Chemical Vapor Deposition*, 17(4-6):135–140, 2011.

[33] B. Huang, W. Yang, Y. Wen, et al. Co_3O_4-Modified TiO_2 Nanotube Arrays via Atomic Layer Deposition for Improved Visible-Light Photoelectrochemical Performance. *ACS Applied Materials & Interfaces*, 7(1):422–431, 2015.

[34] M. Daub, M. Knez, U. Goesele, et al. Ferromagnetic nanotubes by atomic layer deposition in anodic alumina membranes. *Journal of Applied Physics*, 101(9):09J111, 2007.

[35] M. Coll, J. M. Montero Moreno, J. Gazquez, et al. Low Temperature Stabilization of Nanoscale Epitaxial Spinel Ferrite Thin Films by Atomic Layer Deposition. *Advanced Functional Materials*, 24(34):5368–5374, 2014.

[36] J. H. Kim, D. S. Kil, S. J. Yeom, et al. Modified atomic layer deposition of RuO_2 thin films for capacitor electrodes. *Applied Physics Letters*, 91(5):052908, 2007.

[37] X. Jiang, T. M. Gür, F. B. Prinz, et al. Atomic layer deposition (ALD) Co-deposited Pt-Ru binary and Pt skin catalysts for concentrated methanol oxidation. *Chemistry of Materials*, 22(10):3024–3032, 2010.

[38] E. Färm, S. Lindroos, M. Ritala, et al. Microcontact printed RuO_x film as an activation layer for selective-area atomic layer deposition of ruthenium. *Chemistry of Materials*, 24(2):275–278, 2012.

[39] B. Han, J. M. Park, K. H. Choi, et al. Atomic layer deposition of stoichiometric Co_3O_4 films using bis(1,4-di-iso-propyl-1,4-diazabutadiene) cobalt. *Thin Solid Films*, 589:718–722, 2015.

[40] S. Seppälä, J. Niinistö, M. Mattinen, et al. Atomic layer deposition of lanthanum oxide with heteroleptic cyclopentadienyl-amidinate lanthanum precursor - Effect of the oxygen source on the film growth and properties. *Thin Solid Films*, 660:199–206, 2018.

[41] A. L. Johnson and J. D. Parish. Recent developments in molecular precursors for atomic layer deposition. In *Organometallic Chemistry*, volume 42, pages 1–53. American Chemical Society, 2018.

[42] M. Vehkamäki, T. Hatanpää, T. Hänninen, et al. Growth of $SrTiO_3$ and $BaTiO_3$ thin films by atomic layer deposition. *Electrochemical and Solid-State Letters*, 2(10):504–506, 1999.

[43] M. Vehkamäki, T. Hänninen, M. Ritala, et al. Atomic Layer Deposition of $SrTiO_3$ Thin Films from a Novel Strontium Precursor–Strontium-bis(tri-isopropyl cyclopentadienyl). *Chemical Vapor Deposition*, 7(2):75–80, 2001.

[44] A. Devi. 'Old chemistries' for new applications: Perspectives for development of precursors for MOCVD and ALD applications. *Coordination Chemistry Reviews*, 257(23-24):3332–3384, 2013.

[45] M. Vehkamäki, M. Ritala, M. Leskelä, et al. Atomic layer deposition of strontium tantalate thin films from bimetallic precursors and water. *Journal of The Electrochemical Society*, 151(4):69–72, 2004.

[46] J. M. Gaskell, S. Przybylak, A. C. Jones, et al. Deposition of Pr- and Nd-aluminate by Liquid Injection MOCVD and ALD Using Single-Source Heterometallic Alkoxide Precursors. *Chemistry of Materials*, 19(19):4796–4803, 2007.

[47] P. Marchand and C. J. Carmalt. Molecular precursor approach to metal oxide and pnictide thin films. *Coordination Chemistry Reviews*, 257(23-24):3202–3221, 2013.

[48] N. E. Richey, C. de Paula, and S. F. Bent. Understanding chemical and physical mechanisms in atomic layer deposition. *The Journal of Chemical Physics*, 152(4):040902, 2020.

References

[49] K. Bernal Ramos, M. J. Saly, and Y. J. Chabal. Precursor design and reaction mechanisms for the atomic layer deposition of metal films. *Coordination Chemistry Reviews*, 257(23-24):3271–3281, 2013.

[50] F. Grillo, H. Van Bui, J. A. Moulijn, et al. Understanding and Controlling the Aggregative Growth of Platinum Nanoparticles in Atomic Layer Deposition: An Avenue to Size Selection. *The Journal of Physical Chemistry Letters*, 8(5):975–983, 2017.

[51] S. D. Elliott and J. C. Greer. Simulating the atomic layer deposition of alumina from first principles. *Journal of Materials Chemistry*, 14(21):3246, 2004.

[52] R. L. Puurunen. Correlation between the growth-per-cycle and the surface hydroxyl group concentration in the atomic layer deposition of aluminum oxide from trimethylaluminum and water. *Applied Surface Science*, 245(1-4):6–10, 2005.

[53] M. L. Green, M. Y. Ho, B. Busch, et al. Nucleation and growth of atomic layer deposited HfO_2 gate dielectric layers on chemical oxide (Si-O-H) and thermal oxide (SiO_2 or Si-O-N) underlayers. *Journal of Applied Physics*, 92(12):7168–7174, 2002.

[54] Y. Gao, O. Zandi, and T. W. Hamann. Atomic layer stack deposition-annealing synthesis of $CuWO_4$. *Journal of Materials Chemistry A*, 4(8):2826–2830, 2016.

[55] Y. Lu, S. Bangsaruntip, X. Wang, et al. DNA Functionalization of Carbon Nanotubes for Ultrathin Atomic Layer Deposition of High K Dielectrics for Nanotube Transistors with 60 mV / Decade Switching. *Journal of the American Chemical Society*, 2(11):3518–3519, 2006.

[56] G.-D. Zhan, X. Du, D. M. King, et al. Atomic layer deposition on bulk quantities of surfactant-modified single-walled carbon nanotubes. *Journal of the American Ceramic Society*, 91(3):831–835, 2008.

[57] D. B. Farmer and R. G. Gordon. Atomic layer deposition on suspended single-walled carbon nanotubes via gas-phase noncovalent functionalization. *Nano Letters*, 6(4):699–703, 2006.

[58] N. Kemnade, C. J. Shearer, D. J. Dieterle, et al. Non-destructive functionalisation for atomic layer deposition of metal oxides on carbon nanotubes: effect of linking agents and defects. *Nanoscale*, 7: 3028–3034, 2015.

[59] X. Meng, M. Ionescu, M. N. Banis, et al. Heterostructural coaxial nanotubes of $CNT@Fe_2O_3$ via atomic layer deposition: effects of surface functionalization and nitrogen-doping. *Journal of Nanoparticle Research*, 13(3):1207–1218, 2010.

[60] L. Acauan, A. C. Dias, M. B. Pereira, et al. Influence of different defects in vertically aligned carbon nanotubes on TiO_2 nanoparticle formation through atomic layer deposition. *ACS Applied Materials & Interfaces*, 8(25):16444–16450, 2016.

[61] M. Ylilammi. Monolayer thickness in atomic layer deposition. *Thin Solid Films*, 279(1-2):124–130, 1996.

[62] M. Leskelä and M. Ritala. Atomic layer deposition chemistry: Recent developments and future challenges. *Angewandte Chemie International Edition*, 42(45):5548–5554, 2003.

[63] A. Rahtu, T. Alaranta, and M. Ritala. In situ quartz crystal microbalance and quadrupole mass spectrometry studies of atomic layer deposition of aluminum oxide from trimethylaluminum and water. *Langmuir*, 17(21):6506–6509, 2001.

[64] M. A. Mione, R. Engeln, V. Vandalon, et al. Infrared and optical emission spectroscopy study of atmospheric pressure plasma-enhanced spatial ALD of Al_2O_3. *Applied Physics Letters*, 115(8): 083101, 2019.

[65] O. Nilsen and H. Fjellvåg. Measuring the heat evolved from individual reaction steps in atomic layer deposition. *Journal of Thermal Analysis and Calorimetry*, 105(1):33–37, 2011.

[66] J. Dendooven, E. Solano, M. M. Minjauw, et al. Mobile setup for synchrotron based in situ characterization during thermal and plasma-enhanced atomic layer deposition. *Review of Scientific Instruments*, 87(11):113905, 2016.

[67] H. H. Sønsteby, E. Skaar, Ø. S. Fjellvåg, et al. A foundation for complex oxide electronics -low temperature perovskite epitaxy. *Nature Communications*, 11(1):2872, 2020.

[68] A. J. M. Mackus, J. R. Schneider, C. MacIsaac, et al. Synthesis of Doped, Ternary, and Quaternary Materials by Atomic Layer Deposition: A Review. *Chemistry of Materials*, 31(4):1142–1183, 2019.

[69] G. Von Gastrow, S. Li, P. Repo, et al. conference Ozone-based batch atomic layer deposited Al_2O_3 for effective surface passivation. *Energy Procedia*, 38:890–894, 2013.

[70] J. Hämäläinen, M. Ritala, and M. Leskelä. Atomic Layer Deposition of Noble Metals and Their Oxides. *Chemistry of Materials*, 26(1):786–801, 2014.

[71] Database of ALD processes. https://www.atomiclimits.com/alddatabase/.

[72] J. Huang, X. Wang, and Z. L. Wang. Controlled Replication of Butterfly Wings for Achieving Tunable Photonic Properties. *Nano Letters*, 6(10):2325–2331, 2006.

[73] H. Mertens, R. Ritzenthaler, A. Y. Hikavyy, et al. (Invited) Gate-All-Around Transistors Based on Vertically Stacked Si Nanowires. *ECS Transactions*, 77(5):19–30, 2017.

[74] T. W. Kim, S. Uchida, T. Kondo, et al. Optimization of TiO_2 compact layer formed by atomic layer deposition for efficient perovskite solar cells. *Applied Physics Letters*, 115(20):203902, 2019.

[75] Holst Centre Shows Next Step Towards Cheaper Flexible Electronics. https://www.displaydaily.com/article/press-releases/holst-center-researchers-use-sald-to-create-igzo-oled-display-backplanes-on-pen-foils.

[76] E. G. Jeong, Y. Jeon, S. H. Cho, et al. Textile-based washable polymer solar cells for optoelectronic modules: toward self-powered smart clothing. *Energy & Environmental Science*, 12(6):1878–1889, 2019.

[77] M. D. McDaniel, T. Q. Ngo, S. Hu, et al. Atomic layer deposition of perovskite oxides and their epitaxial integration with Si, Ge, and other semiconductors. *Applied Physics Reviews*, 2(4):41301, 2015.

[78] M. Coll, J. Fontcuberta, M. Althammer, et al. Towards Oxide Electronics: a Roadmap. *Applied Surface Science*, 482:1–93, 2019.

[79] T. Vasen, P. Ramvall, A. Afzalian, et al. Vertical Gate-All-Around Nanowire GaSb-InAs Core-Shell n-Type Tunnel FETs. *Scientific Reports*, 9(1), 2019.

[80] X. Wang and G. Yushin. Chemical vapor deposition and atomic layer deposition for advanced lithium ion batteries and supercapacitors. *Energy Environ. Sci.*, 8(7):1889–1904, 2015.

References

[81] X. Meng, X. Wang, D. Geng, et al. Atomic layer deposition for nanomaterial synthesis and functionalization in energy technology. *Materials Horizons*, 4(2):133–154, 2017.

[82] L. E. Black and W. M. Kessels. PO_x/Al_2O_3 stacks: Highly effective surface passivation of crystalline silicon with a large positive fixed charge. *Applied Physics Letters*, 112(20):201603, 2018.

[83] S.-M. Lee, E. Pippel, U. Gosele, et al. Greatly Increased Toughness of Infiltrated Spider Silk. *Science*, 324(5926):488–492, 2009.

[84] M. Choi, S.-R. Bae, L. Hu, et al. Full-color active-matrix organic light-emitting diode display on human skin based on a large-area MoS_2 backplane. *Science Advances*, 6(28):eabb5898, 2020.

[85] K. E. Gregorczyk, D. F. Pickup, M. G. Sanz, et al. Tuning the Tensile Strength of Cellulose through Vapor-Phase Metalation. *Chemistry of Materials*, 27(1):181–188, 2015.

[86] I. Azpitarte, A. Zuzuarregui, H. Ablat, et al. Suppressing the Thermal and Ultraviolet Sensitivity of Kevlar by Infiltration and Hybridization with ZnO. *Chemistry of Materials*, 29(23):10068–10074, 2017.

[87] ALD Deposition System | CTECHNANO. https://ctechnano.com/coating-technologies/ald-deposition-system/.

[88] Spatial ALD equipment - Beneq WCS 600. https://beneq.com/en/products/spatial-ald-equipment/wcs600/.

[89] PICOSUN® Morpher - Picosun. https://www.picosun.com/product/picosun-morpher/.

[90] Atomfab ALD System - Oxford Instruments. https://plasma.oxinst.com/products/atomic-layer-deposition/atomfab.

[91] M. Coll, J. Gazquez, A. Palau, et al. Low temperature epitaxial oxide ultrathin films and nanostructures by atomic layer deposition. *Chemistry of Materials*, 24(19):3732–3737, 2012.

[92] A. J. Mackus, A. A. Bol, and W. M. Kessels. The use of atomic layer deposition in advanced nanopatterning. *Nanoscale*, 6(19):10941–10960, 2014.

[93] M. Coll, A. Palau, J. C. Gonzalez-Rosillo, et al. Integration of atomic layer deposition CeO_2 thin films with functional complex oxides and 3D patterns. *Thin Solid Films*, 553:7–12, 2014.

[94] S. Seo, S. Jeong, H. Park, et al. Atomic layer deposition for efficient and stable perovskite solar cells. *Chemical Communications*, 55(17):2403–2416, 2019.

[95] J. Zhang, G. Zhang, Z. Chen, et al. Emerging applications of atomic layer deposition for lithium-sulfur and sodium-sulfur batteries. *Energy Storage Materials*, 26:513–533, 2020.

[96] M. Coll, J. Gazquez, I. Fina, et al. Nanocrystalline Ferroelectric $BiFeO_3$ Thin Films by Low-Temperature Atomic Layer Deposition. *Chemistry of Materials*, 27(18):6322–6328, 2015.

[97] E. L. Lin, A. B. Posadas, L. Zheng, et al. Atomic layer deposition of epitaxial ferroelectric barium titanate on Si(001) for electronic and photonic applications. *Journal of Applied Physics*, 126(6): 064101, 2019.

[98] H. H. Sønsteby, T. Aarholt, Ø. Prytz, et al. First complex oxide superconductor by atomic layer deposition. *Chemical Communications*, 54(59):8253–8256, 2018.

[99] H. H. Sønsteby, H. Fjellvåg, and O. Nilsen. Functional perovskites by atomic layer deposition-an overview. *Advanced Materials Interfaces*, 4(8):1600903, 2017.

[100] M. Leskelä, M. Ritala, and O. Nilsen. Novel materials by atomic layer deposition and molecular layer deposition. *MRS Bulletin*, 36(11):877–884, 2011.

[101] O. Nilsen, E. Rauwel, H. Fjellvåg, et al. Growth of $La_{1-x}Ca_xMnO_3$ thin films by atomic layer deposition. *J. Mater. Chem.*, 17(15):1466–1475, 2007.

[102] M. Vehkamäki, T. Hatanpää, M. Ritala, et al. Atomic layer deposition of $BaTiO_3$ thin films-effect of barium hydroxide formation. *Chemical Vapor Deposition*, 13(5):239–246, 2007.

[103] M. Cho, H. Bae Park, J. Park, et al. Thermal annealing effects on the structural and electrical properties of gate dielectric stacks grown by atomic layer deposition on si substrates. *Journal of Applied Physics*, 94:2563, 2003.

[104] J. Harjuoja, T. Hatanpää, M. Vehkamäki, et al. New Approach to the ALD of Bismuth Silicates; $Bi(CH_2SiMe_3)_3$ Acting as a Precursor for both Bismuth and Silicon. *Chemical Vapor Deposition*, 11(8-9):362–367, 2005.

[105] M. J. Saly, F. Munnik, R. J. Baird, et al. Atomic layer deposition growth of BaB_2O_4 thin films from an exceptionally thermally stable tris(pyrazolyl)borate-based precursor. *Chemistry of Materials*, 21 (16):3742–3744, 2009.

[106] H. Y. Hwang, Y. Iwasa, M. Kawasaki, et al. Emergent phenomena at oxide interfaces. *Nature Materials*, 11(2):103–113, 2012.

[107] K. Kalantar-zadeh, J. Z. Ou, T. Daeneke, et al. Two dimensional and layered transition metal oxides. *Applied Materials Today*, 5:73–89, 2016.

[108] P. G. Bruce, B. Scrosati, and J.-M. Tarascon. Nanomaterials for rechargeable lithium batteries. *Angewandte Chemie International Edition*, 47(16):2930–2946, 2008.

[109] S. Najib and E. Erdem. Current progress achieved in novel materials for supercapacitor electrodes: mini review. *Nanoscale Adv.*, 1:2817–2827, 2019.

[110] P. Poizot, S. Laruelle, S. Grugeon, et al. Nano-sized transition-metal oxides as negative-electrode materials for lithium-ion batteries. *Nature*, 407(6803):496–499, 2000.

[111] A. L. M. Reddy, M. M. Shaijumon, S. R. Gowda, et al. Coaxial MnO_2/carbon nanotube array electrodes for high-performance lithium batteries. *Nano Letters*, 9(3):1002–1006, 2009.

[112] T. M. Dinh, A. Achour, S. Vizireanu, et al. Hydrous RuO_2/carbon nanowalls hierarchical structures for all-solid-state ultrahigh-energy-density micro-supercapacitors. *Nano Energy*, 10:288 – 294, 2014.

[113] X. Wang, Y. Yin, C. Hao, et al. A high-performance three-dimensional micro supercapacitor based on ripple-like ruthenium oxide–carbon nanotube composite films. *Carbon*, 82:436 – 445, 2015.

[114] J. Li, M. Zhu, Z. An, et al. Constructing in-chip micro-supercapacitors of 3D graphene nanowall/ruthenium oxides electrode through silicon-based microfabrication technique. *Journal of Power Sources*, 401:204 – 212, 2018.

References

[115] Z. Wang and C.-J. Liu. Preparation and application of iron oxide/graphene based composites for electrochemical energy storage and energy conversion devices: Current status and perspective. *Nano Energy*, 11(Supplement C):277–293, 2015.

[116] C. Guan, J. Liu, Y. Wang, et al. Iron oxide-decorated carbon for supercapacitor anodes with ultrahigh energy density and outstanding cycling stability. *ACS Nano*, 9(5):5198–207, 2015.

[117] M. B. Sassin, A. N. Mansour, K. A. Pettigrew, et al. Electroless deposition of conformal nanoscale iron oxide on carbon nanoarchitectures for electrochemical charge storage. *ACS Nano*, 4(8):4505–4514, 2010.

[118] Q. Qu, S. Yang, and X. Feng. 2D sandwich-like sheets of iron oxide grown on graphene as high energy anode material for supercapacitors. *Adv Mater*, 23(46):5574–80, 2011.

[119] W. Shi, J. Zhu, D. H. Sim, et al. Achieving high specific charge capacitances in Fe_3O_4/reduced graphene oxide nanocomposites. *Journal of Materials Chemistry*, 21(10):3422–3427, 2011.

[120] X. Lu, Y. Zeng, M. Yu, et al. Oxygen-deficient hematite nanorods as high-performance and novel negative electrodes for flexible asymmetric supercapacitors. *Advanced Materials*, 26(19):3148–3155, 2014.

[121] Q. X. Low and G. W. Ho. Facile structural tuning and compositing of iron oxide-graphene anode towards enhanced supacapacitive performance. *Nano Energy*, 5:28–35, 2014.

[122] B. Joshi, E. Samuel, H. S. Jo, et al. Carbon nanofibers loaded with carbon nanotubes and iron oxide as flexible freestanding lithium-ion battery anodes. *Electrochimica Acta*, 253:479–488, 2017.

[123] X.-C. Dong, H. Xu, X.-W. Wang, et al. 3D graphene–cobalt oxide electrode for high-performance supercapacitor and enzymeless glucose detection. *ACS Nano*, 6(4):3206–3213, 2012.

[124] S. Yang, X. Feng, S. Ivanovici, et al. Fabrication of graphene-encapsulated oxide nanoparticles: Towards high-performance anode materials for lithium storage. *Angewandte Chemie International Edition*, 49(45):8408–8411, 2010.

[125] F. Söderlind, M. A. Fortin, R. M. Petoral Jr, et al. Colloidal synthesis and characterization of ultrasmall perovskite $GdFeO_3$ nanocrystals. *Nanotechnology*, 19(085608):1–8, 2008.

[126] M. H. Phan, M. B. Morales, C. N. Chinnasamy, et al. Magnetocaloric effect in bulk and nanostructured $Gd_3Fe_5O_{12}$ materials. *Journal of Physics D: Applied Physics*, 42(11):115007, 2009.

[127] D. S. Schmool, N. Keller, M. Guyot, et al. Evidence of very high coercive fields in orthoferrite phases of PLD grown thin films. *Journal of Magnetism and Magnetic Materials*, 195(2):291–298, 1999.

[128] M. Pardavi-Horvath. Microwave applications of soft ferrites. *Journal of Magnetism and Magnetic Materials*, 215-216:171–183, 2000.

[129] M. A. H. T. S. M. Ishibashi Takayuki, Lou Gengjian and N. Takao. Magneto-optical imaging plate using bismuth-substituted iron garnet film prepared by metal-organic decomposition. *Sensors and Materials*, 27(10):965–970, 2015.

[130] M. Sparks, R. Loudon, and C. Kittel. Ferromagnetic relaxation. I. Theory of the relaxation of the uniform precession and the degenerate spectrum in insulators at low temperatures. *Physical Review*, 122(3):791–803, may 1961.

[131] Y. Tokunaga, N. Furukawa, H. Sakai, et al. Composite domain walls in a multiferroic perovskite ferrite. *Nature Materials*, 8(7):558–62, 2009.

[132] D. T. T. Nguyet, N. P. Duong, T. Satoh, et al. Magnetization and coercivity of nanocrystalline gadolinium iron garnet. *Journal of Magnetism and Magnetic Materials*, 332:180–185, 2013.

[133] A. Wu, Z. Wang, B. Wang, et al. Crystal growth and magnetic properties of $GdFeO_3$ crystals by floating zone method. *Solid State Communications*, 185:14–17, 2014.

[134] L. Jiang, S. Yang, M. Zheng, et al. Synthesis and magnetic properties of nanocrystalline $Gd_3Fe_5O_{12}$ and $GdFeO_3$ powders prepared by sol-gel auto-combustion method. *Materials Research Bulletin*, 104:92–96, 2018.

[135] C. Suchomski, C. Reitz, C. T. Sousa, et al. Room temperature magnetic rare-earth iron garnet thin films with ordered mesoporous structure. *Chemistry of Materials*, 25(12):2527–2537, 2013.

[136] X.-H. Zhu, X.-B. Xiao, X.-R. Chen, et al. Electronic structure, magnetism and optical properties of orthorhombic $GdFeO_3$ from first principles. *RSC Adv.*, 7(7):4054–4061, 2017.

[137] A. Panchwanee, V. Raghavendra Reddy, A. Gupta, et al. Study of orthorhombic twins in epitaxial $GdFeO_3$ thin films. *Thin Solid Films*, 669:301–305, 2019.

[138] F. C. Kong, Y. F. Li, C. Shang, et al. Stability and Phase Transition of Cobalt Oxide Phases by Machine Learning Global Potential Energy Surface. *Journal of Physical Chemistry C*, 123(28): 17539–17547, 2019.

[139] X. Xie, Y. Li, Z. Q. Liu, et al. Low-temperature oxidation of CO catalysed by Co_3O_4 nanorods. *Nature*, 458(7239):746–749, 2009.

[140] X. Deng and H. Tüysüz. Cobalt-oxide-based materials as water oxidation catalyst: Recent progress and challenges. *ACS Catalysis*, 4(10):3701–3714, 2014.

[141] D. K. Nandi, J. Manna, A. Dhara, et al. Atomic layer deposited cobalt oxide: An efficient catalyst for $NaBH_4$ hydrolysis . *Journal of Vacuum Science & Technology A: Vacuum, Surfaces, and Films*, 34(1):01A115, 2016.

[142] J. Zhang, Z. Yu, Z. Gao, et al. Porous TiO_2 Nanotubes with Spatially Separated Platinum and CoO_x Cocatalysts Produced by Atomic Layer Deposition for Photocatalytic Hydrogen Production. *Angewandte Chemie International Edition*, 56(3):816–820, 2017.

[143] M. A. Carpenter, S. Mathur, and A. Kolmakov. *Metal oxide nanomaterials for chemical sensors*. Springer New York, 2013.

[144] Y. Ikedo, J. Sugiyama, H. Nozaki, et al. Spatial inhomogeneity of magnetic moments in the cobalt oxide spinel Co_3O_4. *Physical Review B - Condensed Matter and Materials Physics*, 75(5), 2007.

[145] L. Yang, S. Cheng, Y. Ding, et al. Hierarchical network architectures of carbon fiber paper supported cobalt oxide nanonet for high-capacity pseudocapacitors. *Nano Letters*, 12(1):321–325, 2012.

[146] L. Liao, Q. Zhang, Z. Su, et al. Efficient solar water-splitting using a nanocrystalline CoO photocatalyst. *Nature Nanotechnology*, 9(1):69–73, 2014.

[147] B. Kupfer, K. Majhi, D. A. Keller, et al. Thin film Co_3O_4/TiO_2 heterojunction solar cells. *Advanced Energy Materials*, 5(1):1401007, 2015.

References

[148] M. Rooth, E. Lindahl, and A. Hårsta. Atomic Layer Deposition of Co_3O_4 Thin Films Using a CoI_2/O_2 Precursor Combination. *Chemical Vapor Deposition*, 12(4):209–213, 2006.

[149] H. Seim, M. Nieminen, L. Niinistö, et al. Growth of $LaCoO_3$ thin films from β-diketonate precursors. *Applied Surface Science*, 112:243–250, 1997.

[150] K. B. Klepper, O. Nilsen, and H. Fjellvåg. Epitaxial growth of cobalt oxide by atomic layer deposition. *Journal of Crystal Growth*, 307(2):457–465, 2007.

[151] K. B. Klepper, O. Nilsen, and H. Fjellvåg. Growth of thin films of Co_3O_4 by atomic layer deposition. *Thin Solid Films*, 515(20-21):7772–7781, 2007.

[152] E. Ahvenniemi, M. Matvejeff, and M. Karppinen. Atomic layer deposition of quaternary oxide $(La,Sr)CoO_{3-\delta}$ thin films. *Dalton Transactions*, 44(17):8001–8006, 2015.

[153] B. Han, K. H. Choi, K. Park, et al. Low-temperature atomic layer deposition of cobalt oxide thin films using dicobalt hexacarbonyl tert-butylacetylene and ozone. *Electrochemical and Solid-State Letters*, 15(2):D14, 2012.

[154] B. Han, K. Ha Choi, J. Min Park, et al. Atomic layer deposition of cobalt oxide thin films using cyclopentadienylcobalt dicarbonyl and ozone at low temperatures. *Journal of Vacuum Science & Technology A: Vacuum, Surfaces, and Films*, 31(1):01A145, 2013.

[155] S. T. Barry. Amidinates, guanidinates and iminopyrrolidinates: Understanding precursor thermolysis to design a better ligand. *Coordination Chemistry Reviews*, 257(23-24):3192–3201, 2013.

[156] B. S. Lim, A. Rahtu, and R. G. Gordon. Atomic layer deposition of transition metals. *Nature Materials*, 2(11):749–754, 2003.

[157] T. Q. Ngo, A. Posadas, H. Seo, et al. Atomic layer deposition of photoactive $CoO/SrTiO_3$ and CoO/TiO_2 on Si(001) for visible light driven photoelectrochemical water oxidation. *Journal of Applied Physics*, 114(8):084901, 2013.

[158] J. Kim, T. Iivonen, J. Hämäläinen, et al. Low-Temperature Atomic Layer Deposition of Cobalt Oxide as an Effective Catalyst for Photoelectrochemical Water-Splitting Devices. *Chemistry of Materials*, 29(14):5796–5805, 2017.

[159] S. Jung, D. K. Nandi, S. Yeo, et al. Phase-controlled growth of cobalt oxide thin films by atomic layer deposition. *Surface and Coatings Technology*, 337:404–410, 2018.

[160] K. Väyrynen, T. Hatanpää, M. Mattinen, et al. Diamine adduct of cobalt(ii) chloride as a precursor for atomic layer deposition of stoichiometric cobalt(ii) oxide and reduction thereof to cobalt metal thin films. *Chemistry of Materials*, 30(10):3499–3507, 2018.

[161] T. Iivonen, M. Kaipio, T. Hatanpää, et al. Atomic layer deposition of cobalt(ii) oxide thin films from $Co(BTSA)_2(THF)$ and H_2O. *Journal of Vacuum Science & Technology A*, 37(1):010908, 2019.

[162] L. Machala, J. Tucek, and R. Zboril. Polymorphous Transformations of Nanometric Iron(III) Oxide: A Review. *Chemistry of Materials*, 23(14):3255–3272, 2011.

[163] M. Aronniemi, J. Saino, and J. Lahtinen. Characterization and gas-sensing behavior of an iron oxide thin film prepared by atomic layer deposition. *Thin Solid Films*, 516(18):6110–6115, 2008.

[164] J. A. Klug, N. G. Becker, N. R. Groll, et al. Heteroepitaxy of group IV-VI nitrides by atomic layer deposition. *Applied Physics Letters*, 103(21):1–5, 2013.

[165] J. Bachmann, Jing, M. Knez, et al. Ordered iron oxide nanotube arrays of controlled geometry and tunable magnetism by atomic layer deposition. *Journal of the American Chemical Society*, 129(31): 9554–9555, 2007.

[166] Y. Lin, S. Zhou, S. W. Sheehan, et al. Nanonet-based hematite heteronanostructures for efficient solar water splitting. *Journal of the American Chemical Society*, 133(8):2398–2401, 2011.

[167] S. C. Riha, M. J. Devries Vermeer, M. J. Pellin, et al. Hematite-based photo-oxidation of water using transparent distributed current collectors. *ACS Applied Materials and Interfaces*, 5(2):360–367, 2013.

[168] S. Porro, K. Bejtka, A. Jasmin, et al. A multi-level memristor based on atomic layer deposition of iron oxide. *Nanotechnology*, 29(49):495201, 2018.

[169] J. R. Schneider, J. G. Baker, and S. F. Bent. The influence of ozone: Superstoichiometric oxygen in atomic layer deposition of Fe_2O_3 using tert-Butylferrocene and O_3. *Advanced Materials Interfaces*, 7(11):2000318, 2020.

[170] R. K. Ramachandran, J. Dendooven, and C. Detavernier. Plasma enhanced atomic layer deposition of Fe_2O_3 thin films. *Journal of Materials Chemistry A*, 2(27):10662–10667, 2014.

[171] S. C. Riha, J. M. Racowski, M. P. Lanci, et al. Phase discrimination through oxidant selection in low-temperature atomic layer deposition of crystalline iron oxides. *Langmuir*, 29(10):3439–3445, 2013.

[172] O. Nilsen, M. Lie, S. Foss, et al. Effect of magnetic field on the growth of α-Fe_2O_3 thin films by atomic layer deposition. *Applied Surface Science*, 227(1-4):40–47, 2004.

[173] M. Lie, H. Fjellvåg, and A. Kjekshus. Growth of Fe_2O_3 thin films by atomic layer deposition. *Thin Solid Films*, 488(1-2):74–81, 2005.

[174] M. de Ridder, P. C. van de Ven, R. G. van Welzenis, et al. Growth of iron oxide on yttria-stabilized zirconia by atomic layer deposition. *The Journal of Physical Chemistry B*, 106(51):13146–13153, 2002.

[175] J. R. Avila, D. W. Kim, M. Rimoldi, et al. Fabrication of thin films of α-Fe_2O_3 via atomic layer deposition using iron bisamidinate and water under mild growth conditions. *ACS Appl. Mater. Interfaces*, (7):1613816142, 2015.

[176] D. Peeters, A. Sadlo, K. Lowjaga, et al. Nanostructured Fe_2O_3 processing via water-assisted ald and low-temperature CVD from a versatile iron ketoiminate precursor. *Advanced Materials Interfaces*, 4 (18):1700155, 2017.

[177] A. Tanskanen and M. Karppinen. Iron-based inorganic-organic hybrid and superlattice thin films by ALD/MLD. *Dalton Transactions*, 44(44):19194–19199, 2015.

[178] J. E. Bratvold, H. H. Sønsteby, O. Nilsen, et al. Control of growth orientation in as-deposited epitaxial iron-rich nickel ferrite spinel. *Journal of Vacuum Science & Technology A*, 37(2):021502, 2019.

References

[179] X. Lv, J. Deng, B. Wang, et al. γ-Fe_2O_3@CNTs Anode Materials for Lithium Ion Batteries Investigated by Electron Energy Loss Spectroscopy. *Chemistry of Materials*, 29(8):3499–3506, 2017.

[180] A. Tanskanen, O. Mustonen, and M. Karppinen. Simple ALD process for ε-Fe_2O_3 thin films. *APL Materials*, 5(5), 2017.

[181] B. M. Klahr, A. B. Martinson, and T. W. Hamann. Photoelectrochemical investigation of ultrathin film iron oxide solar cells prepared by atomic layer deposition. *Langmuir*, 27(1):461–8, 2011.

[182] V. Bedekar, O. D. Jayakumar, J. Manjanna, et al. Synthesis and magnetic studies of nano-crystalline $GdFeO_3$. *Materials Letters*, 62(23):3793–3795, 2008.

[183] S. Geller and M. A. Gilleo. Structure and ferrimagnetism of yttrium and rare-earth-iron garnets. *Acta Crystallographica*, 10(3):239, 1957.

[184] H. Maier-Flaig, M. Harder, S. Klingler, et al. Tunable magnon-photon coupling in a compensating ferrimagnet-from weak to strong coupling. *Applied Physics Letters*, 110(13):132401, 2017.

[185] M. Bibes, J. E. Villegas, and A. Barthélémy. Ultrathin oxide films and interfaces for electronics and spintronics. *Advances in Physics*, 60(1):5–84, 2011.

[186] M. Lie, O. Nilsen, H. Fjellvåg, et al. Growth of $La_{1-x}Sr_xFeO_3$ thin films by atomic layer deposition. *Dalton Transactions*, (3):481–489, 2009.

[187] S. Vangelista, A. Lamperti, C. Wiemer, et al. Atomic layer deposition of hexagonal $ErFeO_3$ thin films on SiO_2/Si. *Thin Solid Films*, 604:18–22, 2016.

[188] K. Kukli, T. Hatanpää, M. Ritala, et al. Atomic layer deposition of gadolinium oxide films. *Chemical Vapor Deposition*, 13(10):546–552, 2007.

[189] R. Potter, P. Chalker, T. Manning, et al. Deposition of HfO_2, Fe_2O_3 and PrO_x by liquid injection ald techniques. *Chemical Vapor Deposition*, 11(3):159–169, 2005.

[190] J. Niinistö, N. Petrova, M. Putkonen, et al. Gadolinium oxide thin films by atomic layer deposition. *Journal of Crystal Growth*, 285(1):191 – 200, 2005.

[191] S. A. Vitale, P. W. Wyatt, and C. J. Hodson. Plasma-enhanced atomic layer deposition and etching of high-k gadolinium oxide. *J. Vac. Sci. Technol. A*, 30:1–130, 2012.

[192] J. H. Han, L. Nyns, A. Delabie, et al. Reaction chemistry during the atomic layer deposition of Sc_2O_3 and Gd_2O_3 from $Sc(MeCp)_3$, $Gd^iPrCp)_3$, and H_2O. *Chemistry of Materials*, 26(3):1404–1412, 2014.

[193] J. H. Han, A. Delabie, A. Franquet, et al. Ozone-Based Atomic Layer Deposition of Gd_2O_3 from Tris(isopropyl-cyclopentadienyl)gadolinium: Growth Characteristics and Surface Chemistry. *Chemical Vapor Deposition*, 21(10-12):352–359, 2015.

[194] J. Päiväsaari, M. Putkonen, and L. Niinistö. A comparative study on lanthanide oxide thin films grown by atomic layer deposition. *Thin Solid Films*, 472(1):275 – 281, 2005.

[195] A. C. Jones, H. C. Aspinall, P. R. Chalker, et al. Recent developments in the MOCVD and ALD of rare earth oxides and silicates. *Materials Science and Engineering: B*, 118(1-3):97–104, 2005.

[196] A. P. Milanov, K. Xu, A. Laha, et al. Growth of crystalline Fe_2O_3 thin films with a high-quality interface on Si(100) by low-temperature H_2O-assisted atomic layer deposition. *Journal of the American Chemical Society*, 132(1):36–37, 2010.

Chapter 2

EXPERIMENTAL

This chapter includes the description of the thin films preparation and characterization techniques that have been employed in this thesis. Unless stated otherwise, all the tools introduced herein are provided by ICMAB scientific services and Superconducting Materials and Large Scale Nanostructures department (SUMAN).

2.1 Thin films synthesis

2.1.1 ALD equipment

The functional oxide thin films were deposited using a Savannah 100 ALD system (Cambridge NanoTech Inc.) in combination with an LG-7 ozone generator (Corona Discharge), shown in Figure 2.1. The main body of the reactor consists of a reaction chamber located on top of a stainless steel cabinet. The chamber is of the size enough for a 4 inch circular sample and is built with an outer tubular heater and an inner disk heater. Inside the cabinet sit the key components of the reactor, including an electronic control unit, stainless steel cylinders, a high temperature cylinder manifold, a nitrogen manifold, a pressure gauge, an exit valve, an ALD shield vapor trap, and pumping lines. The electronic control unit is attached to the left wall of the cabinet and connected to a computer with control program which will be described in detail later. The electronic control unit hubs various connector ports for the pressure gauge, mass flow controller (MFC), USB cable, power inlet, cylinder heater jackets and resistor temperature detectors. The precursor cylinders are connected to the reaction chamber through a 6 port precursor manifold through Swagelok ALD valves that have pneumatic actuators for high-speed actuation response (ms). Between the back of the ALD valves and the MFC is attached the nitrogen manifold through which the nitrogen carrier flows from the perfluoroalkoxy tubing (PFA) to the cylinders. The nitrogen flow could be adjusted by the MFC between 0 - 100 sccm. Connected to the pumping

line is a vacuum pump for purging the system.

The reactor is equipped with an electric controlling system containing a computer installed with a Savannah software eligible for programming and executing process recipes through the electronic control unit. The computer and the control unit are connected by a USB cable. Through the software panel, one can input set-points and get a reading value for the heating temperatures of for each component. The operating temperature ranges for the system are as follows: the chamber $\leq$ 300 °C, the precursor heater jackets $\leq$ 230 °C, the manifold $\leq$ 200 °C, the high temperature ALD valves, $\leq$ 200 °C and pumping line $\leq$ 200 °C. The carrier gas (N_2) flow range (0-100 sccm) could also be regulated by the software and realized through the mass flow controller. The software also enables real-time monitoring of the pressure changes in the chamber obtained by the pressure sensor. The precursor delivery can be achieved in several valving modes, which will be explained in more detail below.

In the following, we introduce general conditions for the ALD processes, whereas more details for each material were defined specifically in each article regarding the deposition temperature, precursor sublimation temperature, pulse and purge lengths, gas flow and valving modes.

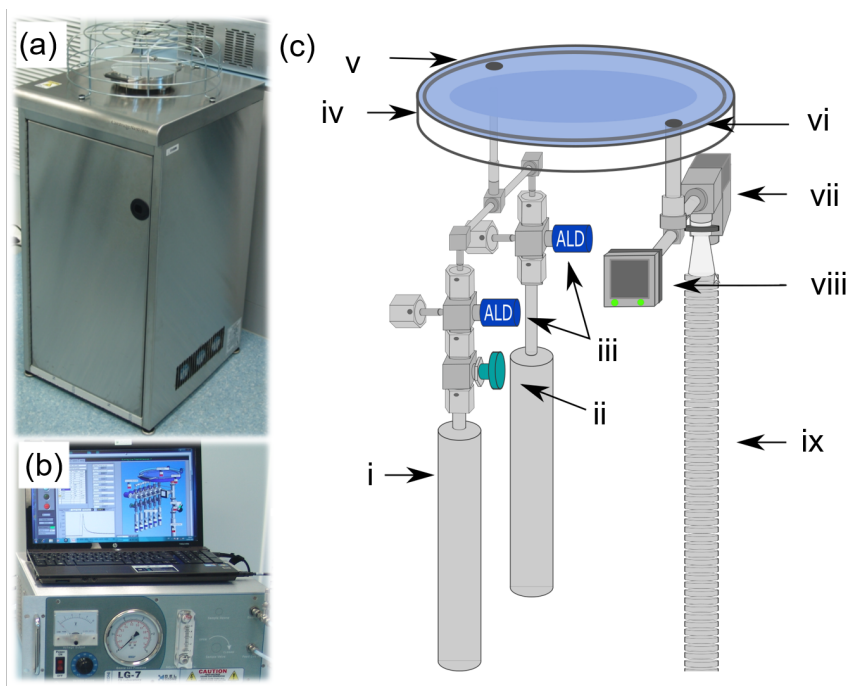**Fig. 2.1** The ALD system used in this thesis: (a) the ALD reactor Savannah 100 from Cambridge NanoTech Inc. (b) the electronic controlling system and an ozone generator (LG-7 Corona Discharge). Panel (c) displays the main components in Savannah 100: i) stainless steel cylinders, ii) manual valves, iii) ALD valves, iv) ALD chamber, v) gas inlet, vi) gas outlet, vii) exit valve, viii) pressure gauge and ix) pumping lines.

Metal precursors   In this thesis, five metalorganic precursors have been investigated, namely Co(DMOCHCOCF$_3$)$_2$ (DMOCHCOHCF$_3$ = 1-(dimethyl-1,3-oxazol-2-yl)-3,3,3-trifluorprop-1-en-2-ol), Fe(Cp)$_2$ (Cp = cyclopentadiene), Fe(^{i}pki)$_2$ (^{i}pki = N-isopropyl ketoiminate), Gd(DMDPG)$_3$ (DMDPG = N,N'-diisopropyl-2-dimethylamido-guanidinato), and GdFe(O^{t}Bu)$_6$(C$_5$H$_5$N)$_2$ (O^{t}Bu = tert-butoxide, C$_5$H$_5$N = pyridine). Amongst these precursors, the Fe precursor ferrocene or (Fe(Cp)$_2$, 98% purity) was purchased from Sigma-Aldrich and used as received. The other metal precursors were tailor-made which have been synthesized and characterized by our collaborators at University of Cologne and Ruhr University Bochum, Germany. The precursors Fe(^{i}pki)$_2$, Gd(DPDMG)$_3$ and GdFe(O^{t}Bu)$_6$(C$_5$H$_5$N)$_2$ were stored and handled in a glove box.

Co-reactants   We investigated ozone (O$_3$) and milliQ water (H$_2$O) as co-reactants with the various metal precursors. O$_3$ was produced from an LG-7 Corona Discharge ozone generator and delivered upon use with a 5 wt.% concentration and an output of 5 g/hr, Figure 2.1a. H$_2$O was filled in a precursor cylinder.

Substrates   We employed a 4 inch Si wafer serving as a sample holder on which were attached the small substrates ranged 0.25 - 4 cm^2 in area. In this thesis, two main types of substrates have been investigated.
(1) Planar substrates: P-type Boron-doped Si (100), SiO$_2$/Si(100) were used for deposition optimization and routinary characterizations in terms of film thickness and composition. These substrates were purchased from Active Business Company GmbH in the form of 4 inch wafers and were cut into small pieces with an average 5 mm × 5 mm size for ALD oxide deposition. SrTiO$_3$ (100) substrates, purchased from CrysTec GmbH, were used when epitaxial growth was pursued. The substrates were cleaned with acetone and ethanol followed by nitrogen gas blow drying before ALD deposition. Prior to film growth, these substrates were kept in a constant high purity nitrogen flow for 10 min and subsequently exposed to ozone pulses to form a hydroxyl-terminated surface.
(2) 3D - substrates: In the case of conformal nanocoatings, high aspect ratio structures - TiO$_2$/C nanofibers and carbon nanotubes (CNTs) were adopted. TiO$_2$/C nanofibers were synthesized at University of Cologne. CNTs were synthesized in the group of Prof. E. Bertran at the University of Barcelona. The CNTs were subsequently treated with H$_2$O and N$_2$ plasma for activating the inert carbon surface with oxygen and nitrogen containing functional groups, to study the ALD oxide nucleation processes. These substrates were used as received without further treatments.

Valving systems   During an ALD process, the manual valves (see Figure 2.1c-ii) always remain open. Depending on the precursors, three different valving systems were used regarding different

configurations of the corresponding ALD valve and the exit valve, namely flow mode (F), pressure-boost (PB) and exposure mode (E), see Figure 2.1c. Under F mode, the inert carrier gas flows constantly and helps to carry the pulsed precursor from the cylinder through the manifold across the chamber to react and then evacuated. The precursor dosing/purging are realized by controlling solely the opening/closing of the ALD valve. PB mode is used in case the precursor has low-vapor pressure. Under this occasion, before precursor pulses the gas exit valve is closed and ALD valve is opened, allowing carrier gas filling up the precursor cylinder and elevating the pressure inside. Subsequently, the exit valve is opened and the chamber pressure lowers. Then the precursor is pulsed with the filled nitrogen. E mode is applied when necessitating long time exposure of the surface to the gaseous precursor for assuring sufficient surface reactions and homogeneity over large and high-aspect ratio substrates. It was realized by closing the gas exit valve for a certain period of time between precursor dosing and purging.

2.1.2   Thermal treatments

Due to the relatively low deposition temperature in ALD, the deposited films are usually amorphous or poorly crystalline. Thus, for these samples, high temperature annealing processes are often needed to enhance crystallinity.

In this thesis, post-deposition thermal treatments were performed using a tubular furnace which is exemplified in Figure 2.2. First, a quartz tube was placed in the furnace subject to a fast heating procedure to the setpoint temperature (450-900 °C) at 660 °C/min heating ramp. Then the sample was introduced rapidly into the pre-heated tube (flash heating) and dwells at the annealing temperature for optimized period of time (10-60 min). At this stage, the atmospheres were either static air or controlled oxygen flow (0.1-0.5 L/min) , specified for each specific material. Quenching was realized by removing the tube from the furnace and cool under annealing atmosphere down to room temperature.
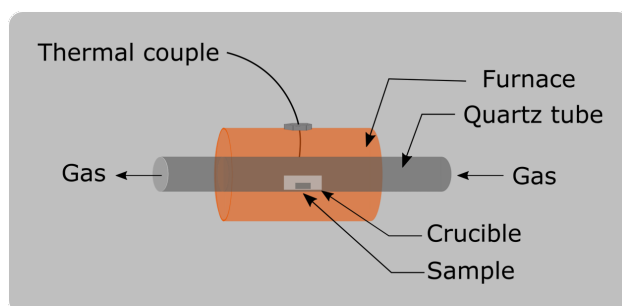

Fig. 2.2 Illustration of the experimental set-up for ALD oxide thin films' post-annealing processes employing a tubular furnace.

2.2   Thin films characterization

In this thesis, various characterization techniques have been employed for studying the phase purity, structure, thickness, composition, morphology, magnetic properties and electrochemical properties of the samples. Specifically, for X-ray diffraction (XRD), X-ray reflectivity (XRR), X-ray photoelectron spectroscopy (XPS), atomic force microscopy (AFM), and superconducting quantum interference device (SQUID) magnetometry, the measurements were carried out by the corresponding technicians, and the data analyses were done by the author. For scanning electron microscopy (SEM), energy-dispersive X-ray spectroscopy (EDX) and spectroscopic ellipsometry (SE), the author was involved in both the data acquisition and analyses. The transmission electron microscopy (TEM), Rutherford backscattering spectroscopy (RBS) and electrochemical measurements were realized in collaboration with experts in the field.

2.2.1   X-ray diffraction (XRD)

XRD is a non-destructive technique to determine the structural composition of the samples. In a conventional XRD laboratory, the X-rays can be generated by electrons bombarding metal anodes such as Cu. The selected monochromatic X-ray wavelengths generally share similar magnitude (~ 1 Å) with the interplanar distances in the crystal lattices, thus are very suitable for probing the atomic structure of materials.[1]

When X-rays travel through the sample, they are scattered by the electron clouds of the atoms.[1,2] Diffraction occurs when two scattered X-rays have integer wavelength difference (constructive interference), defined by Bragg's law in

$$n\lambda = 2d \sin \theta \tag{2.1}$$

where n is an integer, λ is the wavelength of the incident light, d is the interplanar distance in the crystal lattice, and θ is half of the angle between incident and scattered X-rays, as displayed in Figure 2.3a. In this way, the incident angle θ is related inversely to the spacings of atomic planes d.[1]
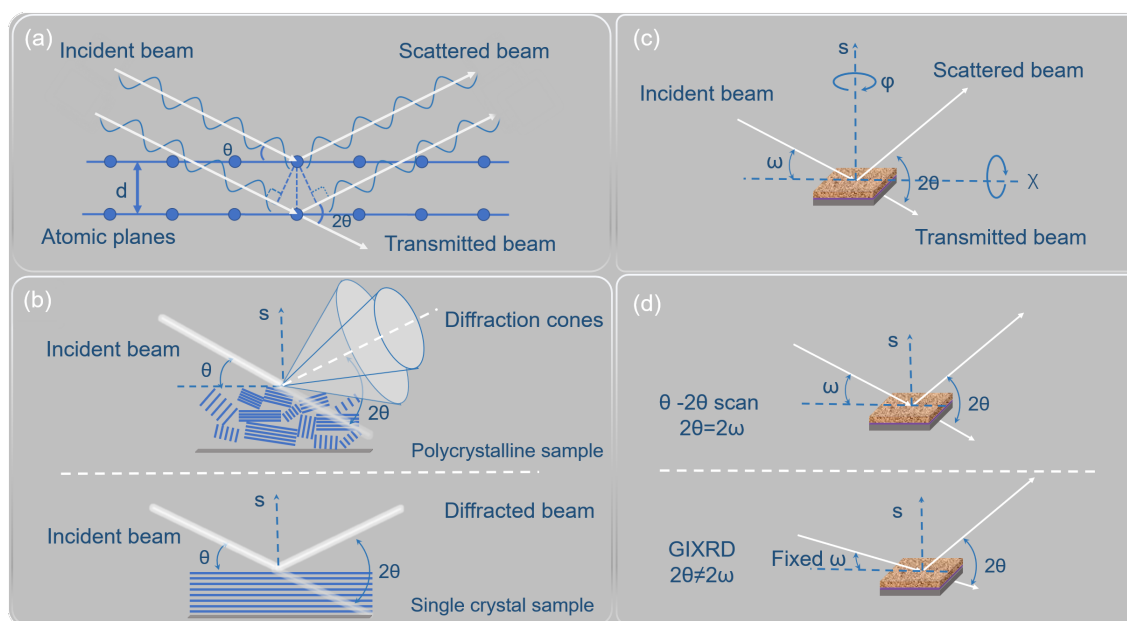
Fig. 2.3 (a) Schematic diagrams illustrating how the X-ray diffraction occurs when Bragg's Law is satisfied for constructive interference between the scattered light beams from the atomic planes. (b) Comparison of the different diffraction phenomena for polyscrystalline and single crystal samples. (c) Different scan modes could be achieved using different diffraction geometries by varying the angles ω, ϕ, χ and 2θ. S stands for the sample normal. (d) Illustration of the diffraction geometries for θ-2θ scan and GIXRD.

An X-ray diffraction pattern, or a diffractogram, is typically plotted as the intensity of diffracted X-rays versus varied detector angles 2theta (2θ). Each specific set of crystal planes, identified with Miller indices (*hkl*), attributes to one diffraction reflection; as a result, the XRD pattern is formed as an addition of diffraction peaks reflecting the phases present in the material of interest. Thus, one can obtain information of the atomic arrangements within the crystal from the Bragg reflections for phase identification, crystallinity evaluation, etc. From the peak position and height, crystal structure could be solved for phase determination, quantitative phase analysis and calculation of lattice parameters. Besides, peak areas, widths and shapes of the Bragg reflections give additional structural information of the investigated materials in terms of crystallite size and strain, etc.[2]

For example, depending on the crystallinity, a materiel could be i) single crystal with long-range ordered atoms throughout the volume of the material, ii) polycrystalline with randomly distributed crystallites with all-orientations, or iii) fully amorphous with short-range ordered atoms. As is depicted in Figure 2.3b, different diffraction phenomena would happen depending on the crystallinity of the studied sample, thus they can be distinguished in XRD. More specifically, for a polycrystalline sample containing crystallites with all orientations, diffraction cones are formed; for a single crystal sample with only one crystallographic orientation, the Bragg condition is met once at a time resulting in isolated diffraction beams; for amorphous samples, only broad humps

with low intensities would be observed due to the short range order.

Different scan types, *e.g.* θ-2θ scan, grazing incidence X-ray diffraction (GIXRD), ϕ scan, rocking curve, etc, can be realized with different XRD geometries by varying the four angles in a 4-circle diffractometer displayed in Figure 2.3c. Specifically, ω is the angle that the incoming X-rays strikes sample surface, 2θ corresponds to the angle between the incident and diffracted X-ray beams, ϕ indicates rotation of the sample around the surface normal S, while χ refers to the angle that the sample plane is rotated with respect to the incident X-ray beams. In the following, we introduce the main principles of θ-2θ scan and GIXRD which were used in this study.

θ-2θ scan is a very common scan type in XRD, which is oftentimes referred to as Bragg-Brentano parafocusing geometry. During the measurements, ω equals θ, so that the incident angle and the detector are rotated in a synchronized motion, see Figure 2.3d, upper panel.[1] This can be achieved by either rotating the X-ray source tube or or by rotating the sample. Under this configuration, only atomic planes that are parallel to the sample surface could be detected. If the film is textured, *i.e.* c-axis oriented, only (00l) planes will be observed in the diffraction spectra. 2D θ-2θ patterns can be acquired using a two-dimensional (2D) areal detector. It allows much faster data collection within the diffraction cone comparing to the conventional θ-2θ measurements that are confined in a diffraction plane. As can be imagined, polycrystalline samples would generate a GADDS frame with diffraction rings, or arcs, depending on the crystallinity and film texture, while single crystal samples would result in diffraction patterns with isolated spots.

GIXRD is a very useful surface-sensitive XRD technique for studying ultrathin films. The reason is that in XRD measurements that use large incidence angles, the penetration depth of X-rays are in the order of micrometers, thereby the diffractogram could be dominated with substrate contributions that hinder the weak signals of the thin films. The use of grazing incident X-rays in GIXRD could maximize the diffraction contributions from film surfaces and lowers intensities from the bulk background.[2,3] In this technique, ω is fixated to small angles ($< 2°$) and the spectrum is collected by moving the detector along the 2theta circle ($\omega \neq \theta$), as is shown in Figure 2.3d, lower panel. For non-textured polycrystalline film, the diffraction pattern will reproduce the intensities as in the reference powder spectrum. However, this configuration is not suitable to identify film epitaxy.

In this study, for investigating phase purity and crystallinity of the ALD thin films, various XRD studies were performed including θ-2θ scan, GIXRD and 2D θ-2θ pattern. The diffractometers employed in this study include a Siemens D5000 diffractometer for standard θ-2θ scan, a Bruker GADDS diffractometer with two-dimensional (2D) areal AXS HI-STAR detector for texture analysis and a Bruker D8 Discover A25 diffractometer for high resolution θ-2θ scan and GIXRD

study, shown in Figure 2.4, respectively. In all cases, the X-ray was generated with Cu K$_\alpha$ radiation source (K$_\alpha$=1.5406 Å).
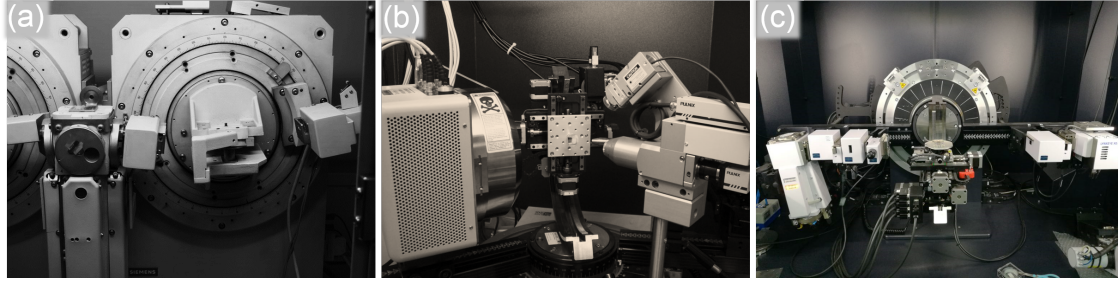

Fig. 2.4 The three diffractometers located at ICMAB that are employed in this thesis: (a) Siemens D5000 diffractometer, (b) Bruker GADDS diffractometer and (c) Bruker D8 Discover A25 diffractometer.[4]

Herein, θ-2θ scans were performed in the 2θ range of 20º - 80º. The GADDS patterns were acquired using standard θ-2θ scan in the 20º-50º, 50º-80º range. The GIXRD measurements were performed using the incident angle of 1º in 20º-80º 2θ range.

2.2.2 X-ray reflectivity (XRR)

XRR is a non-destructive and non-contact analytical technique to determine thickness, roughness and density of layered thin film materials both in the crystalline and amorphous form. It allows for thickness determination in the 2-200 nm range with very high precision (1-3 Å).[1,5]

In XRR measurements, the diffractometer works the same way as in XRD but at much lower angles, which is normally below 1° and usually greater than the critical angle (θ_c) of the studied material. In this occasion, both specular reflection and the penetration into the sample for the incident X-ray beams happen. The X-rays are reflected at the surface of the sample and at the interfaces between different layers due to the discontinuity in the reflective indexes of each material.[1,5] The interference between the reflected lights from different interfaces generates oscillations which are called Kiessig fringes. The period of the fringes vary inversely with the sample thickness by Equation 2.2:

$$d = 2\pi\Delta q_z \tag{2.2}$$

where q_z=$4\pi\sin\theta/\lambda$ (λ is the wavelength of the radiated X-ray). In grazing angles, when calculating in radius $\sin\theta$ could be approximated to θ, thus the thin film thickness can be calculated by the Kiessig fringes interval from

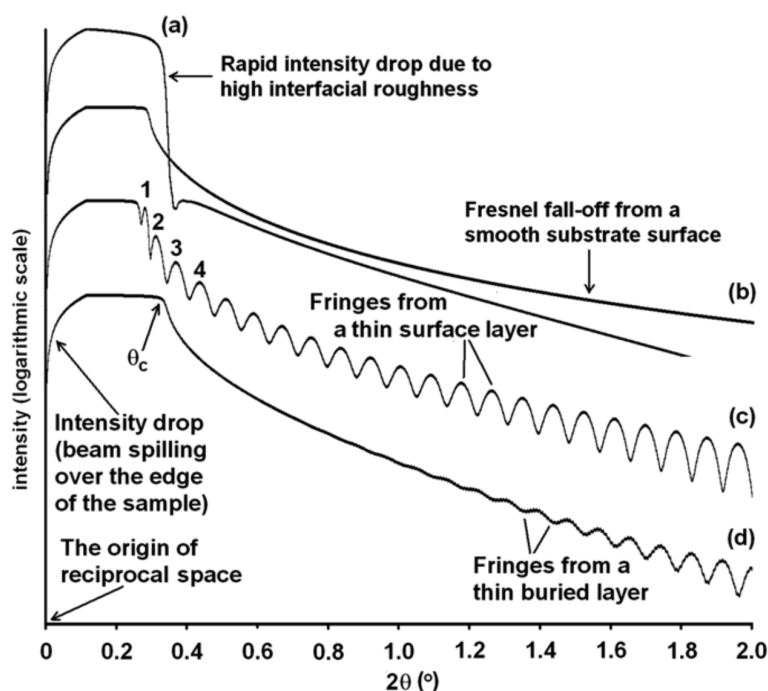$$d = \lambda/2\Delta\theta \tag{2.3}$$

Fig. 2.5 XRR simulations of (a) a rough thin GaN film on an AlN buffer layer, (b) a bare sapphire substrate, (c) a 50 nm AlN layer on sapphire substrate and (d) a 50 nm AlN layer on sapphire substrate with a 500nm thick GaN film ontop (Reproduced from Ref 1).

This technique is highly surface-sensitive, and requires surface and interface roughness below 5 nm. The influence of sample roughness on the shape of XRR curves could be reflected in Figure 2.5, where interfacial roughness causes rapid intensity drop of the interference curve (Line *a*). However, on an smooth substrate surface, the intensity of Fresnel reflectivity falls off gradually with 2θ increasement, see Line *b*. With a smooth thin film on top, the sample gives nice Kiessig fringes characteristic to film thickness (Line *c*). In addition, a buried thin layer shows fringes at higher angle depicted in Line *d*. Through fitting of XRR spectra, the information of film density (related to θ_c) and roughness (related to the fringes amplitude) can be simultaneously obtained.[1] Herein, the XRR measurements were carried out in the 0.5-7° 2θ range with a 0.002° step size using a SIEMENS D5000 diffractometer. The resultant spectra were fitted using ReMagX software[6] using a structural model comprising vacuum/oxide thin film layer/substrate.

2.2.3 Scanning electron microscopy (SEM) and Energy-dispersive X-ray spectroscopy (EDX)

Scanning electron microscopy (SEM) is a type of microscope that uses electrons for imaging objects. The electrons are generated from a hot filament or a cold cathode material.[7] Analogous to optical microscope imaging where a specimen could be studied by collecting the scattered light

(electromagnetic waves) through a few optical focusing lens, imaging an object by an electron microscope is realized by collecting electrons through magnetic lens, see Figure 2.6a.

The resolving limit of light is diffraction-limited, because severe diffraction happens at the sample edges leading to blurred images. And the resolution limit, not considering aberrations and distortions in the system, can be calculated by

$$Resolution = 0.61\lambda/NA \tag{2.4}$$

where λ is the light wavelength, NA is the numerical aperture.[7]

Using optical microscopes, the resolution limit is 200 - 250 nm which varies upon the incident light wavelength. In contrast, using SEM, the theoretical resolution limit is better than 1 nm. The reason is that the diffraction phenomena decreases with the lessening wavelength and the wavelength of electron beams could be adjusted to be very small in order to get clear sharp images. In more detail, the electron wavelength could be obtained applying the de Broglie equation

$$\lambda = h/mv \tag{2.5}$$

where h is the Planck constant, m is electron mass and v is the electron velocity. While the velocity v can be found out using

$$eV = 1/2mv^2 \tag{2.6}$$

where V is the applied voltage. Thus, the electron wavelength could be varied by adjusting the accelerating voltage field V.[7]
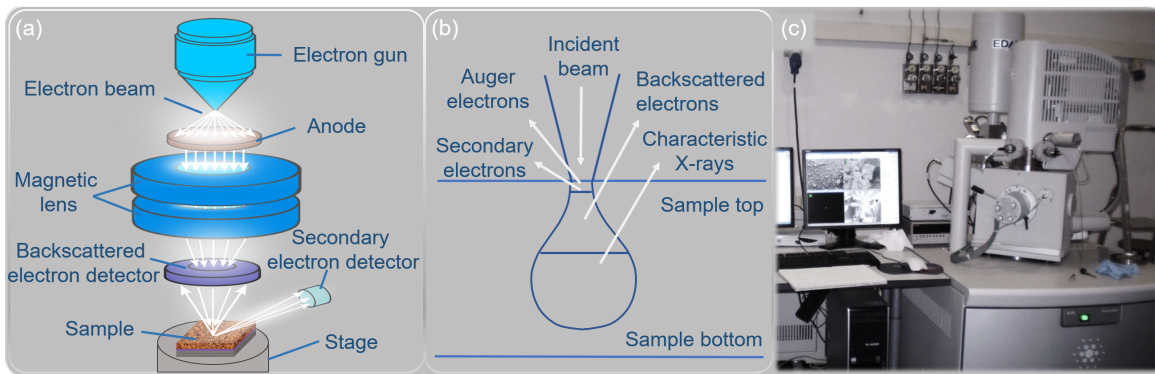

Fig. 2.6 Illustrations of (a) the key components in a scanning electron microscope (Reproduced from Ref 8) and (b) different kinds of interactions between the incident electrons and the sample (Reproduced from Ref 7). (c) Picture of the QUANTA FEI 200 FEG scanning electron microscope at ICMAB that is used in this thesis.

The incident electron beam interacts with the studied sample, causing backscattered electrons, secondary electrons, Auger electrons and characteristic X-rays, as illustrated in Figure 2.6b. In SEM, the secondary electrons and backscattered electrons are simultaneously collected. The secondary electrons are produced by the inelastic interaction between the electron beam and the sample surface or near-surface regions, thereby are very useful for obtaining morphological information of the sample. Meanwhile, the backscattered electrons originate from elastic scattering between the electron beam and the sample and come from deeper interaction region of the sample. The energy of backscattered electrons varies upon the differences in the atomic number in the sample. Thus backscattered electrons imaging could provide compositional information of the sample: the smaller the atomic number, the darker the element appears.

For SEM imaging, the samples must be conductive to avoid charging effect. Insulating or poorly conductive samples can be analyzed with a thin coating layer of metals such as Au. The samples are typically attached to the holder via conductive double-sided carbon tape.[7]

In this study, a QUANTA FEI 200 FEG-ESEM scanning electron microscope at ICMAB was employed for analyzing ALD oxide thin film morphology, see Figure 2.6c. The microscope was operated in high vaccum mode with a working voltage of 15 kV and 3.0 spot size. A field emission JEOL JSM-7001F SEM equipment (JEOL Ltd., Tokyo, Japan) at the University of Barcelona was also employed for analyzing the Fe_2O_3 coated carbon nanotubes. This SEM was operated at 20 kV.

Energy-dispersive X-ray spectroscopy (EDX)   The interactions between electrons with the atoms result in the emission of characteristic X-rays, as anticipated in Figure 2.6b. By analyzing the intensities and energies of these X-rays, one can obtain qualitative or semi-quantitative compositional information about the investigated sample.

The EDX detector in this study was introduced by EDAX Inc and integrated with the SEM system shown in Figure 2.6c. The working conditions were 15 kV voltage under high vacuum for EDX analysis. Each spectrum was collected with > 100 s acquisition time and were analyzed using Genesis software.

2.2.4   Rutherford Backscattering Spectrometry (RBS)

The RBS studies for this thesis were performed by our collaborators with support from the RU-BION (Central Unit for Ion Beams and Radionuclides) at the Ruhr University Bochum, Germany. We will therefore give a brief introductory description for this technique below.

RBS is a powerful analytical technique in materials science for determining the compositional properties and thicknesses of solid materials. In RBS measurements, a high energy incident

ion beam of protons or alpha particles produced by a particle accelerator, impinges onto and recoils out of the sample surface containing heavier atoms, Figure 2.7. The backscattered ions have various energies which are proportional to the energy of the incident beam, and the mass ratio between the surface atoms and the incident ions. Thus, the sample composition could be determined. The probability of scattering at certain angles, or Rutherford scattering cross section, are already known for each element, the absolute number of specific atoms and their abundance could be obtained by counting the yields of scattered particles with no need of standard or reference samples.[9,10]
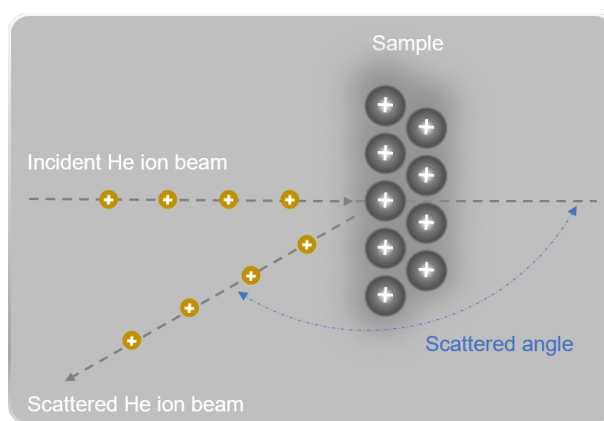

Fig. 2.7 Schematic illustrations of RBS measurements.

Particularly, RBS is suitable to detect heavier atoms and has low sensitivity to the lighter ones. It is also difficult to separate elements with similar atomic number (hence similar masses). Meanwhile, nuclear reaction analysis (NRA) measurements, employing a deuteron ion beam, could induce nuclear reactions between the deuterons and the surface atoms in the sample, producing protons or alpha particles with element specific energies.[11] Consequently, lighter atoms could be detected by NRA, *e.g.* Li, C, N and O, complementing the drawback of RBS.

In this thesis, the RBS studies were combined with NRA studies for obtaining information on the elemental composition and depth profile of the $Gd_xFe_yO_z$ thin films.

In our study, a $^4He^+$ beam was used with energy of 2.0 MeV, intensity of 20 nA – 40 nA and sample tilt angle of 7° in RBS. The Si detector was placed at an angle of 160° for collecting the backscattered particles with a resolution of 16 KeV. For NRA measurements, a $^2H^+$ beam with 1 MeV energy and sample tilt angle of 7° was used. The detector was at an angle of 135° with respect to the beam axis for detecting the emitted protons. To remove elastically scattered deuterons ($^2H^+$), the detector covered a solid angle of 23 msrad and was shielded by a 6 μm nickel foil. During the measurements, the beam was $\sim$ 1mm in diameter with a current of $\sim$ 40 nA. The

collected beam charge for a sample was 12 μC. A SIMNRA program suite was employed for analyzing the RBS and NRA data.[12]

2.2.5 X-ray photoelectron spectroscopy (XPS)

X-ray photoelectron spectroscopy is an accurate analytical method for analyzing the chemical state and quantitative composition of the elements in solid samples. The penetration depth of the incident X-ray is 1-10 μm in the sample, providing valuable information in the surface regions. The X-rays required for this technique are soft X-rays in the 300-1000 eV range, which are suitable for probing core levels of the elements with no dispersion. Conventionally, Mg and Al anodes have been used as emission sources with K_α photon energies of 1256 and 1486 eV, respectively.[7,13] Recent development using synchrotron radiation as an energy source with high brilliance and tunable energy enables shorter data collection times, ambient pressure operations and most of all, overcoming the technical limits of hydrogen and helium detection using anode-based sources.[14] XPS is based on the photoelectric effect. Photon injection into the solid material causes photoemission of the core electrons, leaving the atom in the ionized state, as displayed in Figure 2.8a. The measured kinetic energy of the emitted photons KE is given by

$$KE = h\nu - BE - \phi \tag{2.7}$$

where $h\nu$ is the photon energy of the incident light, BE is the binding energy of the emitted electron to the originated atomic orbital and ϕ is the work function. Thus, with $h\nu$ and ϕ known for the spectrometer and the sample, the BE of the ejected electron could be determined. Specifically, BE corresponds to the energy of the orbital from which the electron is ejected, which is element specific and chemical state dependent, allowing for not only elemental determination but also evaluation of the chemical state of the element by XPS. The chemical state is associated with different oxidation states and chemical environments of the atoms, which would induce chemical shifts in the photoelectron peaks that can be resolved by comparing to standard spectra.[7,13] Relative quantification between two elements in the investigated sample could be calculated using a relative peak area sensitivity factor S, described by

$$\frac{n_1}{n_2} = \frac{I_1/S_1}{I_2/S_2} \tag{2.8}$$

where n is the number of atoms of a specific element per volume (cm^3), I is the number of photoelectrons per second in a specific spectra peak.[13]
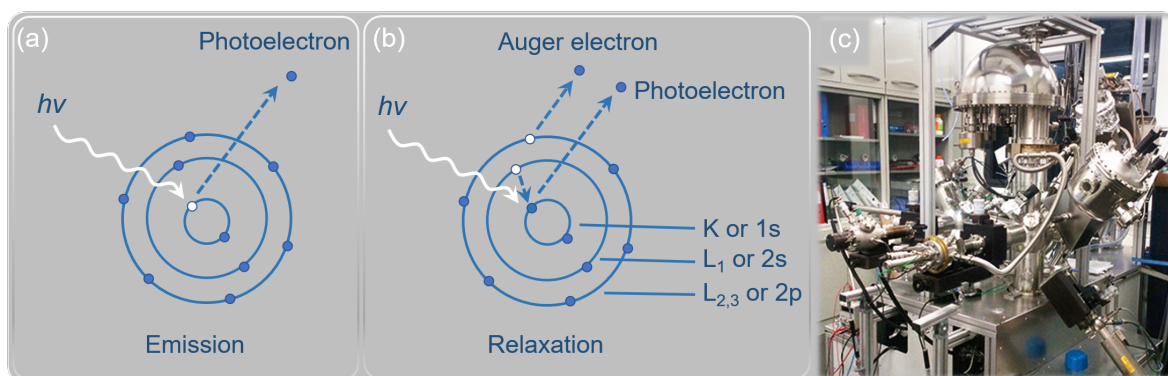
Fig. 2.8 Schematic diagrams showing the principles of XPS for a model atom: (a) during the photoemission process, the injected photon causes the photoelectron ejection from the K level. (b) The relaxation process of the ionized atom results in one outer level electron from L_1 level filling the core hole in K level and the emission of an $L_{2,3}$ Auger electron (Reproduced from Ref 7). (c) Picture of the SPECS PHOIBOS 150 X-ray photoelectron spectrometer used in this study that is provided by Photoemission Spectroscopy (XPS&UPS) Facility in ICN2.

Additional information could be obtained from the Auger electrons that contribute to XPS spectra. Promptly after photoemission event, the relaxation of the excited ions may cause outer shell electrons falling into the inner orbitals, and another outer shell electron (Auger electron) being emitted for the compensation of energy, as is demonstrated in Figure 2.8b. These Auger electrons are element specific and independent on the XPS equipment used, thus are very useful for elemental analysis.[7]

As a surface sensitive technique, XPS samples are particularly susceptible to contamination from the atmosphere or from sample handling. Thus, the sample preparation process is very important. The samples should be completely dry and do not contain volatile substances in order not to damage the vacuum chamber. Powders are commonly prepared by being pressed into a pallet, drop-casted onto a substrate or attached to a conductive carbon tape. The sample surface are ideally uniform and clean to ensure a high signal to noise ratio. Conductive samples are preferred to avoid charging effects, otherwise, the use of sputtered metals or coils in the measurements or post-measurement charge calibrations for data analysis will be necessitated. The sizes of the samples for XPS are usually of $\sim$ 0.5 -1 cm^2 large and < 0.5 mm thick.

In this thesis, surface chemical composition has been evaluated using two different equipment. Initially, survey spectra of the whole sample was obtained for an overall look of all the elements present in the sample. Then high resolution core spectra of specific elements were collected to further study the oxidation state and chemical environment of the element in the sample. Most of the samples were oxide thin films which were analyzed by a SPECS PHOIBOS 150 hemispherical X-ray photoelectron spectrometer from SPECS GmbH, Berlin, Germany, Figure 2.8c located at the Institut Català de Nanociència i Nanotecnologia (ICN2). The measurements were carried out

using Al K_α radiation source with a pass energy of 10 eV at a base pressure of 1×10^{-10} mbar by Photoemission Spectroscopy (XPS&UPS) Facility. Prior to XPS analysis, the samples were exposed to ambient atmosphere before loaded into the chamber. For survey and high-resolution spectra, the step sizes are 1 eV and 0.05 eV, respectively. The spot size shed on the sample is 0.5mm $\times$ 3.5mm. For data interpretation, CasaXPS software was adopted for binding energy determination and element assignment. Spectra calibration were done with reference to adventitious C *1s* reference peak at 284.8 eV.Shirley background were employed in the data fitting process for subtracting the background signals due to inelastic scattering of electrons when travelling through solids.

XPS studies on Fe_2O_3 coated CNTs were carried out in a PHI 5500 Multitechnique System from Physical Electronics, Germany located at the University of Barcelona. The spectrometer is also equipped with a monochromatic Aluminum K_α X-ray source (1486.6 eV of energy and 350 W of power). The system is calibrated using the $3d_{5/2}$ line of Ag with a full width at half maximum (FWHM) of 0.8 eV. The analyzed area was a circle of 0.8 mm diameter. For survey spectra, the selected resolution for the spectra was 187.5 eV of pass energy and 0.8 eV/step size. While for core level spectra, the pass energy is 11.75 eV and the step size is 0.05 eV. All measurements were made in an ultra high vacuum (UHV) chamber pressure between 5×10^{-9} and 2×10^{-8} Torr. In this case, the acquired spectra were fitted using Origin software.

2.2.6   Atomic force microscopy (AFM)

Atomic Force Microscopy is commonly used for probing sample surface morphology and roughness. It is realised with a sharp tip located at the free end of a cantilever interacting with the surface atoms via van der Waals force, as depicted by Figure 2.9a. By rastering the tip across the surface, the small deflections of the cantilever is recorded by the position sensitive photodiode, resolved by the computer and eventually mapped into a topological image.[7,15]
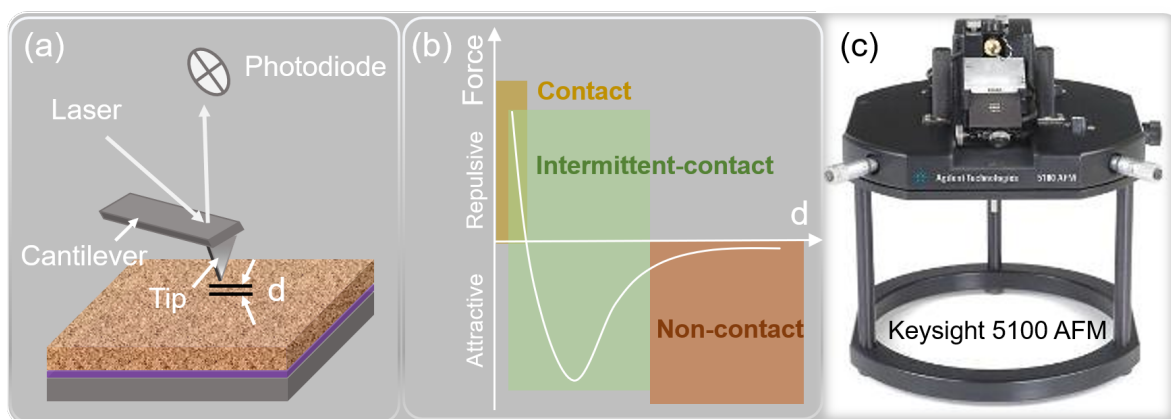
Fig. 2.9 Schematic diagrams of the (a) typical components in an AFM and (b) evolution of the tip-surface force upon tip-surface distance (Reproduced from Ref 15). (c) Picture of the Keysight 5100 Atomic Force Microscope used in this study from the ICMAB scientific services.

Depending on the distances between the tip and the surface, the imaging techniques can be classified into contact mode, non-contact mode and intermittent-contact mode (often referred to as tapping mode). In contact mode, the tip is in close contact with the sample surface, so the tip-surface force is in the repulsive regime, as is illustrated in Figure 2.9b. It is the simplest and commonly used mode in AFM, suitable for measuring "hard" samples. In non-contact mode, the distance between tip and surface is quite far, so there is only weak attractive force between the tip and the sample. As a result, using this non-destructive mode, many "soft" samples such as biomaterials or organic materials could be imaged without surface damages or tip contamination. In tapping mode, the distance of the tip and sample surface is intermediate between contact mode and non-contact mode, and the tip is oscillating just above the surface at a given frequency and large vibrations of amplitudes. Consequently, using tapping mode one can reduce both surface and tip damaging, and gain high resolution topographic imaging. It is the most commonly used mode in ambient conditions or in liquids, advantageous in obtaining effective large area imaging of complex surfaces.[15]

In this thesis, AFM studies were carried out employing a Keysight 5100 microscope as is displayed in Figure 2.9c. The measurements were done using tapping mode. For each studied sample, several 5 μm $\times$ 5 μm areas were analyzed. Topography, phase and amplitude images were acquired simultaneously. We focus on topographic image for sample morphology and surface roughness analysis. The acquired images were processed with Mountains®8 software. The studied area was extracted and leveled, then line profiles and RMS (root mean squared) roughness were extracted therefrom.

2.2.7 Transmission electron microscopy (TEM)

TEM is another powerful type of electron microscope that exploits the wave particle duality of electrons for imaging objects, same as SEM. The imaging process of TEM consists of the electron beam ejected from the electron gun, focused by the condenser lens onto the investigated sample, passing through the sample and imaged by the objective, intermediate and projector lenses onto a fluorescent screen, see Figure 2.10. Digital cameras are implemented for recording the image.[16]
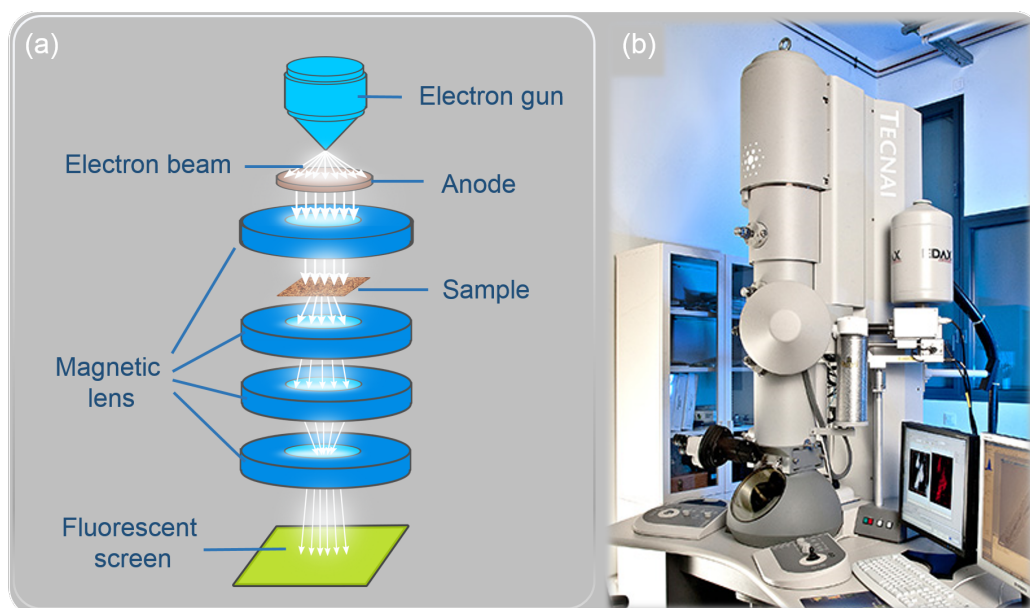

Fig. 2.10 (a) Illustration of the key components of a typical TEM equipment (Reproduced from Ref 17). (b) Picture of the FEI Tecnai G^2 F20 Transmission electron microscope at ICN2 that is used in this study.

Both SEM and TEM require vacuum conditions in order for the electrons to reach the sample, and both use electromagnetic lenses to control the electron beam. However, they differ in that TEMs work at much higher acceleration voltages (typically at 100-300 KV) than SEMs (at 0.5-30 KV). In TEMs the imaging is realized by the transmitted electrons, providing information on the inner microstructure of the investigated sample. In comparison, SEMs mainly give information on the surface regions. As a result, the theoretical spatial resolution is in the picometer level with a TEM, comparing to the nanometer level using an SEM.[16,18]

In TEM mode, the electron beam is focused in a parallel way on the full sample surface area which is primarily used for TEM imaging and by selected area diffraction (SAD) for structural information of the sample. With an additional set of aberration correcting lenses, high resolution TEM (HRTEM) images can be obtained. One can also work in Scanning TEM (STEM) mode, where the electron beam is focused on one point of the sample and is scanned across the sample surface point by point. In this way, the signals from interactions between electrons and the sample are spatially correlated, such as scattered beam electrons, characteristic X-rays, and electron

energy loss. Using different detectors, the scattered beam electrons could be collected for bright field imaging, annular dark-field imaging and high angular annular dark-field imaging, termed BF, ADF, and HAADF respectively. Specially, in HAADF mode the transmitted electrons are scattered at a relatively large angle, which could provide appealing directly interpretable Z-contrast imaging for composition determination. The characteristic X-rays generated during the electron-atom interactions enable X-ray microanalysis such as EDX line profile or mapping providing elemental information for the sample. Electron energy losses as the electrons inelastically travel through the sample could be determined by energy loss spectroscopy (EELS), which could be very versatile for studying the composition, chemical state and environment, and local electronic properties, etc. As mentioned before, the TEM samples have to be very thin so that the electrons can transmit through. This electron-transparency are typically achieved for a thin film sample through a series of cutting, gluing, mechanical thinning and ion milling processes.[16,18] In our study, the Co_3O_4 coated TiO_2/C fibers and Fe_2O_3 coated carbon nanotubes were scratched off the substrates and subsequently dispersed in pure ethanol in ultrasonic bath for 1 hour. Finally, a few drops of the solution were let dry on a copper TEM grid.

Two TEMs were used in this thesis, a FEI Tecnai G^2 F20 S-TWIN HR(S)TEM provided by the Electron Microscopy Unit in ICN2, and a Hitachi H-800 MT TEM from Hitachi Ltd., Tokyo, Japan, located at University of Barcelona. Both are equipped with field emission guns and were operated at 200 kV. HRTEM and STEM images were obtained by technicians for the Co_3O_4 coated TiO_2/C fibers and Fe_2O_3 coated carbon nanotubes, along with EDX elemental profiling and mapping.

2.2.8   Spectroscopic ellipsometry (SE)

Ellipsometry is a non-destructive and non-contact optical approach which allows for obtaining material thickness information along with the optical indices at the meantime. The measurements have almost no restrictions for the size or shape of the samples and can be realized within several minutes, which is much advantageous compared to alternative characterization techniques such as transmission electron microscopy that usually requires hours or even days of sample preparation and characterization. The easy implementation of ellipsometers also makes SE a convenient tool for in-situ studies. In this study, we adopted spectroscopic ellipsometry (SE) measurements to determine the thickness of ALD oxide thin films.

The experimental set-up of an ellipsometer includes a light source, a polarizer, the sample to be analyzed, a polarization analyzer and a detector, shown in Figure 2.11a. The principle for SE is as follows. The sample is shined with an elliptically polarized light beam with characteristic amplitude Ψ and phase Δ which reflects off the surface in an altered state, dependent on the surface

structure of the sample. Those polarization changes are recorded as a function of light wavelength or photon energy. The measurement of relative polarization changes instead of absolute values of the light beams enables high sensitivity of SE, providing versatile information on the material such as film thickness, optical indices, roughness, etc. The film thickness that can be probed by ellipsometry ranges from sub-nanometers to a few microns.

Analysis of SE data involves the following steps. After data acquisition, a structural model would
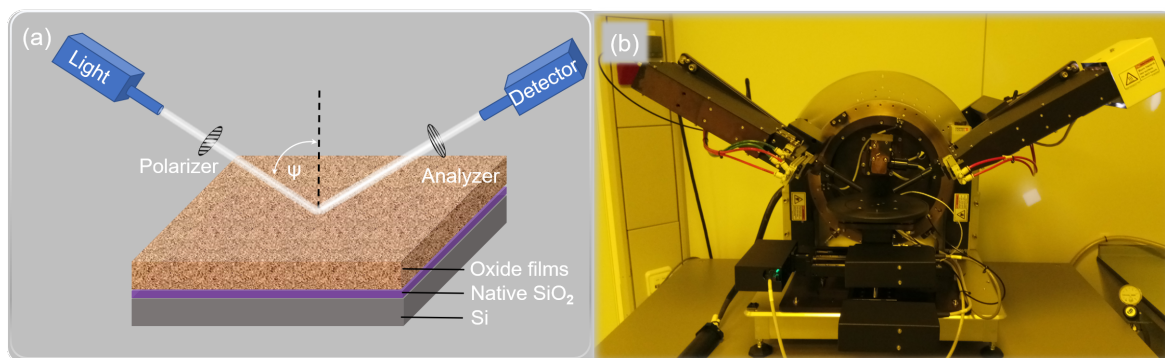
Fig. 2.11 (a) Demonstration of the experimental set-up for spectroscopic ellipsometry (SE) measurements. The structural model of the investigated sample consists of Si substrate, 3 nm native SiO_2 layer, corresponding oxide film layer and on top the ambient material (void). (b) Picture of the SOPRA GES5E Ellipsometer at ICMAB and used in this study.

be built for describing the studied sample, taking into consideration the thickness and optical constants of each layered material. In the following, the predicted curve from the model would be fitted and compared to the experimental curve. The best fitting result is normally achieved with regression.

The equipment used in this study is an GES5E Ellipsometer from SOPRA Optical Platform located at the cleanroom at ICMAB, see Figure 2.11b. The measurements were carried out in reflection mode with variant light incident angle (60 ° - 75 °) and analyzer angle (20 ° - 45 °). The light beam, in the spectral range of 200 - 900 nm, was focused on the sample using the microspot mode. For data interpretation, a multi-layered structural model was built and fitted by WinElli software comprising the Si substrate, a 3 nm native SiO_2 layer, an ALD oxide film layer and on top the ambient material (in this case, void), as exemplified in Figure 2.11. In this structure, Si, SiO_2 and void are defined by loading corresponding optical index (n, k) data files from WinElli database, while the oxide film layer is described with a dispersion law which is a mathematical model for n, k simulations. In the fitting process of the ellipsometric data, sample thickness, peak positions, intensity and peak width were set as variables and regressed with alpha/beta function or Tan(Ψ)/Cos(Δ) function. The number of iterations was set as 50, and the regression procedure were run repeatedly when necessary until the Sigma value below E^{-4} and $R > 0.999$ were obtained.

2.2.9 Superconducting quantum interference device (SQUID) magnetometry

SQUID magnetometers are commonly used for probing magnetic properties of materials. Based on a superconducting quantum interference detector, SQUID magnetometers are suitable for sensing small magnetic signals in thin films with high sensitivity.[19]

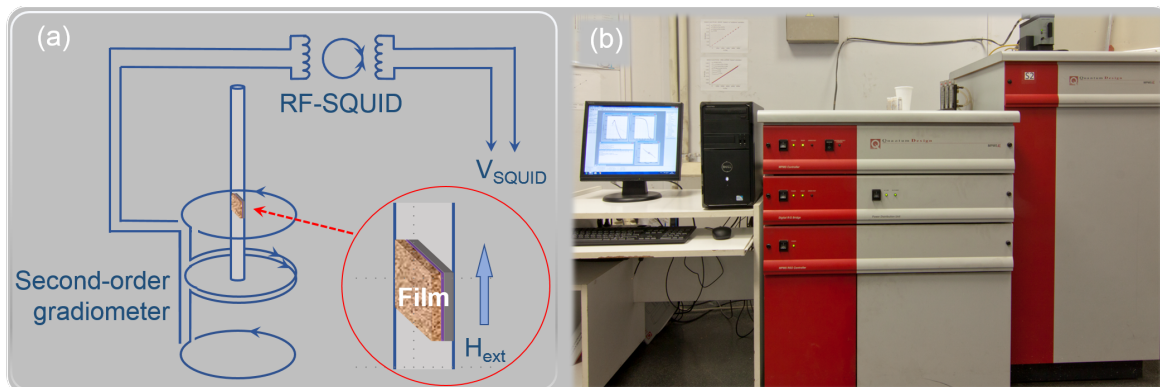The principles of a SQUID based magnetometer is presented in Figure 2.12a.

Fig. 2.12 (a) Scheme of the setup of a SQUID magnetometer with second order gradiometer. The sample is placed inside a drinking straw which moves vertically in the gradiometer inducing magnetic flux changes that will be detected by the RF-SQUID detector. Inset shows the zoom-in scheme of the sample inside the straw with in-plane magnetic field configuration (Adapted from Ref 19). (b) Picture of the MPMS-XL SQUID magnetometer at ICMAB that is employed in the thesis introduced from Quantum Design.

With a specially designed second order gradiometer, the current flows in the pick-up coil in certain direction in order to minimize external magnetic field interference. The sample is placed inside a drinking straw sample holder which moves vertically in the gradiometer. The movements of the sample induce magnetic flux changes that will be detected by the RF-SQUID detector and be converted to voltage changes V_{SQUID} as a function of sample position. In this way, the material's magnetization response could be determined by the electronics of the magnetometer.[19]

In this study, the magnetic properties of ALD oxide thin films were probed by a SQUID based MPMS-XL magnetometer from Quantum Design provided by Low Temperatures and Magnetometry Service in ICMAB, see Figure 2.12b. The external magnetic field was applied in the in-plane direction of the films. Magnetization-temperature curve (M(T)) curves were recorded at 5 KOe in the temperature range of 10-300 K. The magnetic hysteresis loops (M(H)) were investigated at 50 K varying the magnetic field between $\pm$70 KOe.

The amount of material in mass, expressed by $m = S \times t \times d$, where m equals the weight, S is the surface area, t is the film thickness and d equals the film density, was calculated in the following method. The sample area S was obtained using ImageJ software by analyzing an optical image

of the sample.[20] The thickness t and density d of the sample were obtained using XRR or SE as described in the previous sections.

2.2.10   Electrochemical measurements

The electrochemical measurements for this thesis were carried out by our collaborators at the University of Barcelona. Herein, we will introduce the principles and protocols of the measurements briefly.

Electrochemistry deals with the interactions between electricity and chemical reactions. Electrochemical cells are commonly adopted for energy storage systems nowadays, which can be categorized into two main classes: batteries, with high energy density and yet low power density (low recharging speed), and capacitors, with high power density and low energy density. Based on the differences in energy storage mechanisms in these two classes (described below), electrochemical measurements could help distinguish different electrode materials types and their underlining energy storage mechanisms.[21]

Energy can be stored in the form of electric double-layer capacitance by electrostatic effect through adsorption of electrolyte ions onto the electrode surfaces without occurrence of redox reactions (reduction-oxidation). This type of energy storage mechanisms only happens near the electrode/electrolyte interface which enables EDLCs to be recharged rapidly and highly reversibly, as exhibited in Figure 2.13a panel *i-ii* for the various carbonaceous materials. Another form of energy storage is pseudocapacitance realized through redox reactions between the electrolyte and the electrode materials, which is diffusion limited and time consuming. The examples include oxides and ions intercalation, as shown in Figure 2.13a panel *iii* and *iv*. Recent developments of next-generation energy storage devices often involve mixture of different electrode materials for achieving desirable high performances in both energy and power density.
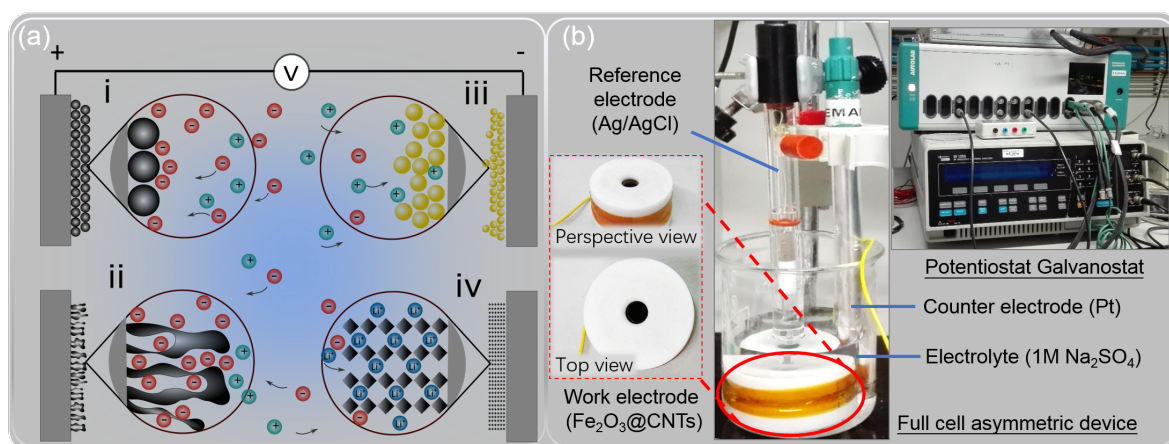
Fig. 2.13 (a) Illustration of different mechanisms of capacitive energy storage. Double-layer capacitance stored in electrodes of (i) carbon particles or (ii) porous carbon; Pseudocapacitance stored in electrodes of (iii) redox materials *e.g.* metal oxides, and (iv) intercalation pseudocapacitance, *e.g.* Li$^+$ ions inserted into the host material (Adapted from Ref 21). (b) The experimental set-up for the electrochemical measurements: the Fe$_2$O$_3$@CNTs half electrode (left panel) is placed in a 1M Na$_2$SO$_4$ electrolyte together with reference Ag/AgCl electrode, counter Pt electrode forming a three-electrode cell (middle panel). The electrochemical behavior was analyzed by a Potentiostat/Galvanostat in the University of Barcelona (right panel).

Cyclic voltammetry (CV) is a versatile electroanalytical technique in electrochemistry for determining stability of electroactive materials, charge transfer kinetics, reversibility of redox reactions, etc. The cyclic voltammograms are plotted as current response of the studied working electrode to the sweeping potential of the studied working electrode, which is ramped linearly up and down in cyclical phases over time. The shape of the CV curves provide both kinetic and mechanistic information. For instance, CV studies can help distinguish different mechanisms for EDLCs and pseudocapacitors by the existence or absence of redox peaks. For EDLCs, cyclic voltammograms possess a rectangular shape; by contrast, cyclic voltammograms for pseudocapacitors show at least one pair of redox peaks. The amplitude of current upon the repeated applied potentials indicates how stable the electrode materials are. The symmetry of cyclic voltammograms reveals the reversibility of the electrochemical reactions in a cell.[22]

Electrochemical impedance spectroscopy (EIS) is a highly sensitive technique for evaluating the conductivity of an electrochemical system to alternating currents (AC) over a range of frequencies. EIS is very useful for studying a wide range of materials for applications in batteries, fuel cells, corrosion and coatings, etc. In EIS measurements, the AC voltage amplitude is usually set to be very low so that the characterization could be realised in a nondestructive way. The result is usually represented graphically as Nyquist diagrams plotting imaginary impedance as a function of real impedance at different frequencies. Equivalent circuit models could be built for fitting the EIS data taking into consideration several components in the system: resistance

between the electrolyte and electrodes, double layer capacitance, the relative diffusion effects (Warburg coefficient), polarization resistance from the anodic and cathodic reactions, etc.[23]

For Article II, electrochemical measurements were performed in order to evaluate the performance of Fe_2O_3@CNTs nanocomposites as electrode materials for supercapacitor application. A three-electrode asymmetric cell was built using the Fe_2O_3@CNTs nanocomposites as working electrode, Pt as counter electrode and Ag/AgCl (3 M KCl internal solution) as reference electrode. The electrolyte was 1M Na_2SO_4 aqueous solution. The electrochemical measurements were done employing an AutoLab PGSTAT30 potentiostat/galvanostat introduced by Eco Chemie B.V., see Figure 2.13b. Cyclic voltammetry (CV) spectra was recorded within -0.7 to 0.3 V vs. Ag/AgCl voltage window at 10 to 150 mV·s^{-1} scan rates. The EIS measurements were performed by applying an ± 10 mV AC voltage and recording the current response at frequencies between 1 - 100 kHz frequency range.

References

[1] M. A. Moram and M. E. Vickers. X-ray diffraction of III-nitrides. *Reports on Progress in Physics*, 72 (3):036502, 2009.

[2] M. Lee. *X-Ray Diffraction for Materials Research*. Apple Academic Press, 2017.

[3] O. Sakata and M. Nakamura. Grazing Incidence X-Ray Diffraction. In *Springer Series in Surface Sciences*, volume 51, pages 165–190. 2013.

[4] ICMAB - Scientific & Tech. Services. https://icmab.es/research/scientific-and-technical-services.

[5] G. Bracco and B. Holst. *Surface science techniques*. Springer.

[6] S. Macke, S. Brück, and E. Goering. ReMagX X-ray magnetic reflectivity tool. *Max Planck–UBC centre for quantum materials. URL www.remagx.org*, 2009.

[7] S. K. Kulkarni. *Nanotechnology: Principles and Practices*. Springer International Publishing, 2015.

[8] Scanning electron microscope. https://www.britannica.com/technology/scanning-electron-microscope.

[9] S. Kostinski and N. Yao. Rutherford backscattering oscillation in scanning helium-ion microscopy. *Journal of Applied Physics*, 109(6):064311, 2011.

[10] L. Palmetshofer. Rutherford Backscattering Spectroscopy (RBS). In *Surface and Thin Film Analysis: A Compendium of Principles, Instrumentation, and Applications, Second Edition*, pages 191–202. Wiley-VCH, 2011.

[11] O. Benka. Nuclear Reaction Analysis (NRA). In *Surface and Thin Film Analysis: A Compendium of Principles, Instrumentation, and Applications, Second Edition*, pages 229–236. Wiley-VCH Verlag GmbH & Co. KGaA, Weinheim, Germany, 2011.

[12] M. Mayer. Improved physics in SIMNRA 7. *Nuclear Instruments and Methods in Physics Research Section B: Beam Interactions with Materials and Atoms*, 332:176–180, 2014.

[13] J. F. Moulder, W. F. Stickle, P. E. Sobol, et al. *Handbook of X-ray photoelectron spectroscopy: a reference book of standard spectra for identification and interpretation of XPS data*. Physical Electronics, Minnesota, 1992.

[14] J.-Q. Zhong, M. Wang, W. H. Hoffmann, et al. Synchrotron-based ambient pressure X-ray photoelectron spectroscopy of hydrogen and helium. *Applied Physics Letters*, 112(9):091602, 2018.

[15] R. Howland and L. Benatar. *A Practical Guide To Scanning Probe Microscopy*. 1996.

[16] D. B. Williams and C. B. Carter. *Transmission electron microscopy: A textbook for materials science*. Springer US, 2009.

[17] Transmission electron microscope. https://www.britannica.com/technology/transmission-electron-microscope.

[18] C. B. Carter and D. B. Williams. *Transmission electron microscopy: Diffraction, imaging, and spectrometry*. Springer International Publishing, 2016.

References

[19] M. Buchner, K. Höfler, B. Henne, et al. Tutorial: Basic principles, limits of detection, and pitfalls of highly sensitive SQUID magnetometry for nanomagnetism and spintronics. *Journal of Applied Physics*, 124(16):161101, 2018.

[20] C. A. Schneider, W. S. Rasband, and K. W. Eliceiri. NIH Image to ImageJ: 25 years of image analysis. *Nature Methods*, 9(7):671–675, 2012.

[21] P. Simon, Y. Gogotsi, B. Dunn, et al. Where do batteries end and Supercapacitors Begin? *Science*, 343(March):1210, 2014.

[22] N. Elgrishi, K. J. Rountree, B. D. McCarthy, et al. A Practical Beginner's Guide to Cyclic Voltammetry. *Journal of Chemical Education*, 95(2):197–206, 2018.

[23] A. Lasia. Electrochemical Impedance Spectroscopy and its Applications. In *Modern Aspects of Electrochemistry*, pages 143–248. Kluwer Academic Publishers, 2005.

Chapter 3

COMPILATION OF ARTICLES

I   A cobalt(II) heteroarylalkenolate precursor for homogeneous Co$_3$O$_4$ coatings by atomic layer deposition

PAPER

Check for updates
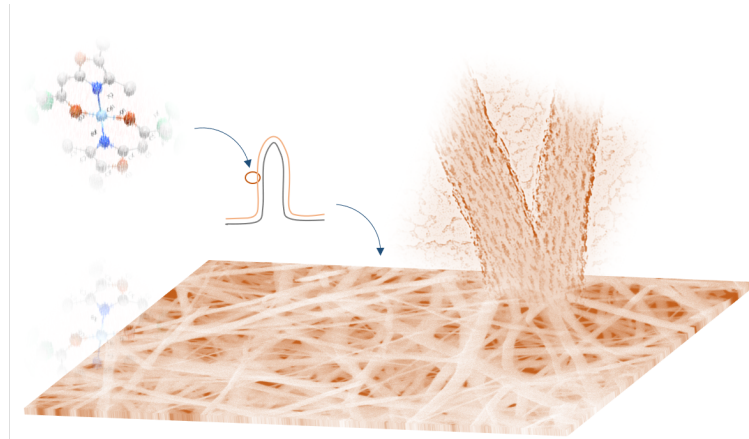
A cobalt(II)heteroarylalkenolate precursor for homogeneous Co₃O₄ coatings by atomic layer deposition†

Mehtap Büyükyazi,[a] Thomas Fischer,[a] Penmgei Yu, [ID] [b] Mariona Coll [ID] *[b] and Sanjay Mathur*[a]

We present a new and efficient cobalt precursor, Co^{II}(DMOCHCOCF$_3$)$_2$, to prepare Co$_3$O$_4$ thin films and conformal coatings. In the synthesis of this Co complex, heteroaryl moieties and CF$_3$-groups were combined leading to the precursor with high thermal stability and volatility. The suitability of this precursor for ALD deposition was tested on flat silicon substrates and TiO$_2$/C nanofibers upon process optimization. Deposition at 200 °C results in homogeneous and smooth Co$_3$O$_4$ thin films with a growth rate of 0.02 nm per cycle. Conformal coatings have been successfully obtained on TiO$_2$/C nanofibers, making them an attractive platform for surface chemistry studies on high aspect ratio structures for future photocatalysts, sensors, supercapacitors and batteries.

Introduction

Cobalt oxide thin films are attracting huge interest for a wide variety of applications including energy storage,[1] conversion,[2,3] catalysis,[4–7] magnetism[8] and also sensor applications.[9] When the surface and interface related effects start to become dominant over the bulk counterpart it is important to use adequate fabrication tools to have precise control at the nanometer scale. Atomic layer deposition (ALD), afforded by the self-limiting reaction mechanism, represents one of the most promising techniques to prepare nanostructures and coatings on high aspect ratio structures with strict control of film thickness and composition.[10] The chemical precursor plays a key role in the deposition parameters and final film properties. Stability, volatility, reactivity, safe handling, low cost and no self-decomposition are some of the general requirements for a suitable ALD precursor where substrate limitations can make this choice even more challenging. Although the number of ALD precursors available increased significantly in the last ten years,

there are still many ALD processes frustrated by the lack of suitable precursors. Therefore, it is important to design new and improved precursor molecules that can broaden the material and process variety in this emerging ALD field.

The preparation of cobalt oxide by ALD has been previously demonstrated using a wide variety of precursors including oxygen-coordinated compounds, Co(thd)$_2$ (Hthd = 2,2,6,6-tetra-methylheptane-3,5-dione)[11,12] and Co (acac)$_3$[13](acac = acetyl-acetonate); halides, CoI$_2$;[14] and organometallics, Co(Cp)$_2$ (Cp = cyclopentadienyl).[15–19] Another interesting and evolving family of ALD precursors is the nitrogen-coordinated precursors (alkylamides, silylamides and amidinates, aromatic heterocycles) which have been studied for the deposition of several metals and metal oxides[20–27] but have barely been explored for the case of Co.[28–30] In addition, the air instability of many Co compounds led to increased focus on research of precursors using new ligand systems.[23–27,31]

In this work we report on the synthesis and characterization of a novel cobalt precursor Co^{II}(DMOCHCOCF$_3$)$_2$ (DMOCHCOHCF$_3$ = 1-(dimethyl-1,3-oxazol-2-yl)-3,3,3-trifluor-prop-1-en-2-ol). The high thermal stability and volatility of this synthesized metal-β-heteroarylalkenolate, owing to the positive inductive effect of the heteroaryl moieties and negative effect of the CF$_3$-groups, make it a very suitable precursor for the preparation of nanostructured ceramic materials by different fabrication methods ranging from solvothermal and microwave synthesis to vapor deposition for thin films (metal–organic chemical vapor deposition (MOCVD), plasma-enhanced chemical vapor deposition (PECVD), atomic layer

[a]Institute of Inorganic Chemistry, University of Cologne, Greinstrasse 6, Cologne 50939, Germany. E-mail: sanjay.mathur@uni-koeln.de

[b]Institut de Ciència de Materials de Barcelona, ICMAB-CSIC, Campus UAB, 08193 Barcelona, Spain. E-mail: mcoll@icmab.es

73

deposition (ALD)). Here, we demonstrate the successful use of this new Co precursor to prepare a uniform ALD thin film on silicon (100) substrates as well as conformal coatings on TiO_2/ C nanofibers. TiO_2/C nanofibers are low-cost, structurally stable and environmentally friendly 1D structures that hold great potential to be used for energy and catalytic applications including anode for ion batteries[32,33] and support for noble metal catalysts.[34] In particular, conformal coatings of dense Co_3O_4 are envisaged as next generation candidates for high capacity anodes in lithium ion batteries for its high theoretical capacity (890 mA h g^{-1}) based on the conversion reaction, compared to commercial graphite (372 mA h g^{-1}).[35]

Results and discussion

Synthesis and characterization of Co^II(DMOCHOCF₃)₂

The cobalt complex $Co^{II}(DMOCHCOCF_3)_2$ was prepared by the reaction of cobalt(II) acetate tetrahydrate with two equivalents of deprotonated ligand 1-(dimethyl-1,3-oxazol-2-yl)-3,3,3-tri-fluorprop-1-en-2-ol (DMOCHCOHCF₃) in a mixture of tetra-hydrofuran (THF) and water, according to the reported procedure.[36] The mixture was stirred for 15 minutes at room temperature and was added dropwise to the solution of $Co^{II}(OOCCH_3)_2 \cdot 4H_2O$ in water. The reaction mixture was stirred overnight at 50 °C. After filtration and drying at room temperature a solid was obtained, which was purified by subli-mation (120 °C, 10^{-3} mbar) to obtain the precursor as a crystal-line red product. The chemical synthesis route is presented in Scheme 1.

The yield of the reaction is 0.76 g (81%). The obtained red product crystallized in the monoclinic space group $P2_1/c$ with four molecules per unit cell, see Table 1.

The molecular structure and the coordination polyhedra of $Co^{II}(DMOCHCOCF_3)_2$ are shown in Fig. 1. The distorted tetra-hedral complex is composed of the central atom Co(II) that is surrounded by two chelate ligands. The reason for the dis-torted structure is the steric hindrance of these ligands that are coordinated with their O- and N-donor sites in a bidentate fashion. In general, the metal–ligand interactions are similar to other reported Co(II) precursors in the literature with the corresponding chelating N, O ligands. The Co–O and Co–N bond lengths were found to be between 1.928(2)–1.944(2) Å and 1.982(3)–1.985(3) Å, respectively, which are comparable to $Co^{II}L_2$ (H–L = Z-4-((2.5-dimethylphenylamino)(phenyl-methylene)-3-methyl-1-phenyl-1H-pyrazol-5(4H)-one))(Co–O = 1.931 Å, Co–N = 1.994 Å) and $Co^{II}L_2$ (H–L = (diethyl-

Table 1 Crystallographic data for Co^II(DMOCHCOCF₃)₂

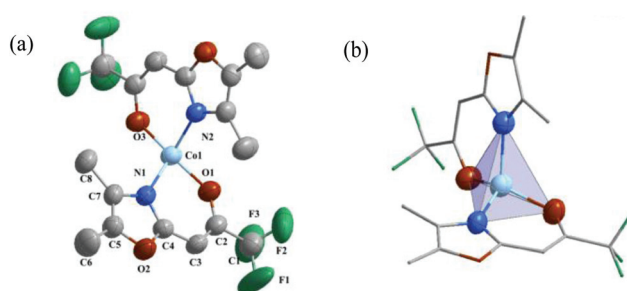| Compound	Co^II(DMOCHCOCF₃)₂
Chemical formula	$C_{16}H_{14}CoF_6N_2O_4$
Molecular weight (g mol^{-1})	471.23
Crystal system	Monoclinic
Space group	$P2_1/c$
a (Å)	8.500(6)
b (Å)	11.800(5)
c (Å)	19.500(1)
α (°)	90.00
β (°)	97.20
γ (°)	90.00
V, $Å^3$	1940.4
Z	4
R_{int}	0.0738
R_1/wR_2 [$I_0 > 2\sigma(I)$]	0.0421/0.1033
R_1/wR_2 (all data)	0.0801/0.1222
Goodness of fit	1.026

Fig. 1 (a) Molecular structure and (b) coordination polyhedra of Co^II(DMOCHOCF₃)₂. Hydrogen atoms are omitted for clarity. Thermal ellipsoids are shown at the 50% probability level. Selected bond lengths (Å) and angles (°): Co1–O1 = 1.944(2), Co1–O3 = 1.928(2), Co1–N1 = 1.982(3), Co1–N2 = 1.985(3), O3–Co1–O1 = 128.06(10), O3–Co1–N1 = 115.75(11), O1–Co1–N1 = 93.87(10), O3–Co1–N2 = 94.25(10), O1–Co1–N2 = 110.40(11), N1–Co1–N2 = 116.05(10).

aminosalicylaldiminato)nitrobenzene)(Co–O = 1.859(5) Å, Co–N = 1.983(6) Å).[37,38] Furthermore, the angles (O1–Co1–N1 = 93.87(10)°, O1–Co1–N2 = 110.40(11)°, O3–Co1–N1 = 115.75(11)°, O3–Co1–N2 = 94.25(10)°) varied slightly from the ideal value (109.47°) of a typical tetrahedral molecular geometry caused by the steric hindrance of the ligands in the com-pound. In addition, intermolecular interactions were observed for this compound. It is particularly noticeable that the molecules are aligned in an antiparallel fashion owing to the Co–O interactions with distances of 3.898 Å, as displayed in ESI, Fig. S1.† Magnetic moment measurement ($M(T)$) of $Co^{II}(DMOCHCOCF_3)_2$ at 1 kOe shows paramagnetic behavior, see Fig. S2.†

The thermogravimetric (TG) and Differential Scanning Calorimetry (DSC) analyses of $Co^{II}(DMOCHCOCF_3)_2$ were carried out under an air atmosphere and ambient pressure between 30 and 600 °C using a heating rate of 10 °C min^{-1} (Fig. 2). The TG curve indicates a rapid single-step mass loss between 100 and 320 °C. The mass loss identified for $Co^{II}(DMOCHCOCF_3)_2$ was 97%, higher than the theoretical value for the formation of Co_3O_4 (83%), which is attributed to
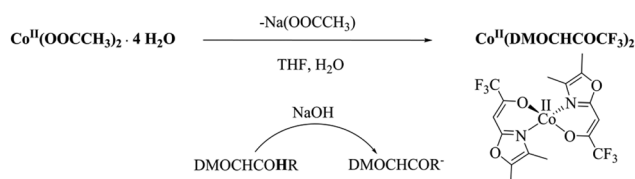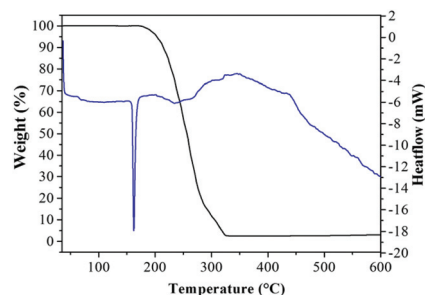

Scheme 1 Synthesis of complex Co^II(DMOCHOCF₃)₂.

Fig. 2 TG (black line) and DSC (blue line) curves of $Co^{II}(DMOCHCOCF_3)_2$.

the sublimation and high volatility of the precursor. This behavior was confirmed by the DSC curve showing one sharp endothermic signal at 160 °C. Importantly this precursor can be stored and handled under ambient conditions having long-term stability of >9 months.

Film deposition

For the cobalt oxide deposition, the $Co^{II}(DMOCHCOCF_3)_2$ precursor was heated at 145 °C and sequentially pulsed with ozone (O_3) on Si(100) substrates and carbon/TiO_2 nanofibers. The ALD optimization process and growth characteristics were performed on Si (100) substrates. Saturation conditions were evaluated varying the Co dose time from 0.5 to 3 s and a constant ozone pulse length of 1 s. It was observed that at a high Co dose time (3 s) the growth rate decreases suggesting the presence of etching reactions, Fig. S3.† Therefore, for subsequent studies, a Co pulse time of 2 s was chosen. A well-defined range with constant growth per cycle (GPC) of 0.02 nm per cycle was identified between 150 °C and 200 °C, see Fig. 3. This deposition rate is similar to that obtained when depositing $Co(thd)_2$ with O_3 on silicon.[39] Metalorganic precursors such as cobaltocene or cyclopentadienyl isopropyl acetamidinato-cobalt lead to higher deposition rates, *i.e.* 0.045–0.05 nm per cycle.[11] Halogen based Co precursors, CoI_2 and liquid cobalt precursors are those that give the highest deposition rates when combined with O_2 or O_3 (0.1–0.2 nm per cycle).[14,17,40,41] A linear dependence of film thickness with the number of ALD cycles was also obtained. Optimized deposition conditions provide continuous thin films with smooth surface morphology (rms ~0.5 nm), as shown in the AFM topo-
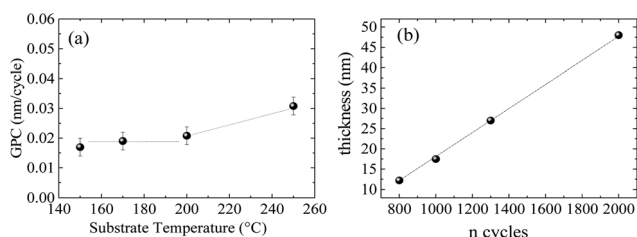
graphic image in Fig. S4.† Preliminary studies on the reactivity of $Co^{II}(DMOCHCOCF_3)_2$ with water (T = 150–250 °C) did not lead to the formation of Co_3O_4.

Fig. 4 shows GIXRD 2θ scans from the as-deposited (200 °C) and post-annealed films. While from the as-deposited film the cobalt oxide peaks can be barely identified, typical reflections of spinel Co_3O_4 are clearly observed in the post annealed one
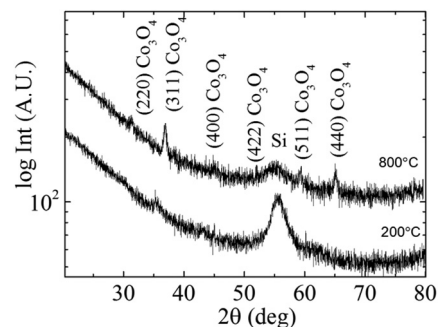

Fig. 4 GIXRD of Co_3O_4 films deposited on Si (100) substrate by ALD (a) as-deposited, (b) post-annealed.

Fig. 3 (a) Cobalt oxide GPC as a function of substrate temperature. (b) Dependence of cobalt oxide film thickness with the number of ALD cycles at 200 °C.
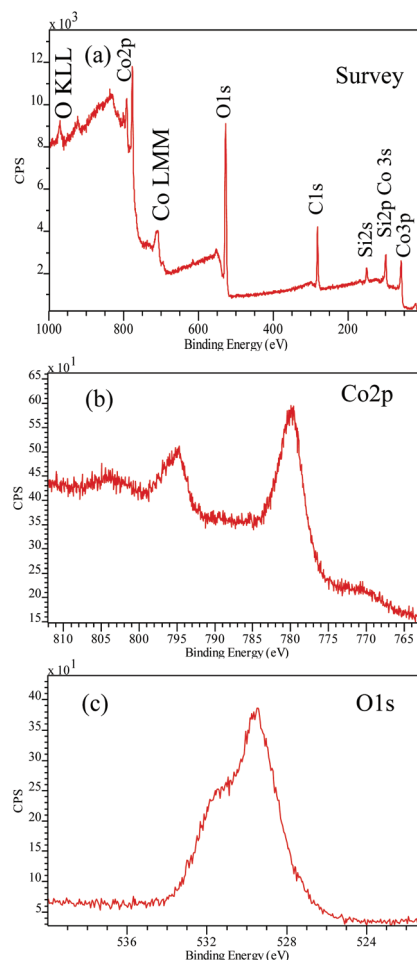

Fig. 5 XPS study of Co_3O_4 film on Si (a) survey spectrum (b) Co 2p and (c) O 1s.

(800 °C for 3 h in static air). Therefore, a polycrystalline Co_3O_4 film was obtained after processing the sample. The mass density of the as-deposited films, an important parameter for high capacity anode materials in lithium-ion batteries, was obtained from X-ray reflectometry analysis (5.84 ± 0.04 g cm^{-3}) and is in agreement with previously reported mass densities of ALD prepared Co_3O_4 films (5.8 g cm^{-3}).[42]

Further analysis on the surface chemical composition was performed by XPS on the as-deposited cobalt oxide/silicon samples after being exposed to air, see Fig. 5. From the survey

spectrum, the presence of Co, Si, O and C was identified, consistent with the expected cobalt oxide deposition on the silicon substrate. Also, the absence of N confirmed that no impurities from the organic precursor remained in the film.

A high resolution Co 2p spectrum, Fig. 5(b), shows two main peaks at 779.9 eV and 795.2 eV attributed to the spin–orbit doublets 2p$_{3/2}$ and 2p$_{1/2}$, with a splitting of 15.3 eV. Also, a broad satellite peak at 803.6 eV was identified. These values and spectrum shape are in agreement with the literature values for Co_3O_4 films. Nonetheless, it is reported that at the initial stages of the film growth of cobalt oxide by ALD, CoO and Co_3O_4 species may coexist changing to pure Co_3O_4 as film thickness increases.[45] The O 1s spectrum is shown in Fig. 5(c). The main contribution is centered at 529.5 eV attributed to the metal–oxide bond. The shoulder that appears at 531.8 eV is due to chemisorbed hydroxyl or carbonyl species formed by the reaction of the oxide surface with moisture in air. High resolution Co 2p and O 1s spectra confirmed the formation of Co_3O_4, in agreement with the literature.[43,44]

$Co^{II}(DMOCHCOCF_3)_2$ was simultaneously deposited on TiO_2/C nanofibers to investigate the ability to coat 3D structures. The SEM images collected from backscattered electrons were acquired from bare TiO_2/C nanofibers and cobalt oxide-coated TiO_2/C nanofibers, Fig. 6(a) and (b), respectively. In both cases well defined nanofibers are observed indicating that the ALD conditions do not degrade the nanofibers. EDX analysis performed at different points of the bare and coated fibers also demonstrates the cobalt deposition in the sample exposed to ALD, Fig. 6(c) and (d), respectively.

The representative STEM image of the 18 nm ALD-Co_3O_4 coated TiO_2/C fiber is shown in Fig. 7(a). Qualitative information on cobalt and titanium elemental distribution was obtained by line-scanning across this nanofiber in several regions. Fig. 7(b), (c) and (d) show the image profile, Ti and Co distribution along the scan identified by a yellow line in Fig. 7(a). Importantly, Co was identified throughout the scan line with lower intensity than Ti which indicates the formation of an ultrathin coating. Also, at the edges of the fiber the intensity of the Co is higher confirming that the titanium is the
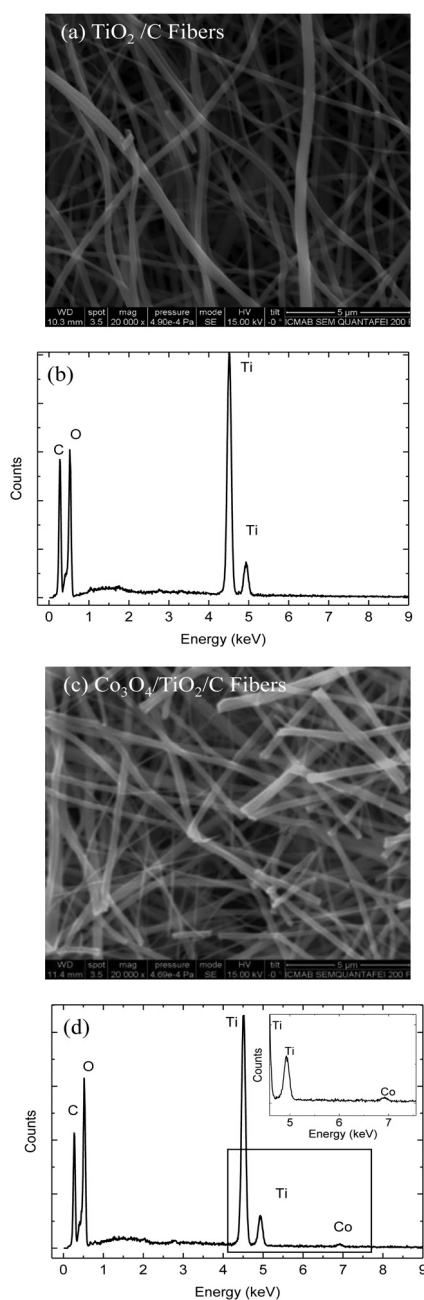

Fig. 6 SEM image of bare TiO_2/C fibers (a) and ALD-Co_3O_4 coated TiO_2/C fibers (c), and the EDX spectrum of the bare fibers (b) and the EDX spectrum of ALD-Co_3O_4 coated fibers (d).
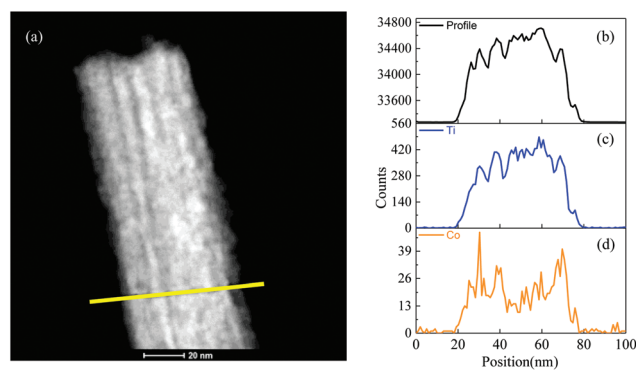

Fig. 7 (a) STEM-EDX analysis of ALD-Co_3O_4 coated TiO_2/C fibers. The yellow line indicates the region where the elemental analysis was acquired, (b) image profile, (c) Ti profile and (d) Co profile.

core of the fiber and Co forms a conformal shell. Therefore, these coated nanofibers could be an attractive support to perform thorough studies on surface reaction mechanisms for future sensors, batteries, supercapacitors and (photo)catalysis-related applications.

Experimental

All chemicals were purchased from Acros Organics and used without further purification. Data collection for X-ray precursor structure elucidation was performed on a STOE IPDS I diffractometer using graphite-monochromated Mo Kα radiation (0.71073 Å). The programs used in this work are STOE's X-Area,[46] and the WINGX suite programs,[47] including SIR-92[48] and SHELXL-97 for structure solution refinement. Fourier transform infrared (FT-IR) measurements were recorded on a PerkinElmer Spectrum 400 and the UV-vis spectrum was recorded on a Lambda 950 device between 250 and 800 nm on 1,2-dichloroethane solutions by using quartz cuvettes. Microanalysis for C, H, and N contents was carried out using a HEKAtech CHNS EuroEA 3000 analyzer. Thermal analyses were performed on a TGA/DSC 1 (Mettler-Toledo-GmbH, Germany) under an air atmosphere (25 mL min^{-1}) at a rate of 10 °C min^{-1} from 30 to 600 °C. EI-MS spectra were obtained on a Finnigan MAT 95 (20 eV) in m/z (relative percentage), operating in positive ion modes.

CHN Anal. Calc.: C, 40.76, N, 5.94, H, 2.97. Found: C, 40.80, N, 5.96, H, 3.78. EI-MS: 471 (100, M$^+$), 402 (8, M$^+$ − CF$_3$), 265 (5, M$^+$ − DMOCHCOCF$_3$). IR (cm^{-1}): ν(C=O) 1666, ν(C=C) 1589, 1536, ν(CF) 1184, γ(=CH) 772. UV–vis (1,2-dichloroethane, λ_{max}/nm): 304, 382, 598–729.

Cobalt oxide thin films (from 12 to 50 nm) were deposited on reference Si (100) substrates and TiO$_2$/C nanofibers by atomic layer deposition, using a thermal Ultratech/Cambridge NanoTech S100 reactor, under a long exposure time. Co^{II}(DMOCHCOCF$_3$)$_2$ was loaded in the ALD cylinder under ambient conditions and sublimed at 145 °C upon optimization (130–160 °C). Before deposition, the substrates were exposed to 150 cycles of ozone. In order to form the cobalt oxide, Co^{II}(DMOCHCOCF$_3$)$_2$ was sequentially pulsed with ozone (O$_3$) provided by using a Del Ozone LG-7 ozone generator. A fixed N$_2$ flow rate of 20 sccm was used. Pulse doses of 2 s and exposure times of 20 s were used for the cobalt precursor to ensure full surface saturation of the 3D fibers. The substrate temperature deposition to identify the ALD window was optimized in this work. 200 °C was chosen as the standard substrate temperature where most of the studies were performed. Post-annealing processes were performed in a tubular furnace at 600 °C–800 °C for 3 h in static air to improve the film crystallinity.

Phase identification and purity were investigated by gracing incidence X-ray diffraction (GIXRD) using a Bruker D8 Discover A25. X-ray reflectometry (XRR) was performed using a SIEMENS D5000 diffractometer to study the cobalt oxide film thickness and density on Si(100) substrates, both operating

with Cu Kα radiation. Surface morphology and chemical composition were evaluated by means of scanning electron microscopy (SEM) and energy dispersive X-ray spectroscopy (EDX) FEI Nova 600 Nanolab Dual-Beam FIB. X-ray photoelectron spectroscopy (XPS) was performed on an ESCA M-Probe (Al Kα) with an energy resolution of 0.8 eV. Binding energies were normalized using the C 1s binding energy (284.8 eV) as a reference. Scanning HAADF STEM images, EDX spectra and STEM-EDX profiles were acquired on an FEI Tecnai G2 F20 microscope operated at 200 kV and equipped with an EDAX super ultra-thin window (SUTW) X-ray detector at ICN2, Barcelona.

Conclusions

We present an effective synthetic approach to prepare the novel Co^{II}(DMOCHCOCF$_3$)$_2$ complex and report its structural and chemical characterization. This precursor, containing heteroaryl moieties and CF$_3$-groups, compared to many existing β-diketonate and cyclopentadienyl-based Co precursors, can be stored and handled under ambient conditions and shows long-term stability. We have also demonstrated the viability of Co^{II}(DMOCHCOCF$_3$)$_2$ for low temperature ALD deposition (200 °C) of spinel Co$_3$O$_4$ with a growth rate of 0.02 nm per cycle. EDX and XPS analyses confirmed the effectiveness of this precursor to generate films free of impurities with a smooth surface (0.5 nm). Homogeneous coatings have been successfully obtained on TiO$_2$/C nanofibers as demonstrated by SEM-EDX and STEM characterization. Therefore, the Co^{II}(DMOCHCOCF$_3$)$_2$ precursor and ALD process reported here offer a valuable and reproducible approach to prepare low temperature high-quality cobalt oxide homogeneous films starting from a stable and easy to handle precursor. Co$_3$O$_4$ conformal coatings on TiO$_2$/C nanofibers could be an attractive architecture to investigate their feasibility for supercapacitors, batteries and even photocatalysts.

Conflicts of interest

There are no conflicts to declare.

Acknowledgements

References

1 L. Yang, S. Cheng, Y. Ding, X. Zhu, Z. L. Wang and M. Liu, *Nano Lett.*, 2012, **12**, 321–325.

2 L. Liao, Q. Zhang, Z. Su, Z. Zhao, Y. Wang, Y. Li, X. Lu, D. Wei, G. Feng, Q. Yu, X. Cai, J. Zhao, Z. Ren, H. Fang, F. R. Hernandez, S. Baldelli and J. Bao, *Nat. Nanotechnol.*, 2014, **9**, 69–73.

3 B. Kupfer, K. Majhi, D. A. Keller, Y. Bouhadana, S. Rühle, H. N. Barad, A. Y. Anderson and A. Zaban, *Adv. Energy Mater.*, 2015, **5**, 1401007-5.

4 X. Xie, Y. Li, Z.-Q. Liu, M. Haruta and W. Shen, *Nature*, 2009, **458**, 746–749.

5 X. Deng and H. Tüysüz, *ACS Catal.*, 2014, **4**, 3701–3714.

6 D. K. Nandi, J. Manna, A. Dhara, P. Sharma and S. K. Sarkar, *J. Vac. Sci. Technol., A*, 2016, **34**, 01A115.

7 J. Zhang, Z. Yu, Z. Gao, H. Ge, S. Zhao, C. Chen, S. Chen, X. Tong, M. Wang, Z. Zheng and Y. Qin, *Angew. Chem., Int. Ed.*, 2017, **56**, 816–820.

8 Y. Ikedo, J. Sugiyama, H. Nozaki, H. Itahara, J. H. Brewer, E. J. Ansaldo, G. D. Morris, D. Andreica and A. Amato, *Phys. Rev. B: Condens. Matter*, 2007, **75**, 054424-8.

9 M. A. Carpenter, S. Mathur and A. Kolmakov, *Metal Oxide Nanomaterials for Chemical Sensors*, Springer, New York, 2012.

10 N. Pinna and M. Knez, *Atomic layer deposition of nanostructured materials*, Wiley-VCH Verlag GmbH & Co KGaA, Germany, 2012.

11 K. B. Klepper, O. Nilsen and H. Fjellvag, *J. Cryst. Growth*, 2007, **307**, 457–465.

12 H. Seim, M. Nieminen, L. Niinisto, H. Fjellvag and L. S. Johansson, *Appl. Surf. Sci.*, 1997, **112**, 243–250.

13 R. L. Puurunen, T. A. Zeelie and A. O. I. Krause, *Catal. Lett.*, 2002, **83**, 27–32.

14 M. Rooth, E. Lindahl and A. Harsta, *Chem. Vap. Deposition*, 2006, **12**, 209–213.

15 M. Diskus, O. Nilsen and H. Fjellvåg, *Chem. Vap. Deposition*, 2011, **17**, 135–140.

16 M. Coll, J. M. M. Moreno, J. Gazquez, K. Nielsch, X. Obradors and T. Puig, *Adv. Funct. Mater.*, 2014, **24**, 5368–5374.

17 B. Han, K. Ha Choi, J. Min Park, J. Woo Park, J. Jung and W.-J. Lee, *J. Vac. Sci. Technol., A*, 2013, **31**, 01A145.

18 B. Huang, W. Yang, Y. Wen, B. Shan and R. Chen, *ACS Appl. Mater. Interfaces*, 2015, **7**, 422–431.

19 M. Daub, M. Knez, U. Goesele and K. Nielsch, *J. Appl. Phys.*, 2007, **101**, 09J111.

20 J. S. Becker, E. Kim and R. G. Gordon, *Chem. Mater.*, 2004, **16**, 3497–3501.

21 W. H. Nam and S. W. Rhee, *Chem. Vap. Deposition*, 2004, **10**, 201–205.

22 H. Wang, R. G. Gordon, R. Alvis and R. M. Ulfig, *Chem. Vap. Deposition*, 2009, **15**, 312–319.

23 L. Appel, R. Fiz, W. Tyrra and S. Mathur, *Dalton Trans.*, 2012, **41**, 1981–1990.

24 L. Bruckmann, W. Tyrra, S. Stucky and S. Mathur, *Inorg. Chem.*, 2012, **51**, 536–542.

25 R. Fiz, L. Appel, A. Gutiérrez-Pardo, J. Ramírez-Rico and S. Mathur, *ACS Appl. Mater. Interfaces*, 2016, **8**, 21423–21430.

26 G. Fornalczyk, M. Valldor and S. Mathur, *Cryst. Growth Des.*, 2014, **14**, 1811–1818.

27 T. Lehnen, J. Schlafer and S. Mathur, *Z. Anorg. Allg. Chem.*, 2014, **640**, 819–825.

28 B. S. Lim, A. Rahtu and R. G. Gordon, *Nat. Mater.*, 2003, **2**, 749–754.

29 J. P. Klesko, M. M. Kerrigan and C. H. Winter, *Chem. Mater.*, 2016, **28**, 700–703.

30 G. Bandoli, D. Barreca, A. Gasparotto, C. Maccato, R. Seraglia, E. Tondello, A. Devi, R. A. Fischer and M. Winter, *Inorg. Chem.*, 2009, **48**, 82–89.

31 M. Büyükyazi, C. Hegemann, T. Lehnen, W. Tyrra and S. Mathur, *Inorg. Chem.*, 2014, **53**, 10928–10936.

32 Y. Xiong, J. Qian, Y. Cao, X. Ai and H. Yang, *ACS Appl. Mater. Interfaces*, 2016, **8**, 16684–16689.

33 Z. Yang, G. Du, Q. Meng, Z. Guo, X. Yu, Z. Chen, T. Guo and R. Zeng, *J. Mater. Chem.*, 2012, **22**, 5848–5854.

34 W. Li, Y. Bai, F. Li, C. Liu, K.-Y. Chan, X. Feng and X. Lu, *J. Mater. Chem.*, 2012, **22**, 4025–4031.

35 X. W. Lou, D. Deng, J. Y. Lee, J. Feng and L. A. Archer, *Adv. Mater.*, 2008, **20**, 258–262.

36 I. Giebelhaus, R. Muller, W. Tyrra, I. Pantenburg, T. Fischer and S. Mathur, *Inorg. Chim. Acta*, 2011, **372**, 340–346.

37 G. Jie, B. Feng, C. Ying, C. Tao, M. Rui, L. Pan, H. Xiaobing, L. Zhenzhen, M. Jianlan and Y. Chunjie, *Appl. Organomet. Chem.*, 2014, **28**, 584–588.

38 P. G. Lacroix, F. Averseng, I. Malfant and K. Nakatani, *Inorg. Chim. Acta*, 2004, **357**, 3825–3835.

39 K. B. Klepper, O. Nilsen and H. Fjellvag, *Thin Solid Films*, 2007, **515**, 7772–7781.

40 B. Han, K. H. Choi, K. Park, W. S. Han and W. J. Lee, *Electrochem. Solid-State Lett.*, 2012, **15**, D14–D17.

41 B. Han, J. M. Park, K. H. Choi, W. K. Lim, T. R. Mayangsari, W. Koh and W. J. Lee, *Thin Solid Films*, 2015, **589**, 718–722.

42 M. E. Donders, H. C. M. Knoops, W. M. M. Kessels and P. H. L. Notten, *J. Power Sources*, 2012, **203**, 72–77.

43 M. C. Biesinger, B. P. Payne, A. P. Grosvenor, L. W. M. Lau, A. R. Gerson and R. S. Smart, *Appl. Surf. Sci.*, 2011, **257**, 2717–2730.

44 S. C. Petitto, E. M. Marsh, G. A. Carson and M. A. Langell, *J. Mol. Catal., A*, 2008, **281**, 49–58.

45 B. Huang, K. Cao, X. Liu, L. Qian, B. Shan and R. Chen, *RSC Adv.*, 2015, **5**, 71816–71823.

46 Stoe and Cie GmbH, ed. Darmstadt, Germany,2003.

47 L. Farrugia, *J. Appl. Crystallogr.*, 1999, **32**, 837–838.

48 A. Altomare, G. Cascarano, C. Giacovazzo and A. Guagliardi, *J. Appl. Crystallogr.*, 1993, **26**, 343–350.

Supporting Information

Cobalt(II)heteroarylalkenolate precursor for homogeneous Co_3O_4 coatings by atomic layer deposition

Mehtap Büyükyazi[a], Thomas Fischer [a], Penmgei Yu[b], Mariona Coll[b]*, Sanjay Mathur[a]*

[a]Institute of Inorganic Chemistry, University of Cologne, Greinstrasse 6, Cologne 50939, Germany

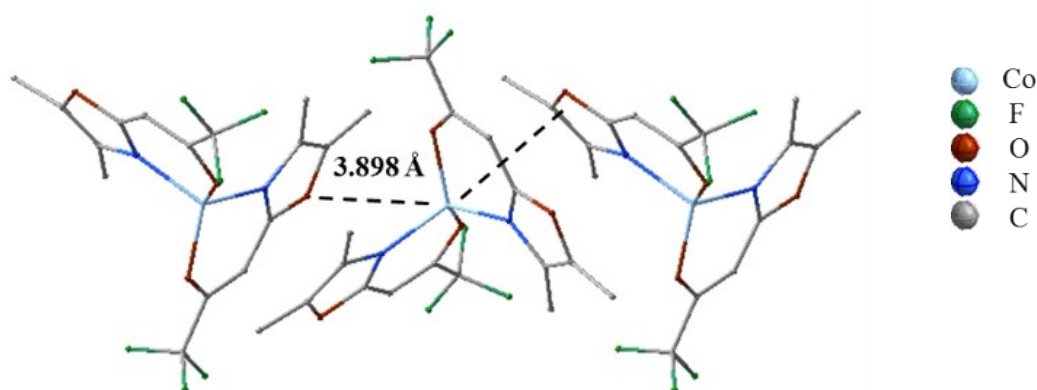[b]Institut de Ciència de Materials de Barcelona, ICMAB-CSIC, Campus UAB, 08193, Barcelona, Spain

Figure S1. Intermolecular interactions of neighbouring molecules in CoDMOX

CCDC 1535898 contain supplementary crystallographic data for this paper. These data can be obtained free of charge from the Cambridge Crystallographic Data Centre via www.ccdc.cam.ac.uk/data_request/cif.
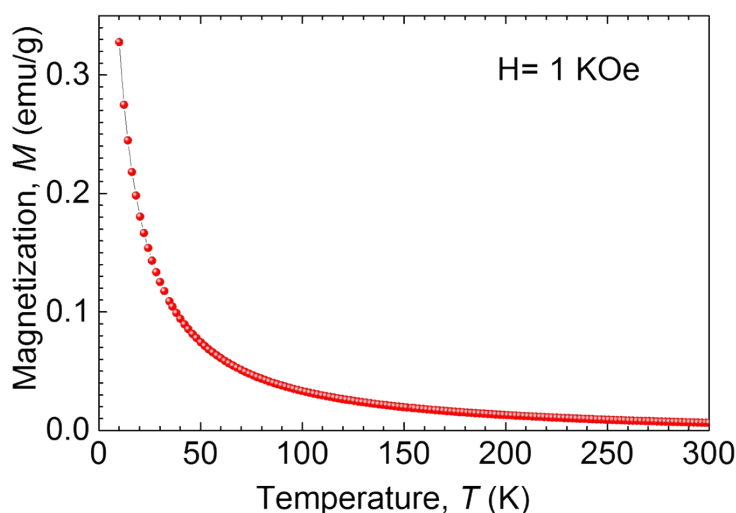

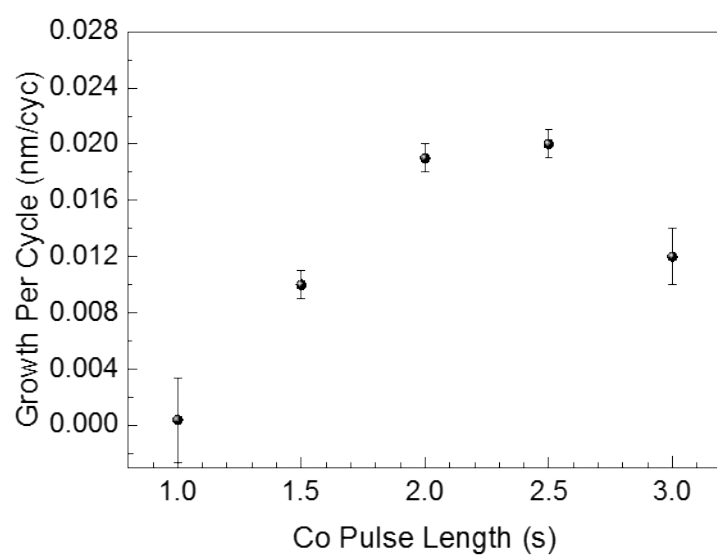**Figure S2** Magnetization vs temperature for CoDMOX complex at 1kOe.

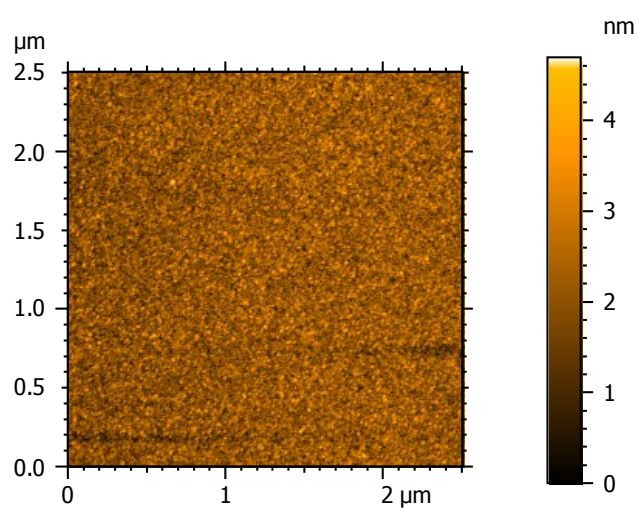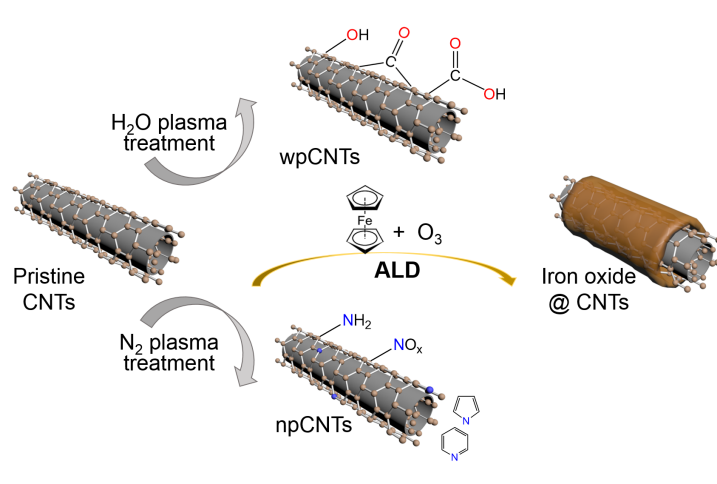**Figure S3** Growth per cycle vs Co precursor pulse time performed at 200ºC and with ozone dose time of 1s

Figure S4: Topographic AFM image of as-deposited Co_3O_4 on Si with an rms < 0.5 nm.

80

II Homogeneous Fe$_2$O$_3$ coatings on carbon nanotube structures for electrochemical energy storage devices

ROYAL SOCIETY OF CHEMISTRY

PAPER

Check for updates

Homogeneous Fe₂O₃ coatings on carbon nanotube structures for supercapacitors†

Pengmei Yu, [a] Mariona Coll, [*a] Roger Amade, [b,c] Islam Alshaikh, [b,c] Fernando Pantoja-Suárez, [b,c,d] Esther Pascual, [b,c] José Luís Andújar [b,c] and Enric Bertran Serra [b,c]

The combination of carbon nanotubes with transition metal oxides can exhibit complementary charge storage properties for use as electrode materials for next generation energy storage devices. One of the biggest challenges so far is to synthesize homogeneous oxide coatings on carbon nanotube structures preserving their integrity. Here we present the formation of conformal coatings of Fe₂O₃ on vertically aligned carbon nanotubes obtained by atomic layer deposition. We investigate the effect of pristine, nitrogen plasma and water plasma treated carbon nanotube surfaces on the ALD-growth of Fe₂O₃ using ferrocene and ozone precursors. The surface morphology, coating thickness, microstructure and surface chemistry of iron oxide–carbon nanotube composites and their ultimate influence on the electrochemical behavior of the composites are evaluated. The most effective surface functionalization is that achieved by H₂O plasma treatment, whereas untreated carbon nanotubes, despite the lack of active sites in the starting pristine surface, can be coated with an inhomogeneous Fe₂O₃ film.

1. Introduction

Miniaturized and powerful electrochemical energy storage systems have been intensively studied because of the increasing need for wireless devices and sensor networks for Internet of Things applications.[1–3] For any electrochemical energy storage devices, such as supercapacitors or rechargeable batteries, electrode materials are key factors for achieving high performances. Electrodes made of carbon nanotubes (CNTs) are commonly studied owing to their outstanding conductive ability, large interfacial surface area and structural and mechanical robustness.[4,5] In particular, electrodes of vertically aligned carbon nanotubes (VACNTs) present a well-ordered nanostructure that allows exposing most of their surface area to the electrolyte and may serve as scaffolds for the deposition of electrochemically active oxides. The charge storage capacity of CNTs is known to increase after performing plasma treatment of their surface,[6–8] which introduces surface functional groups and increases both the number of defects and wettability of the electrodes. However, their low theoretical capacity limits their further applications. The synthesis of composite carbon materials with high capacitance transition metal oxides (TMOs) could show a synergistic effect and fulfill the basic requirements for next-generation energy storage devices.[2,9] Typical TMOs examined in combination with carbonaceous electrodes are TiO₂,[10] V₂O₅,[11] MoO₃₋ₓ,[12] MnO₂,[13] Fe₂O₃,[14–17] Fe₃O₄,[18,19] Co₃O₄,[20,21] and RuO₂.[22–24] Among them, iron oxide is broadly explored as a nontoxic, inexpensive and abundant material with high theoretical capacitance.[25,26] Using a variety of deposition techniques sophisticated Fe₂O₃ nanostructures have been successfully fabricated including nanoparticles,[16–18] nanorods,[15,16] ribbons,[14] sandwich-like sheets[19] and 3D ovoid architectures.[16]

Importantly, the performance of these energy storage devices depends on the thickness and conformality of the TMO coating. Therefore, atomic layer deposition (ALD) provides an attractive way to synthesize such structures. ALD is a well-established thin film deposition technique in which the alternate pulsing of gas-phase precursors reacting in a self-limiting manner with the active sites of the substrate surface allows the fabrication of ultrathin, pin-hole free and highly conformal coatings on complex nanometric structures at relatively low temperature, thus outmatching any other existing thin film deposition technique.[27,28]

ªInstitut de Ciència de Materials de Barcelona (ICMAB-CSIC), Campus de la UAB, 08193 Bellaterra, Barcelona, Spain. E-mail: mcoll@icmab.es; Tel: +34 935801853
ᵇDepartament de Física Aplicada, Universitat de Barcelona, Martí i Franquès 1, 08028 Barcelona, Spain
ᶜInstitute of Nanoscience and Nanotechnology (IN2UB), Universitat de Barcelona, Avda. Joan XXIII, s/n, 08028 Barcelona, Spain
ᵈDepartamento de Materiales, Facultad de Ingeniería Mecánica, Escuela Politécnica Nacional, Ladrón de Guevara, E11-253 Quito, Ecuador

†Electronic supplementary information (ESI) available: EDX mapping of 30 nm and 6 nm Fe₂O₃@wpCNTs, GIXRD and XRR data for ALD Fe₂O₃ films and deconvoluted XPS C 1s spectra of ALD Fe₂O₃@CNTs. See DOI: 10.1039/C9DT04908H

Considering the inertness of the CNT surface, careful interface engineering is called for in order to create binding sites to promote the nucleation and growth of ALD-transition metal oxides. Several strategies have been developed for this purpose. For example, non-covalent modifications using dodecyl sulfate treatment[29] or alternating exposure to nitrogen dioxide gas[30] have proved successful for coaxially coating single-walled carbon nanotubes with Al_2O_3. Acid and oxidative plasma treatments and nitrogen doping can also generate functional groups to tailor the shape and distribution of the TMO coating.[31–33] The performance of these composites could be further improved by better understanding the role of the functional groups present in the CNT surface as anchoring sites for the ALD process and their effect on the electrochemical properties of the composites.

In this work, we investigated the effect of pristine, water plasma and nitrogen plasma treated CNT surfaces on the ALD-growth of Fe_2O_3 using ferrocene and ozone precursors to prepare heterostructural one dimensional coaxial nanotubes with two different iron oxide thicknesses, 6 nm and 30 nm. We compared the coating surface morphology, conformality and induced chemical changes as a function the surface treatment. We also evaluated their effects on the electrochemical performance.

2. Results and discussion

2.1. Morphological, structural and compositional characterization

Typical surface morphologies of untreated CNTs (utCNTs), water plasma CNTs (wpCNTs) and nitrogen plasma CNTs (npCNTs) before and after 6 nm and 30 nm iron oxide coating are shown in Fig. 1.

The uncoated CNTs preserve the vertical alignment regardless of the plasma treatment although the tips of the wpCNTs tend to be narrower and the length decreased, Fig. 1(a–c), as previously reported by Hussain *et al.*[7] Upon 6 nm Fe_2O_3 coating, the diameter of the CNTs increases and the Fe_2O_3 composites of plasma treated CNTs are less aggregated than the untreated ones Fig. 1(d–f). For the sake of clarity, these two scenarios are schematized in Fig. 2(a) and (b). Fig. 2(a) illustrates the structure of conformally coated and discrete CNTs and Fig. 2(b) presents the coated CNTs that show aggregation in some areas as a result of the inhomogeneous Fe_2O_3 coating. For 30 nm coating, the distance between neighbouring CNTs is further decreased and the CNTs remain intact, in good agreement with the formation of a thicker coating, Fig. 1 (g–i). An obvious difference in the 30 nm series is that
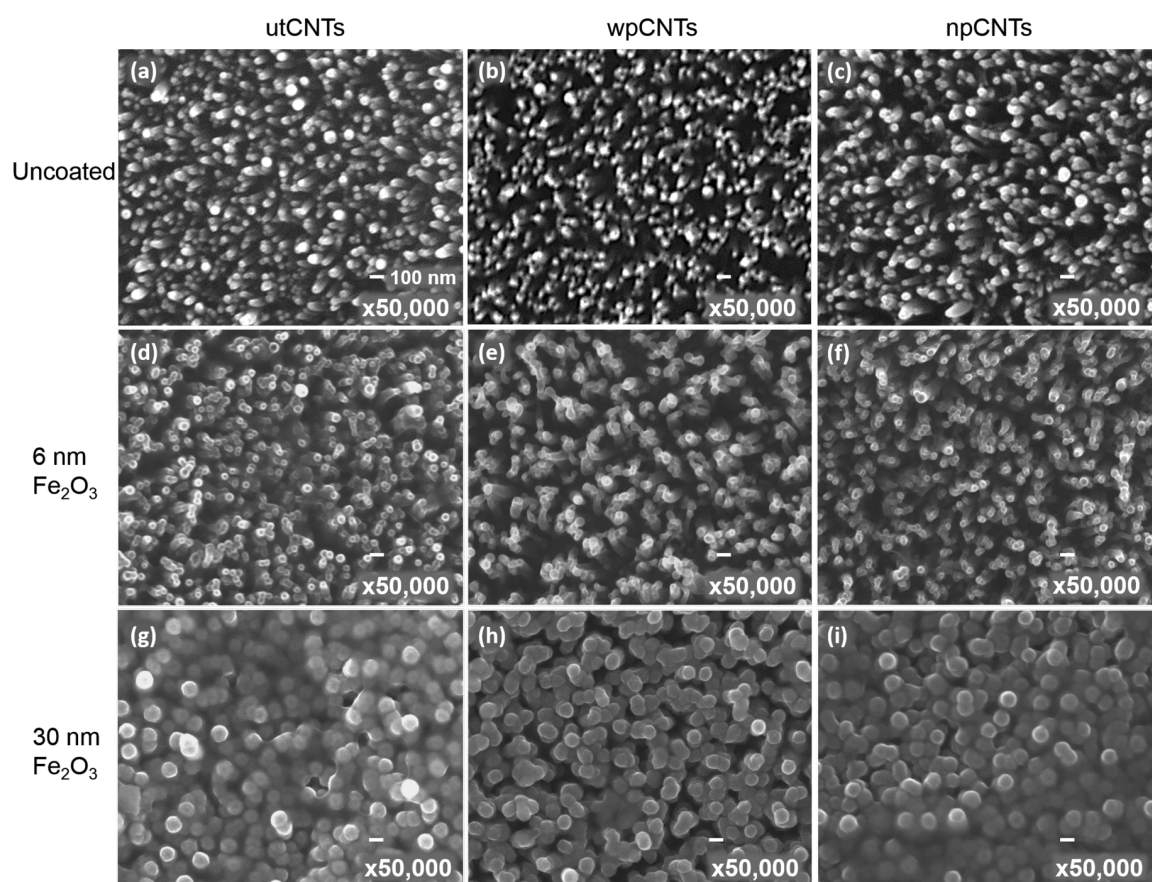

Fig. 1 SEM micrographs of pristine, 6 nm and 30 nm ALD Fe_2O_3 coated untreated (utCNTs), water plasma treated (wpCNTs) and nitrogen plasma treated carbon nanotubes (npCNTs). The bar scale corresponds to 100 nm in all the images.
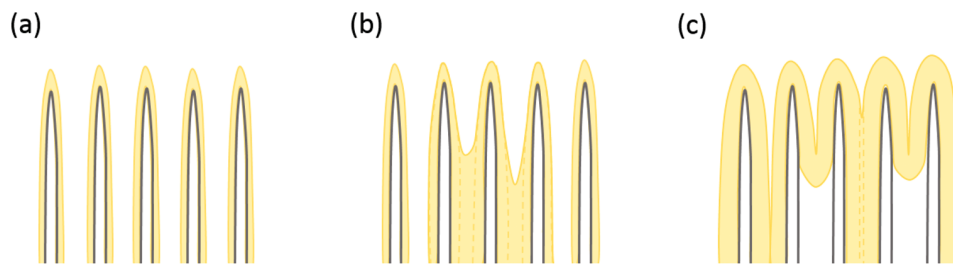
Fig. 2 Illustration of different ALD coatings of Fe_2O_3 on the CNT surface: (a) conformal coating; (b) partial conformal coating and partial CNT aggregation; (c) thicker and non-conformal coating on CNTs.

Fe_2O_3@utCNTs and Fe_2O_3@npCNTs present a continuous film on top of the CNTs, which is schematized in Fig. 2(c), whereas for Fe_2O_3@wpCNTs, the presence of a continuous film is not so evident.

From this surface morphology analysis it is found that iron oxide coating took place regardless of the surface functionalization of the CNT surface although the deposition on the untreated CNTs is less homogeneous. Also, these results contrast with previous studies on CNT@Fe_2O_3 prepared *via* ALD from ferrocene and oxygen which claimed that prior chemical functionalization was needed to anchor the Fe_2O_3 film.[32] We attribute this difference to the use of a more powerful oxidant source than oxygen (*i.e.* ozone) capable of creating active sites during the ALD process, as will be discussed later.

To further investigate the film homogeneity and crystallinity of the CNTs, TEM images were acquired for pristine utCNTs, 6 nm and 30 nm iron oxide coatings and elemental analysis was performed. Fig. 3(a) shows the microstructure of a pristine utCNT covered with amorphous C. The inner membranes with a bamboo-like structure can also be identified as darker areas inside the tube. Fig. 3(b) shows a uniform and continuous film of 6 nm thickness on the wpCNTs. Line profile elemental analysis performed across the coated wpCNTs (identified as a green line in Fig. 3(b)) shows that Fe and O are mostly located in the shell of the CNTs, whereas C dominates in the core of the structure, confirming the conformal coating of the iron oxide layer, Fig. 3(c). Finally, higher magnification TEM images of the 6 nm Fe_2O_3 coating on the

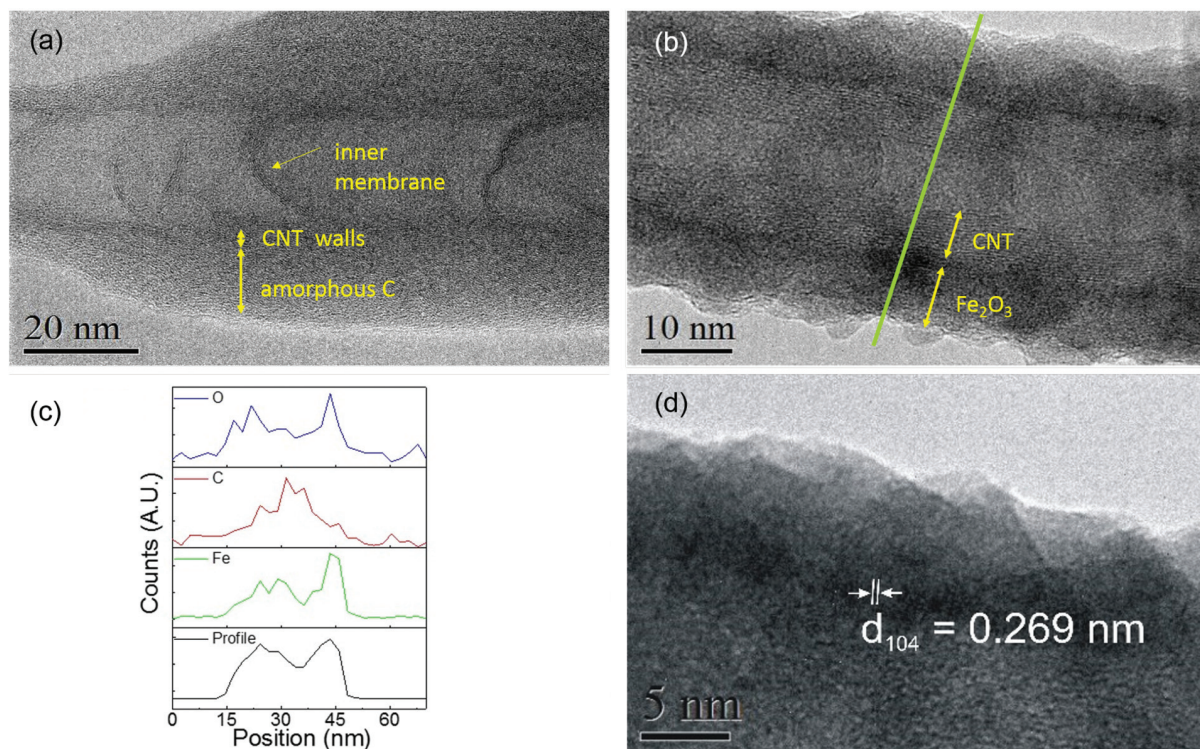**Fig. 3** High resolution TEM analysis of (a) pristine utCNTs. CNT walls, inner membranes and the amorphous C layer are indicated by arrows. (b) 6 nm Fe_2O_3@wpCNTs; (c) elemental line profile of O, C and Fe acquired along the green line marked in (b). (d) High resolution TEM of the Fe_2O_3 coating on wpCNTs revealing an interplanar spacing of $d \sim 0.269$ nm for iron oxide.
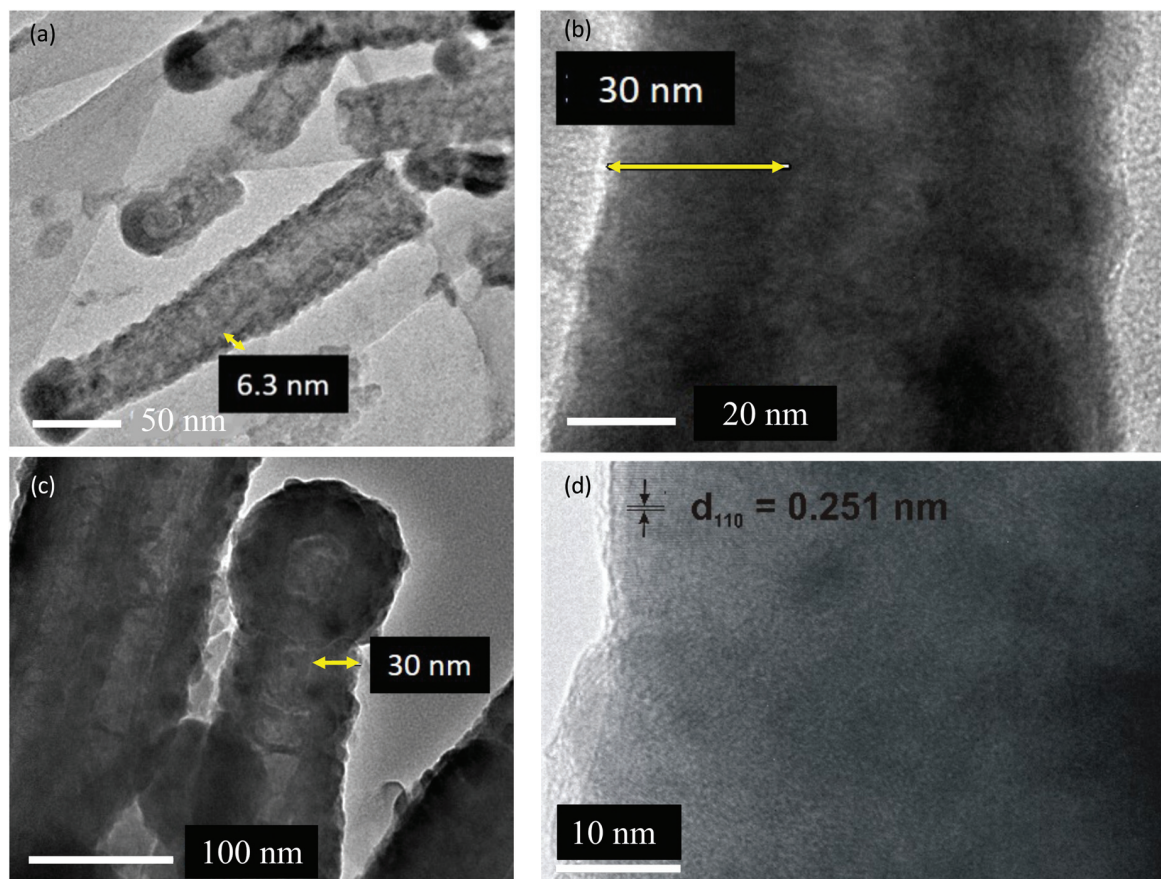
Fig. 4 (a) TEM images of 6 nm Fe_2O_3@npCNTs and (b) 30 nm Fe_2O_3@utCNTs and (c) and (d) high resolution TEM images of 30 nm Fe_2O_3@wpCNTs.

wpCNTs allowed the identification of the interplanar spacing of iron oxide ($d \sim 0.269$ nm), indicating the formation of the α-Fe_2O_3 hematite phase. Also, crystalline iron oxide coexists with isolated areas of amorphous iron oxide. The microstructure of 6 nm Fe_2O_3@npCNTs is shown in Fig. 4(a). The thickness of the coating is in good agreement with the expected value from the ALD cycles and also reveals a conformal coating. The 30 nm coatings on the utCNTs and on wpCNTs are compared in Fig. 4(b) and (c), respectively. Fe_2O_3@wpCNTs exhibits a cleaner morphology than Fe_2O_3@utCNTs. This difference is attributed to the fact that water plasma treatment removed amorphous carbon and it is possible to see graphene membranes inside the nanotubes. Also, the remaining Fe catalyst in the CNT preparation process can be observed on the tips of the nanotubes.[7] Elemental mapping of the 30 nm coatings further confirms the conformal deposition of iron oxide in the thicker films as well, see ESI Fig. S1.†

The surface chemical compositions of the iron oxide coated utCNTs, npCNTs and wpCNTs were further analysed by XPS. High resolution Fe 2p core level spectra are depicted in Fig. 5(a). The spectra reveal a typical spin–orbit doublet feature at 724.7 eV ($2p_{1/2}$) and 711.2 eV ($2p_{3/2}$), and the corresponding satellite peak at 719.4 eV. The difference between $2p_{3/2}$ and its satellite peak is 8.4 eV, confirming the +3 oxidation state of iron[34] in the three different composites.

High resolution C 1s spectra are shown in Fig. 5(b). The main peak is assigned to the graphitic carbon of the CNTs and the low intensity peak located at higher binding energies (288.4 eV) to the C=O bonds. Note that the main peak is centered at slightly different binding energies depending on the plasma treatment. For gaining deeper insight into the bonding chemistry of the graphitic carbon, the C 1s spectra have been deconvoluted into at least four component Gaussian peaks (see Fig. S2†). For Fe_2O_3@utCNTs, the main peak is broad and asymmetric identifying a strong contribution assigned to sp^3 hybridized graphitic-like carbon (C–C), *i.e.* amorphous carbon, and a smaller contribution at a slightly lower binding energy, 284.5 eV, attributed to sp^2 hybridized carbon atoms (C=C).[35] Along with the previously identified contribution of C=O at 288.4 eV, the peak deconvolution identifies a shoulder at 286.6 eV due to the C–O bonds. For Fe_2O_3@npCNTs the main peak is narrower and centered at 285.3 eV, suggesting that the sp^3 contribution dominates. Finally, Fe_2O_3@wpCNTs shows a peak centered at 284.9 eV, revealing that the main contribution arises from the sp^2 hybridized carbon atoms. Therefore, the plasma treated samples show a decreased C sp^3 concentration
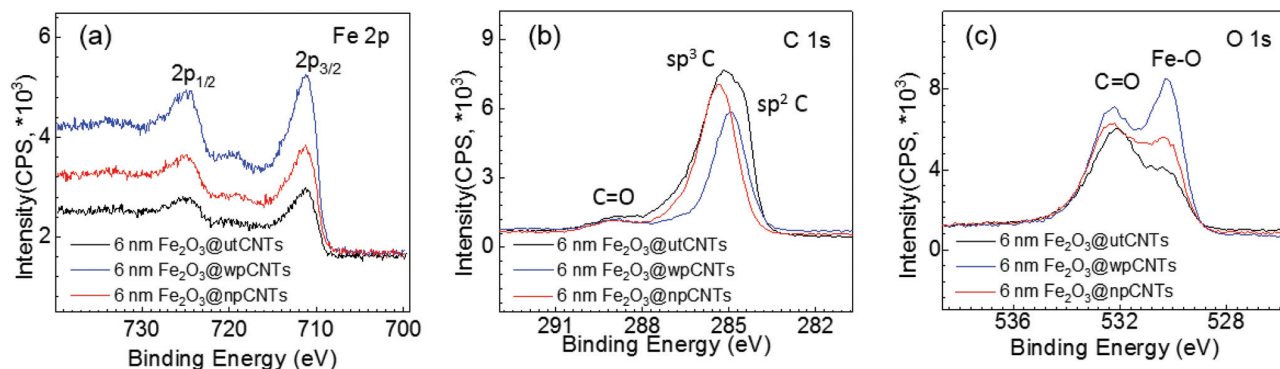
Fig. 5 (a) High-resolution Fe 2p spectra; (b) C 1s spectra and (c) O 1s spectra of 6 nm Fe$_2$O$_3$@CNTs.

compared to the utCNTs, in good agreement with the partial removal of amorphous carbon upon plasma treatment.[8]

By comparing Fe$_2$O$_3$@wpCNTs *vs.* Fe$_2$O$_3$@npCNTs, it is observed that the Fe$_2$O$_3$@npCNTs composite shows a larger contribution of C–C sp^3 hybridization, confirming that the nitrogen plasma treatment is less effective at removing amorphous carbon than water plasma treatment. The amount of sp^3 C and sp^2 C in each composite has been calculated from the C 1s XPS deconvolution and is listed in Table S1.† All three scenarios show the presence of carbon–oxygen bonds, considered to be the main anchoring sites for the iron oxide deposition. Note that the C=C bonds are susceptible to react upon N$_2$ or H$_2$O plasma treatment[7,8] but they could also be oxidized with O$_3$[36] during the ALD process creating C=O or C–O bonds as active sites. This is relevant because covalent functionalization can improve the anchoring of the ALD precursors for the iron oxide coating but it can also change the conductance of the nanotube and can be detrimental to the electrochemical properties,[30] as will be discussed below.

The O 1s high resolution spectra, Fig. 5(c), show two main contributions at 532.2 eV and 530.3 eV attributed to the C=O bonds and Fe–O bonds, respectively. The weight of the two contributions varies depending on the nature of the plasma treatment. Fe$_2$O$_3$@wpCNTs shows the largest contribution of the Fe–O bond, indicating a larger amount of Fe$_2$O$_3$. For Fe$_2$O$_3$@utCNTs, the largest contribution is the one corresponding to C=O. It is important to note that the Fe$_2$O$_3$@utCNTs composite also shows Fe–O bond contribution which is in agreement with the formation of the iron oxide coating.

As anticipated in the SEM analysis, our results suggest that the iron oxide coating can be obtained on CNTs without previous plasma treatment. The O$_3$ gas introduced in the reaction chamber during the ALD process could also promote the transformation of C–C and C=C bonds of the CNTs into C=O and O=C–O[37] increasing the amount of anchoring sites, in good agreement with the species detected by XPS. In fact, this is supported by the formation of Fe$_2$O$_3$ in the three systems regardless of the surface treatment (untreated and N$_2$ and H$_2$O

plasma treated). The non-uniform coverage of the utCNTs identified from the SEM analysis, Fig. 1(g), could lie in the propensity of the carbon bonds at the tips of the CNTs to react under oxidizing conditions (*i.e.* ozone) because they are under higher strain due to their large curvature providing lower activation energy,[38] being the anchoring sites for the subsequent reaction with ferrocene.

According to this observation, the reaction mechanism of iron oxide formation in our composite systems could be similar to that previously described for ferrocene and O$_2$ on modified CNTs.[32] Ferrocene would chemically bond with the functional groups on the CNT surface (–COOH and –OH for wpCNTs and utCNTs upon activation by ozone; graphite-like N and pyridine-like N for npCNTs) and during the ozone pulse the ferrocene ligand will oxidize and create new anchoring sites for the following ALD cycle.

2.2. Electrochemical properties

It is well known that surface modification of as-grown CNTs helps improving the electrochemical response.[7,39] Here we investigate how both surface functionalization and Fe$_2$O$_3$ coating influences the electrochemical properties. The areal capacitance of the samples was calculated from the cyclic voltammograms applying eqn (1),

$$C = \frac{q_a + |q_c|}{2A\Delta V} \tag{1}$$

where C is the areal capacitance in mF cm^{-2}, q_a and q_c are the anodic and cathodic charges, respectively, in mC. A is the geometrical area of the sample in cm^2 and ΔV is the voltage window in V. The cyclic voltammograms of the samples show typical rectangular shapes, illustrating the capacitive behavior of the nanocomposites (Fig. 6(a) and (b)). The water-plasma treated CNTs with 6 nm iron oxide show, in addition, the oxidation and reduction peaks of the iron atom in the electrolyte solution (Fig. 6(a)). However, the shape remains similar even at high scan rates (150 mV s^{-1}, see Fig. 7), which implies excellent capacitive behavior and quasi-reversible redox reactions.[40] The redox peaks of the 6 nm Fe$_2$O$_3$@wpCNTs can be related to the remaining Fe catalyst at the tip of the CNTs utilized to
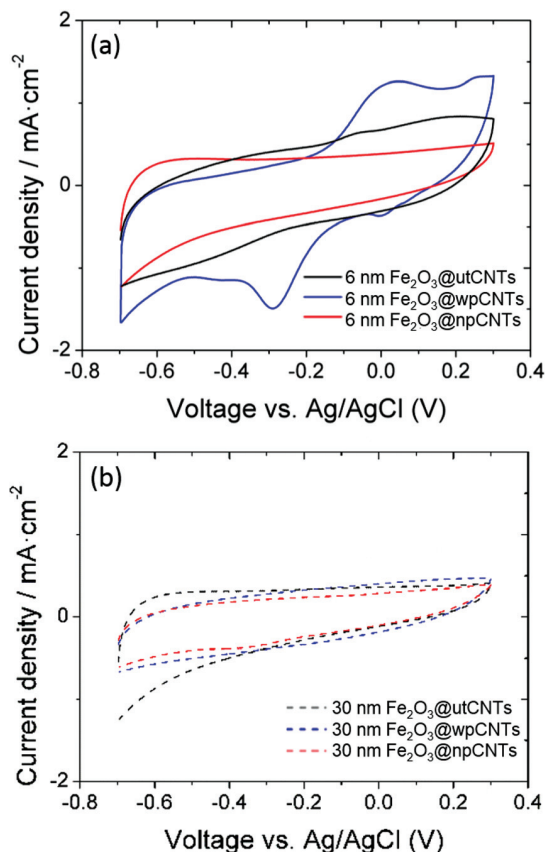
Fig. 6 Areal capacitance of carbon nanotubes with and without plasma treatment, covered with 6 and 30 nm thickness ALD-iron oxide at a 50 mV s^{-1} scan rate.
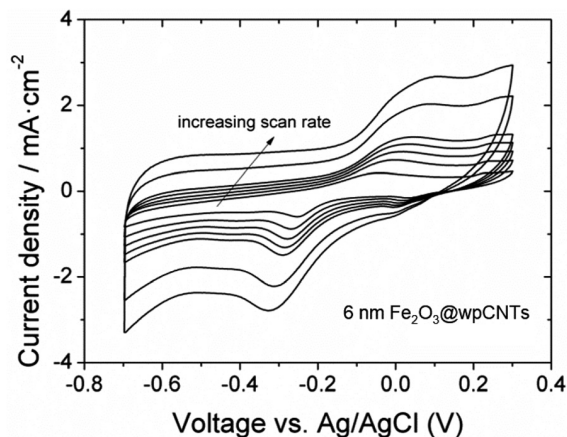

Fig. 7 Cyclic voltammograms of 6 nm Fe$_2$O$_3$@wpCNTs at scan rates from 10 to 150 mV s^{-1}.

grow the nanotubes.[7,41] During the water plasma process, the CNT sites with defects are preferentially etched (*i.e.* the tips of the nanotubes) leaving the Fe-catalyst exposed. Consequently, the 6 nm Fe$_2$O$_3$@npCNTs and Fe$_2$O$_3$@npCNTs do not show the redox peaks because they presumably present a larger
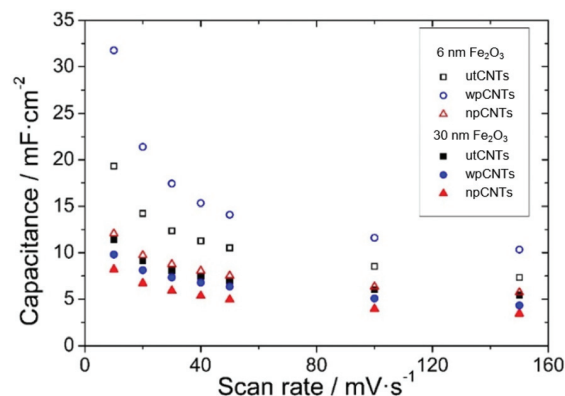

Fig. 8 Areal capacitances of different nanocomposites *versus* scan rates.

amount of amorphous carbon covering the CNTs and thus the Fe catalyst. For the 30 nm coatings, the Fe catalyst is even less exposed due to the thicker iron oxide coating.

The areal capacitance of the carbon nanotubes increases after atomic layer deposition of iron oxide from below 1 mF cm^{-2} for bare CNTs (not shown) up to 32 mF cm^{-2} at a scan rate of 10 mV s^{-1} (6 nm Fe$_2$O$_3$@wpCNTs in Fig. 8). If the layer of iron oxide is too thick, *i.e.*, in the order of the CNT separation distance, the capacitance decreases again due to the reduction of the nanocomposite porosity and thus the electrochemically active surface area. An iron oxide layer of about 6 nm thickness appears to be suitable for high areal capacitance, while a 30 nm thick layer reduces the electrochemically active area of the electrode. In addition, the water plasma treatment of the nanotubes allows the removal of amorphous carbon and surface functionalization with oxygen groups, which result in a better electrochemical performance of the deposited oxide. In contrast, the nitrogen plasma treatment of the CNT surface has a negative effect on the areal capacitance of the nanocomposite. Nitrogen plasma allows the partial removal of amorphous carbon and the introduction of the nitrogen groups on the CNT surface.[39] However, these groups along with a larger amount of amorphous C compared to the water plasma treated samples seem to be detrimental to the formation of an electrochemically active layer of iron oxide for supercapacitor applications.

Electrochemical Impedance Spectroscopy provides further information about the processes taking place at the interfaces and bulk of the samples. The Nyquist plot presents the typical behavior of capacitive porous electrodes with the data becoming steeper in the low-frequency region of the spectra (Fig. 9). A modified Randles circuit allows fitting the experimental points with circuit elements in series and parallel configurations describing charge storage and transfer processes between the electrode and the electrolyte (inset in Fig. 9). The intersection point with the real axis in the Nyquist spectra (see inset graph in Fig. 9) corresponds to the cell internal resistance (R_S). The charge transfer resistance (R_{CT}) describes transfer processes between the electrode and electrolyte and is con-
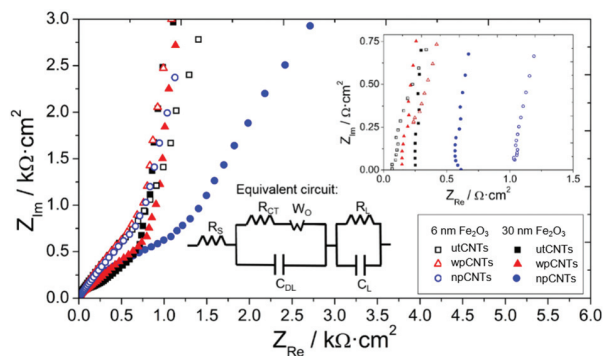
Fig. 9 Nyquist plot of different CNT samples covered with 6 and 30 nm iron oxide by ALD. The inset shows the intersection with the real axis in the high-frequency region and the modified Randles equivalent circuit used to fit the data.

nected in parallel with the double layer capacitance (C_{DL}). In the mid-frequency region of the spectra a Warburg element (W_O) refers to the diffusion of ions through the porous structure of the electrode, expressed by $A/(j\omega)^n$ where A is the Warburg coefficient, ω is the angular frequency and n is an exponent. At low frequencies, the points of the spectra become steeper in accordance with a polarized capacitive behavior which is described by mass capacitance (C_L) in parallel with leakage resistance (R_L). The whole spectra were fitted using ZVIEW software (Version 2.1, Scribner Associates, Inc., Southern Pines, NC, USA) and the equivalent circuit parameters obtained are given in Table 1.

The internal resistances of the samples are similar, which is related to electrolyte resistance, cables, and contact resistances of the cell,[42] and take values in the range of 0.08 to 1.08 Ω cm^2, with the wpCNTs presenting the highest values. This result is assumed to be related to the oxygen groups incorporated on the surface of the CNTs after the water plasma treatment, which may increase the resistance of the nanotubes as observed previously.[43] The charge transfer resistance between the nanocomposite and the electrolyte presents the lowest value for the water-plasma treated samples, which indicates excellent contact between the iron oxide layer and the carbon nanotubes. The untreated sample shows the highest R_{CT} values due to the amorphous carbon present on the surface of the nanotubes which avoids good contact with the oxide coverage and the CNTs. As expected, the R_{CT} value increases with iron oxide thickness due to its low conductivity. The Warburg

coefficient also increases from 6 to 30 nm deposition thickness, in agreement with higher ion diffusion resistance through the pores of the sample. The Warburg exponent values are around 0.45, except for the 6 nm Fe$_2$O$_3$@npCNTs sample, which presents a value of 0.64 related to diffusion taking place only at the surface of the electrode.[44] The double layer capacitance, associated with the electrostatic charging of the electrode, reaches a maximum value for the 6 nm Fe$_2$O$_3$@wpCNTs sample. The leakage resistance presents a minimum for the nitrogen-plasma treated samples (6 and 30 nm iron oxide thickness), which explains the low charge storage capacity of these samples. 30 nm Fe$_2$O$_3$@wpCNTs (0.7 mF cm^{-2}) and 6 nm Fe$_2$O$_3$@npCNTs (7 mF cm^{-2}) present the maximum mass capacitance values for their respective thicknesses. However, the low R_L of the nitrogen-plasma treated sample results in low energy storage capability. Thus, 6 nm Fe$_2$O$_3$@wpCNTs shows optimum values of leakage resistance, double layer and mass capacitances. This is assumed to be related to the more effective removal of amorphous carbon (see Fig. S2†), and the introduction of the oxygen groups that promote a conformal coating and an optimum interface between the CNT and the metal oxide. The nitrogen plasma treatment is not so effective in removing the amorphous carbon (see Fig. S2†) and introduces nitrogen groups that avoid the stable accumulation of charges at the interfacial region between the electrode and electrolyte. The overall capacitance obtained from the fitting of EIS data is of the same order of magnitude as those obtained by cyclic voltammetry. The values are also similar to those already reported in the literature (37 mF cm^{-2}) for vertically oriented CNTs covered with metal oxide nanoparticles.[45] Other works present higher areal capacitance values (around 600 mF cm^{-2}).[26] However, the nanotubes are not vertically aligned but rather randomly oriented and with a higher mass loading (30–50 mg cm^{-2}). Other materials deposited on VACNTs have been studied and show similar areal capacitance values, *i.e.* 37.5 mF cm^{-2} for DC-sputtered vanadium nitrate on VACNTs.[46] Extremely high areal capacitance values have been obtained using asymmetric supercapacitors with binary metal sulfides and polypyrrole on VACNTs (3.3 F cm^{-2}).[47] By analyzing the morphology and thickness of the iron oxide coating from SEM and TEM images, the mass loading of our samples was estimated to be 30–160 μg cm^{-2}, depending on the thickness. This corresponds to a theoretical specific capacitance of about 1000 F g^{-1} at 1 A g^{-1}, which is in agreement with previous works on the ALD of iron oxide on CNTs.[40] These values are also similar to

Table 1 Equivalent circuit parameters obtained from fitting the EIS data for the samples with a modified Randles circuit

Electrode material	R_S (Ω cm^2)	R_{CT} (Ω cm^2)	A (kΩ s^{-n})	n	C_{DL} (mF cm^{-2})	R_L (Ω cm^2)	C_L (mF cm^{-2})
6 nm Fe$_2$O$_3$@utCNTs	0.08	0.37	0.5	0.56	0.20	566	3.5
6 nm Fe$_2$O$_3$@npCNTs	0.12	0.25	5.5	0.64	0.07	68	7.0
6 nm Fe$_2$O$_3$@wpCNTs	1.08	2×10^{-7}	0.5	0.45	0.32	341	6.0
30 nm Fe$_2$O$_3$@utCNTs	0.28	79	2.8	0.40	0.074	1.3	0.30
30 nm Fe$_2$O$_3$@npCNTs	0.18	11	4.0	0.42	0.081	0.42	0.33
30 nm Fe$_2$O$_3$@wpCNTs	0.66	5×10^{-7}	7.0	0.44	0.095	191	0.70

those obtained using other deposition techniques such as the hydrothermal method. Using this technique Fe_2O_3 was deposited on CNT sponges providing 269.3 F g^{-1} specific capacitance,[48] and iron oxide nanoparticles were deposited on nitrogen-doped reduced graphene oxide providing up to 618 F g^{-1}.[49]

3. Experimental

3.1. Growth of carbon nanotubes

Synthesis of 1 μm-long vertically aligned-multiwalled CNTs (VA-MWCNTs) was carried out in a PECVD (plasma-enhanced chemical vapour deposition) reactor which allows to do sputtering, PECVD and plasma functionalization. A Papyex© flexible graphite sheet (n998) of 0.2 mm thickness was used as a substrate. At a chamber base pressure below 4×10^{-4} Pa, 3 nm of the Fe catalyst was sputtered on the graphite substrate using 128 sccm Ar. In order to anneal the catalyst layer, the sample was located below the graphite thermal resistance (2 Ω). The annealing process was achieved at 680 °C under 2 mbar hydrogen pressure with 750 s ramp time and 120 s hold time. Subsequently, the PECVD process was carried out for 15 min, at the same temperature, under 1 mbar pressure, applying 50 W plasma power and with 100 and 50 sccm gas flow of NH_3 and C_2H_2, respectively.

Two different plasma treatments were performed on the CNT samples in order to introduce the nitrogen (nitrogen plasma) and oxygen (water plasma) functional groups on their surface and analyze their effect on the ALD-deposition of iron oxide and the electrochemical properties of the nanocomposites. The conditions for the water plasma treatment were: 30 s, 50 Pa water vapor pressure, and 50 W plasma power, and for the nitrogen plasma treatment: 120 s, 50 Pa nitrogen pressure with a flow of 100 sccm and 50 W plasma power.[8]

3.2. Deposition of Fe_2O_3 coatings

Fe_2O_3 coatings on untreated CNTs (utCNTs), water plasma CNTs (wpCNTs)[7] and nitrogen plasma CNTs (npCNTs)[8] were prepared by atomic layer deposition in a Cambridge NanoTech Savannah 100 ALD system. Reference p-type boron-doped Si (100) pieces were placed in the ALD reactor simultaneously with the CNT samples for determining the Fe_2O_3 growth rate and film thickness. The deposition process was realized *via* alternating ferrocene $Fe(Cp)_2$ (heated at 80–100 °C) and ozone (O_3) pulses at 200–250 °C. Exposure mode was employed by closing the exit valve of the reactor for a certain amount of time before the subsequent purging procedure, allowing precursor penetration into the deep CNT trenches and ensuring adequate reaction time between the precursors and CNT surface groups. The pulse/exposure/purge sequence applied to this system was 2–3.5 s/30–50 s/20–40 s for ferrocene and 0.2–1 s/20–40 s/20–40 s for ozone. A 40 sccm nitrogen gas flow was used as both the carrier and purge gas. The thickness of the coatings (6 nm and 30 nm) was adjusted by varying the number of ALD cycles. Note that below 6 nm the film was not continuous.

3.3. Fe_2O_3@CNTs characterization

The morphological and structural details of the samples were obtained using field emission scanning electron microscopy (SEM) (JEOL JSM-7001F, operated at 20 kV, JEOL Ltd, Tokyo, Japan) and transmission electron microscopy (TEM) (Hitachi H-800 MT, Hitachi Ltd, Tokyo, Japan). The carbon nanocomposites were transferred to the TEM grid by scratching off from the substrates to a pure ethanol solution, dispersed in an ultrasonic bath for 1 hour and a few drops of the solution was allowed to dry on a TEM grid.

The surface chemical composition was studied by X-ray photoelectron spectroscopy (XPS) carried out with a PHI 5500 Multitechnique System (Physical Electronics, Germany) equipped with a monochromatic X-ray source (aluminum Kα line of 1486.6 eV energy and 350 W), placed perpendicular to the analyzer axis and calibrated using the $3d_{5/2}$ line of Ag with a full width at half maximum (FWHM) of 0.8 eV. The analyzed area was a circle of 0.8 mm diameter, and the selected resolution for the spectra was 187.5 eV pass energy and 0.8 eV per step for the general spectra and 11.75 eV pass energy and 0.05 eV per step for the core level spectra. All measurements were made in an ultrahigh vacuum (UHV) chamber with pressure between 5×10^9 and 2×10^8 Torr.

The phase and crystallinity of the iron oxide layer were explored on reference samples by means of Grazing Incidence X-ray Diffraction (GIXRD). Coating thickness analysis was investigated by X-ray reflectivity (XRR). Both studies were performed using a Bruker-AXS model A25 D8 Discover diffractometer (Cu Kα radiation source), revealing that the structure of the as-deposited iron-oxide coating is a pure hematite phase (α-Fe_2O_3), see ESI Fig. S3.†

The electrochemical properties of the samples were analyzed using a potentiostat/galvanostat (AutoLab, PGSTAT30, Eco Chemie B.V., Utrecht, The Netherlands) and a typical three-electrode cell. Different nanocomposite samples were used as the working electrode in 1 M Na_2SO_4 solution. A Pt-ring electrode and an Ag/AgCl electrode (3 M KCl internal solution) served as the counter and reference electrode, respectively. The electrochemical behavior of the samples was investigated using cyclic voltammetry (CV) and electrochemical impedance spectroscopy (EIS). All experiments were carried out at room temperature and the geometrical area of the working electrode was set to a constant value of 0.57 cm^2. The voltage window during CV was −0.7 to 0.3 V *vs.* Ag/AgCl at scan rates between 10 and 150 mV s^{-1}. The EIS analysis was performed by applying an alternating voltage of 10 mV amplitude to the samples and recording the response at frequencies between 1 Hz and 100 kHz in logarithmic spacing.

4. Conclusions

In this work we have prepared Fe_2O_3@CNTs coaxial heterostructures in which the oxide scaffold is grown by ALD. We have investigated the effect of nanotube surface functionalization through different plasma treatments (N_2 and H_2O

plasma) on the deposition of the iron oxide coating and on the electrochemical properties. By using ozone as an oxidant source in the ALD deposition, iron oxide coating can be achieved regardless of the surface treatment. Nonetheless, untreated CNTs result in less homogeneous coatings. The iron oxide coating increases the areal capacitance although too thick coating (30 nm) reduces the active area and the electrochemical performance. We have identified that Fe_2O_3@wpCNTs composites show optimum values of leakage resistance, double layer and mass capacitances. Therefore, the H_2O plasma treatment promotes the best anchoring sites for conformal ALD iron oxide deposition and excellent contact between the oxide coating and the CNTs, by effectively removing amorphous C, for the electrochemical response.

Conflicts of interest

There are no conflicts to declare.

Acknowledgements

References

1 J. I. Hur, L. C. Smith and B. Dunn, *Joule*, 2018, **2**, 1187–1201.
2 C. Lethien, J. Le Bideau and T. Brousse, *Energy Environ. Sci.*, 2019, **12**, 96–115.
3 L. Liu, H. Zhao and Y. Lei, *InfoMat*, 2019, **1**, 74–84.
4 P. G. Bruce, B. Scrosati and J.-M. Tarascon, *Angew. Chem., Int. Ed.*, 2008, **47**, 2930–2946.
5 S. Najib and E. Erdem, *Nanoscale Adv.*, 2019, **1**, 2817–2827.
6 P. Dulyaseree, V. Yordsri and W. Wongwiriyapan, *Jpn. J. Appl. Phys.*, 2016, **55**, 02BD05.
7 S. Hussain, R. Amade, E. Jover and E. Bertran, *Nanotechnology*, 2012, **23**, 385604.
8 S. Hussain, R. Amade, E. Jover and E. Bertran, *J. Mater. Sci.*, 2013, **48**, 7620–7628.
9 M. R. Lukatskaya, B. Dunn and Y. Gogotsi, *Nat. Commun.*, 2016, **7**, 12647.
10 S. Yang, X. Feng and K. Müllen, *Adv. Mater.*, 2011, **23**, 3575–3579.
11 Y.-S. Kim, H.-J. Ahn, S. H. Nam, S. H. Lee, H.-S. Shim and W. B. Kim, *Appl. Phys. Lett.*, 2008, **93**, 103104.
12 X. Xiao, Z. Peng, C. Chen, C. Zhang, M. Beidaghi, Z. Yang, N. Wu, Y. Huang, L. Miao, Y. Gogotsi and J. Zhou, *Nano Energy*, 2014, **9**, 355–363.
13 A. L. M. Reddy, M. M. Shaijumon, S. R. Gowda and P. M. Ajayan, *Nano Lett.*, 2009, **9**, 1002–1006.
14 M. B. Sassin, A. N. Mansour, K. A. Pettigrew, D. R. Rolison and J. W. Long, *ACS Nano*, 2010, **4**, 4505–4514.
15 X. Lu, Y. Zeng, M. Yu, T. Zhai, C. Liang, S. Xie, M. Balogun and Y. Tong, *Adv. Mater.*, 2014, **26**, 3148–3155.
16 Q. X. Low and G. W. Ho, *Nano Energy*, 2014, **5**, 28–35.
17 B. Joshi, E. Samuel, H. S. Jo, Y.-I. Kim, S. Park, M. T. Swihart, W. Y. Yoon and S. S. Yoon, *Electrochim. Acta*, 2017, **253**, 479–488.
18 W. Shi, J. Zhu, D. H. Sim, Y. Y. Tay, Z. Lu, X. Zhang, Y. Sharma, M. Srinivasan, H. Zhang, H. H. Hng and Q. Yan, *J. Mater. Chem.*, 2011, **21**, 3422–3427.
19 Q. Qu, S. Yang and X. Feng, *Adv. Mater.*, 2011, **23**, 5574–5580.
20 X.-C. Dong, H. Xu, X.-W. Wang, Y.-X. Huang, M. B. Chan-Park, H. Zhang, L.-H. Wang, W. Huang and P. Chen, *ACS Nano*, 2012, **6**, 3206–3213.
21 S. Yang, X. Feng, S. Ivanovici and K. Müllen, *Angew. Chem., Int. Ed.*, 2010, **49**, 8408–8411.
22 T. M. Dinh, A. Achour, S. Vizireanu, G. Dinescu, L. Nistor, K. Armstrong, D. Guay and D. Pech, *Nano Energy*, 2014, **10**, 288–294.
23 X. Wang, Y. Yin, C. Hao and Z. You, *Carbon*, 2015, **82**, 436–445.
24 J. Li, M. Zhu, Z. An, Z. Wang, M. Toda and T. Ono, *J. Power Sources*, 2018, **401**, 204–212.
25 Z. Wang and C.-J. Liu, *Nano Energy*, 2015, **11**, 277–293.
26 C. Guan, J. Liu, Y. Wang, L. Mao, Z. Fan, Z. Shen, H. Zhang and J. Wang, *ACS Nano*, 2015, **9**, 5198–5207.
27 J. W. Elam, N. P. Dasgupta and F. B. Prinz, *MRS Bull.*, 2011, **36**, 899–906.
28 M. Coll and M. Napari, *APL Mater.*, 2019, **7**, 110901.
29 G.-D. Zhan, X. Du, D. M. King, L. F. Hakim, X. Liang, J. A. McCormick and A. W. Weimer, *J. Am. Ceram. Soc.*, 2008, **91**, 831–835.
30 D. B. Farmer and R. G. Gordon, *Nano Lett.*, 2006, **6**, 699–703.
31 N. Kemnade, C. J. Shearer, D. J. Dieterle, A. S. Cherevan, P. Gebhardt, G. Wilde and D. Eder, *Nanoscale*, 2015, **7**, 3028–3034.
32 X. Meng, M. Ionescu, M. N. Banis, Y. Zhong, H. Liu, Y. Zhang, S. Sun, R. Li and X. Sun, *J. Nanopart. Res.*, 2010, **13**, 1207–1218.
33 L. Acauan, A. C. Dias, M. B. Pereira, F. Horowitz and C. P. Bergmann, *ACS Appl. Mater. Interfaces*, 2016, **8**, 16444–16450.
34 A. P. Grosvenor, B. A. Kobe, M. C. Biesinger and N. S. McIntyre, *Surf. Interface Anal.*, 2004, **36**, 1564–1574.

35 S. Kim, J. Kim, J. Lim, H. Lee, Y. Jun and D. Kim, *J. Mater. Chem. C*, 2014, **2**, 6985–6990.

36 C. Chen, B. Liang, A. Ogino, X. Wang and M. Nagatsu, *J. Phys. Chem. C*, 2009, **113**, 7659–7665.

37 F. Morales-Lara, M. J. Pérez-Mendoza, D. Altmajer-Vaz, M. García-Román, M. Melguizo, F. J. López-Garzón and M. Domingo-García, *J. Phys. Chem. C*, 2013, **117**, 11647–11655.

38 S. Hussain, R. Amade, E. Jover and E. Bertran, *J. Cluster Sci.*, 2015, **26**, 315–336.

39 S. Hussain, R. Amade, H. Moreno and E. Bertran, *Diamond Relat. Mater.*, 2014, **49**, 55–61.

40 M. Li and H. He, *Vacuum*, 2017, **143**, 371–379.

41 B. E. Conway, *Electrochemical Supercapacitors: Scientific Fundamentals and Technological Applications*, Kluwer Academica Plenum Publishers, New York, NY, USA, 1999.

42 Z. Bo, Z. Wen, H. Kim, G. Lu, K. Yu and J. Chen, *Carbon*, 2012, **50**, 4379–4387.

43 S. Hussain, R. Amade and E. Bertran, *Mater. Chem. Phys.*, 2014, **148**, 914–922.

44 C. Masarapu, H. F. Zeng, K. H. Hung and B. Wei, *ACS Nano*, 2009, **3**, 2199–2206.

45 O. Pitkänen, T. Järvinen, H. Cheng, G. S. Lorite, A. Dombovari, L. Rieppo, S. Talapatra, H. M. Duong, G. Tóth, K. L. Juhász, Z. Kónya, A. Kukovecz, P. M. Ajayan, R. Vajtai and K. Kordás, *Sci. Rep.*, 2017, **7**, 16594.

46 N. Ouldhamadouche, A. Achour, R. Lucio-Porto, M. Islam, S. Solaymani, A. Arman, A. Ahmadpourian, H. Achour, L. Le Brizoual, M. A. Djouadi and T. Brousse, *J. Mater. Sci. Technol.*, 2018, **34**, 976–982.

47 X. Cai, R. V. Hansen, L. Zhang, B. Li, C. K. Poh, S. H. Lim, L. Chen, J. Yang, L. Lai, J. Lin and Z. Shen, *J. Mater. Chem. A*, 2015, **3**, 22043–22052.

48 X. Cheng, X. Gui, Z. Lin, Y. Zheng, M. Liu, R. Zhan, Y. Zhu and Z. Tang, *J. Mater. Chem. A*, 2015, **3**, 20927–20934.

49 Z. Ma, X. Huang, S. Dou, J. Wu and S. Wang, *J. Phys. Chem. C*, 2014, **118**, 17231–17239.

Supporting Information

Homogeneous Fe$_2$O$_3$ coatings on carbon nanotube structures for supercapacitors

Pengmei Yu,[a] Mariona Coll,[a]*Roger Amade,[b,c] Islam Alshaikh, [b,c]
Fernando Pantoja-Suárez, [b,c,d] Esther Pascual, [b,c] José Luís Andújar, [b,c]
and Enric Bertran Serra [b,c]

*[a] Institut de Ciència de Materials de Barcelona (ICMAB-CSIC), Campus UAB 08193 Bellaterra (Barcelona) Spain. Email: mcoll@icmab.es; [b] Departament de Física Aplicada, Universitat de Barcelona, Martí i Franquès 1, 08028 Barcelona, Spain; [c] Institute of Nanoscience and Nanotechnology (IN2UB), Universitat de Barcelona, Avda. Joan XXIII, s/n, 08028 Barcelona, Spain; [d]Departamento de Materiales, Facultad de Ingeniería Mecánica, Escuela Politécnica Nacional, Ladrón de Guevara, E11-253, Quito, Ecuador

1

1 TEM-EDX Elemental mapping

In Figure S1 we display TEM images of ALD-30 nm Fe_2O_3@wpCNTs and ALD-6 nm Fe_2O_3@wpCNTs and their corresponding elemental mapping images and EDX sum spectra. The low amount of material in the 6 nm iron oxide-CNTs composite hinders the extraction of robust information from the elemental mapping. In contrast, the 30 nm composite show clear homogeneous iron oxide covering of the carbon nanotubes. From the EDX sum spectra it can be identified other elements such as Cu, Si, Ca and Cl that come from the TEM grid and sample manipulation during TEM sample preparation.
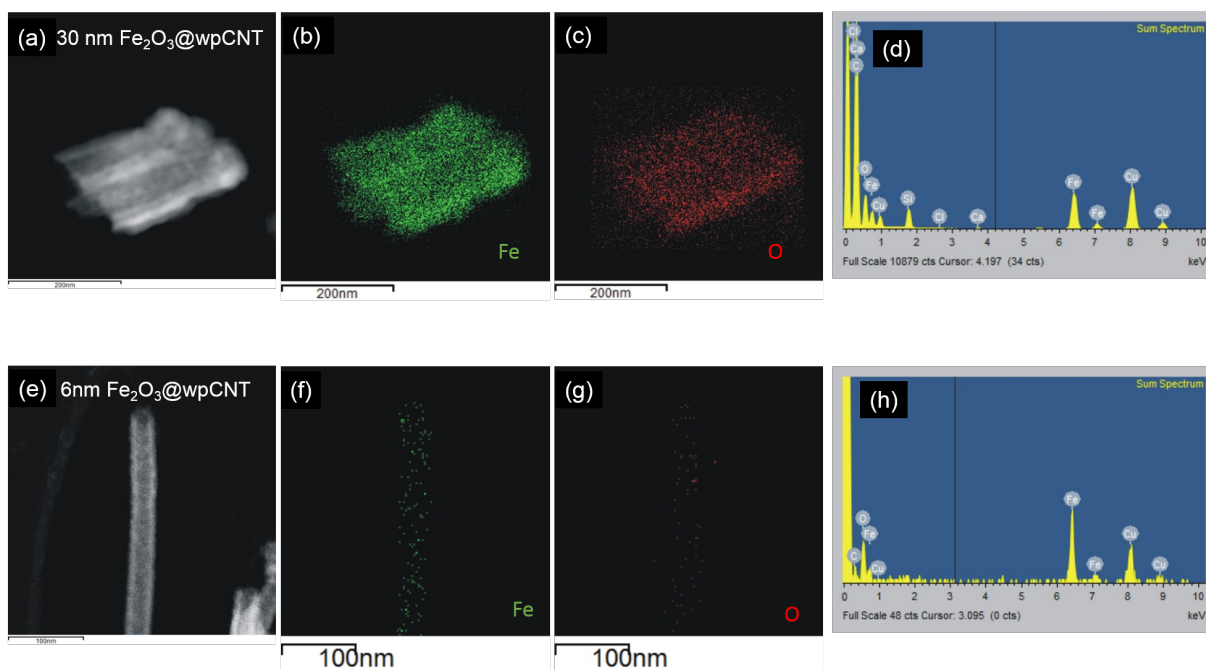

Figure S1: (a) TEM image of ALD-30 nm Fe_2O_3@wpCNTs, (b) elemental mapping of Fe Kα_1 signal, (c) elemental mapping of O Kα_1 signal, (d) EDX sum spectrum of the same region. (e) TEM image of ALD-6 nm Fe_2O_3@wpCNTs with the corresponding (f) elemental mapping of Fe Kα_1 signal and (g) elemental mapping of O Kα_1 signal. (h) EDX sum spectrum performed in (e).

2

2 XPS

The deconvolutions of high resolution XPS C 1s spectra of thinnest and continuous Fe$_2$O$_3$ films coated CNTs samples reveal various carbon environments in the surface: π-π interactions, C=O, C-O, sp^3 carbon and sp^2 carbon. See Figure S2. The areas of sp^3 carbon and sp^2 carbon in the deconvoluted spectra are tabulated in Table S1.
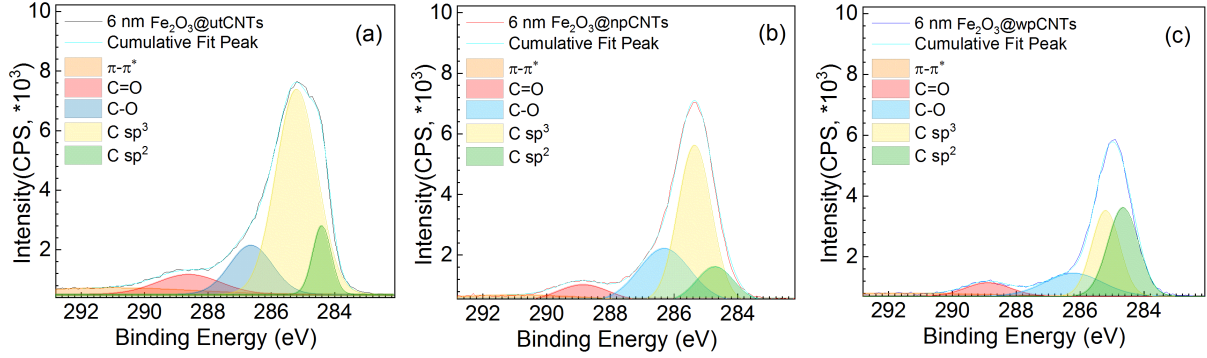

Figure S2: Deconvoluted XPS high resolution C 1s spectra of 6 nm Fe$_2$O$_3$@CNTs samples on (a) untreated CNTs, (b) nitrogen plasma CNTs, (c) water plasma CNTs.

Table S1: Relative area of sp^3 C and sp^2 C in the deconvoluted XPS C 1s spectra

Sample	sp^3 C (area)	sp^2 C (area)
6 nm Fe$_2$O$_3$@utCNTs	11210	1677
6 nm Fe$_2$O$_3$@npCNTs	6750	1650
6 nm Fe$_2$O$_3$@wpCNTs	3067	3500

3

3   GIXRD and XRR

GIXRD were carried out of the as-deposited iron oxide thin film on reference (100) silicon substrate. As is illustrated in Figure S3(a), the well-defined peaks in the diffraction curve can be readily indexed as pure phase α-Fe$_2$O$_3$ without any other impurities (Pdf card: 00-033-0664).

In Figure S3(b) we show a typical X-ray reflectivity curve of ALD-Fe$_2$O$_3$ coated reference Si. By fitting the experimental data, the thickness of ALD-Fe$_2$O$_3$ thin films is determined to be ~ 22.5 nm.
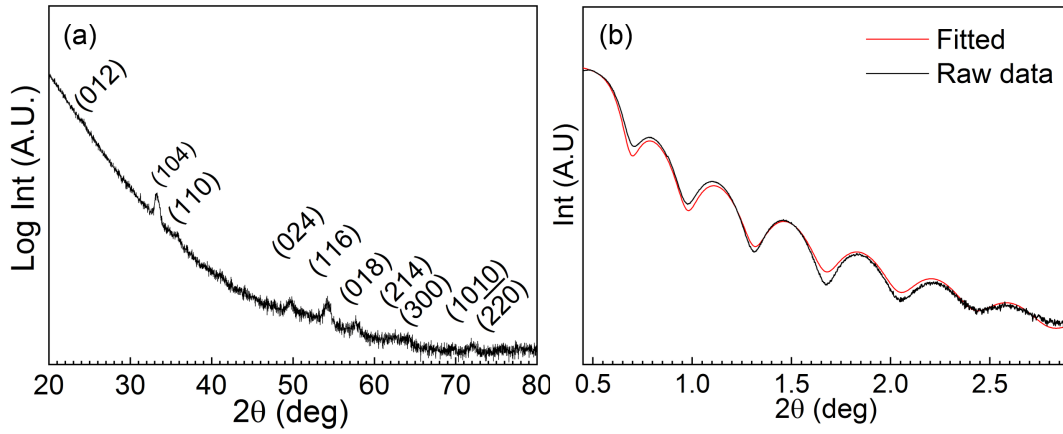

Figure S3: (a) GIXRD spectrum and (b) XRR raw data and fitted curves of ALD α-Fe$_2$O$_3$ thin films deposited at 250 °C on Si (100).

4

III   Atomic scale growth of GdFeO$_3$ perovskite thin films from a single-source heterobimetallic precursor

Atomic scale growth of GdFeO$_3$ perovskite thin films

Christoph Bohr[a,1], Pengmei Yu[b,1], Mateusz Scigaj[b], Corinna Hegemann[a], Thomas Fischer[a], Mariona Coll[b,*], Sanjay Mathur[a,*]

[a] *Institute of Inorganic Chemistry, University of Cologne, Greinstraße 6, D-50939 Cologne, Germany*
[b] *Institut de Ciencia de Materials de Barcelona, ICMAB-CSIC, Campus UAB, 08193 Barcelona, Spain*

A B S T R A C T

Thin films of multiferroic gadolinium orthoferrite (GdFeO$_3$) are of significant interest due to intrinsic coupling of magnetic and ferroelectric order in their monolithic bimetallic structures relevant for potential applications in magneto-optical data storage devices. Formation of this composition in stoichiometric pure form is challenging due to facile formation of the thermodynamically preferred garnet phase (Gd$_3$Fe$_5$O$_{12}$) that mostly coexists as a minor phase in gadolinium orthoferrite films. We report herein the selective epitaxial growth of GdFeO$_3$ films by atomic layer deposition of a single bimetallic precursor [GdFe(O^{t}Bu)$_6$(C$_5$H$_5$N)$_2$] containing Gd:Fe in the required stoichiometric ratio, and using ozone as co-reactant. Intact vaporisation of [GdFe(O^{t}Bu)$_6$(C$_5$H$_5$N)$_2$] in the gas phase and its clean conversion into the complex oxide phase as validated by mass spectral studies and thermogravimetry demonstrate the potential of the Gd-Fe compound as an efficient single-source precursor. Epitaxial growth of GdFeO$_3$ on SrTiO$_3$ substrates was confirmed by X-ray diffraction analysis, whereas the presence of Fe^{3+} and Gd^{3+} without any traces of N species from the ligands was verified by X-ray photoelectron spectroscopy. Magnetic properties of the resulting perovskite films studied by superconducting quantum interference device measurements revealed the superposition of two independent magnetic contributions due to paramagnetic (Gd^{3+}) and ferromagnetic (Fe^{3+}) sublattices in GdFeO$_3$.

1. Introduction

Orthoferrites (MFeO$_3$; M = Ln, Sc, Y) have been extensively studied because of their wide variety of potential applications including magneto-optical devices [1], photocatalysis [2–4], gas sensing [5,6] and contrast agent in clinical magnetic resonance imaging [7]. It is known that the stability of the orthoferrite phase depends on the radius of *Ln* ions. For compositions where the lanthanides (Ln) are larger than terbium (Tb), the garnet structure becomes thermodynamically more stable, whereas smaller ionic lanthanide radius favors the formation of LnFe$_2$O$_4$ spinel phases [8]. In particular, the synthesis of multiferroic GdFeO$_3$ (GFO) [9], (Gd^{3+} = 0.94 Å, similar to Tb^{3+} = 0.92 Å), results in the coexistence of garnet (Gd$_3$Fe$_5$O$_{12}$) or magnetite (Fe$_3$O$_4$) secondary phases [10,11]. Thus, a phase-selective formation for GFO remains a synthetic challenge and requires new procedures.

Many of the applications mentioned above demand the growth of homogeneous thin films on planar and high aspect ratio surfaces. Atomic layer deposition (ALD) has become a fast-growing thin film engineering technique in the semiconductor industry and is rapidly

expanding to newer and wider applications [12–15], owing to its unique capacity to nanoscale control of thickness and composition along with great effectiveness to homogeneously coat complex geometries and high aspect ratio structures. The stabilization of metastable phases by thin film epitaxial growth using ALD has already been demonstrated [16–23]. So far, ALD has been mostly used for binary compositions, where two complementary precursor chemistries are sequentially used in self-limiting surface reactions to build the binary lattice [24,25]. However, growing ternary or more complex compounds is far more challenging, due to the lack of compatible ALD precursors [22,23,26,27] and less known reaction pathways [28].

In view of the above, the development of new precursor systems and cautious evaluation of the metal-ligand chemistry appears to be of great value to control the film stoichiometry for complex compositions [24,29–31]. An attractive approach to simplify the surface reactions that would enable formation of ternary compounds is the use of single-source heterometallic precursors. Intrinsic advantages of bimetallic compounds include simplified precursor delivery system, lowered deposition temperatures, retained stoichiometry and pre-defined chemical

---

compatibility between the target film and selected precursor [32]. The lack of adequate volatility and possible premature fragmentation can however limit the application of this concept in the ALD process [24,29,31]. Moreover, the lack of mechanistic models for the decomposition of bimetallic precursors in an ALD process makes the whole process even more challenging.

In this work, we report on a volatile single-source Gd-Fe bimetallic precursor [GdFe(O^{t}Bu)$_6$(C$_5$H$_5$N)$_2$] and their subsequent deposition to GdFeO$_3$ thin films by ALD. We demonstrate the stabilization of epitaxially grown GdFeO$_3$ thin films on SrTiO$_3$ substrates exhibiting atomically smooth surface morphology upon high temperature thermal treatment. The deposition of the ternary oxide from this heteronuclear precursor reinforces our strategy to develop stoichiometric complex materials with atomic control that can potentially lead to new and improved properties.

2. Experimental section

2.1. Precursor synthesis

2.1.1. General remarks

The synthesis of alkoxide and amide precursors was performed using modified Stock techniques. The hydrocarbon solvents were dried using standard procedures [33] and stored over sodium wire. [Fe(O^{t}Bu)$_3$]$_2$ [34] and [Gd{N(SiMe$_3$)$_2$}$_3$] [35] was synthesized by literature known procedures. Data collection for X-ray structure elucidation was performed on a *Stoe IPDS 2T* diffractometer using graphite monochromated Mo Kα radiation (0.71071 Å). The programs used in this work are STOE's X-Area [36] and the WINGX suite of programs [37], including SIR-92 [38], SHELX and SHELXTL [39] for structure solution and refinement. H atoms were calculated geometrically and a riding model was applied during the refinement process. The supplementary crystallographic data for this paper (CCDC: 1912740) can be obtained free of charge from The Cambridge Crystallographic Data Centre via www.ccdc.cam.ac.uk/data_request/cif. Elemental analysis was carried out on a HEKAtech *CHNS* Euro EA 3000 with helium as carrier gas. Deviations of the *CHNS* data from the calculated values can be attributed to the extraordinary sensitivity of the compound towards moisture and the weakly bound pyridine. Mass spectra were recorded on a *Finnigan* MAT 95 (Electron ionization, 20 eV).

2.1.2. Synthesis of [GdFe(O^{t}Bu)$_6$(C$_5$H$_5$N)$_2$]

A solution of 1.05 g (1.64 mmol) [Gd{N(SiMe$_3$)$_2$}$_3$], dissolved in 5 mL toluene and 1.5 mL pyridine was heated until the colorless solution turned red. Mixing with a solution of 0.45 g (0.82 mmol) [Fe(O^{t}Bu)$_3$]$_2$ in 5 mL toluene and 1 mL pyridine lead to a black solution. The molar ratio of 2:1 was chosen due to the dimeric structure of the iron compound. After addition of 2.5 mL *tert*-butanol the reaction mixture was stirred for 1.5 h at 70 °C. All volatiles were removed under reduced pressure and the crude product was purified by recrystallization from a toluene solution. Yield: Quantitative. Electron ionization mass spectrometry (20 eV, 132 °C): *m/z* (intensity) 956 (10 %) 854 (74 %), 724 (17 %), 637 (12 %), 579 [M]$^+$ (100 %), 477 (15 %), 79 (89 %), 59 (48 %), 52 (20 %). Anal. Calcd C$_{34}$H$_{64}$FeGdN$_2$O$_6$: C 50.42, H 7.96, N 3.46. Found: C 47.03, H 8.09, N 2.44.

2.2. GdFeO$_3$ thin film growth

GFO films were prepared in a Cambridge Nanotech Savannah 100 flow-type ALD reactor. After optimization of the precursor sublimation temperature, the complex [GdFe(O^{t}Bu)$_6$(C$_5$H$_5$N)$_2$] was heated up to 150–170 °C for evaporation. Pulse/purge lengths for [GdFe(O^{t}Bu)$_6$(C$_5$H$_5$N)$_2$] and ozone were alternating pulsed into the reaction chamber as 0.2-1.0 s/1.5–3.0 s, respectively. A nitrogen gas flow of 40 sccm was used as carrier gas and for purging excess precursors and by-products. The substrate temperature was kept constant at 200 °C

throughout the deposition process. 5 mm x 5 mm SrTiO$_3$ (STO) were used as a growth substrate and 1 cm x 1 cm Si(100) pieces were placed next to STO as reference substrates to perform SEM-EDX analysis. Before film growth, substrate surface was activated by 100 ozone pulses. Film thickness was tuned by modifying the number of cycles from 20 nm to 35 nm. The as-deposited films were further annealed for 30 min in oxygen atmosphere at 800 °C in a tubular furnace.

2.3. GdFeO$_3$ thin film characterization

Phase purity and film orientation were investigated from X-ray θ-2θ scans performed on a Bruker D8 Discover A25 diffractometer, with Cu Kα radiation. The film texture was further studied by a D8 Advance diffractometer with a General Area Detector Diffraction System with Cu Kα radiation, Bruker AXS, Inc. Energy Disperse X-ray Spectroscopy (EDX) and Scanning Electron Microscopy (SEM) FEI Quanta 200 FEG were used to study surface morphology and qualitative chemical composition. The operating voltage was 15 kV at 4×10^{-4} Pa. The acquisition time for the EDX analysis was set to 200 s. Surface chemical composition was explored by a SPECS PHOIBOS 150 hemispherical X-ray photoelectron spectroscopy (XPS) analyzer with an Al Kα source (1486.6 eV) from SPECS GmbH, Berlin, Germany. The measurements were performed in a base pressure of 1×10^{-8} Pa with a pass energy of 10 eV, and step size for the high-resolution and survey spectra were of 0.05 eV 30 and 1 eV, respectively. Spectra were calibrated referring to the binding energy of C1s peak at 284.8 eV. An Asylum Research MFP-3D Atomic Force Microscope (AFM) was employed for obtaining topographic images of GdFeO$_3$ film. Film thickness was determined by fitting the X-ray reflectivity data from a SIEMENS D5000 diffractometer using ReMagX software [40]. Magnetic properties of the films, M(T) and M(H), were explored using a Quantum Design MPMS-XL magnetometer based on a superconducting quantum interference device detector. Magnetic measurements were performed along the [001] film direction (in plane) and the diamagnetic contribution of the SrTiO$_3$ substrate was subtracted for all curves.

3. Results and discussion

3.1. Synthesis of heterobimetallic single-source precursor

The heteroleptic single source precursor [GdFe(O^{t}Bu)$_6$(C$_5$H$_5$N)$_2$] has been synthesized by using [Fe(O^{t}Bu)$_3$]$_2$ and [Gd{N(SiMe$_3$)$_2$}$_3$] in a molar ratio of 1:2. Both precursors have been dissolved in toluene and small amounts of pyridine. After mixing both solutions, *tert*-butanol has been added to result in the desired product. Iron and gadolinium ions prefer different coordination spheres when exposed to steric demanding ligands (Fe^{3+} = tetrahedral, Gd^{3+} = octahedral) due to different ionic radii (Fe^{3+} = 0.49 Å, Gd^{3+} = 0.94 Å) [41], therefore, special synthetic conditions are required to maintain both metal centers in a monomeric, heterobimetallic structure. In order to stabilize the octahedral coordination sphere of gadolinium and prevent oligomerization reactions, pyridine as a neutral ligand was added. Yellow/brownish single crystals were accessible and their analysis via X-ray diffractometry resulted in the presented molecular structure, see Fig. 1, Table 1. The polyhedron representation of the triclinic compound with a P 1̄ space group exhibits an edge sharing connected distorted octahedron around gadolinium and a distorted tetrahedron around iron. The nitrogen atoms are in a *trans* orientation and the bond length between gadolinium and nitrogen (Gd-N 2.551 Å) is longer than between gadolinium and oxygen (Gd-O$_{\mu2}$ 2.428, Gd-O$_{terminal}$ 2.109), hinting to weakly bonded pyridine. The observed structure is very similar to literature known bimetallic iron/cerium compounds like [FeCe(O^{t}Bu)$_7$(C$_5$H$_5$N)] [42] and isotypic to [FeEr(O^{t}Bu)$_6$(C$_5$H$_5$N)$_2$] [43]. Both, cerium and erbium have similar large ionic radii compared to gadolinium (Ce^{4+} = 0.87 Å, Er^{3+} = 0.89 Å) [41]. The distance between gadolinium and the pyridine fragments is similar to the erbium compound and shorter than for
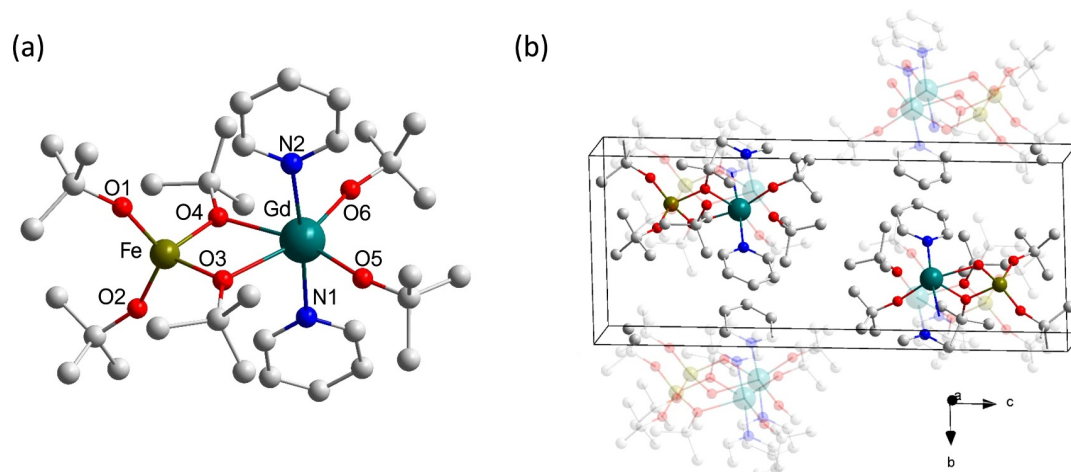
Fig. 1. (a) Molecular structure of $[GdFe(O^tBu)_6(C_5H_5N)_2]$, hydrogen atoms are omitted for clarity. Averaged selected bond lengths in [Å]: Gd – $O_{terminal}$ 2.109, Gd – $O_{\mu2}$ 2.428, Gd – N 2.551, Fe – $O_{terminal}$ 1.783, Fe – $O_{\mu2}$ 1.911. (b) Unit cell of the crystal structure. Two molecules are inside the unit cell, for a better understanding, every contributing molecule is shown but each atom not corresponding to the unit cell is transparent.

Table 1
Details on crystal and structure refinement of $[GdFe(O^tBu)_6(C_5H_5N)_2]$.

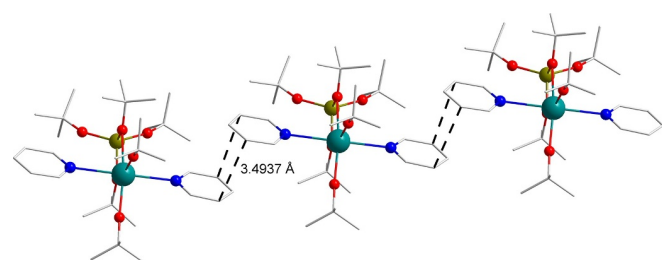| Molecular formula	$C_{34}H_{64}FeGdN_2O_6$
Molecular Mass [g/mol]	809.97
Temperature of Measurement [K]	170(2)
Wavelength [Å]	0.71073 (Mo K$_\alpha$)
Crystal System	Triclinic
Space Group	P $\bar{1}$
Lattice Parameters	a = 9.4659(5) Å α = 86.285(4)°
	b = 10.2824(5) Å β = 82.418(4)°
	c = 23.0723(12) Å γ = 68.374(4)°
Cell Volume [Å^3]	2069.03(19)
Formula Unit	2
Correction of Absorption	numerical
F(000)	840
Measurement Range	1.781 < h < 26.804
	−11 < h < 11
	−13 < k < 13
	−29 < l < 29
Number of Reflexes	23364
Observed Reflexes	8719
Goodness of Fit	1.103
R_1 [$I_0 > 2\sigma(I)$]; all Data	R_1 = 0.0408, R_1 = 0.0560
wR_2 [$I_0 > 2\sigma(I)$]; all Data	wR_2 = 0.0982, wR_2 = 0.1220
$\Delta\rho_{max}$, $\Delta\rho_{min}$	1.186, −1.771 e Å^{-3}

Table 2
Comparison of selected bond length and angles between $[GdFe(O^tBu)_6(C_5H_5N)_2]$ and literature known $[FeEr(O^tBu)_6(C_5H_5N)_2]$ and $[FeCe(O^tBu)_7(C_5H_5N)]$ [42,43].

	[GdFe $(O^tBu)_6(C_5H_5N)_2$]	[FeEr $(O^tBu)_6(C_5H_5N)_2$]	[FeCe $(O^tBu)_7(C_5H_5N)$]
Ln-O$_{term.}$	2.109 Å	2.047 Å	2.094 Å
Ln-O$_{\mu2}$	2.428 Å	2.366 Å	2.442 Å
Fe-O$_{term.}$	1.783 Å	1.771 Å	1.782 Å
Fe-O$_{\mu2}$	1.911 Å	1.914 Å	1.943 Å
Ln-N	2.551 Å	2.500 Å	2.700 Å
Ln-Fe	3.428 Å	3.401 Å	3.4739 Å
O$_{\mu2}$-Ln-O$_{\mu2}$	65.51°	65.94°	65.1°
O$_{\mu2}$-Fe-O$_{\mu2}$	86.87°	84.52°	85.7°
N-Gd-N	175.97°	174.08°	-

Fig. 2. Intermolecular, antiparallel π-stacking in the crystal structure of $[GdFe(OtBu)_6(C_5H_5N)_2]$.
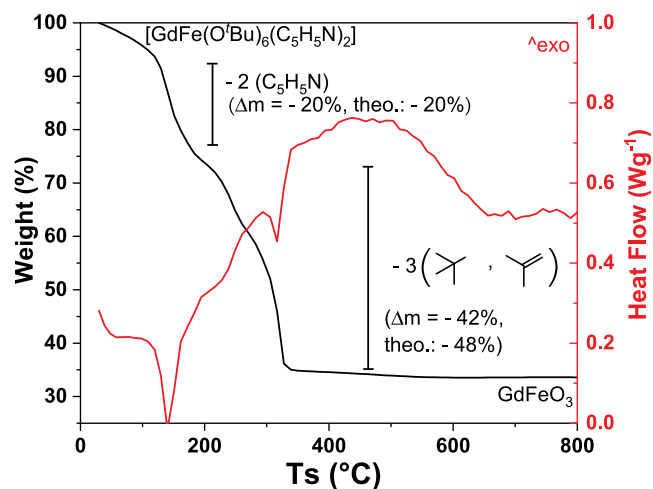
Fig. 3. Thermogravimetric analysis/ Differential scanning calorimetry diagram for $[GdFe(O^tBu)_6(C_5H_5N)_2]$. The compound undergoes a steady degradation towards GdFeO$_3$ (the remaining mass after measurement matches GdFeO$_3$). The missing 6 % mass loss of the second step can be attributed to the initial mass loss at low temperatures.

the cerium one, which can be attributed to the number of bound pyridine entities. In the crystal structure, the pyridine fragments arrange in an antiparallel π-stacking fashion with a distance between the aromatic rings of 3.494 Å (see Fig. 2). This feature is also known for the $[FeEr(O^tBu)_6(C_5H_5N)_2]$ complex [43]. A comparison between selected bond lengths and angles is given in Table 2.

The presented structure is in good agreement with the elemental

analysis, thermogravimetry (Fig. 3) and mass spectrometry (Fig. 4). The compound exhibited a steady degradation process during heating with two clear endothermic transitions at 140 °C and 315 °C. Pyridine fragments evidently split from the molecule at the heating temperature
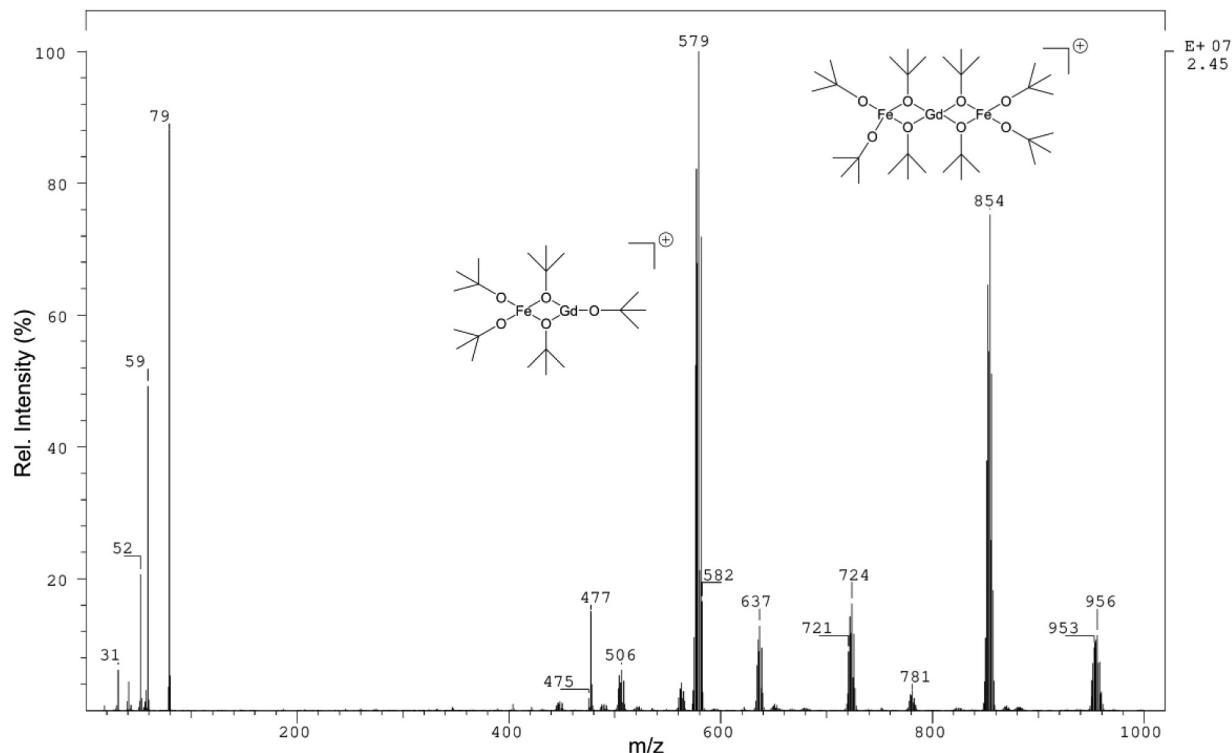
Fig. 4. Electron ionization mass spectra of $[GdFe(OtBu)_6(C_5H_5N)_2]$, ionized at U = 20 eV.

of 130 °C. The remaining mass at high temperatures was attributed to $GdFeO_3$ that based on the calculated weight loss (m: 33.4 %, theo.: 32.2 %) and no further events in the TG profile indicated the formation of solid of definite composition. The mass spectra (Electron ionization, 20 eV) confirmed the volatility and stability of the bimetallic component in the gas phase (Fig. 4). Even without showing the molecular ion peak $[M]^+$, the signal with the highest intensity corresponded to bimetallic fragment $[GdFe(O^tBu)_5]^+$ (579 m/z). The ionization energy during the measurement further induces oligomerization reactions apparently leading to fragments with higher molecular mass that were identified as $[Gd_2Fe_2O_2(O^tBu)_6(O^tBu-Me)]^+$ (956 m/z), $[GdFe_2(O^tBu)_8]^+$ (854 m/z), $[GdFe_2O(O^tBu)_6]^+$ (724 m/z) and $[Fe_2(O^tBu)_5]^+$ (477 m/z).

3.2. Thin film growth by ALD

GFO was deposited on $SrTiO_3$ (STO) at 200 °C by ALD and exposed to 800 °C to crystallize the orthoferrite structure with a film thickness of 20 nm. The film growth per deposition cycle was investigated at 200 °C showed a linear dependence with a growth rate of approximately 0.19 Å per cycle (see Fig. 5). The reported growth rates of ALD oxide thin films grown from single-source heterobimetallic precursors are broad. For instance, the ALD deposited rare earth aluminates prepared from Ln-Al (Ln=La, Pr, Nd) compounds showed growth per cycles (GPC) one order of magnitude higher (0.1-0.5 nm/cycle) than our current ALD $GdFeO_3$ study [44,45]. On the other hand, ALD $SrTa_2O_6$ thin film from a nitrogen-donor-functionalized Sr-Ta alkoxide exhibited GPC around 0.2–0.3 Å per cycle, similar to our work herein [46].

Fig. 6(a) compares the X-ray diffraction θ-2θ scans of bare strontium titanate substrates, STO (black), as-deposited GFO film (green) and post annealed GFO at 800 °C (blue). The as-deposited film showed no extra features except peaks corresponding to STO (001) and k_β, suggesting an amorphous deposited film. After post annealing, a shoulder emerged next to the STO peak at 2θ ~ 47°. A closer look at the GFO phase formation by performing a 2D θ-2θ scan (Fig. 6(b)), allowed the identification of two extra poles at 2θ = 26° (χ = +26° and χ = -27°). The
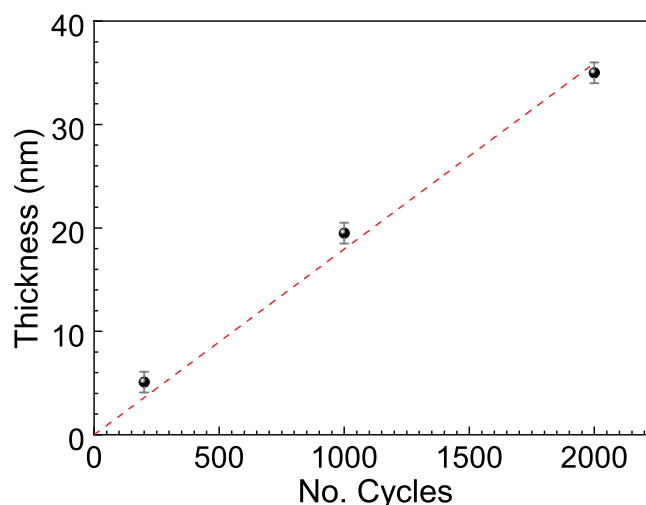

Fig. 5. Variation of $GdFeO_3$ film thickness with number of ALD cycles using Gd-Fe heterobimetallic precursor at a deposition temperature of 200 °C. The data was fitted linearly with the intercept forced to 0.

GFO has a slightly distorted ABO_3 perovskite structure with $a = 5.346$ Å, $b = 5.616$ Å, $c = 7.668$ Å whereas the dimensions of cubic $SrTiO_3$ are $a = 3.905$ Å. Based on this, it is very likely that orthorhombic GFO grows oriented (110)//[001] on STO. No traces of Fe_3O_4 and $Gd_3Fe_5O_{12}$ were observed [1,7,47].

Chemical composition of the as-deposited film was analyzed by EDX (Fig. 7) on GFO / Si (100) reference samples that confirmed the presence of Gd, Fe, Si and O with nearly an equivalent cation ratio (Fe: Gd = 0.9).

The chemical states of GFO thin films on STO was further analyzed by XPS (Fig. 8). The survey spectrum indicated the presence of Gd, Fe, O, C, Sr and Ti, consistent with the $GdFeO_3$ / $SrTiO_3$ structure (Fig. 8a). The presence of C is majorly attributed to the ambient exposure of the
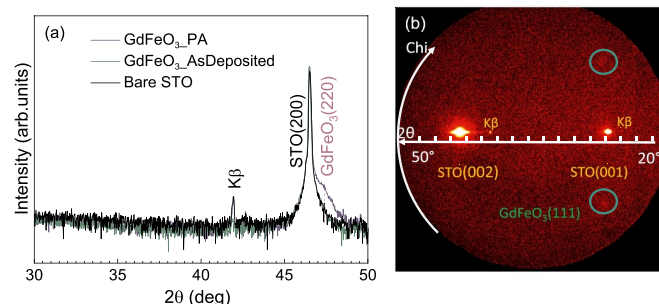
Fig. 6. (a) X-ray diffraction θ-2θ scan of ALD 20 nm thick GdFeO$_3$ films on SrTiO$_3$ (STO) after deposition and after post annealing (PA). (b) X-ray diffraction θ-2θ pattern of post-annealed 20 nm GdFeO$_3$ films on STO.
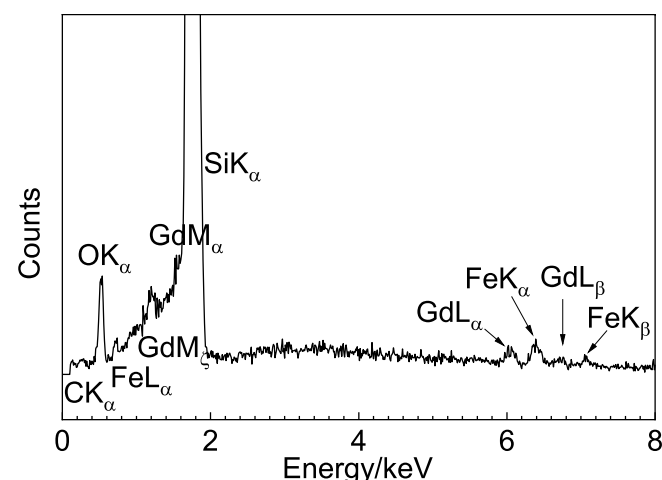

Fig. 9. (a) SEM image of ALD deposited 20 nm GdFeO$_3$ thin film on (100) Silicon; (b) AFM topographic image of post annealed 20 nm ALD GdFeO$_3$ thin film on (100) STO.

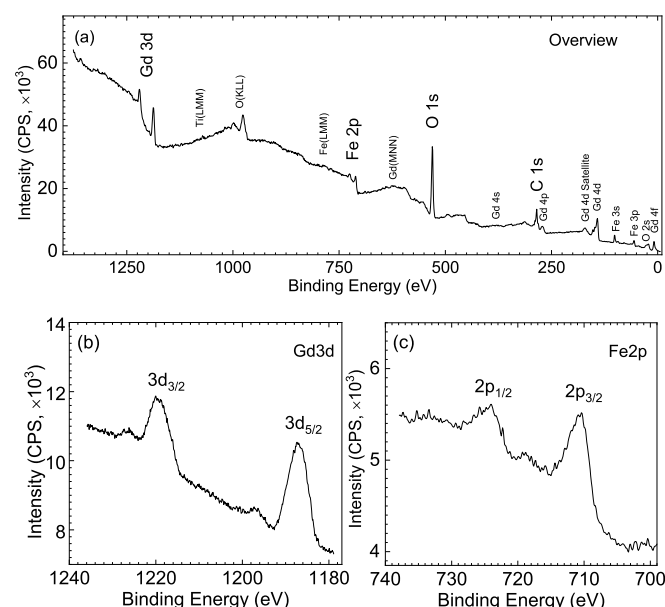**Fig. 7.** EDX spectrum of ALD deposited GdFeO$_3$ thin films on (100) Si.

Fig. 8. XPS spectrum of ALD deposited 20 nm GdFeO$_3$ thin films on (100) STO: (a) Survey spectrum; (b) high resolution Gd(3d) core level spectrum (c) high resolution Fe(2p) core level spectrum.

samples prior to the XPS analysis. No traces of nitrogen were spotted in the film (binding energy N1s = 398.1 eV), suggesting a complete decomposition of the pyridine ligands present on the heterobimetallic
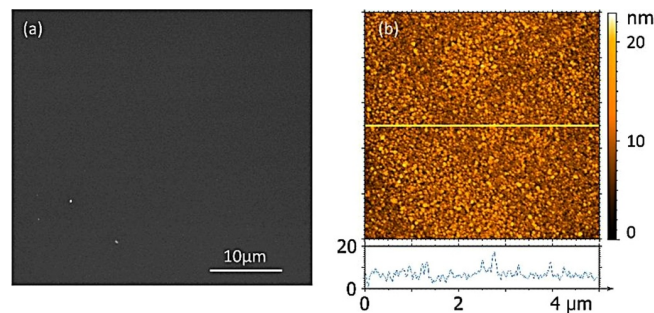
precursor. The Gd(3d) core level spectrum, Fig. 8(b), shows a spin-orbit doublet with binding energies at 1219.3 eV 3d$_{3/2}$ and 1187.3 eV 3d$_{5/2}$, being in good agreement with those reported in literature for GdFeO$_3$ and Gd$_2$O$_3$ [47,48]. Likewise, the Fe(2p) core level spectrum showed a peak at 724.1 eV 2p$_{1/2}$ and at 710.6 eV 2p$_{3/2}$. Moreover, the position of the satellite peak at 718.9 eV appearing 8.3 eV depicted in Fig. 8(c), above the 2p$_{1/2}$ peak which confirms the +3 oxidation state of iron [47,49–51].

The morphology of ALD grown GFO has been studied by SEM and AFM. The sample is homogeneous in a large area as shown in the SEM image in Fig. 9(a). A 5 × 5 μm AFM topographic image and a height profile (indicated by the yellow line) are shown in Fig. 9(b). The topographic image revealed a homogeneous distribution of small grains (~70 nm) with a root mean square roughness of 2 nm.

The temperature dependent magnetization measurements (5-300 K) of GFO thin film on STO under zero field-cooling (ZFC) and field-cooling (FC) at 0.5 Tesla are shown in Fig. 10(a). In this case, thicker films (35 nm) were investigated. Both curves overlap and show no magnetic transition for this temperature range [47,52]. While the magnetization decreases with increasing temperature up to 300 K, the χ^{-1} (T) (χ being the magnetic susceptibility) shows initially an upward curvature and then at ~100 K changes to slightly negative curvature (inset Fig. 10(a)). This dependence in χ^{-1} suggests a ferromagnetic contribution overlapped with the paramagnetic behavior. Fig. 10(b) illustrates the field dependent magnetization curve at 50 K. The net saturation magnetization at 7 Tesla is 82.89 kA/m and the coercive field is 0.0078 Tesla. These values slightly differ from previous studies on GFO nanoparticles [7,53] but resemble those of sol-gel thin films [47] and single crystals [52], showing the difference in magnetic properties depending on the size and crystallinity [54]. Bulk gadolinium orthoferrite is known to be antiferromagnetic with a Néel temperature of 678 K [55]. The magnetic properties of GFO can be understood by the superposition of two independent magnetic systems, Gd^{3+} (paramagnetic contribution) and Fe^{3+} (ferromagnetic contribution) sublattices [55]. Thus, the weak ferromagnetism identified in this
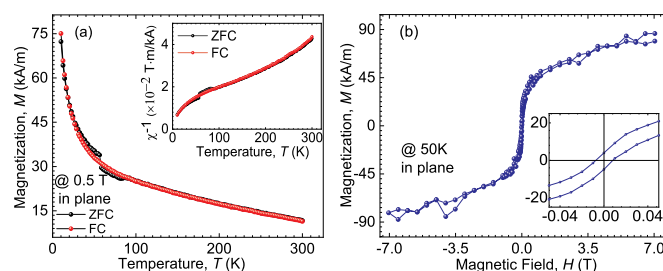

Fig. 10. (a) In-plane magnetization performance as a function of temperature for a 35 nm GdFeO$_3$ thin film. Inset shows the reverse susceptibility behavior versus temperature; (b) Magnetization behavior of 35 nm thick GdFeO$_3$ film as a function of magnetic field at 50 K. Inset shows a zoom-in at a lower field.

ALD fabricated $GdFeO_3$ system is tentatively attributed to slightly canted Fe^{3+} ions [52,56].

4. Conclusion

A volatile heteronuclear precursor $[GdFe(O^tBu)_6(C_5H_5N)_2]$ was demonstrated as an efficient single-source for the atomic layer deposition of ternary oxide $GdFeO_3$. The heterometallic framework is evidently maintained in the gas phase even after the thermolytic cleavage of the coordinated pyridine molecule that supports the formation of stoichiometric ternary oxide. The ALD with the mixed-metal compound on STO substrate with low lattice mismatch produced epitaxial films of $GdFeO_3$ that did not show the presence of impurities and minor phases like garnet $(Gd_3Fe_5O_{12})$, spinel $(GdFe_2O_4)$ or magnetite (Fe_3O_4) compositions that are generally formed in the synthesis of $GdFeO_3$ performed using two monometallic precursors. Advances in precursor design for ALD and epitaxial growth opens a plethora of opportunities to engineer coatings with multimetallic compositions at low temperature and to understand the reaction kinetics which can ultimately improve the capabilities for thin films engineering.

CRediT authorship contribution statement

Christoph Bohr: Conceptualization, Methodology, Investigation, Writing - original draft. **Pengmei Yu:** Investigation, Writing - original draft. **Mateusz Scigaj:** Investigation. **Corinna Hegemann:** Conceptualization, Writing - review & editing. **Thomas Fischer:** Writing - review & editing. **Mariona Coll:** Methodology, Writing - review & editing, Supervision. **Sanjay Mathur:** Conceptualization, Writing - review & editing, Supervision.

Declaration of Competing Interest

The authors declare that they have no known competing financial interests or personal relationships that could have appeared to influence the work reported in this paper.

References

[1] D.S. Schmool, N. Keller, M. Guyot, R. Krishnan, M. Tessier, Magnetic and magneto-optic properties of orthoferrite thin films grown by pulsed-laser deposition, J. Appl. Phys. 86 (1999) 5712–5717, https://doi.org/10.1063/1.371583.

[2] X. Niu, H. Li, G. Liu, Preparation, characterization and photocatalytic properties of $REFeO_3$ (RE = Sm, Eu, Gd), J. Mol. Catal. A Chem. 232 (2005) 89–93, https://doi.org/10.1016/j.molcata.2005.01.022.

[3] J. Tsagaroyannis, K.J. Haralambous, Z. Loizos, G. Petroutsos, N. Spyrellis, Gadolinium-iron ferrites: catalytic effect on the water-gas shift reaction, Mater. Lett. 28 (1996) 393–400, https://doi.org/10.1016/0167-577x(96)00089-4.

[4] J. Ding, X. Lü, H. Shu, J. Xie, H. Zhang, Microwave-assisted synthesis of perovskite $ReFeO_3$ (Re: La, Sm, Eu, Gd) photocatalyst, Mater. Sci. Eng. B Solid-State Mater. Adv. Technol. 171 (2010) 31–34, https://doi.org/10.1016/j.mseb.2010.03.050.

[5] M. Siemons, A. Leifert, U. Simon, Preparation and gas sensing characteristics of nanoparticulate p-Type semiconducting $LnFeO_3$ and $LnCrO_3$ materials, Adv. Funct. Mater. 17 (2007) 2189–2197, https://doi.org/10.1002/adfm.200600454.

[6] X. Niu, W. Du, W. Du, Preparation, characterization and gas-sensing properties of rare earth mixed oxides, Sens. Actuat. B Chem. 99 (2004) 399–404, https://doi.org/10.1016/j.snb.2003.12.006.

[7] F. Söderlind, M.A. Fortin, R.M. Petoral Jr, A. Klasson, T. Veres, M. Engström, K. Uvdal, P.-O. Käll, Colloidal synthesis and characterization of ultrasmall perovskite $GdFeO_3$ nanocrystals, Nanotechnology 19 (2008) 085608, , https://doi.org/10.1088/0957-4484/19/8/085608.

[8] N. Kimizuka, A. Yamamoto, H. Ohashi, T. Sugihara, T. Sekine, The stability of the phases in the Ln_2O_3-FeO-Fe_2O_3 systems which are stable at elevated temperatures (Ln: Lanthanide Elements and Y), J. Solid State Chem. 49 (1983) 65–76, https://doi.org/10.1016/0022-4596(83)90217-7.

[9] S. Geller, Crystal structure of gadolinium orthoferrite, $GdFeO_3$, J. Chem. Phys. 24 (1956) 1236–1239, https://doi.org/10.1063/1.1742746.

[10] I. Warshaw, R. Roy, Stable and metastable equilibria in the systems Y_2O_3-Al_2O_3, and Gd_2O_3-Fe_2O_3, J. Am. Ceram. Soc. 42 (1959) 434–438, https://doi.org/10.1111/j.1151-2916.1959.tb12970.x.

[11] H.J. Van Hook, Phase relations in the system Fe_2O_3–Fe_3O_4–$YFeO_3$ in air, J. Am. Ceram. Soc. 44 (1961) 208–214, https://doi.org/10.1111/j.1151-2916.1961.tb15362.x.

[12] R.W. Johnson, A. Hultqvist, S.F. Bent, A brief review of atomic layer deposition: from fundamentals to applications, Mater. Today 17 (2014) 236–246, https://doi.org/10.1016/j.mattod.2014.04.026.

[13] I. Azpitarte, A. Zuzuarregui, H. Ablat, L. Ruiz-Rubio, A. López-Ortega, S.D. Elliott, M. Knez, Suppressing the thermal and ultraviolet sensitivity of kevlar by infiltration and hybridization with ZnO, Chem. Mater. 29 (2017) 10068–10074, https://doi.org/10.1021/acs.chemmater.7b03747.

[14] N.T. Eigenfeld, J.M. Gray, J.J. Brown, G.D. Skidmore, S.M. George, V.M. Bright, Ultra-thin 3D nano-devices from atomic layer deposition on polyimide, Adv. Mater. 26 (2014) 3962–3967, https://doi.org/10.1002/adma.201400410.

[15] J. Bachmann, Atomic Layer Deposition in Energy Conversion Applications, first ed., Wiley-VCH, 2017.

[16] K.B. Klepper, O. Nilsen, H. Fjellvåg, Growth of thin films of Co_3O_4 by atomic layer deposition, Thin Solid Films 515 (2007) 7772–7781, https://doi.org/10.1016/j.tsf.2007.03.182.

[17] O. Nilsen, E. Rauwel, H. Fjellvåg, A. Kjekshus, Growth of $La_{1-x}Ca_xMnO_3$ thin films by atomic layer deposition, J. Mater. Chem. 17 (2007) 1466–1475, https://doi.org/10.1039/B616982A.

[18] M. Coll, J. Gazquez, A. Palau, M. Varela, X. Obradors, T. Puig, Low temperature epitaxial oxide ultrathin films and nanostructures by atomic layer deposition, Chem. Mater. 24 (2012) 3732–3737, https://doi.org/10.1021/cm301864c.

[19] J.A. Klug, N.G. Becker, N.R. Groll, C. Cao, M.S. Weimer, M.J. Pellin, J.F. Zasadzinski, T. Proslier, Heteroepitaxy of group IV-VI nitrides by atomic layer deposition, Appl. Phys. Lett. 103 (2013) 1–5, https://doi.org/10.1063/1.4831977.

[20] V. Miikkulainen, M. Leskelä, M. Ritala, R.L. Puurunen, Crystallinity of inorganic films grown by atomic layer deposition: overview and general trends, J. Appl. Phys. 113 (2013) 021301, , https://doi.org/10.1063/1.4757907.

[21] M. Coll, J.M. Montero Moreno, J. Gazquez, K. Nielsch, X. Obradors, T. Puig, Low temperature stabilization of nanoscale epitaxial spinel ferrite thin films by atomic layer deposition, Adv. Funct. Mater. 24 (2014) 5368–5374, https://doi.org/10.1002/adfm.201400517.

[22] M. Coll, J. Gazquez, I. Fina, Z. Khayat, A. Quindeau, M. Alexe, M. Varela, S. Trolier-McKinstry, X. Obradors, T. Puig, Nanocrystalline ferroelectric $BiFeO_3$ thin films by low-temperature atomic layer deposition, Chem. Mater. 27 (2015) 6322–6328, https://doi.org/10.1021/acs.chemmater.5b02093.

[23] H.H. Sønsteby, H. Fjellvåg, O. Nilsen, Functional perovskites by atomic layer deposition - an overview, Adv. Mater. Interfaces. 4 (2017) 1600903.

[24] A. Devi, Old Chemistries' for new applications: perspectives for development of precursors for MOCVD and ALD applications, Coord. Chem. Rev. 257 (2013) 3332–3384, https://doi.org/10.1016/j.ccr.2013.07.025.

[25] S.T. Barry, Amidinates, guanidinates and iminopyrrolidinates: understanding precursor thermolysis to design a better ligand, Coord. Chem. Rev. 257 (2013) 3192–3201, https://doi.org/10.1016/j.ccr.2013.03.015.

[26] M. Leskelä, M. Ritala, O. Nilsen, Novel materials by atomic layer deposition and molecular layer deposition, MRS Bull. 36 (2011) 877–884.

[27] P. De Rouffignac, R.G. Gordon, Atomic layer deposition of praseodymium aluminum oxide for electrical applications, Chem. Vap. Depos. 12 (2006) 152–157, https://doi.org/10.1002/cvde.200506377.

[28] M. Coll, M. Napari, Atomic layer deposition of multicomponent functional oxides, APL Mater. 7 (2019) 110901, , https://doi.org/10.1063/1.5113656.

[29] P. Marchand, C.J. Carmalt, Molecular precursor approach to metal oxide and pnictide thin films, Coord. Chem. Rev. 257 (2013) 3202–3221, https://doi.org/10.1016/j.ccr.2013.01.030.

[30] K. Bernal Ramos, M.J. Saly, Y.J. Chabal, Precursor design and reaction mechanisms for the atomic layer deposition of metal films, Coord. Chem. Rev. 257 (2013) 3271–3281, https://doi.org/10.1016/j.ccr.2013.03.028.

[31] T. Hatanpää, M. Ritala, M. Leskelä, Precursors as enablers of ALD technology: contributions from University of Helsinki, Coord. Chem. Rev. 257 (2013)

3297–3322, https://doi.org/10.1016/j.ccr.2013.07.002.

[32] S. Mathur, M. Veith, H. Shen, S. Hu, Structural and optical properties of NdAlO$_3$ nanocrystals embedded in an Al$_2$O$_3$ matrix, Chem. Mater. 14 (2002) 568–582.

[33] D.B.G. Williams, M. Lawton, Drying of organic solvents: quantitative evaluation of the efficiency of several desiccants, J. Org. Chem. 75 (2010) 8351–8354, https://doi.org/10.1021/jo101589h.

[34] S. Mathur, M. Veith, V. Sivakov, H. Shen, H.B. Gao, Composition, morphology and particle size control in nanocrystalline iron oxide films grown by single-source CVD, J. Phys. IV. 11 (2001) 487–494, https://doi.org/10.1051/jp4:2001362.

[35] D.C. Bradley, J.S. Ghotra, F.A. Hart, Three-co-ordination in lanthanide chemistry: Tris[bis(trimethylsilyl)amido]lanthanide(III) compounds, J. Chem. Soc. Chem. Commun. (1972) 349–350.

[36] Stoe & Cie GmbH Darmstadt Deutschland, X-RED32 1.31 (2005) & X-SHAPE 1.06; 1999., X-RED32 1.31 X-SHAPE 1.06, (1999).

[37] L.J. Farrugia, *WinGX* suite for small-molecule single-crystal crystallography, J. Appl. Crystallogr. 32 (1999) 837–838, https://doi.org/10.1107/S0021889899006020.

[38] A. Altomare, G. Cascarano, C. Giacovazzo, A. Guagliardi, M.C. Burla, G. Polidori, M. Camalli, SIRPOW .92 – a program for automatic solution of crystal structure by direct methods optimized for powder data, J. Appl. Crystallogr. 27 (1994) 435–436, https://doi.org/10.1107/S0021889894000221.

[39] G.M. Sheldrick, A short history of SHELX, Acta Crystallogr. Sect. A Found. Crystallogr. 64 (2007) 112–122, https://doi.org/10.1107/S0108767307043930.

[40] S. Macke, A. Radi, J.E. Hamann-Borrero, A. Verna, M. Bluschke, S. Brück, E. Goering, R. Sutarto, F. He, G. Cristiani, M. Wu, E. Benckiser, H.U. Habermeier, G. Logvenov, N. Gauquelin, G.A. Botton, A.P. Kajdos, S. Stemmer, G.A. Sawatzky, M.W. Haverkort, B. Keimer, V. Hinkov, Element specific monolayer depth profiling, Adv. Mater. 26 (2014) 6554–6559, https://doi.org/10.1002/adma.201402028.

[41] R.D. Shannon, Revised effective ionic radii and systematic studies of interatomic distances in halides and chalcogenides, Acta Crystallogr. Sect. A 32 (1976) 751–767, https://doi.org/10.1107/S0567739476001551.

[42] J. Schläfer, S. Stucky, W. Tyrra, S. Mathur, heterobi- and trimetallic cerium(iv) tert-butoxides with mono-, di-, and trivalent metals (M = K(I), Ge(II), Sn(II), Pb(II), Al (III), Fe(III)), Inorg. Chem. 52 (2013) 4002–4010, https://doi.org/10.1021/ic400030j.

[43] J. Schläfer, Neuartige Homo- und Heterometallische Cer-Alkoxide (in German), PhD Thesis University of Cologne, 2014.

[44] J.M. Gaskell, A.C. Jones, H.C. Aspinall, S. Przybylak, P.R. Chalker, K. Black, H.O. Davies, P. Taechakumput, S. Taylor, G.W. Critchlow, Liquid injection ALD and MOCVD of lanthanum aluminate using a bimetallic alkoxide precursor, J. Mater. Chem. 16 (2006) 3854–3860, https://doi.org/10.1039/b609129f.

[45] J.M. Gaskell, S. Przybylak, A.C. Jones, H.C. Aspinall, P.R. Chalker, K. Black, R.J. Potter, P. Taechakumput, S. Taylor, Deposition of Pr- and Nd-aluminate by liquid injection MOCVD and ALD using single-source heterometallic alkoxide precursors, Chem. Mater. 19 (2007) 4796–4803, https://doi.org/10.1021/cm0707556.

[46] M. Vehkamäki, M. Ritala, M. Leskelä, A.C. Jones, H.O. Davies, T. Sajavaara, E. Rauhala, Atomic layer deposition of strontium tantalate thin films from bimetallic precursors and water, J. Electrochem. Soc. 151 (2004) F69–F72, https://doi.org/10.1149/1.1648025.

[47] F. Söderlind, L. Selegård, P. Nordblad, K. Uvdal, P.O. Käll, Sol-gel synthesis and characterization of polycrystalline GdFeO$_3$ and Gd$_3$Fe$_5$O$_{12}$ thin films, J. Sol-Gel Sci. Technol. 49 (2009) 253–259, https://doi.org/10.1007/s10971-008-1859-0.

[48] D. Raiser, J.P. Deville, Study of XPS photoemission of some gadolinium compounds, J. Electron Spectros. Relat. Phenomena. 57 (1991) 91–97, https://doi.org/10.1016/0368-2048(91)85016-M.

[49] A.P. Grosvenor, B.A. Kobe, M.C. Biesinger, N.S. McIntyre, Investigation of multiplet splitting of Fe 2p XPS spectra and bonding in iron compounds, Surf. Interface Anal. 36 (2004) 1564–1574, https://doi.org/10.1002/sia.1984.

[50] E. Paparazzo, Xps analysis of iron aluminum oxide systems, Appl. Surf. Sci. 25 (1986) 1–12.

[51] P.C.J. Graat, M.A.J. Somers, Simultaneous determination of composition and thickness of thin iron-oxide films from XPS Fe 2p spectra, Appl. Surf. Sci. 100–101 (1996) 36–40, https://doi.org/10.1016/0169-4332(96)00252-8.

[52] P. Ramesh Babu, I. Bhaumik, S. Ganesamoorthy, S. Kalainathan, R. Bhatt, A.K. Karnal, P.K. Gupta, Investigation of magnetic property of GdFeO$_3$ single crystal grown in air by optical floating zone technique, J. Alloys Compd. 631 (2015) 232–236, https://doi.org/10.1016/j.jallcom.2015.01.112.

[53] S. Mathur, H. Shen, N. Lecerf, A. Kjekshus, H. Fjellvåg, G.F. Goya, Nanocrystalline orthoferrite GdFeO$_3$ from a novel heterobimetallic precursor, Adv. Mater. 14 (2002) 1405–1409.

[54] S. Carmen-Gabriela, From Bulk to Nano: The Many Sides of Magnetism, 1st ed., Springer, 2008, https://doi.org/10.1007/978-3-540-70548-2.

[55] M.a. Gilleo, Magnetic properties of a gadolinium orthoferrite GdFeO$_3$, crystal, J. Chem. Phys. 24 (1956) 1239–1243, https://doi.org/10.1063/1.1742747.

[56] R.M. Bozorth, Origin of weak ferromagnetism in rare-earth orthoferrites, Phys. Rev. Lett. 1 (1958) 362–363, https://doi.org/10.1103/PhysRevLett.1.362.

Chapter 4

FURTHER INSIGHTS

Fabrication of $Gd_xFe_yO_z$ films using an atomic layer deposition-type approach

Pengmei Yu,[†] Sebastian Beer,[‡] Anjana Devi,[‡] Mariona Coll[†,*]

[†]*Institut de Ciència de Materials de Barcelona (ICMAB-CSIC), Campus de la UAB, 08193 Bellaterra,*
Barcelona, Spain. Tel: +34 935801853, Email: mcoll@icmab.es

[‡]*Inorganic Materials Chemistry, Ruhr-University Bochum, Universitätsstraße 150, Bochum 44801,*
Germany
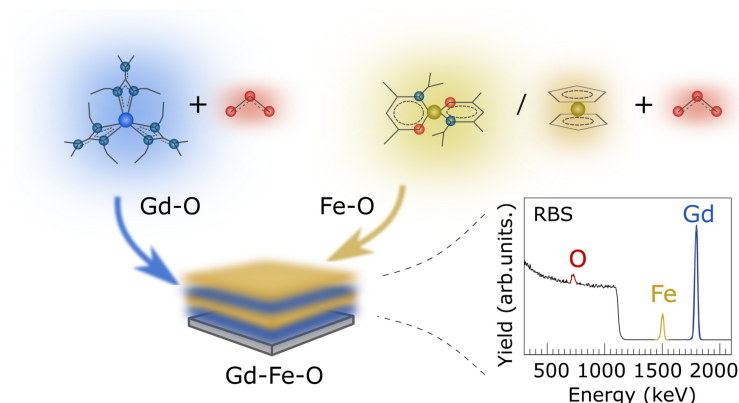
Abstract

The growth of complex oxide thin films with atomic precision offers bright prospects to study improved properties and novel functionalities. Here we tackle the fabrication of gadolinium iron oxide thin films by an atomic layer deposition-type approach in which iron and gadolinium tailor-made metalorganic precursors (bis(N-isopropyl ketoiminate) iron(II), $[Fe(^ipki)_2]$ and tris(N,N'-diisopropyl-2-dimethylamido- guanidinato) gadolinium(III), $[Gd(DPDMG)_3]$) are alternately reacted with ozone and deposited on silicon substrates at 250 °C. The structure, chemical composition and magnetic properties of the resulting films are compared with those obtained from a commercially available ferrocene precursor $[Fe(Cp)_2]$ and $[Gd(DPDMG)_3]$. All films resulted in cation ratio close to nominal stoichiometry with negligible amount of organic species. The tailor-made metalorganic precursors, designed to provide similar thermal behavior, result in the formation of polycrystalline $Gd_3Fe_5O_{12}$ films coexisting with $GdFeO_3$, Gd_2O_3 and Fe_2O_3 whereas the combination of $[Fe(Cp)_2]$ and $[Gd(DPDMG)_3]$ mainly favors the formation of $Gd_3Fe_5O_{12}$ films coexisting with traces of Gd_2O_3. This study demonstrates that this is a viable route to prepare complex $Gd_xFe_yO_z$ films and could be used for the design of complex oxide films with improved properties upon rigorous study of the compatibility of metalorganic precursors.

1   Introduction

$GdFeO_3$ and $Gd_3Fe_5O_{12}$ are two ternary oxide systems sharing fascinating magnetic and magneto-optical properties[1,2] that can open new directions in the field of spintronics and magnonics.[3–7] The ability to prepare stable $Gd_xFe_yO_z$ phases with the appropriate stoichiometry,[8,9] often as coatings of high aspect ratio structures, is becoming relevant to study new physics emerging from the films and at their interfaces.[10,11] The best layer uniformity with atomic scale control is effectively achieved by atomic layer deposition (ALD).[12,13] This is a versatile thin film deposition technique that relies on alternate pulsing of chemical precursors that react with the surface species in a self-limiting manner. Hence, the ALD process consists of a repetition of a basic sequence of reactant pulses and purges, i.e. a cyclic process. These characteristics offer exceptional control in film composition and thickness and excellent step coverage over complex structures. This is a well-established technique to deposit binary compounds[14–16] and its unique deposition characteristics motivates the continuous research to develop deposition process for compositions with increased complexity.[17] Unfortunately, the ALD synthesis of a ternary oxide is, in most of the cases, not a simple addition of the corresponding binary oxide processes.[18,19] The compatibility of different chemical precursors confined under similar deposition conditions together with a varying surface species after every precursor dose increase considerably the level of intricacy.[17,20,21] Indeed, $LaFeO_3$,[18] $La_{1-x}Sr_xFeO_3$[18] and $ErFeO_3$[22] are some of the few examples reported on ALD rare-earth ferrites deposited by alternate pulsing of one reactant per component of the complex oxide. More recently, epitaxial $GdFeO_3$ films have been grown by alternate dosing of a single heterobimetallic precursor, already containing the stoichiometric 1:1 cation ratio, and ozone.[23] Clearly, the development of $Gd_xFe_yO_z$ phases by ALD will require knowledge on the synthetic path which strongly depends on the chemistry of the metalorganic precursors. In this study we are interested in exploring the opportunities that the chemistry of homometallic Gd and Fe compounds can offer to grow Gd-Fe- oxide thin films by an ALD-type approach. To this end, a special focus has to be laid to the compatibility of Fe and Gd precursors in terms of reactivity, volatility and thermal stability[24,25] as the commonly used precursors for these elements do not have matching properties. While there is a rich variety of suitable iron precursors based on cyclopentadienyl, halide, β-diketonate and acetylacetonate ligands, see Table S4.1, there are limited sources for Gd mainly involving silylamide, β-diketonate and cyclopentadienyl-based ligand systems, see Table S4.2. Among these precursors, we investigate the use of the cost-efficient and commercially available ferrocene precursor, $[Fe(Cp)_2]$, in which the metal is bonded to two η^5-cyclopentadienyl rings exhibiting a high thermal stability, versus the use of bis(N-isopropyl ketoiminate) iron(II), $[Fe(^ipki)_2]$,[26] which possesses a ketoiminate ligand with mixed nitrogen and oxygen donors providing reactivity and stability, respectively. Their reactivity is evaluated against tris(N,N'-

diisopropyl-2-dimethylamido- guanidinato)gadolinium(III), [Gd(DPDMG)$_3$][27] which is a fully nitrogen coordinated complex and possesses an enhanced reactivity due to the rare-earth nitrogen bonds, see Scheme 4.1.

First, we have studied the reactivity of each homo-metallic precursor with H$_2$O and O$_3$ to grow the corresponding binary oxides and identify the compatible deposition conditions for the subsequent ternary oxide system. By means of X-ray diffraction (XRD), atomic force microscopy (AFM), X-ray photoelectron spectroscopy (XPS) and Rutherford backscattering spectrometry/nuclear reaction analysis (RBS/NRA), the phase purity, crystallinity, surface morphology and chemical composition of the grown complex compounds have been examined. Finally, the magnetic properties have been evaluated by superconducting quantum interference device (SQUID) magnetometry.
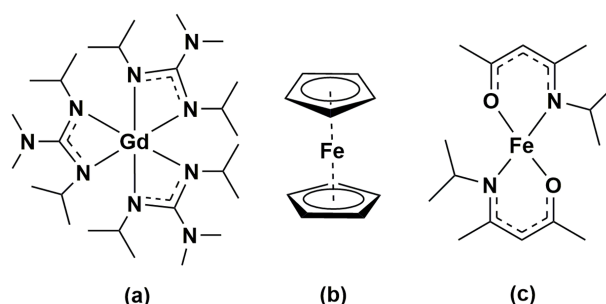
Scheme 4.1 Molecular structure of the Gd and Fe precursors studied in this work: (a) [Gd(DPDMG)$_3$], (b) [Fe(Cp)$_2$], (c) [Fe(^{i}pki)$_2$].

2 Experimental

2.1 Thin film deposition

The Gd$_x$Fe$_y$O$_z$ thin films deposition was carried out in a Savannah 100 ALD system from Cambridge NanoTech Inc. P-type Boron-doped Si(100) and SiO$_2$/Si(100) substrates were purchased from Active Business Company GmbH. Before introduction into the ALD chamber, the substrates were cleaned with acetone and ethanol followed by nitrogen gas blow drying. Prior to film growth, all substrates were kept in a constant high purity nitrogen flow for 10 min and subsequently exposed to ozone pulses to form a hydroxyl-terminated surface. Precursor sources were pulsed into the reaction chamber separated in time and purged by high purity nitrogen with a gas flow between 40 - 70 sccm. Ozone (O$_3$) and milli-Q water (H$_2$O) were considered as oxygen sources. O$_3$ was produced and delivered upon use from an LG-7 Corona Discharge ozone generator with a 5 wt.% concentration and an output of 5 g/h. The generator was modulated to work at 5 V direct current voltage with an adjusted flow of 0.18 L/min. The metalorganic precursors, [Gd(DPDMG)$_3$]

and [Fe(^{i}pki)$_2$] were synthesised as reported[26,27] and handled under inert conditions, while the commercial Fe precursor [Fe(Cp)$_2$] or ferrocene, (bis(cyclopentadienyl)iron (98% purity)), was purchased from Sigma-Aldrich and utilized as received. In this study we utilized three different valving systems that are here identified as flow mode (F), pressure-boost (PB) and exposure mode (E), scheme shown in Figure S4.1. F consists in having a continuous flow of inert gas to carry the precursor to the reaction chamber. For low-vapor pressure precursors, PB is used. That is, before precursor pulses, the gas exit valve was closed and ALD valve opened to allow carrier gas filling up the precursor cylinder and resulting in an elevated pressure in it. Afterwards, the exit valve is opened and the chamber pressure recovered, followed by precursor pulsing along with the filled nitrogen into the chamber. Under certain circumstances, E was applied. In this case, the gas exit valve was closed, exposing the sample to the precursor prolonged time to promote surface reaction and saturation over larger areas. Post-deposition thermal treatments, were performed on selected samples in an oxidising atmosphere (oxygen, 0.3 L/min flow) in a tubular furnace at 450 - 900 °C for 30 minutes.

Gadolinium oxide from [Gd(DPDMG)$_3$]. The deposition of gadolinium oxide was investigated in a chamber temperature range between 160 and 250 °C with the [Gd(DPDMG)$_3$] precursor heated at 120 - 135 °C. Based on the work of Milanov *et al.*[28] the Gd pulse/purge/oxidant pulse/purge duration was adapted in our reactor in the following sequence for H$_2$O 3 s/20 s/1 s/10 s and for O$_3$ 3 s/20 s/0.2 s/7 s.

Iron oxide from [Fe(Cp)$_2$]. The deposition process of iron oxide from [Fe(Cp)$_2$] was explored between the deposition temperature range of 150-250 °C with [Fe(Cp)$_2$] heated at 90 °C. The Fe pulse/purge/oxidant pulse/purge doses were 2 s/4 s/1 s/10 s for H$_2$O and 2 s/4 s/0.2 s/7 s for O$_3$. Longer pulse/purge lengths of [Fe(Cp)$_2$] (5 s/10 s) and O$_3$ (0.3 s/11 s) were investigated in the ternary oxide films as specified in the corresponding section.

Iron oxide from [Fe(^{i}pki)$_2$]. The deposition temperature of iron oxide from [Fe(^{i}pki)$_2$] was also evaluated between 150-250 °C with the [Fe(^{i}pki)$_2$] kept at 100-130 °C. Based on the work of Peeters *et al.*[26] [Fe(^{i}pki)$_2$], H$_2$O and O$_3$ were pulsed/purged by 8 s/10 s, 4 s/10 s and 0.2 s/10 s, respectively.

2.2 Thin film characterization

Qualitative elemental film composition studies were performed by Energy Disperse X-ray Spectroscopy (EDX) employing a FEI Quanta 200 FEG microscope. Each spectrum was collected with 15 keV working voltage, 3.0 spot size for an acquisition time of 100 s. Quantitative compositional studies were carried out using X-ray photoelectron spectroscopy (XPS) using a SPECS PHOIBOS 150 hemispherical X-ray photoelectron spectroscopy analyser (Al K$_\alpha$ source, from SPECS GmbH,

Berlin, Germany). The samples were analyzed with a pass energy of 10 eV at a base pressure of 1 $\times$ 10^{-10} mbar, taking a step size of 0.05 eV and 1 eV for the high-resolution and survey spectra, respectively. The acquired spectra were interpreted with CasaXPS software for binding energy determination and element assignment after spectrum calibration with C *1s* reference peak at 284.8 eV.

Thin film phase purity and crystallinity were investigated by X-ray diffraction (XRD) in the range of 2θ = 20°- 80° by grazing-incidence X-ray diffraction (GIXRD) at the incident angle of 1°. Specific samples were analyzed by θ-2θ scan on a Bruker D8 Discover A25 diffractometer with Cu K_α radiation (K_α=1.5406 Å). The film texture was further evaluated with GADDS (General Area Detector Diffraction System) Bruker AXS, Inc equipped with a 2D detector.

The film thickness was extracted from X-ray reflectivity (XRR) measurements using a SIEMENS D5000 diffractometer and fitted using ReMagX software.[29] It was further validated with spectroscopic ellipsometry (SE) measurements using a GES5E Ellipsometer from SOPRA Optical Platform. The measurements were carried out in reflection mode with variant light incident angles (65 °- 75 °) at 30 °analyzer angle for a spectral range of 200 - 900 nm. Thin film surface morphology was assessed from Atomic Force Microscope topographic images, 5 μm $\times$ 5 μm in size using a Keysight 5100 microscope and further processed with Mountains®8 software.

The magnetic properties were probed by a Quantum Design MPMS-XL magnetometer based on a superconducting quantum interference device (SQUID). In-plane magnetization-temperature curve (M(T)) at 5 KOe and magnetic hysterisis loop (M(H)) at 50 K were explored.

Additional film composition and depth profiles were obtained from Rutherford backscattering spectrometry (RBS) coupled with nuclear reaction analysis (NRA). The experiments were carried out in the RUBION, the Central Unit for Ion Beams and Radionuclides at Ruhr University Bochum. For the measurements, a 2.0 MeV ^{4}He$^+$ beam with an intensity of 20 nA – 40 nA (tilt angle 7°) was used. The backscattered particles were detected at an angle of 160°by a Si detector with a resolution of 16 keV. NRA measurements were carried out with a ^{2}H$^+$ beam (1 MeV). The samples were tilted at an angle of 7 °. The emitted protons were detected at an angle of 135 °with respect to the beam axis. The detector covered a solid angle of 23 msrad and was shielded by a 6 μm Ni foil to eliminate elastically scattered deuterons. Typical beam currents on the samples were close to 40 nA in an area of $\sim$ 1 mm in diameter, whereas the collected beam charge for a sample was 12 μC. The RBS/NRA data were analyzed by means of the SIMNRA program suite.[30]

3   Results and discussion

Prior to study the deposition of ternary oxides, it is necessary to study the independent binary oxide processes, i.e. gadolinium oxide and iron oxide. The optimization procedure includes choice

of oxidant co-reactants, precursor sublimation temperature, deposition temperature, carrier gas flow and valving system (flow, pressure boost, exposure described in the Experimental section), to identify the compatible conditions to finally assess the deposition of the multicomponent $Gd_xFe_yO_z$ system.

3.1 Gd_2O_3 films

The deposition of gadolinium oxide from $[Gd(DPDMG)_3]$ was studied in our reactor according to previous work.[28] The viability of ozone versus water as co-reactant was investigated in the deposition range of 160 - 250 °C with 40 sccm N_2 gas for 500 cycles under flow mode. The precursor sublimation temperature was optimized to 135 °C and the use of pressure boost to enhance its sublimation was evaluated. The use of water as co-reactant did not result in the deposition of gadolinium, regardless of the valving system. On the other hand, combining $[Gd(DPDMG)_3]$ with pressure boost, with ozone at 250 °C, Gd was detected in the films, Figure S4.2. The corresponding AFM topographic image illustrates high degree of film density, surface uniformity with an Root Mean Square (RMS) roughness value below 1 nm, Figure 4.1a.
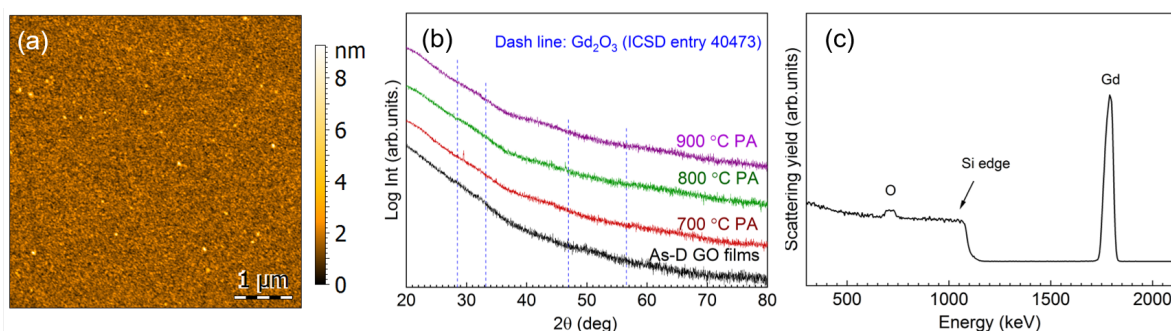
Fig. 4.1 (a) AFM topographic image of an as-deposited sample from $[Gd(DPDMG)_3]$ and O_3 at the deposition temperature of 250 °C. (b) GIXRD spectra of the as-deposited (As-D) and post-annealed (PA) films (700-900 °C). (c) RBS profile of the 800 °C post-anneled sample.

Phase formation and degree of crystallinity of a 30 nm thick film was studied by GIXRD at the as-deposited stage and after different post annealing treatments (700 - 900 °C, 30 min in oxygen atmosphere), see Figure 4.1b. The absence of Bragg reflections in the as-deposited step suggests the formation of amorphous films. The same patterns were obtained after post annealing treatments up to 900 °C, suggesting that the films remain amorphous. From RBS/NRA analysis the chemical composition of the film was studied in detail to rule out the presence of impurities trapped in the film that could hinder the crystallization process,[31,32] see Figure 4.1c. In the RBS profile it can be distinguished the Gd peak and the O peak superimposing the Si signal. Note that the tailing of the Si edge and the tailing of the Gd signal to lower energies indicate a diffusion of

Gd and Si at the interface. This phenomenon can be explained with the tendency of rare-earth to form silicates and silicides at such interfaces,[33] and could contribute to the poor crystallinity of the films in Figure 4.1b. RBS/NBA quantification, Table S4.3, reveals a low nitrogen and oxygen content of 0.4 at.% and < 3 %, respectively. Note that the Gd/O ratio is 0.30 evidencing an oxygen overstoichiometry. Similar observations have been recently reported in ALD iron oxide films and attributed to the prolonged ozone exposure.[34]

To evaluate the deposition homogeneity across a $4''$ Si wafer using [Gd(DPDMG)$_3$], the film thickness was analyzed at six different locations by means of XRR, see Figure S4.3. The areal thickness map was built in which the x axis corresponds to the gas flow pathway in the chamber, the y axis is the direction perpendicular to the flow, while z axis corresponds to the film thickness. As the wafer size is similar to the diameter of the ALD chamber, at x=0 cm one can find the gas inlet whereas at x=10 cm sits the gas outlet. For 40 sccm flow, Figure 4.2a, the maximum thickness achieved is near the gas inlet and decreases along with the gas pathway inlet. This areal thickness gradient can result from insufficient gas flow, a leak upstream of the precursor or inadequate purge times.[35] By increasing the gas flow to 70 sccm, the thickness homogeneity is improved although the areal gradient is still observed, Figure 4.2b. Finally, longer precursor exposure to the reaction surface along with longer purging times (exposure mode) was explored but the amount of Gd deposited was below the EDX and XRR detection limit. This behavior suggests that prolonged exposure of [Gd(DPDMG)$_3$] at 250 °C does not favor a saturation growth model either.
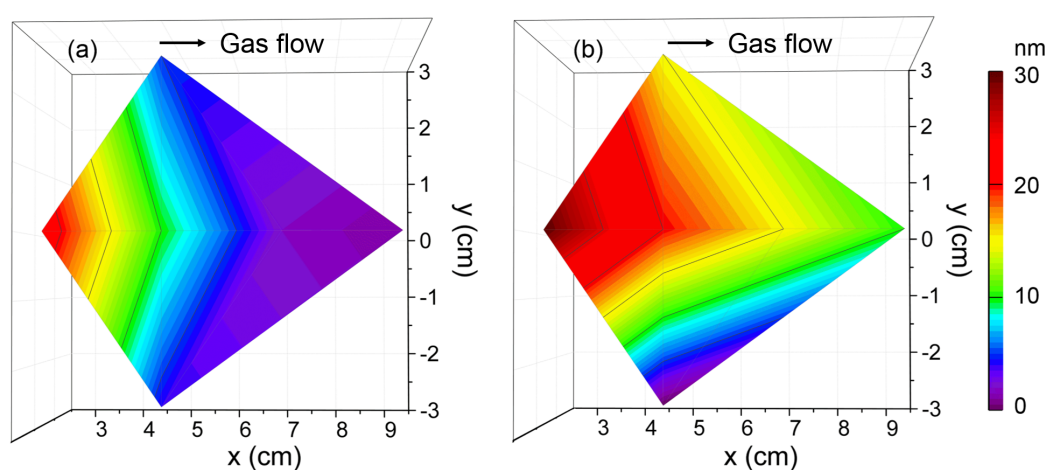

Fig. 4.2 Thickness mappings of Gd$_2$O$_3$ films grown at (a) 40 sccm and (b) 70 sccm N$_2$ flow located at different positions of a $4''$ Si wafer in the ALD chamber. Deposition conditions: T$_{dep}$ = 250 °C with ozone using PB mode, 500 cycles.

From deposition at 250 °C and 70 sccm gas flow, a growth per cycle (GPC) of ~ 0.6 Å/cycle

is obtained near the inlet. Similar growth rates are reported when combined $Gd(thd)_3/O_3$[36] although higher growth rates have been reported when using N-bonded Gd precursors and water (1 Å/cycle).[27] It is very likely that the use of O_3 and N-containing ligands can form intermediate NO_x and $C-O$ species[37] resulting in a more complex surface reaction mechanism affecting the growth rate.[31]

According to this study, the selected Gd_2O_3 deposition conditions for further studies were selected: $T_{Gd-subl}$= 135 °C and pressure boost, T_{dep}= 250 °C, 70 sccm N_2 carrier gas flow and ozone as co-reactant. Note that experimental conditions here reported do not lead to a self-limiting surface reaction.

3.2 Fe_2O_3 films

There is a divergence of deposition conditions reported for the preparation of ALD Fe_2O_3 from ferrocene.[34,35,38–40] One main purpose of our study is to investigate the feasibility of $[Fe(Cp)_2]$ to react with H_2O or O_3 to form Fe_2O_3 in our reactor and to evaluate its compatibility with the $[Gd(DPDMG)_3]$ precursor.

The deposition of $[Fe(Cp)_2]$ was studied in the 160 - 250 °C temperature window in flow mode (70 sccm) repeating 2000 cycles, Figure S4.4. Fe was only detected when ozone was used as co-reactant for a temperature range of 200 - 250 °C. The 15 nm as-deposited films (250 °C) present a mesh-like surface morphology with a surface RMS roughness of 3 nm, Figure 4.3a, and crystallize into the α-Fe_2O_3 phase (ICSD entry 24004), Figure 4.3b. EDX spectrum of an as-deposited film is shown in Figure 4.3c.
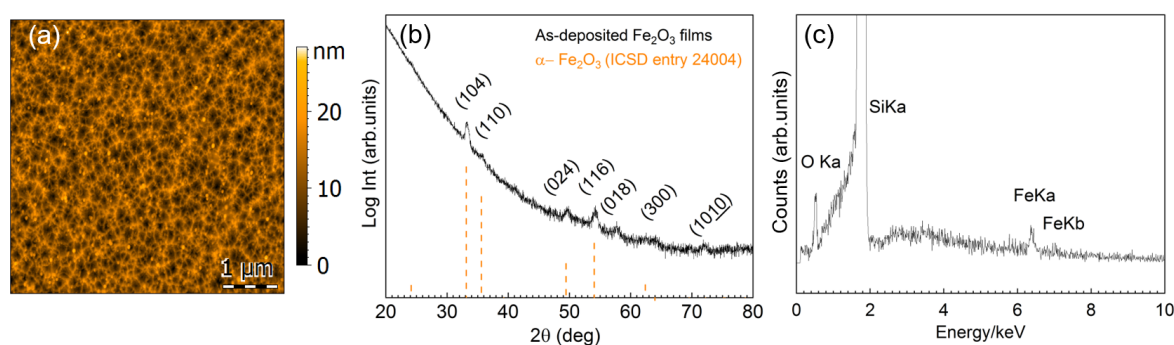
Fig. 4.3 (a) 5 μm × 5 μm AFM topography image from the as-deposited 15 nm film prepared from $[Fe(Cp)_2]$ and ozone at T_{dep} = 250 °C, (b) corresponding GIXRD pattern. (c) EDX spectrum showing Fe in the deposited films.

According to the deposition conditions identified above, the thickness homogeneity along a 4″ silicon wafer was investigated using $[Fe(Cp)_2]$ and ozone at 250 °C at 70 sccm, Figure 4.4a. The

maximum thickness, 15 nm, is identified towards the gas outlet revealing an evident thickness gradient. To improve the Fe_2O_3 deposition homogeneity, exposure mode was adopted enabling ferrocene and ozone to stay longer period of time in the chamber and promote surface saturation. In this case, an average thickness of 20 nm was obtained across the whole Si wafer, Figure 4.4b. The resulting GPC is $\sim$ 0.1 Å/cycle, significantly lower than the reported GPC values when combined $[Fe(Cp)_2]$ and O_3 (0.6 - 1.4 Å/cycle).[39,40] Schneider *et al.*[34] recently reported that lower growth per cycles at 250 °C can be assigned to increased decomposition of ozone.
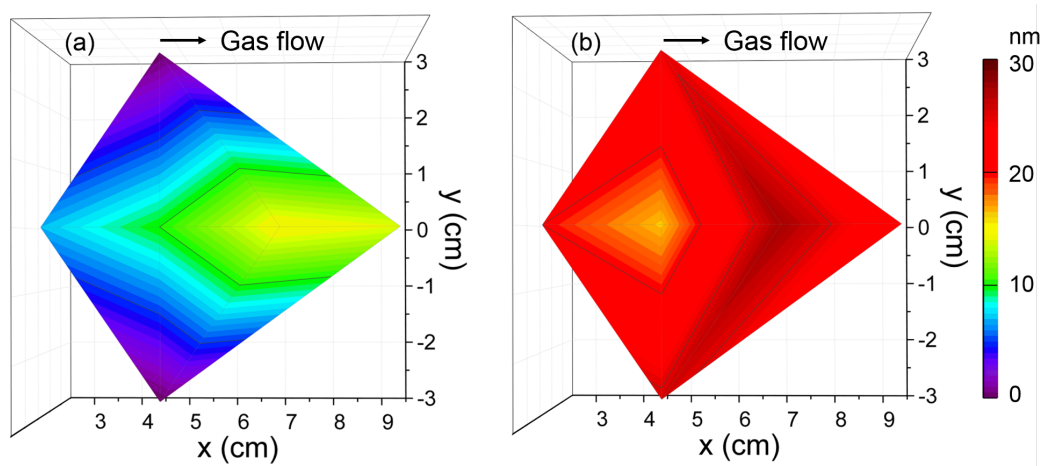
Fig. 4.4 Thickness mappings of Fe_2O_3 films deposited from $[Fe(Cp)_2]$ and O_3 at T_{dep} = 250 °C, 2000 cycles at (a) flow mode and (b) exposure mode with 70 sccm N_2 gas.

From this study the suitable processing conditions identified for Fe_2O_3 using ferrocene are ($T_{Fe-subl}$=90 °C), T_{dep}=250 °C with ozone as co-reactant under 70 sccm N_2 gas and exposure mode, which could be compatible with those previously found for the $[Gd(DPDMG)_3]$ precursor. The suitability of the ketoiminate iron precursor $[Fe(^ipki)_2]$,[26] to deposit Fe_2O_3 films was evaluated and compared to the commercial $[Fe(Cp)_2]$ and to $[Gd(DPDMG)_3]$.

Based on the previous studies on $[Fe(^ipki)_2]$,[26] the iron precursor was sublimed at 100 °C (with and with no pressure boost) in the temperature window of 150-250 °C using H_2O or O_3 as co-reactant under 70 sccm N_2 gas flow for 2000 cycles. Based on EDX studies, no iron was detected at any of these processing conditions, see Figure S4.5. Therefore, the sublimation temperature of $[Fe(^ipki)_2]$ was increased up to 130 °C and the processing conditions were re-evaluated. Depositing Fe_2O_3 using $[Fe(^ipki)_2]$ and O_3 at 250 °C resulted in a 65 nm film, Figure S4.5b-c. AFM analysis on as-deposited films reveals a dense and homogeneous surface with very low surface roughness (RMS $\sim$ 1 nm), Figure 4.5a. The crystallinity of 65 nm Fe_2O_3 films was investigated by GIXRD. In the as-deposited stage, the films are amorphous. Subsequent post thermal treatments for 30 min in oxygen at 500 °C and at 800 °C did not favor the crystallization of Fe_2O_3. However,

117

typical peaks of α-Fe_2O_3 were observed at 900°C, Figure 4.5b. It can be seen from the RBS analysis, Figure 4.5c, that distribution of Fe and O is homogeneous throughout the film thickness with a ratio of Fe to O of 0.52 and C and N abundance below <0.8% indicating a clean surface reaction and desorption of byproducts during the growth of Fe_2O_3 (see Table S4.3).
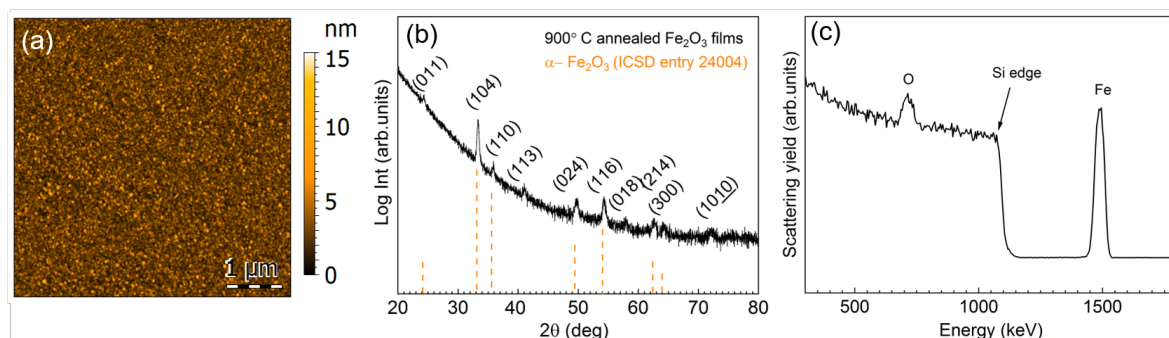
Fig. 4.5 Characteristics of the Fe_2O_3 films prepared by alternate pulsing of [Fe(^{i}pki)$_2$] (in pressure boost mode) and ozone at 250ºC. (a) AFM topological image of the as-deposited Fe_2O_3 films, (b) GIXRD spectrum of a 900 °C annealed sample, (c) RBS spectrum of the Fe_2O_3 annealed at 800 °C.

Figure 4.6 shows the film thickness homogeneity along the 4″ silicon wafer. In this case, a thickness gradient from 65 nm to 45 nm was identified, showing a preferred deposition near the gas inlet, similar to the Gd_2O_3. Accordingly, the preferred conditions for Fe_2O_3 deposition from [Fe(^{i}pki)$_2$] using an ALD-type approach is: $T_{Fe-subl}$=130 °C, T_{dep}=250 °C, ozone as co-reactant at 70 sccm N_2 flow.
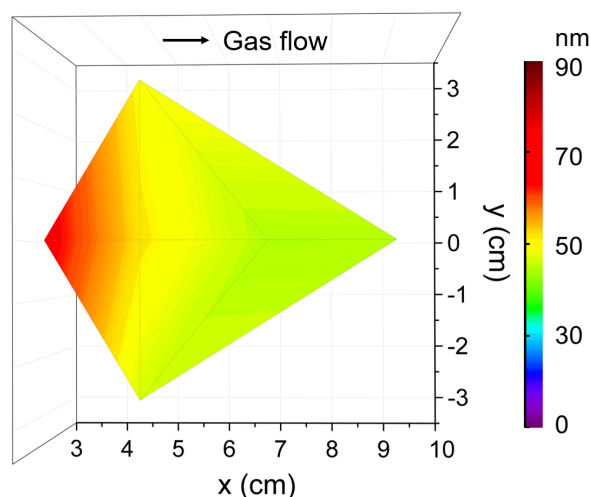
Fig. 4.6 Thickness homogeneity map of Fe_2O_3 films that are located at various chamber positions on a 4″ Si wafer from [Fe(^{i}pki)$_2$] and O_3 under 70 sccm flow at T_{dep}=250 °C with 2000 cycles.

The resultant growth rate of iron oxide films is ~0.4 Å/cycle, which is more than four times

Table 4.1 Selected ALD recipes for Gd-O and Fe-O deposition

Process	T_{dep} (°C)	T_{subl} (°C)	Flow (sccm)	Co-reactant	Mode	Growth Rate (Å/cycle)
Gd-O from [Gd(DPDMG)$_3$]	250	135 PB	70	O$_3$	Flow	0.6
Fe-O from [Fe(Cp)$_2$]	250	90	70	O$_3$	Exposure	0.1
Fe-O from [Fe(^{i}pki)$_2$]	250	130 PB	70	O$_3$	Flow	0.4

higher than that from [Fe(Cp)$_2$] (0.1 Å/cycle). The higher GPC of [Fe(^{i}pki)$_2$] could be attributed to the enhanced reactivity from the mixed N- O- ligand chemistry[26,41] compared to the stable Fe-metallocene bonding in [Fe(Cp)$_2$].[39] The steric hindrance of the ligands will also play a key role. The low reactivity of Cp can certainly slow the reaction mechanism when compared to the ketoiminate ligands.[42–44] This difference in precursor chemistry also affects the surface morphology of the final film noting that [Fe(^{i}pki)$_2$] leads to smooth and dense films whereas [Fe(Cp)$_2$] favors higher degree of porosity (Figure 4.3a).

The optimal deposition conditions for each binary oxide are summarized in Table 4.1.

Along with the difference in GPC of [Fe(Cp)$_2$] compared to [Gd(DPDMG)$_3$] and [Fe(^{i}pki)$_2$] already mentioned above, distinct thickness homogeneity along the silicon wafer was detected (Figure 4.2b, Figure 4.4b, Figure 4.6). [Fe(^{i}pki)$_2$] and [Gd(DPDMG)$_3$] showed a clear trend to be deposited near the gas inlet, whereas [Fe(Cp)$_2$] resulted in a highly homogeneous distribution. This discrepancy could also arise from the pronounced reactivity of the [Gd(DPDMG)$_3$] and [Fe(^{i}pki)$_2$] precursors containing N- and O-metal bonds which are prone to be depleted at the reaction chamber inlet.[28]

It is important to consider the differences observed between the three metal oxides to elaborate the deposition process of the ternary systems. Importantly, when combining the different reactants, i.e. Fe-precursor, Gd-precursor and O$_3$, the active surface sites will differ from the studied binary system and therefore differences in the reactivity, composition and film crystallinity might be expected.[20]

3.3   Gd$_x$Fe$_y$O$_z$ system

The deposition of the Gd$_x$Fe$_y$O$_z$ system was first assessed by studying the combination of [Gd(DPDMG)$_3$] and [Fe(Cp)$_2$] with ozone at 250 °C. The deposition process was designed by alternating nanolaminates of the respective oxides and the influence of subcycle ratio and sequence were evaluated on both film stoichiometry and spatial distribution. Subsequently, the impact of post thermal treatments on phase crystallization were also studied. Table 4.2 lists the investigated ALD subcycle ratio and sequence along with the experimental cation ratios found by EDX analysis.

According to the GPC identified in the binary oxides study (0.6 Å/cycle for Gd-O and 0.1 Å/cycle for Fe-O), a process with larger proportion of Fe-O subcycles over Gd-O subcycles was designed. Nonetheless, from this approach the amount of Gd found in the film largely exceeds that of Fe (GFO-Cp-1). In an attempt to increase the Fe content in the film while minimizing larger bilayer periods, ferrocene pulse and purge length were increased to 5 s/10 s and the superlattice ratio decreased to 10:10 (GFO-Cp-2) which results in the intended increase of Fe content (28%). The number of Cp and DPDMG ligands that react at the Gd-O and Fe-O terminated surfaces, respectively, is very likely to differ from the binary oxide system and therefore the nucleation scenario changes. Decrease in the growth rate of the mixture[18,45] or even etching of the metal-O surface by the precursor ligands may occur.[46] Then, by keeping a theoretical 10:10 supercycle ratio while changing the sequence from Gd-O/Fe-O to Fe-O/Gd-O (sample GFO-Cp-3), the experimental cation ratio went to 49:51 revealing that the sequence of nanolaminates deposition has also a critical role on cation incorporation. It is likely that Si-OH surface are preferred nucleation sites for ferrocene compared to Gd-O terminated surface to activate the growth.

Table 4.2 $Gd_xFe_yO_z$ deposition conditions varying Gd-O/Fe-O subcycle ratios and sequence combining $[Gd(DPDMG)_3]$ and $[Fe(Cp)_2]$. Estimated Gd and Fe at.% from EDX analysis.

Sample	Gd-O subcycles	Fe-O subcycles	Theoretical ratio	Subcycle sequence	Gd (%)	Fe (%)
GFO-Cp-1	10	50	1:5	Gd:Fe	92	8
GFO-Cp-2*	10	10	1:1	Gd:Fe	71	29
GFO-Cp-3*	10	10	1:1	Fe:Gd	49	51

* Samples with $[Fe(Cp)_2]$ 5 s pulse/10 s purge.

The Gd and Fe distribution along a 4″ silicon wafer was investigated by EDX repeating the recipe GFO-Cp-3. The compositional map reveals that Gd is mostly located near the gas inlet (left side of the map), Figure 4.7a, following the same trend observed for the binary Gd_2O_3 process (Figure 4.2).

Taking advantage of this spatial Gd/Fe distribution, samples located at three different regions of the chamber corresponding to Gd/Fe ratio of 11.5, 0.6 and 1 were investigated by GIXRD analysis, Figure 4.7b. In the as-deposited stage, all films turned out to be amorphous (not shown). Then, these three samples were exposed to a post annealing process at 800 °C under 0.3 L/min oxygen flow for 30 min. Gd-rich films (Gd/Fe=11.5) show the characteristic Bragg reflections corresponding to the cubic Gd_2O_3 phase (ICSD entry 40473). For the Gd/Fe = 0.6 sample, the formation of crystalline $Gd_3Fe_5O_{12}$ (garnet) film is obtained (ICSD entry 27127) with minor traces of Gd_2O_3. Finally, for the Gd/Fe=1 sample, the film remains amorphous. Therefore, gadolinium orthoferrite has not been stabilized under these conditions.
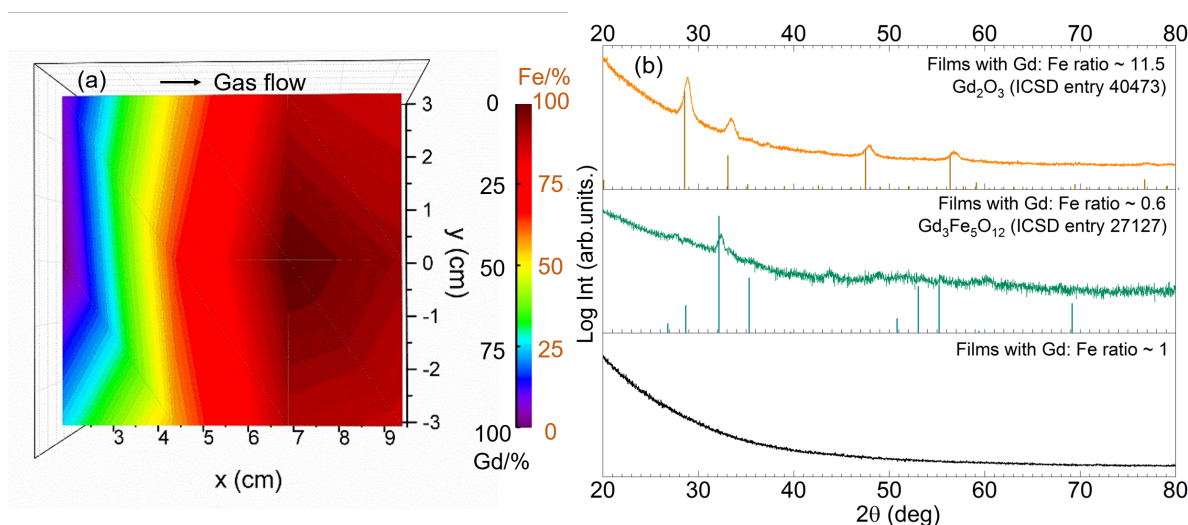
Fig. 4.7 (a) Elemental distribution map of $Gd_xFe_yO_z$ films under GFO-Cp-3 conditions. The ALD process was carried out using $[Gd(DPDMG)_3]$, $[Fe(Cp)_2]$ and O_3 at the deposition temperature of 250 °C. (b) GIXRD spectra of post-annealed Gd-Fe-O samples from $[Fe(Cp)_2]$ and $[Gd(DPDMG)_3]$ which are Gd:Fe = 11.5, Gd:Fe = 0.6 and Gd:Fe = 1. Reference XRD patterns from Gd_2O_3, and $Gd_3Fe_5O_{12}$ are displayed under each panel.

To further investigate the chemical composition and cation valence state of the post annealed $Gd_3Fe_5O_{12}$ sample, RBS and XPS studies were performed.

From the RBS spectrum of the $Gd_3Fe_5O_{12}$ film post annealed at 800°C, O, Gd and Fe are present, superimposed to the signal from the Silicon substrate, see Figure 4.8. The elemental composition of Gd, Fe and O has been determined from RBS/NRA and listed in Table S4.3. The Gd/Fe/O amount is 12.4/17.6/67.6 in at.% close to the ideal $Gd_3Fe_5O_{12}$ stoichiometry. Also, C and N content remain below 2% revealing once more that the reactivity of the precursor towards ozone is sufficient to ensure a clean reaction of the surface species with desorption of the organics. On the other hand, from XPS analysis (survey spectrum shown in Figure S4.6) of the Gd 3d and Fe 2p core level spectra were investigated to elucidate the oxidation state, Figure 4.9a,b respectively. For Gd 3d core level spectra, main peaks of 3$d_{3/2}$ and 3$d_{5/2}$ were found at 1221.1 eV and 1189.1 eV, respectively. These values are slightly shifted to higher binding energy than the ones reported, yet the spin-orbit splitting energy difference $\Delta E_{Gd\ 3d_{3/2}\text{-}Gd\ 3d_{5/2}}$ is 32.0 eV, in good agreement with the average value 32.1 ± 0.3 eV for Gd^{3+} containing compounds[47] therefore confirming the Gd $^{3+}$ oxidation number, see Table S4.4. For Fe 2p, the peaks appearing at $\sim$ 725.0 eV and 711.4 eV coincide with 2$p_{1/2}$ and 2$p_{3/2}$ doublets. The Fe 2$p_{3/2}$ peak position and $\Delta E_{2p_{1/2}\text{-}2p_{3/2}}$ being 13.6 eV indicate the +3 oxidation state of iron.[48,49] The shake-up energy separation of the 2$p_{3/2}$ satellite peak was found to be 7.8 eV from the main peak, in accordance with literature for Fe^{3+} compounds (see Table S4.4), further corroborating the Fe^{3+} oxidation state.[50,51]

Then, the magnetic properties were further explored by SQUID magnetometry on a 30 nm thick
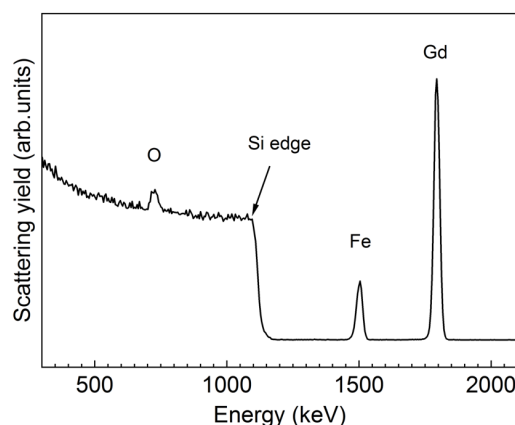
Fig. 4.8 RBS profile spectrum of a 30 nm thick $Gd_3Fe_5O_{12}$ film annealed at 800°C for 30 min in oxygen.
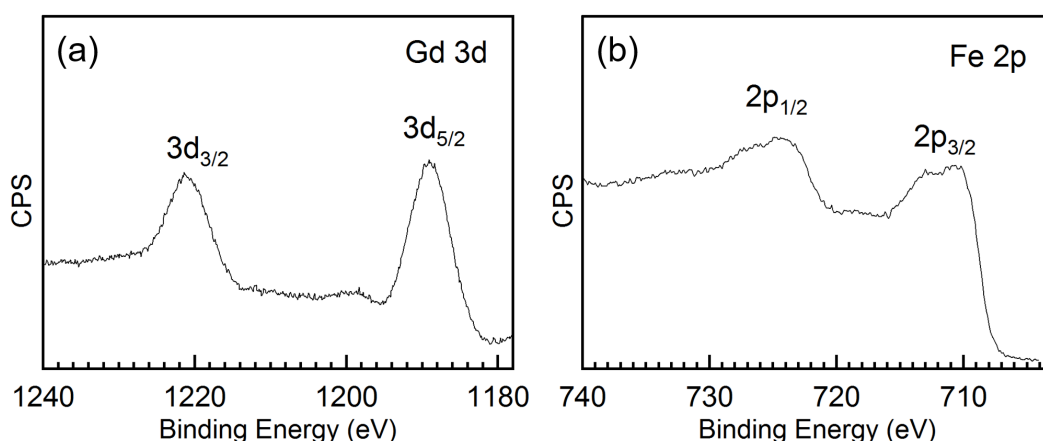
Fig. 4.9 (a) Gd $3d$ core level and (b) Fe $2p$ core level spectra of a 30 nm thick $Gd_3Fe_5O_{12}$ film annealed at 800°C for 30 min in oxygen.

$Gd_3Fe_5O_{12}$ film. Figure S4.7a presents the field dependent magnetic hysteresis loop (M-H) of the sample at 50 K with the magnetic field applied along the in-plane direction. The curve shows fast response upon magnetic field and a trend of saturation.[52] From the hysteresis loop, a saturation magnetization (M_s) of 8.5 emu/g, remnant magnetization M_r of 2.86 emu/g and coercive field (H_c) of 130 Oe can be abstracted. Compared to $\sim$ 500 nm thick sol-gel $Gd_3Fe_5O_{12}$ films,[51] our samples show significantly lower M_s and larger H_c values. We attribute this difference to the small presence of Gd_2O_3 secondary phase identified by XRD and surface imperfections,[53] see Figure S4.8.

The temperature dependent magnetization behavior (M-T) was investigated in the range of 10-350 K at 5 KOe magnetic field under zero field cooling (ZFC) and field cooling conditions (FC). A rapid decrease of magnetization was observed below 50 K with temperature increase, then this trend diminished in 50-350 K with magnetization approaching zero. $Gd_3Fe_5O_{12}$ bulk material has a typical compensation point at the vicinity of $\sim$ 300 K where Gd and Fe moments reverse

directions and result in the total magnetization crosses zero. In our investigation, no compensation temperature (T_{comp}) was observed, see Figure S4.7b. Shifts in T_{comp} from the bulk value has been attributed to cation stoichiometry but also to a thickness/strain effect. Indeed, ultra-thin films can result in a significant rising of T_{comp}.[53–55] Therefore, it is very likely that the 30 nm thickness could contribute to an increase of T_{comp} not being detected under our measuring conditions.

Finally, the synthesis of $Gd_xFe_yO_z$ films from $[Gd(DPDMG)_3]$ and $[Fe(^ipki)_2]$ precursors is here investigated. The starting recipes are shown in Table 4.3.

In this case, as the respective binary oxide GPC are very similar ($[Fe(^ipki)_2]$ 0.4 Å/cycle vs $[Gd(DPDMG)_3]$ 0.6 Å/cycle), simple alternate subcycles was performed (no nanolaminates). Note that alternating the subcycles sequence the final composition of the film is not affected (being 50: 50), which is probably due to the resemblance of the precursor chemistry.

Table 4.3 $Gd_xFe_yO_z$ deposition varying Gd-O/Fe-O subcycle ratios or sequence combining $[Gd(DPDMG)_3]$ and $[Fe(^ipki)_2]$. Cation atomic percentages are obtained from EDX.

Sample	Gd-O subcycles	Fe-O subcycles	Theoretical ratio	Subcycle sequence	Gd (%)	Fe (%)
GFO-Ki-1	2	1	2:1	Gd:Fe	50	50
GFO-Ki-2	2	1	2:1	Fe:Gd	50	50

Analogous to $Gd_xFe_yO_z$ study from $[Gd(DPDMG)_3]$ and $[Fe(Cp)_2]$ sources, the samples were attached in different positions in the chamber to study the elemental distribution. Based on the EDX spectra (Figure S4.9), a Gd/Fe ratio map is generated and shown in Figure 4.10a. Samples near the gas inlet are identified with ~ 1 Gd/Fe cation ratio, the rest of the area is Gd-deficient which is consistent with the high reactivity of $[Gd(DPDMG)_3]$ and its susceptibility to be depleted near the inlet. In addition, the pulse sequence does not affect the stoichiometry of the films which could be ascribed to the chemistry resemblance between $[Gd(DPDMG)_3]$ and $[Fe(^ipki)_2]$.

In order to evaluate the film crystallinity and phase formation of the Gd/Fe ~ 1 samples, XRD θ-2θ scan was carried out. In the as-deposited stage the films are amorphous. Upon 800 °C annealing, two intense reflections are observed at 32- 33 °, see Figure 4.10b. The most intense reflection at 32.5 ° agrees well with the main reflection of $Gd_3Fe_5O_{12}$ phase. Also, weak peaks at 2θ of 28.5°, 36° and 54° would further support the formation of $Gd_3Fe_5O_{12}$. The Bragg reflection that appears as a shoulder at 33 ° could be attributed to $GdFeO_3$, Fe_2O_3 and Gd_2O_3 which hinders an unambiguously identification of this peak. Therefore, the coexistence of $Gd_3Fe_5O_{12}$ with $GdFeO_3$, Fe_2O_3 and Gd_2O_3 is in well agreement with the reported difficulty to stabilize pure phase $GdFeO_3$.[9]

From RBS/NRA, the elemental composition was estimated allowing a comparison of the Fe/Gd and M/O ratio exhibiting values of 0.96 and 0.5, respectively, see Table S4.3, consistent with the
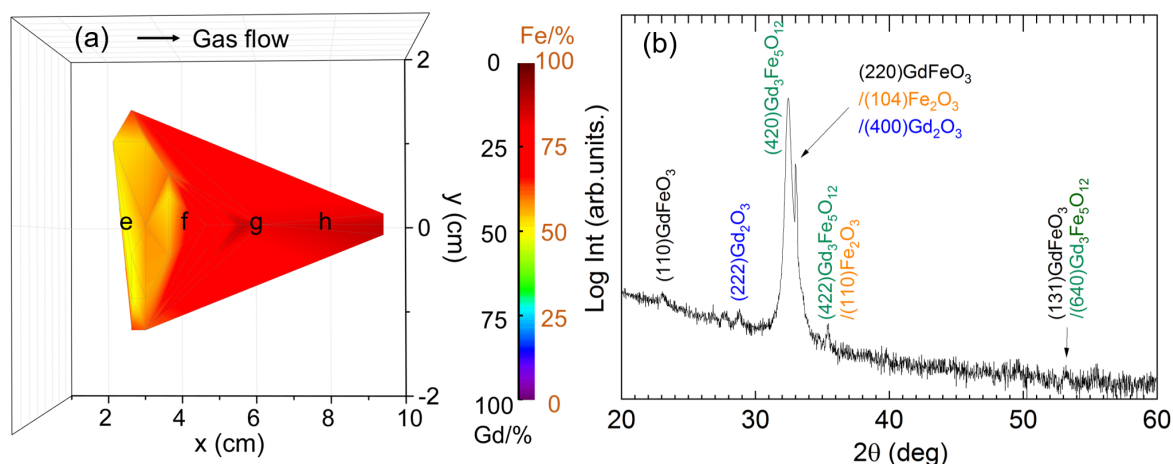
Fig. 4.10 (a) Gd/Fe map of $Gd_xFe_yO_z$ films from 2Gd: 1Fe deposition process combining $[Gd(DPDMG)_3]$ and $[Fe(^ipki)_2]$. (b) XRD θ-2θ scan of a 800 °C annealed 120 nm thick Gd-Fe-O thin films with Gd/Fe ratio ~ 1 prepared from $[Gd(DPDMG)_3]$ and $[Fe(^ipki)_2]$ at 250 °C.

EDX data presented in Table 4.3. The level of C and N contamination was found to be low with 0.9 at.% and 0.3 at.%, respectively. This indicates that the growth mechanisms of the subcycles are not influenced by the different active surface sites. The thin film thickness of 120 nm was calculated from RBS and it is in good agreement with XRR. However, from the RBS graph it is visible that a gradient of Gd and Fe is formed at the interface. This phenomenon could be in part explained because of the initial deposition of Gd_2O_3 cycles acting as seeding layer for the garnet. Consequently, the concentration of Gd at the Si interface is higher, whereas the Fe signal decreases at the low energy edge indicating a decreased Fe concentration in this area. Nonetheless, it is well reported that gadolinium oxide tend to precipitate during the growth of garnet resulting in a gradient depletion along the garnet matrix,[55] which could also contribute to the compositional gradient identified from the RBS profile spectrum.

Fig. 4.11 RBS profile spectrum of a 120 nm thick $Gd_xFe_yO_z$ film annealed at 800°C for 30 min in oxygen.

124

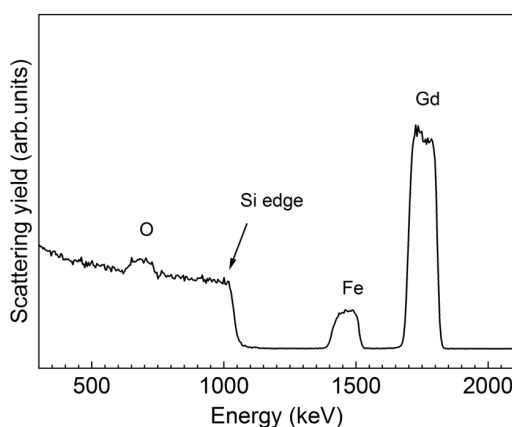Magnetic properties of the 1Gd:1Fe Gd-Fe-O sample were explored using SQUID magnetometry with the magnetic field applied in the in-plane direction. From the magnetic hysteresis loop at 50 K, a M_s value of 26.7 emu/g, M_r of 13.7 emu/g, and coercive field (H_c) of 0.036 KOe were observed, Figure S4.10a. The magnetization as a function of temperature was investigated at 5 KOe from 5 - 300 K, Figure S4.10b. The curve shows no phase transitions in this temperature range. Compared to the previous sample prepared from [Gd(DPDMG)$_3$] and [Fe(Cp)$_2$], here it is observed stronger M_s although no T_{comp} is observed. We attribute this different behavior to the existence of Gd gradient composition along with the coexistence of GdFeO$_3$, Gd$_2$O$_3$ and Fe$_2$O$_3$ both being already identified as key factors on the magnetic behavior of garnet films.[53]

4   Conclusions

We have evaluated the chemical compatibility of tailor-made [Gd(DPDMG)$_3$] and [Fe(^{i}pki)$_2$] and the traditional [Fe(Cp)$_2$] precursors to be deposited by an ALD-type approach. Compatible deposition conditions at 250ºC using ozone as co-reactant and 70 sccm N$_2$ carrier gas flow have been identified and subsequently tested to prepare a series of Gd$_x$Fe$_y$O$_z$ thin films. RBS/NRA analysis helped identifying the metal to oxygen ratio while confirming that ozone ensured a clean reaction of the surface species with complete desorption of the organics. The combination of [Fe(Cp)$_2$] with [Gd(DPDMG)$_3$] resulted in the formation of garnet Gd$_3$Fe$_5$O$_{12}$ as the main phase showing weak magnetic response while the combination of [Fe(^{i}pki)$_2$] and [Gd(DPDMG)$_3$], led to a mixture of crystalline Gd$_3$Fe$_5$O$_{12}$, GdFeO$_3$, and Gd$_2$O$_3$ and traces of Fe$_2$O$_3$ showing strong magnetization response. Therefore, an ALD-type approach has been successfully used to stabilize garnet thin films mixed with minor oxide secondary phases offering new opportunities to advance in the synthesis of complex compounds, difficult to obtain by traditional deposition techniques. Importantly, thorough understanding of the reaction mechanism during the film growth enabled by the use of in-situ characterization tools will be key factors to fully unravel the synthesis of pure phase garnet films.

References

[1] S. Geller. Crystal structure of gadolinium orthoferrite, $GdFeO_3$. *The Journal of Chemical Physics*, 24 (6):1236–1239, 1956.

[2] M. A. Gilleo. Magnetic Properties of a Gadolinium Orthoferrite, $GdFeO_3$, Crystal. *The Journal of Chemical Physics*, 24(6):1239–1243, 1956.

[3] Y. Tokunaga, N. Furukawa, H. Sakai, et al. Composite domain walls in a multiferroic perovskite ferrite. *Nature Materials*, 8(7):558–62, 2009.

[4] A. Panchwanee, V. Raghavendra Reddy, A. Gupta, et al. Study of orthorhombic twins in epitaxial $GdFeO_3$ thin films. *Thin Solid Films*, 669:301–305, 2019.

[5] E. E. Anderson, J. R. Cunningham, and G. E. McDuffie. Magnetic Properties of the Mixed Garnets $(3-x)Y_2O_3 \cdot xGd_2O_3 \cdot 5Fe_2O_3$. *Physical Review*, 116(3):624–625, 1959.

[6] Y. Tokunaga, Y. Taguchi, T.-h. Arima, et al. Electric-field-induced generation and reversal of ferromagnetic moment in ferrites. *Nature Physics*, 8(11):838–844, 2012.

[7] A. A. Serga, A. V. Chumak, and B. Hillebrands. YIG magnonics. *Journal of Physics D: Applied Physics*, 43(26):264002, 2010.

[8] C. Suchomski, C. Reitz, C. T. Sousa, et al. Room temperature magnetic rare-earth iron garnet thin films with ordered mesoporous structure. *Chemistry of Materials*, 25(12):2527–2537, 2013.

[9] N. Kimizuka, A. Yamamoto, H. Ohashi, et al. The stability of the phases in the Ln_2O_3-FeO-Fe_2O_3 systems which are stable at elevated temperatures (Ln: Lanthanide elements and Y). *Journal of Solid State Chemistry*, 49(1):65 – 76, 1983.

[10] M. Bibes, J. E. Villegas, and A. Barthélémy. Ultrathin oxide films and interfaces for electronics and spintronics. *Advances in Physics*, 60(1):5–84, 2011.

[11] M. Coll, J. Fontcuberta, M. Althammer, et al. Towards oxide electronics: a roadmap. *Applied Surface Science*, 482:1–93, 2019.

[12] J. Schmitz. Low temperature thin films for next-generation microelectronics (invited). *Surface and Coatings Technology*, 343:83 – 88, 2018. Selected papers of the "E-MRS 2017 – Symposium Q".

[13] H. H. Sønsteby, E. Skaar, Ø. S. Fjellvåg, et al. A foundation for complex oxide electronics-low temperature perovskite epitaxy. *Nature Communications*, 11(1):1–7, 2020.

[14] M. Ritala and M. Leskelä. Atomic layer deposition. In *Handbook of Thin Films*, pages 103–159. Elsevier, 2002.

[15] S. M. George. Atomic Layer Deposition: An Overview. *Chemical Reviews*, 110(1):111–131, 2010.

[16] H. Knoops, S. Potts, A. Bol, et al. Atomic Layer Deposition. In *Handbook of Crystal Growth*, volume 3, pages 1101–1134. Elsevier, second edition, 2015.

[17] M. Coll and M. Napari. Atomic layer deposition of functional multicomponent oxides. *APL Materials*, 7(11):110901, 2019.

References

[18] M. Lie, O. Nilsen, H. Fjellvåg, et al. Growth of $La_{1-x}Sr_xFeO_3$ thin films by atomic layer deposition. *Dalton Transactions*, (3):481–489, 2009.

[19] A. J. M. Mackus, J. R. Schneider, C. MacIsaac, et al. Synthesis of doped, ternary, and quaternary materials by atomic layer deposition: A review. *Chemistry of Materials*, 2019.

[20] J.-H. Kim, J.-Y. Kim, and S.-W. Kang. Film growth model of atomic layer deposition for multicomponent thin films. *Journal of Applied Physics*, 97(9):093505, 2005.

[21] H. H. Sønsteby, H. Fjellvåg, and O. Nilsen. Functional perovskites by atomic layer deposition-an overview. *Advanced Materials Interfaces*, 4(8):1600903, 2017.

[22] S. Vangelista, A. Lamperti, C. Wiemer, et al. Atomic layer deposition of hexagonal $ErFeO_3$ thin films on SiO_2/Si. *Thin Solid Films*, 604:18–22, 2016.

[23] C. Bohr, P. Yu, M. Scigaj, et al. Atomic scale growth of $GdFeO_3$ perovskite thin films. *Thin Solid Films*, 698:137848, 2020.

[24] R. G. Gordon. ALD Precursors and Reaction Mechanisms. In C. S. Hwang, editor, *Atomic Layer Deposition for Semiconductors*, chapter 2, pages 15–46. Springer, Boston, MA, 2014.

[25] T. Hatanpää, M. Ritala, and M. Leskelä. Precursors as enablers of ALD technology: Contributions from university of helsinki. *Coordination Chemistry Reviews*, 257(23-24):3297–3322, 2013.

[26] D. Peeters, A. Sadlo, K. Lowjaga, et al. Nanostructured Fe_2O_3 processing via water-assisted ald and low-temperature CVD from a versatile iron ketoiminate precursor. *Advanced Materials Interfaces*, 4 (18):1700155, 2017.

[27] A. P. Milanov, R. A. Fischer, and A. Devi. Synthesis, characterization, and thermal properties of homoleptic rare-earth guanidinates: Promising precursors for MOCVD and ALD of rare-earth oxide thin films. *Inorganic Chemistry*, 47(23):11405–11416, 2008.

[28] A. P. Milanov, K. Xu, A. Laha, et al. Growth of crystalline Fe_2O_3 thin films with a high-quality interface on Si(100) by low-temperature H_2O-assisted atomic layer deposition. *Journal of the American Chemical Society*, 132(1):36–37, 2010.

[29] S. Macke, A. Radi, J. E. Hamann-Borrero, et al. Element specific monolayer depth profiling.

[30] M. Mayer. Improved physics in SIMNRA 7. *Nuclear Instruments and Methods in Physics Research Section B: Beam Interactions with Materials and Atoms*, 332:176–180, 2014.

[31] Y. Wang, M. Dai, M.-T. Ho, et al. Infrared characterization of hafnium oxide grown by atomic layer deposition using ozone as the oxygen precursor. *Applied Physics Letters*, 90(2):022906, 2007.

[32] F. Sandiumenge, A. Cavallaro, J. Gàzquez, et al. Mechanisms of nanostructural and morphological evolution of CeO_2 functional films by chemical solution deposition. *Nanotechnology*, 16(9):1809–1813, 2005.

[33] S. Seppälä, J. Niinistö, M. Mattinen, et al. Atomic layer deposition of lanthanum oxide with heteroleptic cyclopentadienyl-amidinate lanthanum precursor - Effect of the oxygen source on the film growth and properties. *Thin Solid Films*, 660:199–206, 2018.

[34] J. R. Schneider, J. G. Baker, and S. F. Bent. The influence of ozone: Superstoichiometric oxygen in atomic layer deposition of Fe_2O_3 using tert-Butylferrocene and O_3. *Advanced Materials Interfaces*, 7 (11):2000318, 2020.

[35] H. H. Sønsteby, A. Yanguas-Gil, and J. W. Elam. Consistency and reproducibility in atomic layer deposition. *Journal of Vacuum Science & Technology A*, 38(2):020804, 2020.

[36] J. Niinistö, N. Petrova, M. Putkonen, et al. Gadolinium oxide thin films by atomic layer deposition. *Journal of Crystal Growth*, 285(1):191 – 200, 2005.

[37] B. Han, J. M. Park, K. H. Choi, et al. Atomic layer deposition of stoichiometric Co_3O_4 films using bis(1,4-di-iso-propyl-1,4-diazabutadiene) cobalt. *Thin Solid Films*, 589:718–722, 2015.

[38] B. M. Klahr, A. B. Martinson, and T. W. Hamann. Photoelectrochemical investigation of ultrathin film iron oxide solar cells prepared by atomic layer deposition. *Langmuir*, 27(1):461–8, 2011.

[39] A. B. F. Martinson, M. J. DeVries, J. A. Libera, et al. Atomic layer deposition of Fe_2O_3 using ferrocene and ozone. *The Journal of Physical Chemistry C*, 115(10):4333–4339, 2011.

[40] X. Li, N. C. Fan, and H. J. Fan. A micro-pulse process of atomic layer deposition of iron oxide using ferrocene and ozone precursors and Ti-doping. *Chemical Vapor Deposition*, 19(4-6):104–110, 2013.

[41] A. Devi. 'Old chemistries' for new applications: Perspectives for development of precursors for MOCVD and ALD applications. *Coordination Chemistry Reviews*, 257(23-24):3332–3384, 2013.

[42] M. Leskelä and M. Ritala. Atomic layer deposition chemistry: Recent developments and future challenges. *Angewandte Chemie International Edition*, 42(45):5548–5554, 2003.

[43] A. Zydor, V. G. Kessler, and S. D. Elliott. First principles simulation of reaction steps in the atomic layer deposition of titania: dependence of growth on lewis acidity of titanocene precursor. *Phys. Chem. Chem. Phys.*, 14:7954–7964, 2012.

[44] G. Dey and S. D. Elliott. Quantum chemical study of the effect of precursor stereochemistry on dissociative chemisorption and surface redox reactions during the atomic layer deposition of the transition metal copper. *The Journal of Physical Chemistry C*, 119(11):5914–5927, 2015.

[45] K. L. Pickrahn, A. Garg, and S. F. Bent. ALD of ultrathin ternary oxide electrocatalysts for water splitting. *ACS Catalysis*, 5(3):1609–1616, 2015.

[46] J. W. Elam and S. M. George. Growth of ZnO/Al_2O_3 alloy films using atomic layer deposition techniques. *Chemistry of Materials*, 15(4):1020–1028, 2003.

[47] D. Raiser and J. P. Deville. Study of XPS photoemission of some gadolinium compounds. *Journal of Electron Spectroscopy and Related Phenomena*, 57(1):91–97, 1991.

[48] E. Paparazzo. XPS analysis of iron aluminum oxide systems. *Applied Surface Science*, 25(1):1–12, 1986.

[49] A. P. Grosvenor, B. A. Kobe, M. C. Biesinger, et al. Investigation of multiplet splitting of Fe 2p XPS spectra and bonding in iron compounds. *Surface and Interface Analysis*, 36(12):1564–1574, 2004.

[50] P. C. J. Graat and M. A. J. Somers. Simultaneous determination of composition and thickness of thin iron-oxide films from XPS Fe 2p spectra. *Applied Surface Science*, 100-101:36–40, 1996.

References

[51] F. Söderlind, L. Selegård, P. Nordblad, et al. Sol–gel synthesis and characterization of polycrystalline GdFeO$_3$ and Gd$_3$Fe$_5$O$_{12}$ thin films. *Journal of Sol-Gel Science and Technology*, 49(2):253–259, 2009.

[52] M. Pardavi-Horvath. Microwave applications of soft ferrites. *Journal of Magnetism and Magnetic Materials*, 215-216:171–183, 2000.

[53] E. Sawatzky and E. Kay. Magnetic and Structural Properties of Epitaxial and Polycrystalline GdIG Films Prepared by rf Sputtering. *Journal of Applied Physics*, 42(1):367–375, 1971.

[54] E. Sawatzky and E. Kay. Preparation of garnet films by sputtering. *Journal of Applied Physics*, 39 (10):4700–4706, 1968.

[55] M. Oron, I. Barlow, and W. Traber. Ferrimagnetic garnet thin films: Growth, structure and some magnetic properties. *Journal of Materials Science*, 4(3):271–281, 1969.

Supporting Information for

Fabrication of $Gd_xFe_yO_z$ films using an atomic layer deposition-type approach

Pengmei Yu,[†] Sebastian Beer,[‡] Anjana Devi,[‡] Mariona Coll[†,*]

[†]*Institut de Ciència de Materials de Barcelona (ICMAB-CSIC), Campus de la UAB, 08193 Bellaterra, Barcelona, Spain. Tel: +34 935801853, Email: mcoll@icmab.es*

[‡]*Inorganic Materials Chemistry, Ruhr-University Bochum, Universitätsstraße 150, Bochum 44801, Germany*

5 Fe precursors for ALD

The deposition of iron oxide by ALD has seen a rich variety of precursors explored, *viz.* β-diketonates, alkoxide, halides, metallocenes, amidinate, ketoiminate, etc. as tabulated in Table S4.1. Among these precursors ferrocene ($[Fe(Cp)_2]$) has been intensively studied due to its commercial availability and low cost. However, despite the fact that its high stability enables safe handling in ambient conditions, ALD iron oxide from $[Fe(Cp)_2]$ requires relatively high temperature with molecular O_2[1,2] (> 350 °C) or a strong oxidant like O_3.

Nonetheless, the deposition with ferrocene has been reported challenging. For instance, Klahr *et al.*[3] observed a decreased GPC after the first few hundred of cycles, which was believed to be caused by the self-catalytic decomposition of $[Fe(Cp)_2]$. Linear deposition rate was demonstrated to be achieved by introducing TiO_2 co-deposition.[4] In addition, Avila *et al.* once described $[Fe(Cp)_2]$ condensation in the pump and generation of pump malfunction.[5]

6 Gd precursors for ALD

In Table S4.2, the precursors adopted for the ALD Gd_2O_3 synthesis are summarised. β-diketonate $Gd(thd)_3$ and cyclopentadienyl $Gd(^iPrCp)_3$ precursors were mainly used for ALD Gd_2O_3, however the films were mostly reported to be contaminated. Other studies performed combining water and Gd cyclopentadienyl $Gd(CpCH_3)_3$, alkoxide $Gd(mmp)_3$, silylamide $Gd[N(SiMe_3)_2]_3$, where either non-saturative ALD growth or carbon/hydrogen contamination were observed.[19] ALD Gd_2O_3 process was observed to be self-limiting from another alkoxide $Gd(DMB)_3$ with water, nonetheless the films were also found with carbon and hydrogen impurities. Milanov *et al.*[20] demonstrated an alternative Gd guanidinate $[Gd(DPDMG)_3]$ (employed in the current study) with

Table S4.1 Fe_2O_3 precursors tested in atomic layer deposition process

Fe precursor	Oxygen source	Deposition temperature	GPC (/cycle)	Impurity	Ref
$Fe(acac)_3$	O_2	RT-150	-	-	6
$Fe(thd)_3$	O_3	186	0.11	-	7
$Fe(thd)_3$*	O_3	138-380	0.1-1	-	8
$Fe_2(O^tbu)_6$*	H_2O	130-170	0.26±0.04	-	9
$Fe_2(O^tbu)_6$*	H_2O	180	0.62	-	10
$FeCl_3$	H_2O	500	0.2	-	11
$FeCl_3$	H_2O	200-350	0.6	Cl	12
$FeCl_3$	H_2O	210-360	0.65	Cl	13
$Fe(Cp)_2$	O_2	350-500	1.4	C	1
$Fe(Cp)_2$	O_2	367-534	0.15	-	2
$Fe(Cp)_2$	O_3/O_2 mixture	200	0.2	-	14
$Fe(Cp)_2$	O_3	200	0.62	-	3
$Fe(Cp)_2$	O_3	170-350	1.4	H	15
$Fe(Cp)_2$	O_3	200-325	0.4-0.5	-	4
$Fe(2,4-C_7H_{11})_2$*	H_2O_2	60-120	0.4-0.6	-	16
$Fe(2,4-C_7H_{11})_2$*	O_2	60-120	0.2-0.3	-	16
$Fe(2,4-C_7H_{11})_2$*	O_3	60-120	0.5-0.9	-	16
$Fe(hfa)_2TMEDA$*	O_3	150-350	<0.2	C,H	17
FeAMD	H_2O	130-200	0.55±0.05	-	5
$Fe(^ipki)_2$*	H_2O	100-275	0.47-1.1	C	18

* synthesized

acac = acetylacetonate

$2,4-C_7H_{11}=2,4-$methylpentadienyl

hfa = 1,1,1,5,5,5-hexafluoro-2,4-pentanedionate, TMEDA = N,N,N$'$,N$'$-tetramethylethylenediamine

^{i}pki = N-isopropyl ketoiminate

Table S4.2 Gd- precursors tested in atomic layer deposition process

Gd precursor	Oxygen source	Deposition temperature (°C)	GPC (/cycle)	Impurity	Ref
$Gd[N(Si(Me)_3)_2]_3$	H_2O	150-300	0.6-2.4	-	21
$Gd(thd)_3$*	O_3	300	0.3	C,F,H	22
$Gd(thd)_3$*	O_3	225-400	0.3	C,H	23
$Gd(MeCp)_3$	H_2O	150-350	0.75-2.5	H	23
$Gd(mmp)_3$*	H_2O	200-300	0.1-1	-	24
$Gd(DMB)_3$*	H_2O	300-400	0.3-0.5	C,H	25
$Gd(DPDMG)_3$*	H_2O	160-300	1.1	-	20
$Gd(^iPrCp)_3$	O_2 plasma	150-350	1-3.5	-	26
$Gd(^iPrCp)_3$	H_2O	300	0.5-2	H	27
$Gd(^iPrCp)_3$	O_3	250	0.1-0.4	C	28
$Gd(^iPrCp)_2(^iPr-amd)$*	H_2O	200-325	0.7-1.7	C,H	29
$Gd(^iPrCp)_2(^iPr-amd)$*	O_3	200-350	0.4-1.3	C	29

* synthesized
thd = 2,2,6,6-tetramethylheptane-3,5-dione
mmp = $OCMe_2CH_2OMe$
DMB = $OC(CH_3)_2CH(CH_3)_2)$
DPDMG = $(^iPrN)_2CNMe_2$
amd = Amidinate

considerable thermal stability and optimal reactivity toward H_2O to facilitate higher growth rates, leading to well-defined Gd_2O_3 deposition behaviour.

7 ALD valving systems

In Figure S4.1 it is shown a scheme of the ALD reactor that is employed in this study. Three different valving systems, that are here identified as flow mode (F), pressure-boost (PB) and exposure mode (E), could be achieved by manipulating the exit valve and ALD valves highlighted in the picture. In F mode a continuous flow of inert gas carries the precursor to the reaction chamber. For low-vapor pressure precursors, PB mode is used with an elevated vapor pressure before precursor pulses. E mode was applied to enable sufficient surface reaction and deposition homogeneity. In this case, the gas exit valve was closed after precursor dosing. These three modes are explained in more detail in the Experimental part of the main manuscript.

8 Gd_2O_3 films from [Gd(DPDMG)$_3$]

The optimization parameters for gadolinium oxide deposition using an ALD-type approach are displayed in Figure S4.2a heating Gd(DPDMG)$_3$ at $T_{Gd-subl}$=135 °C under pressure-boost
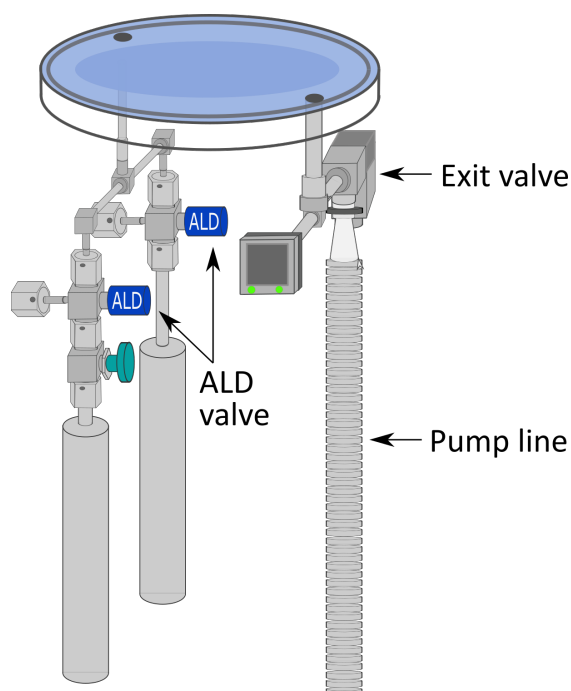
Fig. S4.1 Illustration of the valving system of the ALD reactor: different modes (specifically, flow mode, pressure-boost or exposure mode) can be realised by manipulating the valve opening and closure. (Adapted from Savannah 100 user manual[30]).

(PB)/flow (F) mode at 160 - 250 °C deposition temperature. Upper panel (blue) identifies depositions investigated using H_2O as co-reactant. Lower panel identifies those tested using ozone as oxidant. EDX spectrum from the sample prepared in pressure-boost with ozone at 250 °C is shown in Figure S4.2b.
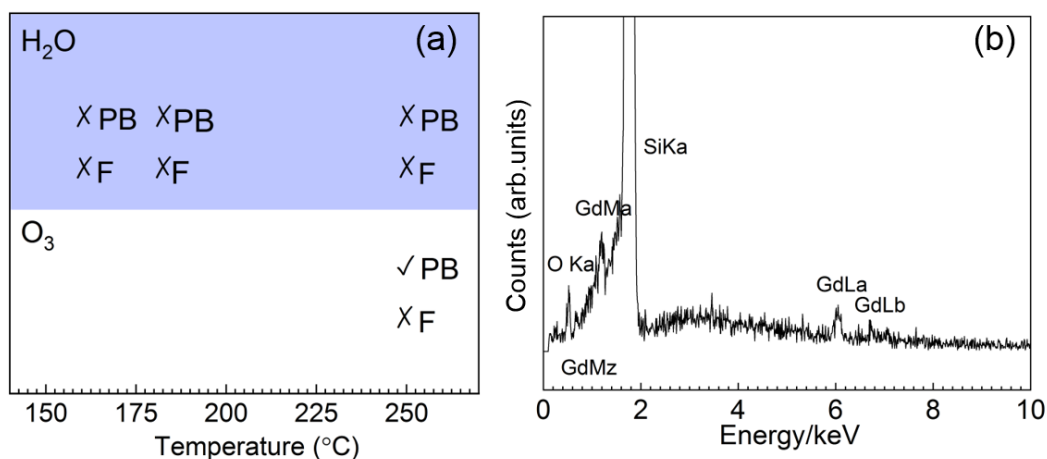

Fig. S4.2 (a) Optimization of Gd_2O_3 deposition temperature from [Gd(DPDMG)$_3$] and O_3/H_2O at sublimation temperature of 135 °C using pressure-boost (PB)/flow (F) mode. (✗: no Gd detection; ✓: Gd detection). (b) EDX spectra from as-deposited sample from [Gd(DPDMG)$_3$] and O_3 at the deposition temperature of 250 °C.

The element concentrations, ratio and film thicknesses obtained from RBS studies for the optimized samples in this work are listed in Table S4.3.

Table S4.3 Summary of composition and thickness for Gd_2O_3, Fe_2O_3, Gd-Fe-O ([Fe(Cp)$_2$]+[Gd(DPDMG)$_3$]) and Gd-Fe-O ([Fe(^{i}pki)$_2$]+[Gd(DPDMG)$_3$]) samples from RBS study

Sample	C (%)	N (%)	O (%)	Fe (%)	Gd (%)	Metal/O	Fe/Gd	Thickness (nm)
Gd_2O_3	3.3 ± 0.2	0.4 ± 0.5	73.8 ± 0.8	0.2 ± 0.0	22.3 ± 0.1	0.30	-	80
Fe_2O_3	0.8 ± 0.1	0.3 ± 0.4	65.0 ± 0.7	33.8 ± 0.2	0.0 ± 0.0	0.52	-	60
Gd-Fe-O from ([Fe(Cp)$_2$]+[Gd(DPDMG)$_3$])	1.4 ± 0.3	1.0 ± 0.8	67.6 ± 1.4	17.6 ± 0.2	12.4 ± 0.1	0.44	1.41	30
Gd-Fe-O from ([Fe(^{i}pki)$_2$]+[Gd(DPDMG)$_3$]	0.9 ± 0.1	0.2 ± 0.2	63.2 ± 0.5	17.5 ± 0.1	18.2 ± 0.1	0.5	0.96	120

Figure S4.3 shows typical XRR pattern of Gd_2O_3 films that allowed to build the thickness map in the main manuscript (Figure 4.2).
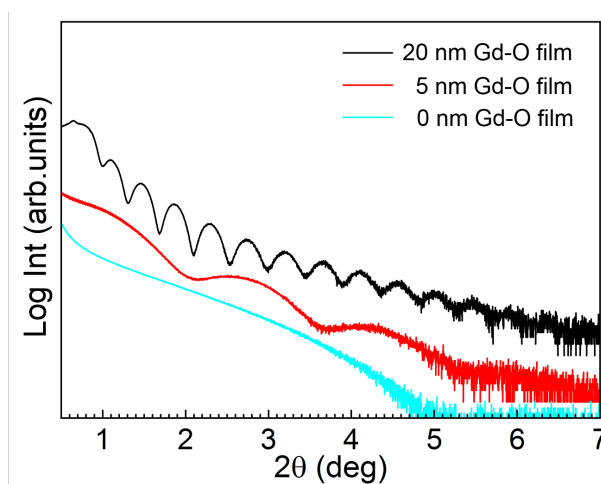

Fig. S4.3 XRR curves of Gd_2O_3/Si samples located at different chamber positions deposited using 40 sccm gas flow.

9 Fe_2O_3 films from [Fe(Cp)$_2$]

The deposition of Fe_2O_3 using [Fe(Cp)$_2$] was studied in the 150 - 250 °C temperature window in flow mode (70 sccm) repeating 2000 cycles. Fe was only detected when ozone was used as co-reactant for a temperature range of 200 - 250 °C, see Figure S4.4a. Typical EDX analysis from an as-deposited film is shown in Figure S4.4b.
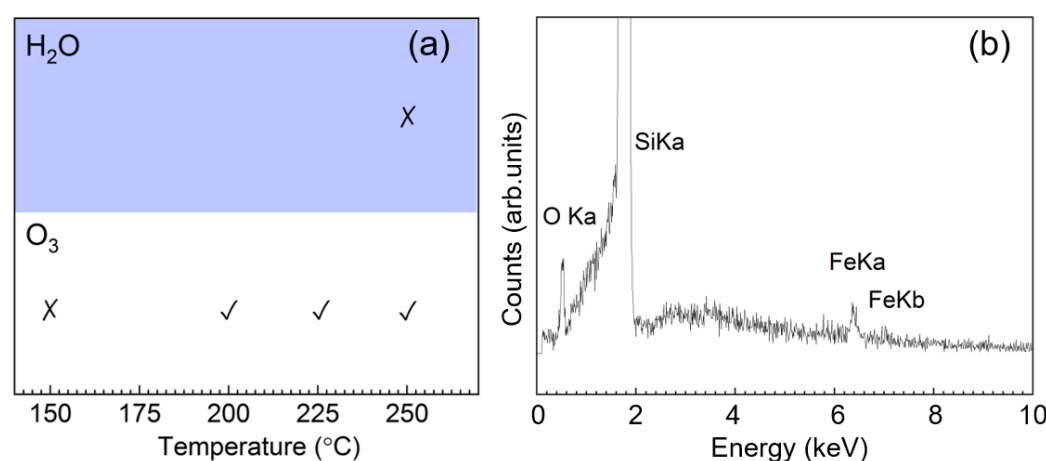
Fig. S4.4 (a) Optimization of Fe_2O_3 deposition from $[Fe(Cp)_2]$ and ozone/water using flow mode with 70 sccm flow. (✗: no Fe detection; ✓: Fe detection) (b) EDX spectrum of as-deposited 15 nm film prepared from $[Fe(Cp)_2]$ and ozone at T=250 °C.

10 Fe_2O_3 films from $[Fe(^ipki)_2]$

Scheme of the parameters investigated to optimize the deposition of Fe_2O_3 from $[Fe(^ipki)_2]$ at $T_{Fe\text{-}subl}$= 100 °C using ozone and water as co-reactant under pressure boost or flow mode at deposition temperature window of 150-250 °C is shown in Figure S4.5a. No iron was detected in the films for these conditions. Therefore, sublimation temperature was increased to 130 °C, Figure S4.5b. EDX spectrum shows the presence of Fe in the deposited films performed at 250 °C with ozone, heating the iron precursor at 130 °C, Figure S4.5c.
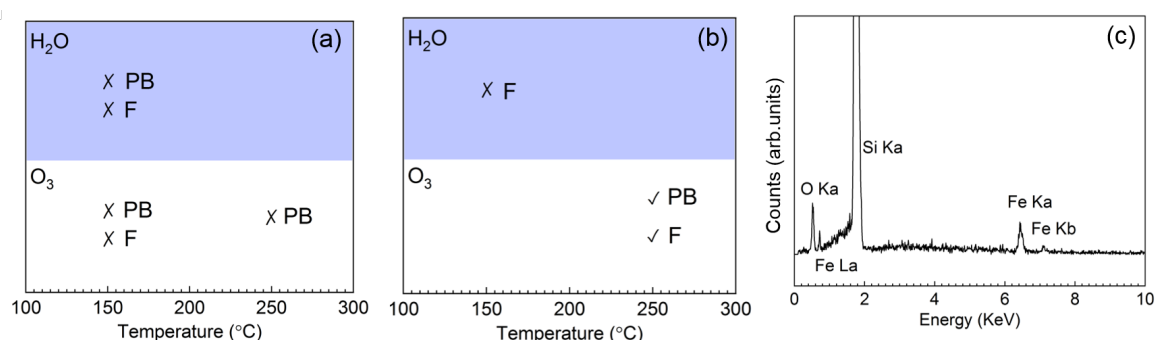
Fig. S4.5 Optimization of Fe_2O_3 deposition from $[Fe(^ipki)_2]$ and H_2O/O_3 at sublimation temperature at (a) 100 °C and (b) 130 °C; PB is under pressure boost mode while F means using flow mode. The processes were carried out with precursor sublimation temperature at 100 °C under 70 sccm flow with 2000 cycles. (✗: no Fe detection; ✓: Fe detection). (c) Exemplary EDX spectra of the deposited Fe_2O_3 films.

11 $Gd_xFe_yO_z$ from [Gd(DPDMG)$_3$] and [Fe(Cp)$_2$]

XPS survey spectrum from $Gd_xFe_yO_z$ sample combining Gd(DPDMG)$_3$ and Fe(Cp)$_2$ reveals the existence of Gd, Fe, O, C and Si, Figure S4.6. The absence of the N *1s* peaks at ~ 400 eV indicates the decomposition of nitrogen containing DPDMG ligand. The quantitative ratio of Gd and Fe in the $Gd_3Fe_5O_{12}$ film was extracted from the survey spectrum taking into consideration the relative sensitivity factors (RSF) for each element.[31] The cation ratio Gd/Fe is found to be 1.77 which is very close to the theoretical value 1.67 calculated from the chemical formula of $Gd_3Fe_5O_{12}$.
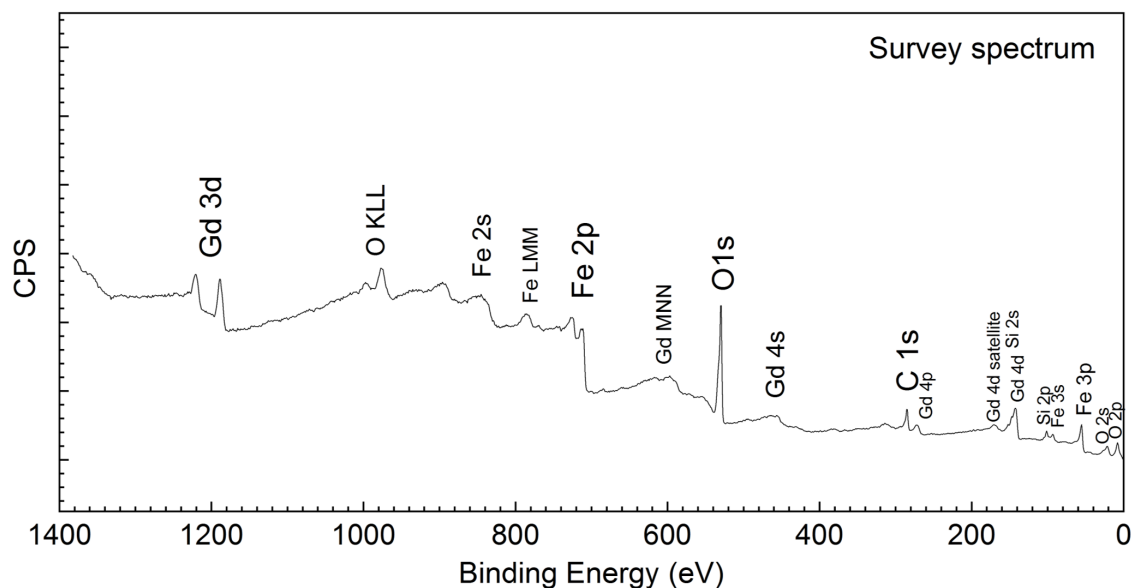

Fig. S4.6 XPS survey spectrum of a 30 nm thick $Gd_3Fe_5O_{12}$ film annealed at 800°C for 30 min in oxygen.

Reported binding energy values for of Gd *3d* and Fe *2p* core level spectra in $Gd_3Fe_5O_{12}$, Gd_2O_3 and Fe_2O_3 are summarized in Table S4.4 and compared with our data.

Table S4.4 The binding energy positions of Gd 3d and Fe 2p core level spectra in $Gd_3Fe_5O_{12}$, Gd_2O_3 or Fe_2O_3 samples

	Gd 3$d_{3/2}$ (eV)	Gd 3$d_{5/2}$ (eV)	Fe 2$p_{1/2}$ (eV)	Fe 2$p_{3/2}$ (eV)	$\Delta E_{(Satellite-Fe2p_{3/2})}$ (eV)	Ref.
$Gd_3Fe_5O_{12}$ thin films	1221.1	1189.1	725.0	711.4	7.8	This work
$Gd_3Fe_5O_{12}$ films	-	1186.5	-	710.5	-	[32]
Gd_2O_3 thin films	1219.4	1187.0	-	-	-	[33]
Gd_2O_3 powder	1219.6	1187.6	-	-	-	[34]
Gd_2O_3 powder	-	1187.5	-	-	-	[35]
Gd_2O_3 nanocrystal	1220.4	1187.9	-	-	-	[36]
Fe_2O_3 films	-	-	724.3	711.2	-	[37]
Fe_2O_3 films	-	-	724.5	710.9	-	[18]
Fe_2O_3 powder	-	-	-	711.2	7.8	[38]
$\alpha-Fe_2O_3$ powder	-	-	-	710.8	8.5	[39]
$\gamma-Fe_2O_3$ powder	-	-	-	711.0	8.3	[39]
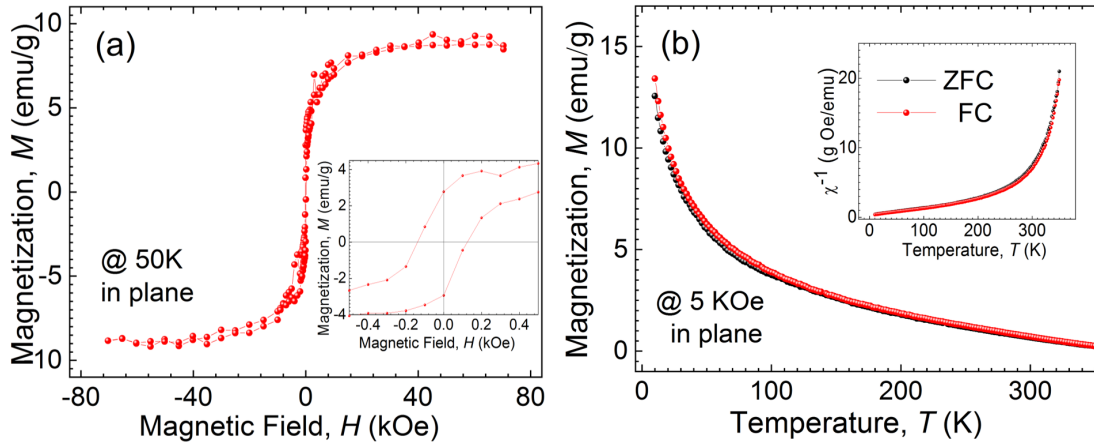
Fig. S4.7 In plane magnetic measurements of a 30 nm thick $Gd_3Fe_5O_{12}$ sample annealed at 800°C for 30 min in oxygen: (a) field-independent magnetic hysteresis loop (M-H) at 50 K (zoom-in spectra see inset panel); (b) temperature-dependent magnetization curve (M-T) under ZFC-FC conditions at 5 KOe. Inset in (b) shows the derived reversed susceptibility under the same conditions.

The post-annealed $Gd_3Fe_5O_{12}$ film morphology was analyzed by SEM. The overall films are homogeneous and smooth, however surface imperfections are identified, Figure S4.8.

138

Fig. S4.8 SEM image showing the morphology with surface defects on a 30 nm thick $Gd_3Fe_5O_{12}$ film annealed at 800°C for 30 min in oxygen.
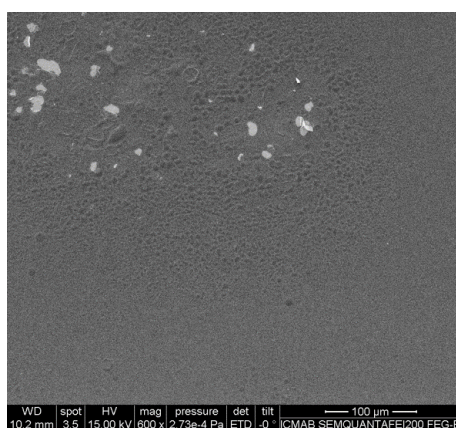
12 $Gd_xFe_yO_z$ from [Gd(DPDMG)$_3$] and [Fe(^{i}pki)$_2$]

The EDX spectra of samples located at different places along the gas flow path in the chamber are illustrated in Figure S4.9 (from **e** to **h** moving from gas inlet toward outlet). At position **e** the well-defined peaks of Gd and Fe are observed; moving to the gas outlet the films become Fe rich. This observation is also true when the Gd_2O_3, Fe_2O_3 subcycles are reversed.
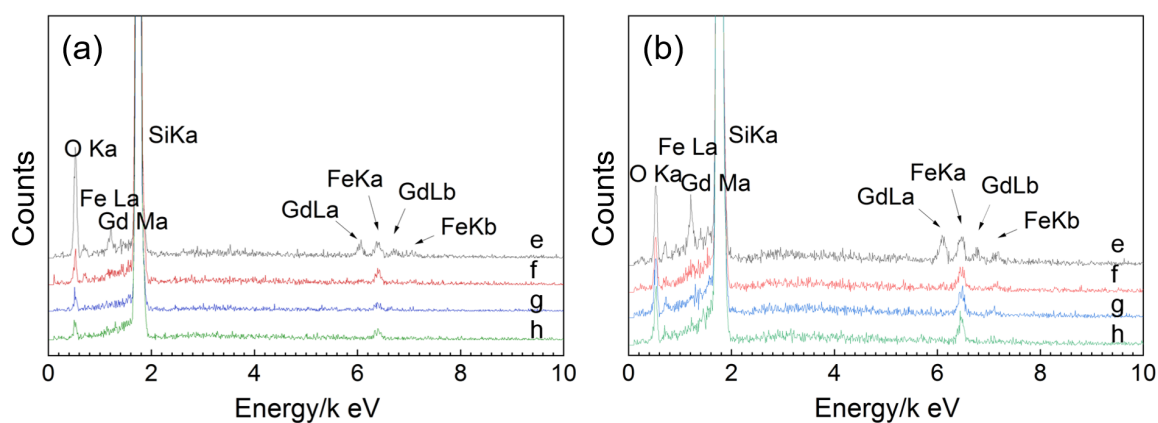
Fig. S4.9 EDX spectra of Gd-Fe-O samples from 2Gd: 1Fe and 1Fe: 2Gd deposition process combining [Gd(DPDMG)$_3$] and [Fe(^{i}pki)$_2$] that are located at different places along the gas flow path in the reaction chamber (corresponding to the marks in Figure 4.10a).
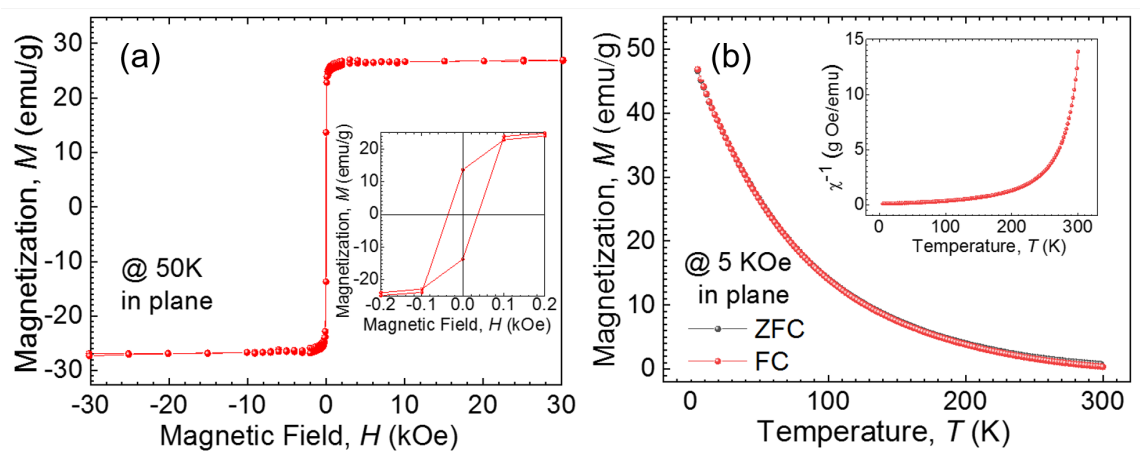
Fig. S4.10 In plane magnetic measurements of a 120 nm thick $Gd_xFe_yO_z$ sample prepared from [$Gd(DPDMG)_3$] and [$Fe(^ipki)_2$] annealed at 800°C for 30 min in oxygen: (a) field-independent magnetic hysteresis loop (M-H) at 50 K (zoom-in spectra see inset panel); (b) temperature-dependent magnetization curve (M-T) under ZFC-FC conditions at 5 KOe. Inset in (b) shows the derived reversed susceptibility under the same conditions.

References

[1] M. Rooth, A. Johansson, K. Kukli, et al. Atomic layer deposition of iron oxide thin films and nanotubes using ferrocene and oxygen as precursors. *Chemical Vapor Deposition*, 14(3-4):67–70, 2008.

[2] J. R. Scheffe, A. Francés, D. M. King, et al. Atomic layer deposition of iron(iii) oxide on zirconia nanoparticles in a fluidized bed reactor using ferrocene and oxygen. *Thin Solid Films*, 517(6): 1874–1879, 2009.

[3] B. M. Klahr, A. B. Martinson, and T. W. Hamann. Photoelectrochemical investigation of ultrathin film iron oxide solar cells prepared by atomic layer deposition. *Langmuir*, 27(1):461–8, 2011.

[4] X. Li, N. C. Fan, and H. J. Fan. A micro-pulse process of atomic layer deposition of iron oxide using ferrocene and ozone precursors and Ti-doping. *Chemical Vapor Deposition*, 19(4-6):104–110, 2013.

[5] J. R. Avila, D. W. Kim, M. Rimoldi, et al. Fabrication of thin films of α-Fe$_2$O$_3$ via atomic layer deposition using iron bisamidinate and water under mild growth conditions. *ACS Appl. Mater. Interfaces*, (7):1613816142, 2015.

[6] M. de Ridder, P. C. van de Ven, R. G. van Welzenis, et al. Growth of iron oxide on yttria-stabilized zirconia by atomic layer deposition. *The Journal of Physical Chemistry B*, 106(51):13146–13153, 2002.

[7] O. Nilsen, M. Lie, S. Foss, et al. Effect of magnetic field on the growth of α-Fe$_2$O$_3$ thin films by atomic layer deposition. *Applied Surface Science*, 227(1-4):40–47, 2004.

[8] M. Lie, H. Fjellvåg, and A. Kjekshus. Growth of Fe$_2$O$_3$ thin films by atomic layer deposition. *Thin Solid Films*, 488(1-2):74–81, 2005.

[9] J. Bachmann, Jing, M. Knez, et al. Ordered iron oxide nanotube arrays of controlled geometry and tunable magnetism by atomic layer deposition. *Journal of the American Chemical Society*, 129(31): 9554–9555, 2007.

[10] Y. Lin, S. Zhou, S. W. Sheehan, et al. Nanonet-based hematite heteronanostructures for efficient solar water splitting. *Journal of the American Chemical Society*, 133(8):2398–2401, 2011.

[11] M. Aronniemi, J. Saino, and J. Lahtinen. Characterization and gas-sensing behavior of an iron oxide thin film prepared by atomic layer deposition. *Thin Solid Films*, 516(18):6110–6115, 2008.

[12] J. A. Klug, N. G. Becker, N. R. Groll, et al. Heteroepitaxy of group IV-VI nitrides by atomic layer deposition. *Applied Physics Letters*, 103(21):1–5, 2013.

[13] A. Tanskanen, O. Mustonen, and M. Karppinen. Simple ALD process for ε-Fe$_2$O$_3$ thin films. *APL Materials*, 5(5), 2017.

[14] J. Escrig, J. Bachmann, J. Jing, et al. Crossover between two different magnetization reversal modes in arrays of iron oxide nanotubes. *Physical Review B*, 77(21):214421, 2008.

[15] A. B. F. Martinson, M. J. DeVries, J. A. Libera, et al. Atomic layer deposition of Fe$_2$O$_3$ using ferrocene and ozone. *The Journal of Physical Chemistry C*, 115(10):4333–4339, 2011.

[16] S. C. Riha, J. M. Racowski, M. P. Lanci, et al. Phase discrimination through oxidant selection in low-temperature atomic layer deposition of crystalline iron oxides. *Langmuir*, 29(10):3439–3445, 2013.

[17] J. E. Bratvold, G. Carraro, D. Barreca, et al. An iron(II) diketonate-diamine complex as precursor for thin film fabrication by atomic layer deposition. *Applied Surface Science*, 347:861–867, 2015.

[18] D. Peeters, A. Sadlo, K. Lowjaga, et al. Nanostructured Fe_2O_3 processing via water-assisted ald and low-temperature CVD from a versatile iron ketoiminate precursor. *Advanced Materials Interfaces*, 4 (18):1700155, 2017.

[19] A. Devi. 'Old chemistries' for new applications: Perspectives for development of precursors for MOCVD and ALD applications. *Coordination Chemistry Reviews*, 257(23-24):3332–3384, 2013.

[20] A. P. Milanov, K. Xu, A. Laha, et al. Growth of crystalline Fe_2O_3 thin films with a high-quality interface on Si(100) by low-temperature H_2O-assisted atomic layer deposition. *Journal of the American Chemical Society*, 132(1):36–37, 2010.

[21] A. C. Jones, H. C. Aspinall, P. R. Chalker, et al. Recent developments in the MOCVD and ALD of rare earth oxides and silicates. *Materials Science and Engineering: B*, 118(1-3):97–104, 2005.

[22] J. Päiväsaari, M. Putkonen, and L. Niinistö. A comparative study on lanthanide oxide thin films grown by atomic layer deposition. *Thin Solid Films*, 472(1):275 – 281, 2005.

[23] J. Niinistö, N. Petrova, M. Putkonen, et al. Gadolinium oxide thin films by atomic layer deposition. *Journal of Crystal Growth*, 285(1):191 – 200, 2005.

[24] R. Potter, P. Chalker, T. Manning, et al. Deposition of HfO_2, Fe_2O_3 and PrO_x by liquid injection ald techniques. *Chemical Vapor Deposition*, 11(3):159–169, 2005.

[25] K. Kukli, T. Hatanpää, M. Ritala, et al. Atomic layer deposition of gadolinium oxide films. *Chemical Vapor Deposition*, 13(10):546–552, 2007.

[26] S. A. Vitale, P. W. Wyatt, and C. J. Hodson. Plasma-enhanced atomic layer deposition and etching of high-k gadolinium oxide. *J. Vac. Sci. Technol. A*, 30:1–130, 2012.

[27] J. H. Han, L. Nyns, A. Delabie, et al. Reaction chemistry during the atomic layer deposition of Sc_2O_3 and Gd_2O_3 from $Sc(MeCp)_3$, $Gd^iPrCp)_3$, and H_2O. *Chemistry of Materials*, 26(3):1404–1412, 2014.

[28] B. Han, J. M. Park, K. H. Choi, et al. Atomic layer deposition of stoichiometric Co_3O_4 films using bis(1,4-di-iso-propyl-1,4-diazabutadiene) cobalt. *Thin Solid Films*, 589:718–722, 2015.

[29] S. Seppälä, J. Niinistö, M. Mattinen, et al. Atomic layer deposition of lanthanum oxide with heteroleptic cyclopentadienyl-amidinate lanthanum precursor - Effect of the oxygen source on the film growth and properties. *Thin Solid Films*, 660:199–206, 2018.

[30] savannah 100 & 200 atomic layer deposition system user manual. cambridge nanotech inc.

[31] NIST X-ray Photoelectron Spectroscopy (XPS) Database. https://srdata.nist.gov/xps/main_search_menu.aspx.

[32] F. Söderlind, L. Selegård, P. Nordblad, et al. Sol–gel synthesis and characterization of polycrystalline $GdFeO_3$ and $Gd_3Fe_5O_{12}$ thin films. *Journal of Sol-Gel Science and Technology*, 49(2):253–259, 2009.

[33] A. P. Milanov. *MOCVD and ALD of rare earth containing multifunctional materials: from precursor chemistry to thin film deposition and applications*. Thesis, 2010.

[34] D. Raiser and J. P. Deville. Study of XPS photoemission of some gadolinium compounds. *Journal of Electron Spectroscopy and Related Phenomena*, 57(1):91–97, 1991.

[35] Y. Uwamino, T. Ishizuka, and H. Yamatera. X-ray photoelectron spectroscopy of rare-earth compounds. *Journal of Electron Spectroscopy and Related Phenomena*, 34(1):67 – 78, 1984.

[36] F. Söderlind, H. Pedersen, R. M. Petoral, et al. Synthesis and characterisation of Fe_2O_3 nanocrystals functionalised by organic acids. *Journal of Colloid and Interface Science*, 288(1):140 – 148, 2005.

[37] P. C. J. Graat and M. A. J. Somers. Simultaneous determination of composition and thickness of thin iron-oxide films from XPS Fe 2p spectra. *Applied Surface Science*, 100-101:36–40, 1996.

[38] E. Paparazzo. XPS analysis of iron aluminum oxide systems. *Applied Surface Science*, 25(1):1–12, 1986.

[39] A. P. Grosvenor, B. A. Kobe, M. C. Biesinger, et al. Investigation of multiplet splitting of Fe 2p XPS spectra and bonding in iron compounds. *Surface and Interface Analysis*, 36(12):1564–1574, 2004.

Chapter 5

CONCLUSIONS AND FUTURE PERSPECTIVES

In this thesis, we investigated the development of ALD processes for the synthesis of functional transition metal oxide-based thin films using novel or tailor-made precursors. The materials that have been investigated can be classified in the following categories: ALD Co_3O_4 thin films, ALD $Gd_xFe_yO_z$ ternary oxide thin films, and ALD Fe_2O_3@CNTs nanocomposites.

ALD Co_3O_4 thin films

Herein, we investigated a homometallic precursor $Co(DMOCHCOCF_3)_2$ for the synthesis of Co_3O_4 by ALD. $Co(DMOCHCOCF_3)_2$ is a robust complex due to the mixed O,N-coordination groups and CF_3- functional groups. As a result, this novel Co precursor could be safely handled in ambient conditions and exhibits long term stability. In our ALD system, the $Co(DMOCHCOCF_3)_2$ precursor was sublimed at 145 °C and combined with O_3 for cobalt oxide ALD. Well-defined ALD window has been identified in the 150 - 200 °C range with a constant GPC of 0.2 Å/cycle, which is comparable to commercial Co precursors. A linear thickness dependence on number of cycles has also been established, showing optimal behavior of this Co complex as an ALD precursor. The resultant films show poor crystallinity at the as-deposited stage. Pure phase polycrystalline Co_3O_4 can be obtained upon high temperature annealing process.

The ability to coat 3D structures by ALD Co_3O_4 from the novel Co precursor $Co(DMOCHCOCF_3)_2$ was investigated on TiO_2/C nanofibers under exposure mode. Results have shown well-defined nanofiber morphology after ALD coating procedure indicating that not degradation occurred under the studied ALD conditions. Qualitative STEM line profile confirmed the ideal core-shell structure of the ALD Co_3O_4 coated nanofiber which would be an attractive architecture for electrochemical energy storage devices.

CONCLUSIONS AND FUTURE PERSPECTIVES

Based on our experience in the novel ALD precursors, it can be safely stated that the mixing of functional O, N ligands, and the introduction of bidentate structures and CX_3^- (X being halide elements) moieties can be versatile solutions for designing and producing more powerful precursors with improved properties.

ALD $Gd_xFe_yO_z$ ternary oxide

For the synthesis of $Gd_xFe_yO_z$ ternary oxide system, two approaches have been explored. The first approach is the use of a novel heterobimetallic Gd-Fe precursor $GdFe(O^tBu)_6(C_5H_5N)_2$ with pre-fixed 1Gd:1Fe stoichiometry targeted for the synthesis of metastable $GdFeO_3$ orthoferrite. The heterometallic complex mainly contains alkoxide ligands, while pyridine as a neutral ligand was added to stabilize the Gd octahedral coordination sphere preventing oligomerization reactions. Upon optimization, the ALD process has been established for $GdFeO_3$ deposition with the precursor $GdFe(O^tBu)_6(C_5H_5N)_2$ heated at 170 °C and combined with O_3 at the deposition temperature of 200 °C, with the Gd-Fe stoichiometry successfully delivered into the films. With this complex, the phase-selective epitaxial growth of $GdFeO_3$ perovskite on (100)STO substrate has been achieved after post-annealing. The growth rate at 200 °C is ~ 0.19 Å per cycle, comparable to what has been reported for heterobimetallic precursors in literature. A linear thickness dependence has also been established so the $GdFeO_3$ film thickness could be easily tuned by varying the number of ALD cycles.

In the meanwhile, separate metalorganic sources, particularly, $Fe(Cp)_2$ or $Fe(^ipki)_2$ as Fe precursors and $Gd(DMDPG)_3$ as Gd precursor have been studied. Each iron oxide and gadolinium oxide binary process has been first established and optimized in our ALD system, then alternatively combined for building the ternary oxide under the compatible deposition conditions with 70 sccm N_2 carrier gas flow and O_3 as co-reactant at 250 °C. It has been observed that the iron oxide films from $Fe(Cp)_2$ and O_3 are polycrystalline in the as-deposited stage, with a mesoporous surface morphology, while the films from $Fe(^ipki)_2$ and O_3 are amorphous, dense and homogeneous. The spatial distribution of iron oxide in the chamber is also different. While with $Fe(Cp)_2$ homogeneous distribution can be obtained under exposure mode, with $Fe(^ipki)_2$ preferred deposition near the gas inlet has been identified, due to the high reactivity of this complex containing mixed O,N-coordination groups. Similar preferred deposition pattern has been observed for the gadolinium oxide deposition from $Gd(DPDMG)_3$ with all N-coordinated ligands. For ternary oxides, nominal stoichiometry has been obtained for all the samples and the films seem to have negligible contamination levels. The distinct chemistry in the two Fe sources has resulted in varied outcome of the $Gd_xFe_yO_z$ ternary oxide. Combining $Gd(DPDMG)_3$ and $Fe(Cp)_2$ has led to $Gd_3Fe_5O_{12}$ formation with traces of Gd_2O_3. However, using $Gd(DPDMG)_3$ and $Fe(^ipki)_2$ has resulted in

$Gd_3Fe_5O_{12}$ films coexisting with $GdFeO_3$, Gd_2O_3 and Fe_2O_3.

Regarding the synthesis of complex ternary oxide, the single-source heterobimetallic precursors seem to offer a straight-forward solution in obtaining ternary oxide with the matched stoichiometry and low temperature stabilization of metastable phases. On the other hand, the multisource supercycle approach appear to be more sophisticated and challenging. It can be expected that with additional aid from theoretical calculations or in-situ characterization tools, one can obtain more insight into the ALD surface reaction mechanisms to facilitate the synthesis of pure phase complex oxide thin films and further tuning the material properties.

ALD Fe_2O_3@CNTs nanocomposites

For this system, we have focused on studying the surface chemistry between ALD Fe_2O_3 and CNTs using using a commercial precursor $Fe(Cp)_2$ and O_3 to prepare Fe_2O_3@CNTs nanocomposites for supercapacitor applications. Conformal and homogeneous iron oxide coatings (6 nm and 30 nm thick) on CNTs have been realized via alternating $Fe(Cp)_2$ and O_3 pulses at 200–250 °C. As mentioned before, the CNTs surface are chemically inert and can subsequently hurdle ALD oxide nucleation. In this work, we have compared ALD Fe_2O_3 deposition on untreated CNTs (utCNTs) and two kinds of surface functionalized CNTs, specifically, water plasma treated CNTs (wpCNTs) and nitrogen plasma treated CNTs (npCNTs). It has been found that under the investigated conditions, ALD Fe_2O_3 nucleation took place regardless of the surface conditions, which could be attributed to the employment of strong oxidant O_3. However, less homogeneous Fe_2O_3 coatings has been identified in untreated CNTs. The evaluation of the electrochemical properties of the Fe_2O_3@CNTs nanocomposites revealed that Fe_2O_3@wpCNTs show optimal leakage resistance, double layer and mass capacitances. The result indicates that water plasma can effectively remove amorphous C and prepare the carbonaceous surface with sufficient anchoring sites for uniform ALD oxide coatings and intimate contact between Fe_2O_3 and CNTs, which is essential for obtaining the best electrochemical response. Besides, our study illustrates that the oxide coating layer should not be too thick, for example, the 30 nm Fe_2O_3@CNTs composites showed reduced active area and deteriorated electrochemical performance compared to the 6 nm ALD Fe_2O_3@CNTs.

With high quality continuous, smooth and conformal coatings demonstrated, this study confirms the capacity of ALD in the development of TMOs@C nanocomposites. Empowered by deepening knowledge of the interfacial chemistry during the ALD reactions, more stable and efficient electrode systems could be expected for improving the energy storage systems such as batteries or supercapacitors.

CONCLUSIONS AND FUTURE PERSPECTIVES

Currently, ALD is playing an increasingly important role for the processing of numerous novel materials besides oxides, enabled by its merits of atomic control over the depositing and engineering procedure. There has been continuous progress in the development of novel ALD precursors and ALD processes for multicomponent compounds. Still, more fundamental research are required for setting guidelines for precursor designing, achieving perfection for nanocomposites synthesis, and gaining profound comprehension of the underlining mechanisms for many ALD reactions, especially for complex multicomponent materials, which will no doubt fuel greatly the development of new architectures with fascinating new functions. Furthermore, with the current trend for building more heterostructures and inorganic/organic hybrid systems for miniaturized devices, ALD, along with other atomic layer processing techniques, can be envisaged to gain more attention and act as an essential tool for not only the semiconductor industry but also for many other application fields.